MULTIPHASE FLOW AND TRANSPORT IN FRACTURED GEOLOGIC ENVIRONMENTS

By

David Andrew Reynolds

A thesis submitted to the Department of Civil Engineering in conformity with the requirements for the degree of Doctor of Philosophy

Queen's University
Kingston, Ontario, Canada

August, 2001

Abstract

Two multiphase, multi-component compositional simulators have been developed and tested to serve as the tools for a detailed investigation of the physics of DNAPL (Dense, Nonaqueous Phase Liquid) flow through fractured porous and consolidated media. The movement of both the nonwetting and the aqueous phases have been studied at four levels of increasing complexity: single fracture, fracture network in a homogeneous porous medium, fractured lenses in a correlated random permeability field, and naturally fractured granite.

The single most important control on the rate of migration of DNAPL through a fracture is the aperture. The inclination of the fracture becomes increasingly important as it approaches horizontal and the gravity component of the driving gradient becomes zero. The influence of mass lost to the matrix through dissolution and subsequent diffusion is minor except in certain cases. A high solubility, low density, high viscosity DNAPL in a small (<15 μm) aperture fracture will exhibit noticeable retardation of the nonwetting phase migration rate.

The migration rate of Trichloroethylene (TCE) through fractured clay was found to be rapid, on the order of 10 m of vertical migration daily under a capillary driving force of approximately 14000 Pa. The existence of sand lenses within the clay unit increase the storage capacity of the system, and significantly reduce the migration time of the nonwetting phase through the system. The presence of a downward wetting phase gradient (upward flow) can arrest migration in the case of a finite volume release, and retards the nonwetting phase migration in the case of a continuous release. The loss of mass to the matrix through diffusion, while not affecting the

migration time of the nonwetting phase, effectively stopped the migration of the aqueous phase ahead of the nonwetting phase.

The presence of fractures in a spatially correlated permeability field ranging from coarse sands to clays is less significant in a global sense than the case of a layered system. The existence of fractures across otherwise impermeable capillary barriers does change the local scale distribution of the nonwetting phase, and allows for deeper penetration into the subsurface. Slow migration of the nonwetting phase is still occurring in all cases after 15 years. The rate of migration is a function of the system, the volume released, and the form of the constitutive relations used.

Large-scale capillary pressure-saturation curves for a two-dimensional representation of a fractured granite are producible, and a Representative Elementary Volume (REV) for the chosen system exists at a level allowing for tractable simulation. The underlying statistics of the aperture distribution control the shape and scaling of the curves similar to porous media. The large-scale effective permeability (combined intrinsic and relative permeability) curves are less affected by the aperture distribution, but exhibit significant anisotropy and saturation dependent behaviours. Dead-end fractures, which are hydraulically isolated, bias the large-scale relationships towards higher nonwetting phase saturations and reduce the apparent capillary hysteresis within the system.

Dedication

To Liam, for showing me that there will always be new aspects to life, and Lisa for showing that some things only get better.

Acknowledgements

The work contained in this thesis was supported, in part, through funding supplied by the Natural Science and Engineering Research Council of Canada through research grants to my supervisor Dr. Bernard Kueper and by the province of Ontario and Queen's University in Kingston, Ontario through scholarships to the author. Additional funding was supplied by PPG Industries in the form of a research grant to Dr. Kueper.

Dr. Bernard Kueper is acknowledged for his guidance in the matters of things computational and physical and appreciated for his dedication to the research program from which I have benefited greatly. Special thanks to Dr. Jonathan Shewchuk for use of Triangle© to generate Delaunay discretizations, and Judy Ehlan and Dawn Shuttle for access to field data on fractured granites. Jason Gerhard and Dr. Julie Konzuk are also acknowledged for showing interest and providing directions when the modelling was not going as well as it should.

Forward

This thesis has been written in manuscript form. Chapter 1 consists of an introduction to the general goals of the research contained within, and chapter 2 provides an overview of the current state of knowledge of numerical simulation of flow and transport in fractured media. Chapters 3 through 6 consist of manuscripts submitted to refereed journals for publication. Chapter 7 provides concluding comments to the thesis. The appendices present the details of the model development and validation/verification not present in the manuscripts.

Chapters 3 through 6 have been submitted to various referred journals, with David A. Reynolds listed as the primary author on the papers. Chapters 3, 5, and 6 are in submission to the Journal of Ground Water, Journal of Contaminant Hydrology, and Water Resources Research, respectively. Chapter 4 has been published in the Journal of Contaminant Hydrology (Vol 51, No. 1-2). All models described in this thesis have been developed by the author with contributions from Dr. B. Kueper. A summary of the major nomenclature used in this work is included immediately before Chapter 1.

Table Of Contents

List of Tables

List of Figures

GLOSSARY

Capillary Pressure – Pressure differential across the interface between two fluids

Displacement Pressure – Capillary pressure required for nonwetting fluid to enter a wetting fluid saturated medium

Intrinsic Permeability – The property of a porous material that is related to the ease with which gases and liquids can pass through it.

Relative Permeability – A factor between 0 and 1 which expresses the reduction in permeability of one fluid due to the presence of a second fluid

Effective Permeability – The combination of relative and effective permeability

DNAPL – Dense, Non-aqueous Phase Liquid

PSLG – Planar Straight Line Graph

REV – Representative Elementary Volume

TCE – Trichloroethylene

Compositional Simulator – A numerical model based on a mass balance of the components

CHAPTER 1 – INTRODUCTION

Dense, non-aqueous phase liquids (DNAPLs) represent a class of organic groundwater contaminants whose remediation poses a significant challenge from a technical standpoint. The extensive use of these chemicals in the past century, coupled with poor disposal practices has led to their widespread occurrence in groundwater worldwide. A particular class of these chemicals, known as chlorinated solvents, has become a common contaminant found in drinking water supplies in the United States (Pankow et al., 1996). Historical worldwide production of the four most common types (Trichloroethylene, Tetrachloroethylene, 1,1,1-Trichloroethane, and Methylene Chloride) is estimated in the tens of billions of kilograms (Pankow et al., 1996).

Design of effective remediation procedures for drinking water supplies contaminated with chlorinated solvents requires an accurate understanding of the physics involved in the migration of the various phases of the contaminants (pure, dissolved, and volatalized) as well as a sound understanding of the geology through which the contaminant is moving. A complicated situation exists when during the course of a DNAPL's migration it encounters a low permeability barrier that is not a perfect capillary barrier and allows DNAPL passage through imperfections such as fractures or root holes. Historically these capillary barriers have been viewed as an effective method of preventing downward migration of surface contaminants. The presence of hydraulically active and interconnected fractures in these barriers, however, provides a migration pathway through the system.

The migration of contaminants through fractured geologic systems has been the focus of intense study in the previous decade, primarily due to the growing interest in the disposal of spent nuclear fuel in deep crystalline bedrock. The development of numerical models capable of simulating the migration of organic contaminants in fractured environments has historically followed two paths, those dealing with the migration of the aqueous phase (Sudicky and Frind, 1982; Harrison et al., 1992) and those dealing with the migration of the non-aqueous phase (Kueper and McWhorter, 1991; Pruess and Tsang, 1990). Given the large number of physical processes occurring during the migration of a DNAPL through a fractured environment (phase partitioning, sorption, matrix diffusion, etc.) the use of models capable of dealing with all these factors is desirable.

The use of compositional simulators in porous media (Forsyth, 1991; Unger et al., 1995; Reitsma and Kueper, 1998) has shown their exceptional abilities in dealing with the complexities of phase migration and transitioning. The use of compositional simulators in a fractured environment has been limited to a multiple porosity approach used by Pruess (1991), and that of Slough and Sudicky (1999).

The focus of this work is to develop an understanding of the physics controlling the migration of the nonwetting and dissolved phases through fractured geologic environments. This is accomplished through the development of two individual codes, FRACAS, a two-dimensional Control Volume Finite Element formulation that is used to model non-orthogonal situations, and QUMPFS, a three-dimensional Control Volume formulation restricted to orthogonal fracture situations. The analyses of successively more complex environments is undertaken, using the

developed models as tools. QUMPFS is used to perform a comprehensive study of DNAPL migration in fractured non-consolidated environments, beginning at the single fracture scale, and progressing through layered and heterogeneous geologic environments. FRACAS is then employed in a Representative Elementary Volume Study in a fractured consolidated environment, to determine the possibility of dimensionality reduction (performing predictive simulations in two-dimensions) in the simulation of DNAPL migration.

1.1 References

Forsyth, P.A. 1991. A Control Volume Finite Element Approach to NAPL Groundwater Contamination, *SIAM J. Sci. Stat. Comp.*, 12, p 1029-1057.

Gerhard, J.I., Kueper, B.H., and G.R. Hecox. 1998. The Influence of Waterflood Design on the Recovery of Mobile DNAPLs. *Ground Water*, 36(12), p 283-292.

Harrison, B. Sudicky, E.A., and J.A. Cherry. 1992. Numerical Analysis of Solute Migration Through Fractured Clayey Deposits Into Underlying Aquifers, *Water Res Res*, 28(2), p 515-526.

Kueper, B.H. and E.O. Frind. 1991. Two-phase Flow in Heterogeneous Porous Media: 2. Model Application. *Water Res. Res.*, 27(6), p 1049-1057.

Kueper, B.H., and D.B. McWhorter. 1991. The Behaviour of Dense, Non-Aqueous Phase Liquids in Fractured Clay and Rock, *Ground Water*, 29, p 716-728.

Kueper, B.H., and D.B. McWhorter. 1992. The Use of Macroscopic Percolation Theory to Construct Large-scale Capillary pressure Curves, Water Res. Res., 28(9), p 2425-2436.

Pankow, J.F., and J.A. Cherry. 1996. *Dense Chlorinated Solvents and Other DNAPLs in Groundwater*, Waterloo Press, Portland, Oregon.

Pruess, K., and Y.W. Tsang. 1990. On Two-phase Relative Permeability and Capillary Pressure of Rough-walled Rock Fractures, *Water Res. Res.*, 26(9), p 1915-1926.

Pruess, K. 1991. TOUGH-2 – A General Purpose Numerical Simulator for Multiphase Fluid and Heat Flow, *Rep. LBL-29400, Lawrence Berkeley Lab.*

Reitsma, S. and B.H. Kueper. 1998. Non-equilibrium Alcohol Flooding Model for Immiscible Phase Remediation: 1. Equation Development, *Adv. Water Res.*, 21(8), p 663-678.

Sudicky, E.A., and E.O. Frind. 1982. Contaminant Transport in Fractured Porous Media: Analytical Solutions for a System of Parallel Fractures, *Water Res. Res.*, 18(4), p 1634-1642.

Unger, A.J.A., Forsyth, P.A., and E.A. Sudicky. 1996. Variable Spatial and Temporal Weighting Schemes for use in Multi-Phase Compositional Problems, *Adv. In Water Res.*, 19(1), p 1-27.

CHAPTER 2 – LITERATURE REVIEW

This chapter presents an overview research on wide range of topics focused on the requirements necessary for the modelling of fluid flow and transport in fractured porous media. Emphasis will be placed on the secondary porosity features such as fractures, as the majority of fluid flow through crystalline rock occurs in these spaces. The requirements for accurate modelling in these types of geologic environments can be grouped into two categories; the representation of the physical geology and the numerical approach used in the simulation. Key requirements for the translation of the field geology into a tractable modelling domain are estimations of fracture frequency and intensity, aperture distribution, and bulk rock properties. The numerical process used in the simulations will be a function of the goals of the modelling and the level of simplifying assumptions that can be made.

2.1 Physical Properties of Fractured Geology

2.1.1 Spacing, Trace Length, and Orientation of Fractures

Snow (1970) visually determined fracture frequency in granites up to 400 feet deep from seven boreholes. It was determined that the spacing of fractures tended to increase with depth, and that the distributions were not well represented by common statistical distributions and were strongly skewed towards the small frequencies (lower intensities). Ehlan (1999) studied the distribution of fracture spacing in granites across Southeast Asia, and found that for horizontal fractures

lognormal, normal, exponential, and Weibull distributions provided fits at the 95% confidence interval in weathered granites, but no distribution adequately fit the data for fresh granites. In general, Ehlan (1999) found that vertical and sub vertical fracture spacing could not be adequately represented with any of the proposed distributions. Narr and Suppe (1991) investigated the fracture spacing in the sedimentary rocks composing the Monterey Formation and found that the fracture spacing within individual beds tended to follow a lognormal distribution. In addition to fracture frequency, other fracture parameters, such as fracture length, trace length, and orientation, can also be expressed in the form of statistical distributions.

In a study to examine the effects of geometry in fracture flow modelling, Andersson and Dverstorp (1987) showed that the population of fractures intersecting a plane ($g'(r)$), if the fractures are assumed to be circular discs, is a biased representation of the fracture radius distribution ($g(r)$):

$$g'(r) = \frac{rg(r)}{\int_0^\infty rg(r)dr} = \frac{rg(r)}{r'} \qquad [2\text{-}1]$$

where r is the fracture radius, and r' is the expected fracture radius. Using this, the trace lengths observed in a field data set can be fitted to a lognormal distribution. The fracture density distribution in the model was produced using a Poisson distribution similar to that of Snow (1970).

Kulatilake et al. (1993) sampled a 36 m long ventilation drift in a granitic rock mass to investigate different geometrical approaches to the modelling of fracture networks. In a 10m long statistically homogeneous section of the drift, it was found that either a gamma or an exponential distribution best fit the trace length data, with the gamma distribution being slightly better than the exponential.

Ehlan (1999) found that trace length as a property was the least important criteria when matching a synthetic three-dimensional fracture network to a mapped data set. Assuming that a three-dimensional feature is a disk, one cannot determine from a typical outcrop or pavement whether one is measuring a minimum, a maximum, or an intermediate distance across the disk. Assumptions about the relationship between the observed trace lengths and the actual fracture diameters must be made, and little data exists for these predictions.

Robertson (1970) mapped more than 9000 traces from the De Beers mine in South Africa and found that the strike length and dip length traces have approximately the same distribution, implying that the form of the fractures may be equidimensional. Bridges (1975) however, indicated that fractures are not equidimensional and show preferential elongation. The equidimensional assumption is commonly used in the development of joint network models (Dershowitz et al., 1995).

The statistical representation of the orientation of fractures has traditionally relied upon strike and dip measurements taken in outcrops and, in certain cases, boreholes or tunnels. Stereo plots of the poles (orthogonal unit vectors) allows for grouping of fractures into sets which are they modelled distinctly using some distribution to represent the variation in orientation. Dershowitz et al. (1995) present five different approaches to the probability distribution for the directional orientation data; the univariate and bivariate Fisher, the bivariate normal, the bivariate Bingham, and the spherical Dirac delta distribution.

Cacas et al. (1990) took 1000 fracture orientation measurements from field data and applied a Fisher-von-Mises probability density function to the data:

$$f(\alpha) = \frac{\overline{K}}{2\sin(\overline{K})} e^{\overline{K}\cos(\alpha)} \sin(\alpha) \qquad [2\text{-}2]$$

where $\overline{K}$ is the propagation of the probability density function (pdf) and α is the angle between the mean direction of the ensemble of fracture poles and any individual fracture pole. Kulatilake et al. (1993) found that neither a Bingham nor a spherical distribution was an adequate match to the data sampled from the ventilation drift.

Long and Witherspoon (1985) in a detailed study found that fracture frequency and orientation, even if known explicitly, is not enough to define a fracture network for modelling purposes. For a complete assessment, the aperture of the fractures, and specifically the aperture distribution must be known and taken into account.

2.1.2 Fracture Aperture

Historically, the modelling of flow through fractures has used the approach where the fracture is represented by two parallel plates a set distance apart (Long and Witherspoon, 1985). Given the surface roughness of naturally occurring fractures, this solution is, at best, only an approximation. To fully define permeability and flow in a fractured environment the aperture of each fracture must be known precisely, and, as the aperture varies within every fracture, the aperture distribution is also required.

Gokhale and Underwood (1990) presented a study of a method for determining the surface roughness of a fracture by sectioning planes normal to the average topographic plane of the fracture surface. The quantitative descriptor of the surface roughness, the surface roughness parameter R_s, is defined as:

$$R_s = \frac{S}{A_p} \qquad [2\text{-}3]$$

where S is the true surface area, and A_p is the apparent projected area parallel to the average topographic plane of the surface. The profile roughness parameter (R_L) is analogous and defined as:

$$R_L = \frac{L}{L_p} \qquad [2\text{-}4]$$

where L is the true length of the profile and L_p is the apparent length. They found that with a small number of vertical image analyses on the fracture surface, the surface roughness parameter could be accurately found. In a second paper (Gokhale and Drury, 1990) the practical considerations of the approach are addressed, finding that with as few as three vertical images the surface roughness factor can be approximated with less than 6 percent error within the 95% confidence interval.

Patir (1978) presented a numerical method for the production of Gaussian and non-Gaussian surface roughness profiles. With a prescribed frequency distribution and autocorrelation function Patir (1978) determined profiles using linear transformations on random matrices produced under the statistical requirements. Comparison to actual surface profiles in tribological applications yielded encouraging results.

Several other experimental techniques have been developed to determine the aperture distribution of single isolated fractures. Myer et al. (1985, 1986) used a low melting point metal invasion technique, Witherspoon and Long (1987) used a form of mercury porosimitry, Gale (1987) and Gentier et al. (1989) used various forms of resin injection, and Brown et al. (1986) tried composite topography.

The purpose of these methods, in some form or other, was to attempt to produce an accurate statistical representation of the aperture distribution in a single fracture. The most significant problem with these physical methods is their inability to produce results without destroying the fracture, and the limited applicability of the generated data to large systems. The determination of the statistical parameters defining the aperture distribution of a single fracture is not sufficient, as slight perturbations or different realizations will have significantly different flow patterns. Vickers et al. (1992) found that correlations at two different scales existed even within a single fracture, one on the order of millimetres, and the other over tens of centimetres.

Investigations into the aperture distribution across networks began with the work of Bianchi (1968) who showed that the distribution of fracture apertures found in 225 samples of a granite outcrop obeyed a lognormal distribution. This was not, of course, the distribution of apertures within a single fracture, but rather the distribution of apertures in the fracture set. Assuming that this is indicative of a similar distribution at depth, Snow (1970) developed equations representing the distribution of aperture sizes (2b), based on a probability distribution function of aperture cubed:

$$\eta_1 = \frac{2\eta^{5/9}}{\left(\eta^2 + \omega^2\right)^{1/9}} \qquad [2\text{-}5]$$

$$\omega_1^2 = \frac{4\eta^{8/9}}{\left(\eta^2+\omega^2\right)^{1/9}} - \frac{4\eta^{10/9}}{\left(\eta^2+\omega^2\right)^{2/9}} \qquad [2\text{-}6]$$

where η and ω^2 are the mean and variance of the probability density function describing the aperture cubed, and η_1 and ω_1 the mean and variance in aperture (2b).

Snow (1970) calculated the statistical parameters for 127 data sets, consisting of cumulative frequency plots of exposed fracture apertures, from different depth zones at 29 sites in a variety of rocks. It was found that the computed apertures of joints in granite, gneiss, meta-volcanics, schists, slates, and sandstones differ less from site to site at the same depth than they do within a single site as depth increases. This would indicate that the compressive stress, or stress history of a fractured rock mass may be a controlling factor in the determination of statistically described apertures.

It is easy to envision that a fracture will close with the application of normal stress, either through the compression or destruction of the points of contact (asperities) within the fracture. In fact Raven and Gale (1985) found that complete closure often occurred beyond 5 MPa of applied normal stress (approximately 200 m depth). Brown and Schulz (1985) and Zimmerman (1990) found that the increase in the contact area in a fracture was roughly proportional to the increase in the applied normal stress given that some elastic behaviour was occurring. Raven and Gale (1985) and Gale (1987) found, however, that cyclic loading gave rise to permanent deformation in the fracture through crushing of asperities and local shear transformations.

2.1.3 Permeability of Fracture Networks

Snow (1970) interpreted permeability distributions generated through repetitive packer testing along a single borehole to be composed of two variables, each with their own distribution: the number of fractures per test length, and the apertures of those fractures.

Constant flow rate water injection tests in a borehole can be used to find permeability through:

$$k = \frac{Q}{S_h h} \qquad [2\text{-}7]$$

where Q is the discharge, h is the net head (water column at collar of packer test plus depth to the watertable), and S_h is the shape factor given by:

$$S_h = \frac{2\pi L}{\ln(2L/d)} \qquad [2\text{-}8]$$

where L is the length, and d is the diameter of the hole.

Snow (1970) initially assumed that a Poisson distribution holds for the number of fractures intersected, and this distribution is defined by the zero discharge points (test lengths intersecting no conductive fractures) of the well tests, which are taken as the frequency of zeros in a Poisson distribution. Tsang and Witherspoon (1983), however, pointed out that fractures must be inherently random to obey a Poisson distribution, which is seldom the case in nature. The assumed randomness of fractures in space will be discussed in a later section.

The visual observations of Snow (1970) also exhibited the trend towards congregation of fracturing (an observation which supports the position of Tsang and Witherspoon (1983)). Snow (1970)

compared fracture distribution statistics generated through the measured permeability of fractured rock masses (obtained through water injection tests) to the visual studies. In the study it was found that the average number of fractures per test predicted from the Poisson distribution was approximately 80% of the visually measured data.

Snow (1970) adjusted the Poisson distribution from the packer tests to achieve concordance with the visual observations by adding approximately 20% more fractures. With this adjustment the discharge (Q) for a uniform parallel fracture set of equivalent fractures normal to a borehole can be defined as:

$$\overline{Q} = 0.62Q \qquad [2\text{-}9]$$

This represents a physical scenario of three randomly oriented orthogonal sets with uniform spacings.

Using the theory of conditional expectation, the statistical parameters of the distributions of individual discharges may be obtained from the parameters of distributions of total discharges through:

$$\eta_{\dot{Q}} = \eta_{\overline{Q}} / \kappa \qquad [2\text{-}10]$$

$$\varepsilon^2_{\dot{Q}} = \frac{\varepsilon^2_{\overline{Q}}}{\kappa} - \frac{\eta^2_{\overline{Q}}}{\kappa} \qquad [2\text{-}11]$$

where η and ε are the mean and standard deviation of the individual fractures (Q) and the total discharges (Q) respectively, and κ is the average number of fractures per test length. Snow (1970) found that for the 127 sets of discharge data the following least squares fit was obtained:

$$\log(\varepsilon_Q) = 0.098 + 1.055\log(\eta_Q) \qquad [2\text{-}12]$$

Snow (1969) developed an anisotropic permeability model of fractured rock having non-orthogonal fracture sets with distributed apertures (constant aperture within a single fracture). Using the Navier-Stokes equation for parallel plate flow, and statistical representation of fracture orientations and spacings, the permeability tensor of a single fracture set can be defined as:

$$k_{ij} = \frac{2}{3}\sum \frac{(b)^3}{\left|n_i \overline{D}_i\right|}\left(\delta_{ij} - m_{ij}\right) \qquad [2\text{-}13]$$

where n_j is the normal vector, D_i is the distance between fractures along a sampling line (not necessarily orthogonal to the fractures), δ is the Kronecker delta, and $m_{ij}=n_i n_j$, where n_i is the direction cosine of the fracture. For the special case of parallel fractures (orientation n_i identical) with n_i also a coordinate axis (say the 3 axis), $n_1=n_2=0$ and $n_3=1$ so:

$$\begin{vmatrix} k_{11} & k_{12} & k_{13} \\ k_{21} & k_{22} & k_{23} \\ k_{31} & k_{32} & k_{33} \end{vmatrix} = \frac{2}{3D}\begin{vmatrix} 1 & 0 & 0 \\ 0 & 1 & 0 \\ 0 & 0 & 1 \end{vmatrix}\sum b^3 \qquad [2\text{-}14]$$

or:

$$k_{11} = k_{22} = \frac{2}{3D}\sum b^3 \quad , \quad k_{33} = 0 \qquad [2\text{-}15]$$

Snow (1969) coupled this approach with the work of Snow (1970) to compute the permeability of fractures sets in one, two, and three dimensions. Evaluation of the permeability tensor, however, requires a relationship between an aperture and each fracture orientation. Given the difficulty in obtaining such data from real rock masses, a Monte Carlo approach was used. Through such an analysis Snow determined that the anisotropic permeability ellipsoid of a single set of fractures is an oblate spheroid, which will flatten as fracture alignment improves. Two orthogonal sets of fractures with equal statistical properties will plot as a prolate spheroid, with its maximum parallel to the intersection of the sets and twice that on an isotropic plane normal to both sets. With this

approach, three equal homogenous fracture sets represent a statistically isotropic media. The principal axis of any arbitrary system can be estimated from a stereo plot of their normal vectors, but cannot be specified without a measured aperture distribution.

The basis for the formulation of equation [2-13] was revisited by Oda and Hatsuyama (1985) to account for the concept of non-infinite fracture lengths. Their approach produces an expression for the equivalent permeability tensor:

$$k_{ij} = \chi\left(P_{kk} D_{ij} - m_{ij}\right) \qquad [2\text{-}16]$$

where:

$$D_{ij} = \frac{\pi\rho}{4}\int_0^{t_m}\int_0^{r_m}\int_\Omega (2r)^2 t^3 n_i n_j E(n,r,t)\, d\Omega\, dr\, dt \qquad [2\text{-}17]$$

where χ is a dimensionless constant between 0 and 1/12, approaching 1/12 with increasing size of the fracture (areal size), ρ is the dimensionless volumetric density of the fractures, r is the fracture areal radius, t is the fracture aperture diameter, $E(n,r,t)$ is a probability density function describing the occurrence of fractures, and Ω is the solid volume. The approach provided an improved fit to the data of Snow (1969), but is inherently cumbersome to use.

Long and Witherspoon (1985) examined the permeability of a two dimensional network of fractures where all fractures have the same aperture and length. The networks are thus homogeneous, and any decrease in permeability from Snow's theory is due entirely to reduced interconnectivity between fractures. They found that, as fracture length increases, the degree of interconnectivity increases and the permeability increases, with the endpoint of the system (representing total inter-connectivity) approaching a porous medium.

Renshaw (1996) has raised a significant question about the use of stochastically generated fracture systems to model physical systems, specifically in regards to fracture connectivity and flow. In an investigation centred on assessing the importance of "realistic" fracture networks produced through fracture growth models, he found that the flow characteristics of stochastically generated fracture systems with randomly located fractures may not be representative of naturally occurring fracture systems. Specifically he found that the flow characteristics of networks generated with a growth rate exponent (a power law function of the energy available for fracture growth) of greater than 1 form connected pathways at significantly lower spatial densities than those predicted by stochastic methods. The production of such networks (with growth rate exponents greater than 1) is not precluded in nature.

2.1.4 Hydraulic Testing of Fractures

Preliminary hydrogeologic investigations in fractured rock environments often use single hole packer tests to produce estimates of hydraulic conductivity and specific storage. The analysis of these tests is somewhat more complicated than similar tests in porous media, as the actual transmissivity of the fracture is independent of the packer interval. The possibility of short-circuiting of flow through open boreholes in fractured rock, in addition to the domination of flow by the most permeable units make the use of packer testing preferable to open hole testing.

Analysis of hydraulic testing completed in single boreholes tends to treat the tested interval as an isotropic porous medium intersected by a single permeable fracture. Flow in the test interval can

be thought of as occurring in one of three ways; spherical, radial, or linear (NRC, 1996). Spherical flow is the closest approximation to porous media, where the equipotentials are concentric spheres around a spherical cavity extending in three dimensions. Radial flow (or cylindrical flow) approximates flow to the borehole as occurring in a homogeneous confined layer of infinite horizontal extent. The equipotential surfaces in this case are cylinders centred about the well axis. Linear flow is non-variant in space, and is conceptualized as flow oriented perpendicular to the fracture plane, causing equipotentials to be planar and parallel to the plane of the fracture.

Combinations of these three base states are possible, and a continuum between them was proposed by Barker (1988) with the concept of a fractional flow dimension. This term describes the power law relationship between the distance from the test interval and the area available for flow. This relationship can be generalized as:

$$A = \alpha_d r^{d-1} \qquad [2\text{-}18]$$

where A is the area available for flow, α_d is a proportionality constant that is a function of d, the Euclidean integer dimension (1, 2, or 3), and r is the distance from the well. If the value of d is allowed to be real (as opposed to integer) the fractional flow represents combinations of the three models. Barker (1988) hypothesizes that the fractional flow number represents a fracture network that exhibits fractal geometry.

2.1.5 Fractures as Fractals

The field of fractal geometry was developed by Mandelbrot (1983) to describe a large class of irregular and fragmented patterns found in natural settings. In general, fractal objects are the result

of the repetition of a given algorithmic rule or pattern over a multitude of separate and differing length scales. Two properties of fractals are particularly applicable to the study of fractured rock: first, the concept of integer spatial dimension (1 for a line, 2 for a plane, 3 for a volume) expanded to become a parameter characterizing rough or heterogeneous items in nature; and second, the scaling invariance of a fractal structure.

If a fracture is indeed a fractal entity then a rough profile of the fracture measured across a large path will be geometrically similar to a fine profile taken across a smaller pathline. Given the difficulty in obtaining fracture aperture data for *in-situ* circumstances, and allowing for the applicability of fractal theory to fracture representation, fractal scaling properties may be used to deduce geometric structures at small scales from large-scale measurements. Under these assumptions Oron and Berkowitz (1998) demonstrated a non-linear increase in contact area and a faster than cubic decrease in hydraulic conductivity with decreasing aperture. In addition they found that the aperture distribution was not lognormal or gamma, but was of a truncated normal form.

Using log-log variogram analysis Wang et al. (1988) performed a study on aperture correlations using a single fractal fracture with fractal dimension between 2 and 3. They took a single mirror image fracture and displaced it incrementally through space to simulate shear movement. They found that, if the fractal nature of the fracture surface can be proven, the aperture of a smooth fracture (D close to 2) is highly correlated over distances much larger than the shear displacement. For rougher fractures (D closer to 3) however, the aperture becomes uncorrelated within a range shorter than the shear displacement. In addition, for the special case of D=2.5, the variogram

describing the aperture correlation is proportional to the lag distance, the same relationship as is employed in the spherical model used widely in geostatistical analysis (Kriging for example).

Barton and Larsen (1985) measured all fracture traces greater than 20 cm in length on three ash-flow tuffs pavements in Nevada. They found that the distribution of trace lengths was lognormal, and the orientation could not be adequately represented statistically. Using a graphical plotting method, they found that each laterally separated pavement was indeed a fractal entity, and the fractal dimensions were tightly clustered (1.12 to 1.16). This was in spite of the fact that visually, the individual fracture networks appeared quite different. The study also found that the network patterns were scale independent over two orders of magnitude ranging from 20 cm to 25 m. In a related work Barton and Hsieh (1989) found, however, that a power law could also be used in the representation of the fracture trace lengths that were recorded.

Acuna and Yortsos (1995) combined an investigation of fractal fracture representation and transient flow through a fracture network. In producing a fractally governed fracture network, the theory of fragmentation (Gilvarry, 1964) was adopted. It is based upon the probability that a fragment with length between l and $l+dl$ will be further fragmented. Acuna and Yortsos found that, in a space of dimension D, if each block creates an average of S_{pf} new blocks, a power law could describe the resulting size distribution with exponent:

$$D = \frac{\ln\left(S_{pf}\right)d}{\ln S} \qquad [2\text{-}19]$$

where d is the dimension of the system, and S is the reciprocal of the size of the new blocks. This is also the fractal dimension obtained through the method of Barton and Larsen (1985).

Barnsley (1988) introduced the Iterated Function System (IFS) to construct fractal images. With this technique a fractal is obtained from an initial simple shape by iteratively applying a set of numerical transformations. After several iterations the superimposed sets converge to a fractal. Using IFS and fragmentation theory Acuna and Yortsos (1995) produced 3-D fracture sets to be used in flow analysis.

In general, with an increase in the fractal dimension fewer of the original blocks remain unfractured, the number of fractures increases, and the size of the fractures may increase. For an integer value of D, a single pattern must repeat throughout the domain, and it must be of a similar size.

2.2 Single Phase Flow in Fractures

2.2.1 Single Phase Flow in a Single Fracture

Single-phase flow in fractures was initially investigated over twenty years ago (Wilson and Witherspoon (1974)), and has remained an area of intense study (Witherspoon et al. (1980), Neuzil and Tracy (1981)). The majority of work has been based on the premise of parallel plate flow, where a fracture is conceptualized as two smooth parallel plates of infinite extent that are not in contact. If the flow is steady and isothermal, the equation for one-dimensional flow between two parallel plates is:

$$Q = \frac{b^3}{12\mu}\nabla P \qquad [2\text{-}20]$$

where Q is the volumetric flow rate per unit width, b is the distance between the plates, ∇P is the pressure gradient, and μ is the dynamic viscosity. This formulation is commonly referred to as the cubic law. This formulation is also presentable in terms analogous to Darcy's law, in which the permeability k, is equivalent to the aperture squared over 12 so that:

$$Q = \frac{kb}{\mu}\nabla P \qquad 2\text{-}21]$$

In recognizing that rock fractures are not smooth surfaces, but rather highly rough surfaces, the flow through a single parallel plate fracture can be expressed in terms of a friction factor f (Romm, 1966; Witherspoon et al., 1980):

$$Q = \frac{1}{f}\frac{b^3}{12\mu}\nabla P \qquad [2\text{-}22]$$

Witherspoon et al. (1980) found that, in artificially induced fractures in granite, basalt, and marble, f ranged from 1.04 to 1.65. Other approaches have been taken to model flow through a rough walled fracture; Tsang and Witherspoon (1981) replaced the parallel plate aperture with an average over the surface of the fracture, and Walsh (1981) computed a correction to the cubic law which is proportional to the ratio of inter-fracture space to theoretical space.

Neuzil and Tracy (1981) also modified the cubic law to account for roughness of fracture walls. In this case the aperture distribution is no longer a delta function (0 closed, 1 open), but rather some other shape. Given the aperture density distribution n(b), Neuzil and Tracy proposed a modified cubic law formulation:

$$\frac{Q}{\Delta h} = C\int_0^\infty (2b)^3 n(b)db = C\left\langle (2b)^3 \right\rangle \qquad 2\text{-}23]$$

This corresponds to a physical situation where the openings of the fracture vary only in the direction normal to flow, resulting in fluid movement along parallel paths that involve no tortuosity.

Tsang (1984) performed a theoretical investigation of the effects of path tortuosity and connectivity on fluid flow rate through a single rough walled fracture (using an electrical analogue similar to that of Sundaram and Frink (1983)), to asses the effects of aperture variation parallel to the hydraulic gradient. Tsang found that the more small apertures there are in the aperture distribution, the larger the effect of tortuosity. When the fraction of contact area between the fracture surface rises above 30%, the aperture distributions are invariably large at small apertures, and the effect of fracture roughness and flow path tortuosity depress flow rate from the predictions of the parallel plate model by three or more orders of magnitude.

More advanced conceptualization of single-phase flow through a rough walled fracture requires a different approach (Brown, 1987). The simplified Reynolds equation, a particular form of the Navier-Stokes equation for steady state flow of an incompressible fluid between two stationary plates can be written as:

$$\nabla \cdot \left(\frac{d^3}{12\mu} \Delta p \right) = 0 \qquad [2\text{-}24]$$

where $d(x,y)$ is the local thickness of the fluid film and $p(x,y)$ is the local fluid pressure. Equation (24) can also be developed if it is assumed that the cubic law is valid at a local-scale and that mass is conserved (Walsh, 1981):

$$\nabla \cdot Q = 0 \qquad [2\text{-}25]$$

The Reynolds equation is particularly valid for the simulation of fractures that are not completely open. Brown (1987) uses the Reynolds equation and a fractal model of fracture surfaces (See Part I) to investigate the effects of surface roughness on flow through a single fracture. He found that actual flow between rough surfaces, at the range of closure expected during elastic deformation, was about 70-90% of that predicted by the parallel plate model.

Muralidhar (1990) performed a comprehensive evaluation of the effects of tortuosity (due to contact area) on fluid flow in a fracture. He found that the equivalent permeability of a fracture depends on both the aperture and the contact area. The Darcy model was found to be applicable if the ratio of the mean fracture aperture to the characteristic length of the fracture was less than 0.016. Above this level tortuosity effects become important and the Reynolds equation must be used. It was also found that permeability does depend on the pattern of distribution of contact area, however, the dependence becomes less significant as the mean aperture decreases. Oron and Berkowitz (1998) support these findings, and suggest that contact ratios as small as 0.03 to 0.05 can impart enough tortuosity to significantly affect the assumed hydraulic conductivity of a fracture.

Tsang and Tsang (1987) presented a model of flow through fractures termed the channel model. In this approach the entire fracture space is represented as a series of tortuous and intersecting channels with varying aperture along their length (a concept similar to that of a heterogeneous distribution of apertures). The parameters that characterize the channels are: the aperture distribution; the effective channel length and width; and the aperture spatial correlation length,

which gives the spatial range within which the aperture values are correlated. This channel model will be described further in the context of flow in fracture systems.

Tsang and Tsang (1989) also presented a simulation of flow in a single fracture represented by a strongly heterogeneous permeable medium. A lognormal aperture distribution, in conjunction with a spatial correlation length and an anisotropy ratio, was used to develop a 2-D flow field in a single fracture. A square portrayal of a fracture was discretized into square meshes to which different aperture values, subject to the statistical parameters, were assigned. Darcy's law was assumed to be valid within each subdivision, where the permeability was assumed to be proportional to the square of the local aperture. The fluid pressure may then be computed at each node assuming a constant pressure difference across the single fracture on two opposite boundaries with no-flow conditions on the other two boundaries. The flow rates can then be calculated from the potentials at each node.

The previously summarized work has identified the requirement of an accurate knowledge of the fracture aperture distribution for simulation of single-phase flow in a fracture. The difficulties of obtaining a representative distribution were identified in Part I, and therefore some balance needs to be achieved between the complexities and uncertainties regarding the aperture distribution and the requirements of the modelling process. The use of the Reynolds equation provides a more flexible solution technique but is significantly more challenging than the cubic law approach, and may not be required in most cases. Reitsma (1992) defines four flow regimes that will dictate the approach required for successful modelling:

1) If the fracture is very open, flow may be indistinguishable from the parallel plate model;
2) If the fracture is partially closed and the contacts are localized in sparse clusters the flow may be non-linear even at low Reynolds numbers and flux will not be proportional to gradient;
3) If the fracture is partially closed but the contacts are finely distributed, flow may be close to that of a porous medium, meaning that flux is linearly related to the gradient and potential theory applies;
4) If the fracture is very closed the flow may be in tortuous channels, producing an essentially 2-D network of 1-D conductors.

2.2.2 Single Phase Flow in a Network or Set of Fractures

The expansion from single-phase flow in a single fracture to flow in a fracture system is a large mathematical leap rather than a large conceptual one when fractures are treated explicitly, as flow within each individual fracture is still governed by the above equations. Factors such as numerical solution method, domain discretization levels, and computational implementation have dominated the published literature on this subject. Beyond the numerical aspects of simulation of single-phase flow in fracture networks, alternative conceptualizations of the problem have also been introduced. Conceptual models of single-phase flow in a set of fractures can be broken into three broad categories: discrete fracture approaches, where each individual fracture is modelled as a discrete entity in an impervious rock matrix; equivalent porous medium approaches, where the entire rock mass is conceptualized as a porous medium which combines both flow through fractures and through the rock matrix itself; and dual porosity or dual continuum representations,

where transfer between the rock matrix is coupled to flow through the fractures through some mathematical approach. It should be noted that these three approaches are also applicable to single phase flow in a single fracture, but are more commonly associated with flow in networks.

2.2.2.1 Discrete Fracture Representations

Discrete fracture models are based on the premise that the behaviour of fluids within the system can be predicted based on the knowledge of the fracture geometry. This requires that either the location, size, orientation, and aperture distribution of each fracture be known explicitly, or the statistics governing the distributions of each feature can be measured and used to generate different realization of the networks with the same properties. The requirements for the distributions, and the difficulties in their interpretation were presented in section 2.1 of this chapter.

The uncertainties of the statistical distributions can be overcome to some degree by conditioning the system based on available data. Anderson and Thunvik (1986) found that preserving the location of more known features with each realization decreased the uncertainties when using discrete fracture models as predictive tools. They also found that knowledge of the bulk permeability of a fracture network reduced the uncertainties more so than the collection of further geometric data.

Three basic approaches to the modelling of fluid flow in discrete fractures have been adopted; semi-analytical methods (Long et al., 1985), reduction of three-dimensional fracture representations to a series of one-dimensional pipes (Segan and Karasaki, 1993), and the planar discretization of a three-dimensional assemblage of two-dimensional fracture features (Dershowitz et al., 1995). The recent emergence of low-cost, high performance computers has led to the

adoption of the third approach in many situations. A brief history of the most significant of the approaches follows.

Elsworth (1986) used a boundary element procedure to simulate flow through a statistically constructed framework of fractures represented as Poisson discs. The procedure was found to work well, especially at reducing the required computational effort. Unfortunately the solution is only capable of handling fractures of constant, or average hydraulic, aperture. A similar model was proposed by Andersson and Dverstorp (1987), which had the advantage of a more realistic fracture generation system (see Part I) and incorporated a search algorithm (which occurred before the solution procedure) to remove fractures that did not affect the flow regime.

Cacas et al. (1990) presented a model for a discrete fracture system, with a similar physical representation to that of Elsworth (1986), with the addition of channelling effects. The nodes of their network no longer represented the fracture intersections, but rather the fracture disc centres. Flow is assumed through bonds joining the centre of each disc to an adjacent disc, provided the fractures are connected. The bonds are composed of two parts, one for each fracture, meeting at the intersection of the two discs. Each part is assumed to be equivalent to the set of channels inside that fracture that ensure the hydraulic linkage with the connected fracture. Each portion of a bond is assigned a hydraulic conductivity representative of the fracture as a whole. The drawback of this method is that it is not a true discrete representation, and requires field-testing for the values of hydraulic conductivity in the bonds. These are not equivalent to the values of the fracture, as the bond depiction alters reality by arbitrarily increasing the length of the connection.

Nordqvist et al. (1996) presented a model written to investigate the effects of high transmissivity fractures on solute transport. The method combined the models of Andersson and Dverstorp (1987) and Moreno et al. (1988). This gave a Poisson distribution of circular fractures in a 3-D network, each composed of a 2-D network of varying aperture distribution. The model is solved by first considering the flow in the single fractures and producing an equivalent transmissivity for a unit hydraulic gradient across a unit width. The actual orientation and sizes of the fractures in the set modify these transmissivities by assuming that each individual fracture transmissivity is linearly dependent on fracture intersection width, and inversely proportional to distance within the network. A hydraulic gradient is then applied across the entire domain, and with appropriate boundary conditions and the previously calculated transmissivities, the head values at each fracture are found. The model's particular application, solute transport, allows for this rather broad simplification to be valid, as the errors in the transport procedure greatly outweigh the flow solution errors.

Miller et al. (1995) produced an adaptable discrete fracture simulator (MAFIC), which allowed for simulation of transient flow and transport through three-dimensional networks of triangular finite elements. The matrix is either represented explicitly through a Galerkin finite element approach, or a dual-porosity generic matrix block scheme.

Several other researchers have presented discrete fracture models that discretize the matrix and the fractures in one continuum, and apply differing hydrogeologic properties to each individual element of the discretization (Therrien and Sudicky, 1998; Slough and Sudicky, 1999). These will

be discussed in section 2.4 as they are primarily focused on multi-phase flow and transport in fractured environments.

2.2.2.2 Dual-Porosity Representations

The major conduits for fluid flow in saturated fractured rock environments are the fractures, with the surrounding matrix providing storage capacity, but very little actual transfer of fluid. In the majority of dual-porosity representations, the matrix is assigned a non-zero porosity but has no interconnectivity with itself and can play a significant role in the transient response of a fractured rock mass. The two different porosities are treated as overlapping continua, with the actual shapes of the matrix blocks being idealized based on some simplifying assumptions.

The first dual-porosity formulation was introduced by Warren and Root (1963) and further refined by Barenblatt et al. (1969) in which fractured rock is treated as a medium with coupled fracture and matrix porosities, in which averaged hydraulic parameters are used for both the matrix and the fractures. The location and behaviour of individual fracture elements need not be specified in this approach, which makes it applicable to situations where data on individual fractures cannot be obtained. A drawback of this approach is the complete reliance upon the statistical method adopted in the continuum representation.

Other works have focused on the mathematical aspects of a dual-porosity representation. Wilson and Witherspoon (1974) presented a finite element simulation of dual-porosity flow through fractured rock under a dam. The method was limited, however, as no direct coupling of the fracture and matrix flows was performed to link the continua and simplify the equations. Streltsova (1976) presented an analysis of dual-porosity behaviour by performing a Theis-type

analysis and representing the matrix-fracture system as an aquifer (fracture) with a leaky aquitard (matrix). This approach is a convoluted method of solution, but has the advantage of being semi-analytical in nature.

Duguid and Lee (1977) presented the first comprehensive analysis of dual-porosity simulation of a fractured rock mass. They realized that two sets of governing equations were required, one for each type of porosity. The storage equation in the primary (matrix) pores is:

$$(1-\phi_2)\phi_1\beta\frac{\partial P_1}{\partial t}+(1-\phi_2)\phi_2\beta\frac{\partial P_2}{\partial t}+\frac{\Gamma}{\rho}-\frac{k_1}{\mu}\nabla^2 P_1=0 \qquad [2\text{-}26]$$

where ϕ is the porosity, β is the coefficient of compressibility of water, P is the space averaged incremental pressure in the matrix, v is the velocity, Γ is the mass flow rate from block to fracture, ρ is the density of water, k is the intrinsic permeability, and the subscripts *1* and *2* refer to the matrix and fracture respectively. Similarly the continuity equation for fluid flowing in the fractures is:

$$(1-\phi_1)\phi_1\beta\frac{\partial P_1}{\partial t}+(1-\phi_1)\phi_2\beta\frac{\partial P_2}{\partial t}-\frac{\Gamma}{\rho}+\nabla\langle v_{2s}\rangle=0 \qquad [2\text{-}27]$$

where q_{2s} is the space-averaged velocity in the fractures relative to the solid. The coupling equation takes the form of:

$$\langle v_{2s}\rangle=-\left(\frac{k_2}{\mu}\right)\left[\rho\left(\frac{\partial\langle v_{2s}\rangle}{\partial t}\right)+\nabla P_2\right] \qquad [2\text{-}28]$$

Duguid and Lee (1977) solved the system of governing equations with the Galerkin finite element method and performed various iterations to assess the response of the coupled system to different drawdown scenarios. For cases of a permeable matrix they showed that the first response in the system was seen in the fractures due to the large relative size difference between the fractures and

the matrix pores. For drainage, the matrix first supplied fluid to the fractures, which in turn transmitted it through the system. This finding revealed that without consideration of a porous matrix, the rate of response in the fractures to a drawdown scenario would increase substantially.

The model of Duguid and Lee (1977) proved adequate but cumbersome and computationally inhibited. Huyakorn et al. (1983) describe three different approaches to the solution of the governing equations for dual-porosity flow developed by Duguid and Lee (1977) based on differing representations of the fracture-matrix fluid interaction (quasi-steady and unsteady state leakage). The primary focus of the paper, however, is on comparison of numerical techniques in the solution of the equations, rather than on the performance of the different representations.

Moench (1984,1995) expands the dual-porosity model to include the effects of fracture skin, a common coating of fracture surfaces found in many crystalline rocks. He found that the formulation of Duguid and Lee (1977), and Huyakorn et al. (1983) in respect to the coupling term was a special case of his general formulation, and in fact the quasi-steady state model of Huyakorn et al. (1983) required some form of lower conductivity feature (such as a fracture skin) impeding flow between the matrix and the fracture.

Moench (1984,1985) also found that the presence of a fracture skin gave transient matrix to fracture flow. When the skin has a lower permeability than the matrix, the resistance to flow through the skin homogenizes the gradient within the matrix. This gave a theoretical justification for the pseudo steady state linkage of Duguid and Lee (1977), in which the mass flow decreases with time to a steady state value, and the divergence of flow in the blocks is ignored.

Hamm and Bidaux (1996) extended the work of Moench (1984,1985) with respect to fracture skin effects through the use of a fractal analysis of the system. Their model is compared to field data composed of observation well response to drawdown from a pumping well in a fractured system. The fractal approach allowed for a better representation than a Euclidian approach, but cannot be used in a predictive sense for a second observation well.

2.2.2.3 Equivalent Porous Medium Representations

In a conventional representation of an equivalent porous media (EPM) approach, individual fractures are not explicitly rendered, and the hydraulic properties of the domain represent the volume-averaged contributions of many fractures. The size of the region under consideration must be large enough that there is no dependence upon a single feature's hydraulic or physical properties. The application of EPM theory is best suited to cases dealing with flow from large and extensively fractured and connected rock masses. In cases where fracture density or connectivity is low, the single continuum assumption may be inadequate.

One of the first attempts to represent a fractured rock medium with an equivalent porous medium was conducted by Long et al. (1982). In their assessment they concentrated on the required elements for a basis of similarity between porous and fractured media. One of the major requirements for Darcy's law in three-dimensions to be valid is a symmetric permeability tensor. This means that for a fractured rock mass to behave in a homogeneous, anisotropic manor, it must be able to be represented with a symmetric permeability tensor, a situation that cannot be directly measured at a large (field) scale. To fulfil the homogeneity requirement, a definable representative elementary volume (REV) must be able to be defined. The work of Snow (1969) has shown that

such a volume may not exist for a fractured rock mass, and that the permeability of fractured rock may continue to increase with the volume tested. Overall, two main points were raised from this study, both of which must hold for a fractured rock mass to be treated as a homogeneous anisotropic porous medium; first, there is an insignificant change in the value of the equivalent permeability tensor with a small addition or subtraction to the test volume (test volume provides a good statistical sample of the heterogeneities); and second, an equivalent permeability tensor exists which predicts the correct flux when the direction of gradient in a REV is changed (independent of boundary conditions).

Sagar and Runchal (1982) also presented an equivalent porous medium model, in which a fictitious continuum was established based on a similarity of permeabilities between the fractured rock and the equivalent porous medium. They pointed out that the general assumption of extensive and continuous fractures, which is geologically incorrect, has a great affect on the equivalent permeability of the model domain. They also pointed out that for the permeability tensor to be symmetric three conditions must hold; first, the fractures are extensive (or infinite); second, the fracture plates have a rectangular shape; and third, the fractures lie in three orthogonal planes defined by the coordinate system. Given the fact that most crystalline rock is beset by a minimum of three sets of non-orthogonal fractures (see Part I), these conditions would seem impossible in a realistic setting.

2.2.2.4 Percolation Theory

The simulation of water flow through fracture networks has also been investigated with the use of percolation theory (Engleman et al., 1983; Berkowitz, 1995) in which random geometries of fractures can be mapped to an orthogonal network of bonds with open bonds distributed randomly

according to a given probability, and lattices linking bonds in three directions. By allowing the bond aperture to vary, aperture variability within a fracture can be simulated. The critical values of probability at which the network becomes conductive are termed the percolation threshold.

The total discharge through the network (Q_{tot}) is:

$$Q_{tot} = \sum_{i=1}^{L} \frac{P_{i,L-1} - P_2}{l} \left(\frac{r_{i,L-1/2} w}{12\mu} \right) \qquad [2\text{-}29]$$

where P is the pressures in connected sites, l is the bond length, w is the bond width orthogonal to the flow direction, and μ is the dynamic viscosity. The flow rate in a bond is proportional to r^3 in two dimensions.

Margolin et al. (1999) used percolation theory to study the dependence of the hydraulic conductivity of fracture systems on aperture variability and interconnectivity, in addition to describing a relationship between simulation scale and permeability. The most important finding from their work was a rapid decrease in bulk hydraulic conductivity with increasing standard deviation of the aperture distribution. This relationship becomes more important as the percolation threshold in reached, and is similar to findings using the cubic law.

2.2.2.5 Other Representations

Shapiro and Andersson (1983) presented a unique approach to the debate between discrete and continuum approaches by producing a model that integrates the two approaches, as well as flow through a porous matrix. In areas where knowledge of the fractures is extensive, the model used a boundary element approach to solve for the flow in the fractures and coupled flow in the porous

matrix through a similar method to that of Duguid and Lee (1977). In areas where fracture data is less defined, or only global effects are required, the domain was represented with an EPM approach. Elsworth (1987) used an isoparametric coupled boundary element-finite element procedure to improve on the results of Shapiro and Andersson (1983) by improving computational efficiency and therefore increasing accuracy through greater discretization and a more efficient and robust solution method.

The previously mentioned channel model presented by Tsang and Tsang (1987) is a simplification of a discrete fracture model, with inherent empirical properties. Flow through a tight (non-porous) rock medium was conceptualized as being through a limited number of tortuous and intersecting channels. This hypothesis was arrived at upon inspection of work into flow visualization (Pyrak et al. (1985), Bourke et al. (1985)), which showed the formation of preferential pathways in single fractures at both the lab and the field scale. The proposed channels have varying apertures along their length and are characterized by an aperture density distribution, an effective length and width, and a spatial correlation length. No physical basis exists in this model to distinguish between flow through a single fracture or channel and flow through the connected fractures in a multi-fracture network. In this way the channel model is similar to an equivalent porous representation.

Tsang and Tsang (1987) formulated their model with a uniform aperture density distribution and a specified correlation length, from which they generated 1-D channels using standard geostatistical methods (Journel and Huijbregts, 1978). In cases where measured aperture distributions do not follow a normal or lognormal distribution, the data is modified to a common cumulative frequency. Tsang and Tsang (1987) compared their model to tracer data breakthrough curves for a single

fracture and reported reasonable agreement. The jump to a fully 3-D representation, however, requires some knowledge of the network parameters, and for systems where fracture spacings and sizes are comparable to the characteristics lengths of measurement, the statistical approach is not valid, and the channel length needs to be treated in a deterministic manner, thus reducing the simplicity and applicability of the model.

Acuna and Yortsos (1995) hypothesized that the fractal properties of a network of fractures can be inferred from log-log plots of well pressure vs. time in a fractured rock aquifer. Assuming that Darcy's law applies in each fracture, that all fractures have the same permeability, and that aperture and length are uncorrelated, their theory proved to be sustainable provided that a significant number of fracture generations was allowed, or, equivalently, that the object is fractal over a large enough range of scales.

Acuna et al. (1992) performed fractal based analyses on several sets of well data taken from the literature. They found that the majority of the responses could be termed fractal, and most tend to have a dimension less than 2, either because production thickness is small when compared to areal extent or due to the presence of impermeable layers. The theories proposed by Acuna and Yortsos (1995) and Acuna et al. (1992) do not allow for the determination of all fractal parameters from a single test well, and also do not consider correlations of aperture or length. In the case of a positive correlation between fracture aperture and length, large fractures may dominate transient behaviour at early time, thus producing a fractal-like response from a Euclidean network, and thus invalidating the approach.

The selection of a "most accurate" or "best" approach to single phase flow modelling in a network of fractures cannot be made in a generic sense. Trade-offs must be made between data acquisition and computational efficiency. Given the hypothetical situation of exact data of fracture statistics (aperture, length, frequency, and orientation distributions, and interconnectivity) and unlimited computational power, the use of the Reynolds or cubic equations in a discrete fracture system would yield the most accurate solution. The exchange relationship between matrix and fracture in such a system remains, however, to be exactly defined and modelled.

2.3 Mass Transport

In conjunction with hydraulic testing, tracer tests are often used in to explore the interconnectivity of the fracture network, as well as to provide an estimate of the transport properties (i.e. dispersivity), and chemical reaction parameters (i.e. distribution coefficient). The analysis consists of selecting a conceptual model for the behaviour of the system, and then numerically attempting to simulate the field test through parameter estimation. Three types of tracer tests are commonly conducted; natural gradient, convergent/divergent, and two-well.

The use of natural gradient tracer tests, in which a tracer is injected into the natural flow system and monitored at a downgradient grid of wells, is the ideal method for studying the natural flow system as little or no perturbations are involved. In fractured rock environments, however, serious difficulties exist in providing a sampling grid dense enough to capture a significant amount of the tracer, given the tortuous and braided pathways taken by the solute (Abelin et al., 1991). In

addition, in low permeability systems the extraction of samples from the monitoring wells will stress the system and change the natural conditions (Lapsevic et al., 1999)

Convergent/divergent tracer tests involve establishing an artificial flow field through the injection (divergent) or extraction (convergent) of water from a single borehole. Once a steady state situation has been developed, a tracer is placed into the system (either in the injection well for divergent or at another well for the convergent) and its arrival is monitored at the extraction well for convergent tests or at other wells for the divergent test.

Two-well tracer tests involve the extraction of water from a single borehole, and re-introducing that water into the injection borehole. After the flow system is at steady state a tracer is added to the injection well and the breakthrough curves from the extraction well are used in the analysis. A serious drawback of this approach is the arrival time of each particle of solute is dependent upon the streamline it has followed, and the breakthrough curve is therefore less a function of dispersion than of path.

Solute transport in fractured rock environments operates under similar processes as that of porous media, with a few significant conceptual differences. The advection and dispersion of mass within the system is described through the use of the average velocity field, and the local-scale dynamics through the use of a dispersion tensor. Dagan (1986) and Gelhar (1986) have suggested that the classical Fickian approach to the simulation of dispersion in porous media may not be valid for the analysis of tracer tests, as the relatively short distance of travel may not allow true Fickian dispersion to evolve. Sonnenborg et al. (1999) also found indications that, at the lab scale, the

parameters required to accurately simulate breakthrough curves in fractured permeable media, were not representative of the Fickian dispersivity of the system. Stafford et al. (1999) found that the inclusion of several truncated discrete fractures to promote transverse dispersivity within an EPM approach allowed for adequate simulation of a field scale tracer experiment. The values for transverse dispersivity within the EPM were set to zero such that only the presence of the fractures (as well as numerical dispersion) would provide transverse spreading. Novakowski (1992) also hypothesises that the large values of dispersivity that are commonly returned from tracer test analysis are due, in part, to large mixing volumes in test boreholes.

The four conceptual models presented in section 2.2 for single-phase flow also have their equivalents in terms of representing solute transport in fractured environments. The concept of an appropriate scale for the single porosity approach is again a serious issue in the development of the required effective porosity and dispersion terms. The standard assumption of an isotropic dispersion tensor is almost certainly invalid in fractured media given the anisotropy prevalent in the hydraulic conductivity field. Neuman (1990, 1994) has proposed an approach to scale the dispersivity of fractured environments with domain size, but there has been no work to provide a field evaluation of this approach.

A significant difference between the conceptual models for flow in a porous media and flow in a fractured rock environment is the existence of a large immobile zone representing the matrix in fractured rock. The loss of solute mass to the rock matrix (when there is little or no fluid exchange between the fractures and the matrix) is known as matrix diffusion, and can account for significant retardation of the solute plume when matrix porosities are large. Typically the matrix blocks are

approximated with an appropriate geometric shape similar to methods used for dual porosity flow studies. Sudicky (1990) proposed a geometry-dependent mass transfer parameter (α) to simulate the exchange between fracture and matrix:

$$\alpha = \frac{d\theta_{im} D^{*}_{im}}{B^{2}} \qquad [2\text{-}30]$$

where d is an integer equal to 3 for a slab approximation to the matrix and 15 for a sphere approximation, θ_{im} is the immobile zone (matrix) porosity, D^{*}_{im} is the immobile zone effective molecular diffusion coefficient, and B is either the fracture spacing for slabs or the sphere radius.

2.4 Two Phase Flow in Fractures

In the analysis of multiphase flows it is important to distinguish between the fluid phases and the components. Throughout a fluid phase, properties such as pressure, temperature, and viscosity vary continuously and smoothly from point to point, while these properties undergo discontinuous changes at phase boundaries. The interfacial tension effects at the interface between fluids gives rise to capillary pressure, and fluid components may distribute themselves among phases according to solubility and volatility. For this work, only two-phase systems will be considered, primarily those composed of organic chemical NAPLs and water. Unlike a water-water vapour system, in an oil-water system the phase saturation in a region can only change if the invading phase occupies a continuous flow path through the region. The occupancy of any area in the domain for an oil-water system, therefore, depends on a local "allowability" criterion and a global "accessibility" criterion.

2.4.1 Two Phase Flow Fundamentals

2.4.1.1 Capillary Pressure

As mentioned previously, the effects of interfacial tension between two phases gives rise to capillary pressure. The capillary pressure is defined as the difference in pressures across the interface between two immiscible fluids. The greater pressure will exist in the fluid on the concave side of the interface, this being termed the nonwetting fluid. This terminology evolved from the fact that in the presence of a solid surface, one fluid will preferentially "wet" the surface. The wetting criterion is defined through the use of the contact angle, the angle that the interface makes with the solid surface. The wetting fluid is the fluid through which the contact angle is measured to be less than 90 degrees, consistent with the convex side of the interface.

Capillary pressure may be quantitatively defined as:

$$P_c = P_{nw} - P_w \qquad [2\text{-}31]$$

where P_c is the capillary pressure, P_{nw} is the nonwetting phase pressure, and P_w is the wetting phase pressure. In order for the nonwetting phase (usually the NAPL in a water-NAPL system) to enter a "void" occupied by the wetting phase, the capillary pressure must be large enough that the interface between the two fluids is of such a form as to allow entrance. For entrance into a fracture, Kueper and McWhorter (1991), assuming that locally the fracture resembles a parallel plate opening, performed a force balance for entry into the fracture:

$$P_e = \frac{2\sigma\cos\theta}{e} \qquad [2\text{-}32]$$

where P_e is the entry pressure of the fracture, σ is the interfacial tension between the two fluids, θ is the contact angle measured through the wetting phase, and e is the fracture aperture giving rise to the first continuity of the nonwetting phase. Assuming a circular aperture, rather than the parallel plate approach yielded:

$$P_e = \frac{4\sigma\cos\theta}{e} \qquad [2\text{-}33]$$

Kueper and McWhorter (1991) postulate that the true entry pressure for a fracture will lie somewhere between the values given by (2-32) and (2-33), but most likely closer to (2-32).

By examining equations (2-32) and (2-33) it can be seen that the entry pressure is directly proportional to the interfacial tension, and inversely proportional to the aperture. Given a variable aperture fracture of large extent in both directions orthogonal to aperture, it can be seen that the amount of nonwetting phase in that fracture will increase for larger fractures, and for lower interfacial tensions. The specific relationship between the capillary pressure in the system and the amount of nonwetting phase in the fracture (also termed saturation) is commonly quantified through the use of a capillary pressure-saturation curve. These curves are readily measured in the laboratory for porous media, but are less readily available for fractured media. Figure 2-1 depicts a capillary pressure-saturation curve for a single fracture taken from Reitsma and Kueper (1994). The data is well fit by a Brooks-Corey relationship (Brooks and Corey, 1966):

$$S_e = \left(\frac{P_c}{P_D}\right)^{-\lambda} \qquad [2\text{-}34]$$

where P_c is the capillary pressure of interest, P_d is the displacement (or entry) pressure, λ is a pore-size distribution index (or aperture distribution index) and S_e is an effective wetting phase saturation given by (Brooks and Corey, 1966):

$$S_e = \frac{S_w - S_r}{1 - S_r}, \quad 0 \le S_e \le 1 \qquad [2\text{-}35]$$

where S_w is the wetting phase saturation, and S_r represents the residual wetting phase saturation.

2.4.1.2 Relative Permeability

When two fluids are present in a rock fracture, the presence of each will interfere with the mobility of the other. This is expressed in terms of relative permeability, k_r, so that for a medium with intrinsic permeability k, the effective permeability to fluid 1, given the presence of fluid 2, is kk_{r1}. The relative permeability varies from 0 to 1, with 0 expressing severe (total) interference and total immobility of the phase.

The effective wetting phase saturation is related to relative permeability for the water phase through (Brooks and Corey, 1966):

$$k_{rw} = S_e^{((2+3\lambda)/\lambda)} \qquad [2\text{-}36]$$

and to the nonwetting phase through (Brooks and Corey, 1966):

$$k_{r_{nw}} = (1 - S_e)^2 \left(1 - S_e^{\left(\frac{2+3\lambda}{\lambda}\right)}\right) \qquad [2\text{-}37]$$

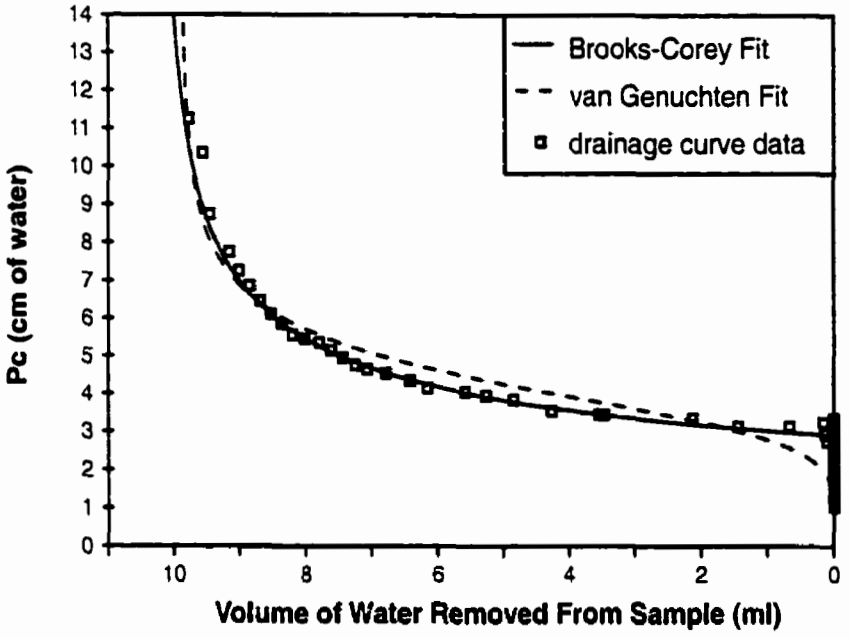

Figure 2-1. Capillary Pressure Curve for Single Rough Walled Fracture (Reitsma and Kueper, 1994)

Very few references can be found in the literature to studies conducted which solely examine relative permeability effects in fractures (Reitsma (1992), Reitsma and Kueper (1994), Pruess and Tsang (1990), Mendoza (1992), and Persoff and Pruess (1995)), but the work of Reitsma (1992) has lent credence to the fact that similarities exist between fracture behaviour and the much more intensely studied porous media behaviour.

Fulcher et al. (1985) studied the effects of Capillary Number and its constituents on relative permeability curves in porous rock. They found that k_{rnw} was only a function of interfacial tension

and viscosity, and not of capillary number (defined as the ratio of viscosity times velocity to interfacial tension times porosity). The wetting phase permeabilities, on the other hand, were a function of capillary number. They also observed no rate effects with flow rates between 16 and 80 ft/day.

Persoff and Pruess (1995) performed laboratory tests on replicated natural rough-walled fractures to measure relative permeability for a gas-liquid system. They found that even at rigorously controlled pressure boundary conditions, instabilities developed within the fracture due to capillary effects and pressure drops due to viscous flow. Measurements of relative permeability showed significant phase interference, with relative permeabilities drastically reduced at intermediate saturations. They also found that the proposed relationship $k_{rw}+k_{rnw}=1$ for a gas-liquid system (Gilman and Kazemi (1983), Rossen and Kumar (1992)) was not valid except for at very small wetting/nonwetting saturations.

Simulation of fracture flow can be considered either as a limiting case of flow in a porous medium or as an elaboration of pipe flow. Historically, the porous medium approach has been used for situations involving saturated flow. This approach, when extended to two-phase flow, emphasises the importance of capillary and viscous forces, and neglects inertial forces. Under conditions of high velocity and relatively open fractures, such as near a production well, the mechanisms may involve inertial and/or turbulent flow effects. In such situations, a two-phase pipe flow approach may be warranted.

The following sections provide a brief outline of modelling efforts to date on two-phase flow in fractures. They are broken down into three distinct categories, representing the different special interest groups which are actively researching the areas: Air/Water systems, Gas/Oil systems, and NAPL/Water systems.

2.4.2 Two-Phase Air/Water Systems

The majority of work on two-phase flow in fractures to date has dealt with the special case of air-water flows, particularly as they related to high-level radioactive waste storage in unsaturated rock masses. Fourar et al. (1993) performed a series of air/water experiments in smooth and artificially roughened fractures (glass plates). They found that the relationship between pressure drop and flow rate was not linear for any situation other than a smooth, parallel fracture. This deviation from linearity indicated a deviation from Darcy's law (see section 2.2), but not necessarily turbulent flow. The experiments also showed that no static flows existed, but rather moving structures in which only one phase is continuous were formed. This behaviour was found at hydraulic apertures of approximately 1.0 mm, for a range of hydraulic gradients of 1 to 20 kPa/m.

To account for the deviation from Darcy's law, Fourar et al. (1993) formulated an amendment to Darcy's law based on an empirical correction factor (B) calibrated from the flow rate vs. pressure drop data:

$$-\frac{dp}{dx} = \frac{12\mu}{b_h^3} Q + B\frac{\rho}{b_h^3} Q^2 \qquad [2\text{-}38]$$

where Q is the volumetric flow rate per unit width, and b_h is the hydraulic aperture derived from the intrinsic permeability:

$$k = \frac{(2b)^2}{12} \qquad [2\text{-}39]$$

Fourar et al. (1993) used the data from their experimental work to assess three different models for two-phase flow in a fracture: porous medium (Darcy's Law); pipe flow (Navier Stokes); and equivalent homogeneous flow.

For the Darcy model, as the flow regime is air/water, capillary pressure is negligible and the relative permeability values are solely functions of the viscosity, fluid velocities, pressure gradient and hydraulic aperture. Experimental work found that the relative permeabilities were not purely functions of saturation under these conditions, and Darcy's law was inaccurate at the Reynolds numbers in the experimental set-up. The pipe flow model was a better fit to the data than the Darcy model, but the homogeneous model, with all fluid properties averaged was found to give the best fit for the experimental data. In this model, however, the pressure drop was solved through a correlation between an empirical friction factor, and the average Reynolds number of the two fluids. This procedure is of little practical use to large-scale problems.

Peters and Klavetter (1988) developed a continuum approach model to the simulation of water flow in a porous, fractured, unsaturated rock mass. In this situation, as pressure head is negative, most of the water in the rock will be in the porous matrix, with only small pendulous rings and films within the fractures. The fracture conductivity in this case will approach, but not be equal to, zero. As the matrix saturation increases, the fracture saturation will also increase, but in a highly

non-linear manner. The conductivity of the fracture will also increase, up to the point of zero pressure head, or saturated conditions.

The method of Peters and Klavetter (1988) used a continuum approach, developed from the methods of Duguid and Lee (1977) that equates the fluxes through the matrix and the fractures. They developed their model based on the assumption that the pressure heads in the fractures and the matrix are identical in a direction perpendicular to flow. They validated their model through comparison to an analytical model of matrix recharge from partially saturated fractures. The 1-D recharge model, however, was extremely limited by assumptions required for solution

Rasmussen (1991) used a boundary integral method to simulate flow and transport in a partially saturated vertical fracture, and a theoretical fracture set. Using a sharp interface approach (different from the continuum approach of Peters and Klavetter (1988)) Rasmussen (1991) found good agreement between his method and analytical solutions and laboratory experiments. His simulations produced a point of interest: that zones of water were present under both positive and negative pressure head. The implications of this are twofold: first, the equivalent continuum models which assume uniform pressure heads within a fracture may provide inaccurate predictions of velocities; and second, regions of saturation will be present in vertical fractures at pressures heads greater than the critical capillary suction of the fracture (pressure head at which fracture de-saturates). Unfortunately the discrete fracture approach, solved through the BIM, requires significant computational space, so much so as to make modelling of realistic scales presently impossible.

Wang and Narasimhan (1985) performed a modelling study to investigate the aspects of air/water flow in a fractured porous medium. They hypothesized that, as the material drains, the water will be held in by capillarity in the finer grained matrix. In addition, as fracture surfaces are not smooth, where fracture apertures are small, islands of water film will be held (after significant drainage), joining adjacent matrix blocks across an otherwise impermeable fracture. With the presence of high air phase saturations, the conductivity of the fracture will decline significantly, eventually becoming lower than that of the porous matrix.

Wang and Narasimhan (1985) developed theoretical relationships between fluid pressure head and fracture saturation, pressure head and fracture conductivity, and pressure head and the portion of the surface that remains wetted. With some simplifying assumptions, they found that simulation of flow under partially saturated conditions could be adequately modelled with a minimum of specific fracture data. The highly transient system response in going from saturated to partially saturated conditions was, however, extremely sensitive to the actual fracture properties, and, therefore, the inherent assumptions.

Abdel-Salam and Chrysikopoulos (1996) coupled several diverse aspects of fracture flow (fracture skin, stochastic aperture distribution, and dual-porosity) in a quasi-three dimensional (the matrix is represented by a series of 2-D grids linked orthogonal to a fracture) finite element model. Their results are experimentally supported by Wan et al. (1996) who found that increased matrix permeability tends to reduce the formation of wetting phase fingering in the fracture. Abdel-Salam and Chrysikopoulos (1996) also found that an increase in the standard deviation of the fracture

aperture distribution led to a faster increase in potential across the system, and an increase in correlation length led to a decrease in total flux across the fracture.

The experimental work of Wan et al. (1996) also proved the theoretical results of several others researchers, that with initial wetting phase saturation of fractures from a porous matrix, great increases in transmissivity are gained through small increases in the wetting phase saturation. The mechanism for this is through the formation of preferential flow "wedges" along contact of the matrix blocks.

Therrien (1992) examined saturated/unsaturated flow and contaminant transport in a three-dimensional space consisting of fractured rock with a porous matrix. In contrasting the effects of matrix permeability, he found that when the matrix had a high permeability it controlled the overall flow and concentration profiles in the sandstone, and no preferential migration of the contaminant along the fractures was seen until complete wetting phase saturation was achieved. This finding is in contradiction to the experimental work of Wan et al. (1996).

2.4.3 Two-Phase Gas/Oil Systems

Horie et al. (1990) presented a laboratory study investigating the degree of capillary interconnection across matrix blocks in a gas/oil system. Using a series of stacked column experiments, in which matrix blocks were stacked vertically in a core holder, the investigation showed strong capillary interaction between neighbouring blocks. Three models were proposed for the capillary pressure of the fracture: $P_c=0$, $P_c=Constant\ (non\text{-}zero)$, and $P_c=P_c(S_w)$. Their

results showed that, for two-phase flow, the first two models were inconsistent with the laboratory data. They could not, however, propose a functional for the third model, but reasoned that, given the failure of the first two representations, the third seemed logical.

Firoozabadi and Hague (1990) expand upon the work of Horie et al. (1990) by further investigation of the form of the capillary pressure functional in the fractures of an oil/gas dual porosity system. Assuming that the form of the capillary pressure relationship is similar to that of porous media, and based on the work of Iwai (1976) and Schrauf and Evans (1986), Firoozabadi and Hague (1990) conceptualized a fracture as a pair of parallel plates with shallow cone shaped asperities extending from each plate to touch at their tips. Using a graphical procedure to solve, explicitly, for the shape of the liquid bridge between solid surfaces, the saturation-capillary pressure relationship is found. With this relationship it was found that the maximum capillary pressure at 100% saturation (for an asperity angle of incidence of 5 degrees) was $1.8\sigma/b$ (where b is the fracture aperture). This is in comparison to the parallel plate model where $Pc=2\sigma/b$. In the cases where the angle of incidence rises to 15 and 30 degrees, the maximum capillary pressures are $1.46\sigma/b$ and $0.35\sigma/b$, respectively, showing that the parallel plate approximation becomes less valid as the angle of incidence increases. The physical effect of the increase in the angle of incidence is to increase the aperture of the fracture, as well as the porosity, and to decrease the tortuosity. This will most likely decrease viscous effects, and lower the capillary pressure. This is in direct contrast to the generally accepted fact that, in non-contact scenarios, as the aperture increases, the parallel plate approximation becomes more valid.

In a discussion of Firoozabadi and Hague (1990), Sahdi (1991) found great fault with their conceptual and experimental approach. His comments are specified in three main points: first, that the calculated value of fracture capillary pressure was incorrect; second, that the use of a single capillary pressure curve for imbibition and drainage was incorrect; and third, that the maximum value of P_{cf} (fracture capillary pressure) was too high. Sahdi (1991) examined the results of Firoozabadi and Hague (1990) from a constriction approach, where the interaction between matrix blocks is limited by some constriction coefficient, based on the work of Dodson and Carwell (1945) for slotted well liners. In a reply to the discussion of Sahdi (1991) Firoozabadi (1991) defends each point well, but the overall applicability of the initial paper is difficult to assess, and, if Sahdi's (1991) comments are taken as correct, limited.

The basic difference between the formulations of Firoozabadi and Hague (1990) and Sahdi (1991) lie in the components that control the system. Firoozabadi and Hague (1990) found that the fracture capillary pressure is the controlling factor over the matrix saturation levels, whereas Sahdi (1991), based on unpublished data, found exactly the opposite. The finding of Sahdi (1991) implies that the fracture capillary pressure has no effect on the wetting fluid saturation in the matrix. This seems intuitively incorrect, but may be true given certain boundary conditions.

Land (1968) presented a series of relationships for the capillary pressure-saturation dependence for both two- (gas/liquid) and three-phase (gas/oil/water) systems in rock. The focus was to produce equations which satisfied an empirical relationship of residual nonwetting phase saturation to initial nonwetting phase saturation that was hypothesized based on reported work published to that

point. The work develops similarly to that for porous systems, and deals only with intact rock matrices (which are treated as a porous medium), not fractured systems.

Babadagli and Ershaghi (1992) studied imbibition into the rock matrix under fracture flow conditions and found that it was a strong function of fracture flow rate, matrix capillary pressure, and matrix permeability. In the study they produced composite (fracture-matrix) relative permeability curves, and in turn used these to model a dual porosity system as a fracture network model. The use of the Effective Fracture Relative Permeability (EFRP) concept was limited to the case where experimental data was available for the particular system under study. Babadagli and Ershaghi (1993) extended this concept to field scale modelling applications. Limitations to this approach included the lack of consideration of oil viscosity, the inability to model different matrix block sizes, and the effects of gravity.

2.4.4 Two-Phase Water/NAPL Systems

The consideration of systems composed of water and organic chemical NAPLs is a relatively new aspect of research, and has emerged to assist in the understanding of environmental contamination. Historically the two main factions conducting research into fracture flow have concentrated on the movement of the wetting phase across the fractures (in nuclear disposal research and in the oil industry) rather than on the movement of the nonwetting fluid within the fractures.

The approaches to simulating water/NAPL systems have mimicked the results of similar research in porous media. Outside of the obvious physical differences, two main differences in behaviour

have become apparent. First, since fracture flow is essentially a two-dimensional phenomena, after imbibition the residual nonwetting phase saturations may be higher in a fracture than in porous media, due to the decreased possibility of by-passing, and second, with a permeable matrix, a fracture system is essentially composed of two overlapping continua, which means that the irreducible wetting phase saturation is not purely a function of pore size distribution and trapping, as with an increase of capillary pressure, wetting phase is able to escape through the matrix. These two points, though seemingly minor, compose the bulk of the difference between the water/NAPL flow behaviours in porous and fractured materials.

Pruess and Tsang (1990) presented a conceptual and numerical model of multiphase flow in fractures. The void space of real rough-walled rock fractures was conceptualized as a two-dimensional heterogeneous porous medium, characterized by a lognormal aperture distribution with an exponential spatial covariance. Pruess and Tsang use a 2mm nodal spacing in discretizing a 40 mm by 40 mm domain for their modelling.

Pruess and Tsang (1990) use the parallel plate permeability expression at each node, and the capillary pressure criteria to assess allowability. No consideration is given for dynamic phenomena, and the solution only considers the possibility of a single moving fluid.

Pruess and Tsang (1990) used their conceptualization and model to produce capillary pressure-saturation curves for their hypothetical fracture. Given the inherent limitations of the approach, the resemblance to curves from porous media is not surprising. Using the same approach the authors also investigate hypothetical relative permeability relationships for the system. The most

remarkable finding of the simulations is the degree of interference between the phases, similar to that found experimentally by Persoff and Pruess (1995). The residual nonwetting phase saturation varied from 51.5 % to 84 % in the simulations, significantly higher than the value found experimentally by Longino and Kueper (1999). Some runs also found that there was virtually no situation in which both phases would be mobile. A general conclusion was made that significant simultaneous movement of both phases was more favoured with increasing anisotropic aperture distributions, and with increasing spatial correlation length in the direction of flow.

The reason for the behaviour observed in the simulations can be traced to three factors: the lognormal distribution; the two-dimensionality of the system; and the five-point finite difference scheme employed. As the lognormal distribution is skewed towards smaller apertures, for a continuous nonwetting phase flowpath to exist, the few large apertures and some of the smaller apertures would have to be filled with the nonwetting phase. In a two-dimensional system there exist fewer bypassing routes than in a three-dimensional one, which will increase phase interference effects. This fact may be offset in the simulations by the tendency of anisotropic spatial correlation to segregate small and large aperture pathways, thus artificially raising the relative permeability characteristics of the system.

Rossen and Kumar (1992) extend the work of Pruess and Tsang (1990) with the development of the Effective Medium Approximation (EMA) that calculates relative permeabilities and saturations in two dimensional network problems similar to that of Pruess and Tsang (1990). Their approach essentially replaces the physical heterogeneous network with a homogeneous network of bonds of uniform conductivity, in which individual bonds are replaced at random with values from the

aperture distribution of the fracture. This results in a distortion in the pressure drop across that bond. In the EMA approach, the network is sequentially replaced with the fracture apertures such that the network conductivity distortion is zero. The EMA approach improved upon the small scale and computer intensive approach of Pruess and Tsang (1990), but also included several significant disadvantages. The approach itself is only an approximate solution for conductivity, and is an especially poor one as relative permeabilities (either wetting or nonwetting) approach zero. This problem develops from the fact that EMA is a bond percolation approach, whereas fracture conductivity is governed by site percolation theory. In addition, EMA cannot handle situations where spatial correlations exist in the aperture distribution, an error that becomes more pronounced as correlation lengths decrease.

Haghighi et al. (1994) performed a series of micromodel experiments to investigate the exchange of fluid between matrix and fractures. Through the use of carefully etched glass micromodels, they simulated matrix flow through a triangular and square lattice type arrangement of identical pores coupled to a fracture of approximately twice the size. These studies revealed that matrix invasion only occurred above a certain flow rate in the fracture (represented by the critical capillary number of the matrix pores). The experimental results were simulated with a network model, as the exact spatial distribution of pores and sizes was known. With these results, effective relative permeabilities were found to depend on the viscosity ratio, contrary to homogeneous systems. The work was limited by its restriction to two dimensions and the regularity of the matrix discretization.

Through a series of experiments Reitsma and Kueper (1994) presented an analysis of the hysteretic relationship between capillary pressure and fluid saturation for a single rough walled rock fracture. They found that the Brooks-Corey relationship used in porous media was adequate in describing relative permeability in rock fractures, and that the Brooks-Corey equation proved superior to the van Genuchten form. This result was also found (numerically) by Mendoza (1992), but the Brooks-Corey relationship was found to be inferior to a power law formulation for the nonwetting phase transmissivity. From the capillary pressure-saturation curves Reitsma and Kueper (1994) attempted to derive an aperture distribution for the fracture studied. Under the assumption that the entire fracture can be represented as an assemblage of subdivisions each represented by two parallel plates separated by a discrete distance and having a definable areal extent, three approaches were taken to develop aperture distributions.

In the type I conceptual model, all regions having local entry pressure less than the capillary pressure of the system are assumed to be invaded. The type II model uses the assumptions from type I, with the further caveat that order of encounter in considered, i.e. only those regions which are hydraulically connected by the nonwetting phase to the edge of the fracture plane can be invaded. The type III model is identical to the type II, with the exception of the exclusion of theoretical matrix flow. In the type II model, if the entry capillary pressures in the small apertures surrounding an isolated large aperture region are exceeded, nonwetting phase flow occurs into the region, but the only exit for the wetting phase is through matrix flow, a factor not explicitly considered in the experimental work. In the type III model, there is no consideration of matrix flow, and an isolated region of large apertures would remain as irreducible wetting phase.

Reitsma and Kueper (1994) developed an apparent aperture distribution from their data by assuming a series of discrete volume elements (based on the aperture and areal extent of their subdivisions) representing the fracture volume. The volume invaded with each rise in capillary pressure is known from the experimental data, thus a summation throughout the test results in a cumulative normalized area of the fracture invaded at a given capillary pressure. From this, a corresponding aperture was calculated, and could be plotted as a cumulative probability curve. A correction factor was required in the work, the value of which (0.9) was chosen to provide the best fit to the data, as an actual value could not be determined from the experiments.

2.4.4.1 Numerical Simulation of Two-Phase Water/NAPL Systems

Kueper and McWhorter (1991) simulated simultaneous two-phase flow in a single vertical fracture using a mass conservation approach:

$$\frac{\partial\left(\rho_w q_{w_i} e\right)}{\partial x_i} = \frac{\partial\left(\phi S_w \rho_w\right)}{\partial t} e, \quad i,j = x,z \qquad [2\text{-}40]$$

$$\frac{\partial\left(\rho_{nw} q_{nw_i} e\right)}{\partial x_i} = \frac{\partial\left(\phi S_{nw} \rho_{nw}\right)}{\partial t} e, \quad i,j = x,z \qquad [2\text{-}41]$$

where q_{wi} and q_{nwi} are the fluxes of the wetting and nonwetting phases respectively. They assume that both phases occupy their own set of flow channels within the fracture plane, and taking z in the vertical direction, the fluxes can be represented by Darcy's law:

$$q_{wi} = \frac{k_{ij} k_{rw}}{\mu_w}\left(\frac{\partial P_w}{\partial x_j} + \rho_w g \frac{\partial z}{\partial x_j}\right), \quad i,j = x,z \qquad [2\text{-}42]$$

$$q_{nwi} = \frac{k_{ij} k_{rnw}}{\mu_{nw}}\left(\frac{\partial P_{nw}}{\partial x_j} + \rho_{nw} g \frac{\partial z}{\partial x_j}\right), \quad i,j = x,z \qquad [2\text{-}43]$$

Equations (42) and (43) can be reduced to a form with only 2 dependent variables, through the capillary pressure relationship, and subject to $S_w+S_{nw}=1.0$. Assuming locally isotropic conditions, the cross derivatives in (40) and (41) can be ignored:

$$\frac{\partial}{\partial x}\left[\frac{ekk_{rw}}{\mu_w}\left(\frac{\partial P_w}{\partial x}\right)\right]+\frac{\partial}{\partial z}\left[\frac{ekk_{rw}}{\mu_w}\left(\frac{\partial P_w}{\partial z}+\rho_w g\frac{\partial z}{\partial z}\right)\right]=\phi e\frac{\partial S_w}{\partial t} \qquad [2\text{-}44]$$

$$\frac{\partial}{\partial x}\left[\frac{ekk_{rnw}}{\mu_{nw}}\left(\frac{\partial P_{nw}}{\partial x}\right)\right]+\frac{\partial}{\partial z}\left[\frac{ekk_{rnw}}{\mu_{nw}}\left(\frac{\partial P_{nw}}{\partial z}+\rho_{nw} g\frac{\partial z}{\partial z}\right)\right]=\phi e\frac{\partial S_w}{\partial t} \qquad [2\text{-}45]$$

These equations are highly non-linear in form, due to the dependence of the relative permeabilities and the capillary pressure on saturation. Kueper and McWhorter (1991) simulate a fracture similar to that of Pruess and Tsang (1990), with a lognormal aperture distribution following a stationary, exponential autocorrelation with principal correlation lengths of 4.4 and 13.3 percent of the domain size in the x and z directions.

In sensitivity analyses, Kueper and McWhorter (1991) found that the time taken for a DNAPL to traverse a fractured aquitard is inversely proportional to the height of DNAPL above the fracture (available capillary pressure), the aperture of the fracture, and the dip of the fracture to the horizontal.

Huyakorn et al. (1994) presented a three-dimensional three-phase model for simulation of the movement of non-aqueous-phase liquids in porous and fractured media. The model uses a combination of Galerkin finite element, upstream weighted finite difference, hybrid spatial approximation, and other procedures. Primarily designed to work in porous media, they expand the formulation to include both discrete fracture and dual-porosity representations. No ability to

handle aperture distributions is included, and matrix contributions are treated as superpositional sources within the framework. The dual porosity approach is identical to that of Barenblatt et al. (1960), with two discrete yet fully overlapping continua and a quasi-steady state approximation for the matrix/fracture fluid transfer term. The paper focuses on the solution techniques to the problem and not on the physical representation.

An explicit saturation approach to the simulation of two-phase flow in a fracture was presented by Murphy and Thomson (1993). The developed model represented the flow system as incompressible parallel plate flow within two-dimensional subregions of constant aperture. The model is formulated through the use of a five-spot finite volume technique and by treating the fluid-fluid interface as a discrete pressure discontinuity. As in the work of Rasmussen (1991) this treatment of the interface requires an exact representation of the interface location. Rather than the numerically elegant but computationally cumbersome boundary formulations of Rasmussen (1991) and others, Murphy and Thomson (1993) meet this requirement by not only defining the degree of saturation for each cell, but also the specific distribution of the phases. This approach is possible through a step-by-step application of Darcy's law creating a series of steady-state approximations completed in two steps. Specifically, a pressure solution for both phases throughout the domain is calculated at time t, followed by a flow solution (using the above mentioned technique) from t to $t+\Delta t$, and then a new pressure solution for $t+\Delta t$.

The distribution of the phases is represented by one of 15 possible scenarios, which the authors believe to be sufficient to cover all possible phase distributions within a cell. The distribution within a cell in conjunction with phase saturations will determine several practical points such as:

flow volumes in an out of the cell, trapping criteria, and saturation. A limit of this system, however, is that flow across a boundary is limited to one phase only. To ensure that this has a minimal effect, a suitably fine discretization is required.

Some of the main conclusions of this paper were: nonwetting phase globules may undergo repeated pinching as other flow paths open during drainage; nonwetting fluids may be excluded from open fracture regions by intervening tight aperture regions; a fluid may migrate downslope, opposite to the flow of a less dense fluid if the buoyant force is sufficient; and that isolated ganglia may migrate due to pressure gradients in the surrounding fluid. All these points predict similar behaviour for two-phase flow in fractures and porous media.

Gilman (1986) presented a finite-difference model to simulate multiphase flow in a double porosity reservoir. Using the assumption that the flow is dominated and controlled by the fractures, the matrix blocks must, therefore, act as sources to the fractures. Specific interest was shown to the effects of phase segregation in the matrix blocks and its effect on the recoveries from the system. This was achieved through the subdivision of the discrete matrix blocks into either stacked or nested subdomains. Comparisons with single matrix block simulations showed marked differences when the effects of phase segregation are taken into account. The effect of block discretization was to increase the wetting phase saturation in the matrix blocks with time, or from a petroleum industry standpoint, to increase the apparent production of the system. Unfortunately the model was only a 1-D representation, and computational time was found to increase by up to 80% for each matrix block subdivision. In addition, the required capillary pressure to cause nonwetting phase matrix invasion is extremely high for most rock types, and is not likely to be encountered.

Braester (1972) formulated an analytical solution to the situation of two-phase flow through a fractured porous media, for the case of horizontal displacement of a nonwetting fluid in one dimension. The work was limited in two main areas: the medium was treated as being homogenous with respect to fractures and matrix, and the effects of capillarity in the fractures was ignored. The matrix is simulated as a bundle of randomly oriented capillary tubes to derive the source function to the fracture. Braester (1972) found that the ratio of the volume of nonwetting fluid expelled from a system during imbibition to the volume of wetting fluid that entered the system is dependent upon the total flux. This is in contrast to porous media where the ratio is independent of the flux.

Thomas et al. (1983) developed a three dimensional model for simulating three phase flow of gas, oil, and water in a fractured medium using the dual porosity approach. The system was modelled as being composed of a continuous fracture system filled with discontinuous reservoir blocks of known properties and geometric shape. Local flow was assumed to occur only in the fractures with the matrix blocks acting as sink or source terms. The model was shown to agree well with that of Kazemi et al. (1976) for simulations of single block and five-spot recovery tests. The expansion of the model to simulating three-dimensional field examples can only be viewed as a qualitative exercise, given the ambiguities of the dual porosity approach. Simplifying assumptions were also incorporated, such as straight-line fracture relative permeabilities, and fracture capillary pressures of zero. An example of this is the almost identical performance of the three dimensional example to that of a single block surrounded by water. The pitfalls of the dual porosity approach are especially apparent here, as the model's results infer that scale is not a factor in the problem.

In another purely numerical investigation, Mendoza (1992) investigated two-dimensional two-phase flow in a parallel plate scenario. Using micro-discretizations across the fracture plane, each having a unique entry pressure and transmissivity, the macroscopic capillary pressure was determined through percolation theory. This approach allowed for an in-depth investigation of the physical dependencies of the capillary pressure and transmissivity. Mendoza (1992) found that the capillary pressure was directly dependent upon the mean geometric aperture, and the nonwetting phase transmissivity upon the variance of the aperture field. Both quantities were found to be independent of the inclusion of a porous matrix component.

The use of the fractional flow approach to the simulation of multi-phase flows was investigated by Binning and Celia (1999). The fractional flow approach uses a governing saturation equation suitable to solution through method of characteristics, coupled to a global pressure equation. The approach is computationally efficient on small homogeneous problems, but has yet to be expanded to include general boundary formulations or heterogeneous material properties.

Fully compositional three-dimensional simulation of multiphase flow and transport in fractured systems was presented by Slough et al. (1999a) in which the matrix and fracture systems are both treated explicitly, and no equilibrium assumptions are made. The model is used to examine the effects of matrix diffusion upon the migration of a DNAPL through fractured clay. The use of a constant nonwetting phase injection boundary condition, however, prevents the system from performing in a natural manner, and causes an overestimation of the effects of matrix porosity on the rate of DNAPL migration. The model of Slough et al. (1999a) is further limited by the lack of

differentiation between drainage and imbibition in the functional relationships for capillary pressure and relative permeability. Ross and Lu (1999) also investigate the retardation of a DNAPL moving down a vertical fracture due to mass lost to the matrix. With an analytical formulation, they concluded that significant retardation of the nonwetting phase of common organic contaminants would not occur in rock, except for in fractures with apertures less than 10 μm. Ross and Lu (1999) report similar results for high porosity clays, but the aperture increases to approximately 20 μm. The formulation of Ross and Lu (1999), due to its analytical nature, does not incorporate relative permeability, nor capillary over-pressuring (the existence of capillary pressure greater than the entry pressure of the fracture).

2.5 References

Abelin, H., Birgersson, L., Moreno, L., Widen, H., Agren, T., and I. Neretnieks. 1991. A Large-scale Flow and Tracer Experiment in Granite 2. Results and Interpretation, *Water Res. Res.*, 27(12), p 3119-3135.

Abdel-Salam, A., and C.V. Chrysikopoulos. 1996. Unsaturated Flow in a Quasi-Three-Dimensional Fractured Medium with Spatially Variable Aperture, *Water Res. Res.*, 32(6), p 1531-1540.

Acuna, J.A., Ershaghi, I., and Y.C. Yortsos. 1992. Practical Application of Fractal Pressure Transient Analysis of Naturally Fractured Reservoirs, *SPE 24705*, Soc. Pet. Eng., Washington, D.C.

Acuna, J.A. and Y.C. Yortsos. 1995. Application of Fractal Geometry to the Study of Networks of Fractures and Their Pressure Transient, *Water Res. Res.*, 31(3), p 527-540.

Anderson, J. and R. Thunvik. 1986. Predicting Mass Transport in Discrete Fracture Networks with the Aid of Geometrical Field Data, *Water Res. Res.*, 22(8), p 1941-1950.

Andersson, J. and B. Dverstorp. 1987. Conditional SImulation of Fluid Flow in Thre-Dimensional Networks of Discrete Fractures, *Water Res. Res.*, 23(10), p 1876-1886.

Babadaghli, T. and Ershaghi, I. 1992. Imbibition Assisted Two Phase Flow in Natural Fractures, *Paper SPE 24044*, presented at the Western Regional Meeting, Bakersfield, CA, Mar. 30-Apr. 1, p 189-198.

Babadaghi, T. and Ershaghi, I. 1993. Improved Modeling of Oil/Water Flow in Naturally Fractured Reservoirs Using Effective Fracture Relative Permeabilities, *Proc. SPE Western Regional Meeting*, Anchorage Alaska, 26-28 May 1993, SPE 26076, p 463-476.

Barker, J.A. 1988. A Generalized Radial Flow Model for Hydraulic Tests in Fractured Rock, *Water Res. Res.*, 24(10), p 1796-1804.

Barnsley, M.F. 1988. Fractals Everywhere, Academic, San Diego, Ca.

Barrenblatt, G.I., Zheltov, Iu. P., and I.N. Kocina. 1960. Basic Concepts in the Theory of Seepage of Homogeneous Liquids in Fissured Rocks, *J. Appl. Math. Mech. Engl.* Transl., 24, p 1286-1303

Barton, C.C. and E. Larsen. 1985. Fractal Geometry of Two-Dimensional Fracture Networks at Yucca Mountain, Southwestern *Nevada, Proc. Int. Sym. Fundamentals Rock Joints*, Sweden, 15-20 September, p 77-84.

Barton, C.C. and P.A. Hsiegh. 1989. Physical and Hydrological-Flow Properties of Fractures, T385, AGU, Washington, D.C.

Berkowitz, B. 1995. Analysis of Fracture Network Conductivity using Percolation Theory, *Math. Geol.*, 27, p 467-483.

Binning, P., and M.A. Celia. 1999. Practical Implementation of the Fractional Flow Approach to Multi-phase Flow Simulation, *Adv. Water Res.*, 22(5), p 461-478.

Bourke, P.J., Dunance, E.M., Health, M.J. and D.P. Hodglinson. 1985. Fracture Hydrology Relevant to Radioneuclide Transport, *Rep. R11414*, At. Energy Res. Establishment, Hartwell, England.

Cacas, M.C., Ledoux, L., de Marsily, G., Tillie, B., Barbreau, A., Durand, E., Feuga, B. and P. Peaudecerf. 1990. Modelling Fracture Flow with a Stochastic Discrete Fracture Network: Calibration and Validation 1. The Flow Model, *Water Res. Res.*, 26(3), p 479-489.

Dershowitz, W. Lee, G., Geier, J., Hitchcock, S., and P. La Pointe. 1995. *Fracman*, Interactive Discrete Feature Data Analysis, Geometric Modelling, and Exploration Simulation, User Documentation, Version 2.5: Seattle, Washington, Golder Associates Inc., 171 pgs.

Dodson, C.R. and W.T. Cardwell Jr. 1945. Flow Into Slotted Liners and an Application of the Theory to Core Analysis, *Trans. AIME*, 160, p 56-64.

Duguid, J.O. and P.C.Y. Lee. 1977. Flow in Fractured Porous Media, *Water Res. Res.*, 13(3), p 558-566.

Ehlan, J. 1999. Fracture Characteristics in Weathered Granites, *Geomorphology*, 31, p 29-45.

Elsworth, D. 1986. A Model to Evaluate the Transient Hydraulic Response of Three-Dimensional Sparsely Fractured Rock Masses, *Water Res. Res.*, 22(13), p 1809-1819.

Elsworth, D. 1987. A Boundary Element-Finite-Element Procedure for Porous and Fractured Media Flow, *Water Res. Res.*, 23(4), p 551-560.

Englman, R., Gur, Y., and Z. Jaeger. 1983. Fluid Flow Through a Crack Network in Rocks, *J. Appl. Mech.*, 50, p 707-711.

Firoozabadi. A. and J. Hauge. 1990. Capillary Pressure in Fractured Porous Media, *J. Pet. Tech.*, 42, p 784-791.

Fourar M., Bories, S, Lenormand, R. and P. Persoff. 1993. Two-Phase Flow in Smooth and Rough Fractures: Measurement and Correlation by Porous-Medium and Pipe Flow Models, *Water Res. Res.*, 29(11), p 3699-3708.

Fulcher Jr., R.A., Ertekin, T. and C.D. Stahl. 1985. Effect of Capillary Number and Its Constituents on Two-Phase Relative Permeability Curves, *J. Pet. Tech.*, p 249-260.

Gilman, J.R. 1986. An Efficient Finite-Difference Method for Simulating Phase Segregation in the Matrix Blocks in Double-Porosity Reservoirs, *SPE Res. Eng.*, SPE 12271, p 403-413.

Gilman, J.R., and H. Kazemi. 1983. Improvements in Simulation of Naturally Fractured Reservoirs, *Soc. Pet. Eng. J.*, 23(4), p 695-707.

Gokhale, A.M. and E.E. Underwood. 1990. A General Method for Estimation of Fracture Surface Roughness: Part I. Theoretical Aspects, *Mett. Trans. A*, 21A, p 1193-1200.

Gokhale, A.M. and W.J. Drury. 1990. A General Method for Estimation of Fracture Surface Roughness: Part II: Practical Considerations, *Mett. Trans. A*, 21A, p 1201-1207.

Hamm, S-Y., and P. Bidaux. 1996. Dual-Porosity Fractal Models for Transient Flow Analysis in Fissured Rocks, *Water Res. Res.*, 32(9), p 2733-2745.

Haghighi, M., Xu, B, and Y.C. Yortsos. 1994. Visualization and Simulation of Immiscible Displacement in Fractured Systems Using Micromodels: 1. Drainage, *J. Coll. Int. Sci.*, 166, p 168-179.

Horie, T., Firoozabadi, A. and K. Ishimoto. 1990. Laboratory Studies of Capillary Interaction in Fracture/Matrix Systems, *SPE Res. Eng.*, 5, p 353-360.

Huyakorn, P.S., Lester, B.H., and C.R. Faust. 1983. Finite Element Techniques for Modelling Groudwater Flow in Fractured Aquifers, *Water Res. Res.*, 19(4), p 1019-1035.

Huyakorn, P.S., Panday, S. and Y.S. Wu. 1994. A Three-Dimensional Multiphase Flow Model for Assessing NAPL Contamination in Porous and Fractured Media, 1. Formulation, *J. Cont. Hyd.*, 16, p 109-130.

Iwai, K. 1976. Fundamental Studies of Fluid FLow Through a Single Fracture, Ph.D. Thesis, Univ. of Cal. Berkeley,

Journel, A.G. and C.T. Huijbregts. 1978. Mining Geostatistics, Academic Press, Orlando, Fla., 600 pps.

Kazemi, H., Merrill, L.S., Porterfield, K.L., and P.R. Zeman. 1976. Numerical Simulation of Water/Oil Flow in Naturally Fractured Reservoirs, *Soc. Pet. Eng. J.*, p 317-326.

Kueper, B.H. and D.B. McWhorter. 1991. The Behaviour of Dense, Nonaqueous Phase Liquids in Fractured Clay and Rock, *Ground Water*, 29(5), p 716-728.

Kulatilake, P.H.S.W., Wathugala, D.N., and O. Stephansson. 1993. Joint Network Modelling with a Validation Exercise in Stripa Mine, Sweden, *Int. J Mech. Min. Sci. and Geo. Abs.*, 30(5), p 503-526.

Land, C.S. 1968. Calculation of Imbibition Relative Permeability for Two- and Three-Phase Flow From Rock Properties, *SPEJ*, p 149-156.

Lapsevic, P.A., Novakowski, K.S., and E.A. Sudicky. 1999. The Interpretation of a Tracer Experiment Conducted in a Single Fracture Under Conditions of Natural Groundwater Flow, *Water Res. Res.*, 35(8), p 2301-2312.

Long, J.C.S., Remer, J.S., Wilson, C.R. and P.A. Witherspoon. 1982. Porous Media Equivalents for Networks of Discontinuous Fractures, *Water Res. Res.*, 18(3), p 645-658.

Long, J.C.S., Gilmour, P., and P.A. Witherspoon. 1985. A Model for Steady State Flow in Random, Three-dimensional Networks of Disk-shaped Fractures, *Water Res. Res.*, 21(8), p 1150-1115.

Long, J.C.S. and P.A. Witherspoon. 1985. The Relationship of the Degree of Interconnection to Permeability in Fracture Networks, *J. Geophys. Res.*, 90(B4), p 3087-3098.

Longino, B.L., and B.H. Kueper. 1999. Nonwetting Phase Retention and Mobilization in Rock Fractures, *Water Res. Res.*, 35(7), p 2085-2093.

Mandelbrot, B.B. 1983. The Fractal Geometry of Nature, W.H. Freeman, New York.

Miller, I., Lee, G., Dershowitz, W., and G. Sharp. 1995. MAFIC, User Documentation, Version 1.5, Golder Associates, Redmond, WA.

Moench, A.F. 1984. Double-Porosity Models for a Fissured Groundwater Reservoir with Fracture Skin, *Water Res. Res.*, 20(7), p 831-846.

Moench, A.F. 1995. Convergent Radial Dispersion in a Double-Porosity Aquifer with Fracture Skin: Analutical Solution and Application to a Field Experiment in Fractured Chalk, *Water Res. Res.*, 31(8), p 1823-1835.

Muralidhar, K. 1990. Flow and Transport in Single Rock Fractures, *J. Fluid Mech.*, 215, p 481-502.

Murphy, J.R. and N.R. Thomson. 1993. Two-Phase Flow in a Variable Aperture Fracture, *Water Res. Res.*, 29(10), p 3453-3476.

Narr, W. and J. Suppe. 1991. Joint Spacing in Sedimentary Rocks, *J. Struc. Geo.*, 13(9), p 1037–1048.

Neuman, S.P. 1990. Universal Scaling of Hydraulic Conductivities and Dispersivities in Geologic Media, *Water Res. Res.*, 26(8), p 1749-1758.

Neuzil, C.E., and J.V. Tracy. 1981. Flow Through Fractures, *Water Res. Res.*, 17(1), p 191-199.

Nordqvist, A.W., Tsang, Y.W., Tsang, C-F., Dverstorp, B. and J. Andersson. 1996. Effects of High Variance of Fracture Transmissivity on Transport and Sorption at Different Scales in a Discrete Model for Fractured Rocks, *J. Cont. Hyd.*, 22, p 39-66.

Novakowski, K.S. 1992. The Analysis of Tracer Experiments Conducted in Divergent Radial Flow Fields, *Water Res. Res.*, 28(12), p 3215-3225.

Oda, M. and Y. Hatsuyama. 1985. Permeability Tensor for Jointed Rock Masses, In: *Fundamentals of Rock Joints*, Proc. Int. Sym. on Fundamentals Rock Joints, Bjorkliden, Sweden, 15-20 September, p 303-312.

Oron, A.P., and B. Berkowitz. 1998. Flow in Rock Fractures: The local Cubic Law Assumption Re-examined, *Water Res. Res.*, 34(11), p 2811-2815.

Peters, R.R. and E.A. Klavetter. 1988. A Continuum Model for Water Movement in an Unsaturated Fractured Rock Mass, *Water Res. Res.*, 24(3), p 416-430.

Persoff, P. and K. Pruess. 1995. Two-Phase Flow Visualization and Relative Permeability Measurement in Natural Rough-Walled Rock Fractures, *Water Res. Res.*, 31(5), p 1175-1186.

Pruess, K. and Y.W. Tsang. 1990. On Two-Phase Relative Permeability and Capillary Pressure of Rough Walled Rock Fractures, *Water Res. Res.*, 26(9), p 1915-1926.

Pyrak, L.R., Myer, L.R. and N.G.W. Cook. 1985. Determination of Fracture Void Geometry and Contact Area at Different Effective Stress, *Eos Trans. AGU (Abstract)*, 66(46), pg 903.

Rasmussen, T.C. 1991. Steady Fluid Flow and Tracer Times in Partially Saturated Fractures Using a Discrete Air-Water Interface, *Water Res. Res.*, 27(1), p 67-76.

Reitsma, S. 1992. Laboratory Measurement of Capillary Pressure-Saturation Relationships in Natural Rock Fractures, M.Sc. Thesis, University of Waterloo, Waterloo, Ontario, Canada, 152 pgs.

Reitsma, S.R. and B.H. Kueper. 1994. Laboratory Measurement of Capillary Pressure-Saturation Relationships in a Rock Fracture, *Water Res. Res.*, 30(4), p 856-878.

Renshaw, C.E. 1996. Influence of Subcritical Fracture Growth on the Connectivity of Fracture Networks, *Water Res. Res.*, 32(6), p 1519-1530.

Rocha, M. and F. Franciss. 1977. Determination of Permeability in Anisotropic Rock Masses from Integral Samples, In: Structural and Geotechnical Mechanics, ed. by W.J. Hall, Prentice-Hall, New York, p 178-202.

Ross, B., and N. Lu. 1999. Dynamics of DNAPL Penetration into Fractured Porous Media, *Ground Water*, 37(1), p 140-147.

Rossen W.R., and A.T.A. Kumar. 1992. Single- and Two-phase Flow in Natural Fractures, *Paper SPE-24195 presented at the 67th Annual Technical Conference of the Society of Petroleum Engineers*, Washington, D.C., Oct. 4-7.

Sagar, B. and A. Runchal. 1982. Permeability of Fractured Rock: Effect of Fracture Size and Data Uncertainties, *Water Res. Res.*, 18(2), p 266-274.

Saidi, A.M. 1991. Discussion of Capillary Pressure in Fractured Porous Media, *J. Pet. Tech.*, 47, p 233-238.

Schrauf, T.W. and D.D. Evans. 1986. Labortatory Studies of Gas Flow Through a Single Natural Fracture, *Water Res. Res.*, 22(6), p 1038-1050.

Segan, S., and K. Karasaki. 1993. TRINET: a Flow and Transport Code for Fracture Networks, LBL-34834, Lawrence Berkeley Laboratory, Berkeley, CA.

Shapiro, A.M. and J Andersson. 1983. Steady State Fluid Response in Fractured Rock: A Boundary Element Solution for a coupled, Discrete Fracture Continuum Model. *Water Res. Res.*, 19(4), p 959-969.

Slough, K.J., Sudicky, E.A., and P.A. Forsyth. 1999a. Numerical Simulation of Multiphase Flow and Phase Partitioning in Discretely Fractured Geologic Media, *J. Cont. Hyd.*, 40, p 107-136.

Slough, K.J., Sudicky, E.A., and P.A. Forsyth. 1999b. Grid Refinement for Modelling Multiphase Flow in Discretely Fractured Porous Media, *Adv. Water Res.*, 23, p 2671-269.

Snow, D.T. 1969. Anistrpoic Permeability of Fractured Media, *Water Res. Res.*, 5(6), p 1273-1289.

Snow, D.T. 1970. The Frequency of Fractures and Apertures in Rock, *Int. J. Rock Mech. Min. Sci.*, 7, p 23-40.

Sonnenborg, T.O., Butts, M.B., and K.H. Jensen. 1999. Aqueous Flow and Transport in Analog Systems of Fractures Embedded in Permeable Matrix, *Water Res. Res.*, 35(3), p 719-729.

Stafford, P., Toran, L., and L. McKay.1998. Influence of Fracture Truncation on Dispersion: A Dual Permeability Model, *J. of Cont. Hyd.*, 30, p 79-100.

Streltsova T.D. 1976. Hydrodynamics of Groundwater Flow in a Fractured Formation, *Water Res. Res.*, 12(3), p 405-414.

Sudicky, E.A. 1990. The Laplace Transform Galerkin Technique for Efficient Time-Continuous Solution of Solute Transport in Double-Porosity Media, *Geoderma*, 47, p 209-232.

Sundaram, P.N. and D. Frink. 1983. Electrical Analogy of Hydraulic Flow Through Rock Fractures, *Geotech. Test. J.*, 6(1), p 3-9.

Tsang, Y.W., and P.A. Witherspoon. 1981. Hydromechanical Behaviour of a defoemable rock fracture subjected to normal stress, *J. Geophys. Res.*, 86, p 9287-9298.

Tsang, Y.W. 1984. The Effect of Tortuosity on Fluid Flow Through a Single Fracture, *Water Res. Res.*, 20(9), p 1209-1215.

Tsang, Y.W. and K. Pruess. 1987. A Study of Thermally Induced Convection Near a High-Level Nuclear Waste Repository in Partially Saturated Fractured Tuff, *Water Res. Res.*, 23(10), p 1958-1966.

Tsang, Y.W. and C.F. Tsang. 1987. Channel Model of Flow Through Fractured Media, *Water Res. Res.*, 23(3), p 467-479.

Tsang, Y.W. and C.F. Tsang. 1989. Flow Channelling in a Single Fracture as a Two-Dimensional Strongly Heterogeneous Permeable Medium, *Water Res. Res.*, 25(9), p 2076-2080.

Vickers, B.C., Neuman, S.P., Sully, M.J., and D.D. Evans. 1992. Reconstruction and Geostatistical Analysis of Multiscale Fracture Apertures in a Large Block of Welded Tuff, *Geophys. Res. Lett.*, 19(10), p 1029-1032.

Walsh, J.B. 1980. The Effect of Pore Pressure and confining pressure on fracture permeability, *Int. J. Rock. Mech. Min. Sci. Geo.. Abst.*, 18, p 429-435.

Wan, J., Tokunaga, T.K., Tsang, C-F., and G.S. Bodvarsson. 1996. Improved Glass Micromodel Methods for Studies of Flow and Transport in Fractured Porous Media, *Water Res. Res.*, 32(7), p 1955-1964.

Wang, J.S.Y., Narasimhan, T.N. and C.H. Scholz. 1988. Aperture Correlation of a Fractal Fracture, *J. Geophys. Res.*, 93(B3), p 2216-2224.

Warren, J.E. and P.J. Root. 1963. The Behaviour of Naturally Fractured Reservoirs, *Trans. AIME*, 228, p 245-254.

Wilson, C.R., and P.A. Witherspoon. 1974. Steady State Flow in Rigid Networks of Fractures, *Water Res. Res.*, 10(2), p 328-335.

Witherspoon, P.A., Wang, J.S.Y., Iwai, K., and J.E. Gale. 1980. Validity of Cubic Law for Fluid Flow in a Deformable Rock Fracture, *Water Res. Res.*, 16(6), p 1016-1024.

CHAPTER 3 – FACTORS AFFECTING DNAPL MIGRATION IN A SINGLE FRACTURE[1]

3.1 Introduction

The presence of DNAPL in the subsurface is recognized as a significant source of long-term groundwater contamination at many sites throughout North America and Europe (Cherry et al., 1996; Freeze and McWhorter, 1997). DNAPLs of environmental concern include PCB oils, chlorinated solvents, coal tar, and creosote. A release of DNAPL to the subsurface will distribute itself as both disconnected blobs and ganglia of liquid referred to as residual, and in continuous distributions referred to as pools. The relative proportions of residual and pooled DNAPL depends upon a number of factors including DNAPL density, interfacial tension, capillary properties, release rate, and hydraulic gradient. At many sites in North America, the volume of DNAPL released to the subsurface is sufficient to penetrate bedrock and fractured clay aquitards located beneath the watertable.

Kueper and McWhorter (1991) developed a conceptual model for DNAPL flow through saturated fractured environments, pointing out that once entering a fracture network DNAPL will migrate preferentially through the largest aperture fractures and will in general prefer to migrate vertically downwards in response to gravity forces. Lateral flow will also occur, provided the entry pressure of intersecting horizontal fractures is overcome, and any vertical migration

[1] Submitted to Journal of Groundwater

pathways are incapable of accepting the incoming flux of DNAPL, or are non-existent. Because DNAPL is more dense than water, it will also enter dead-end vertical fractures and in the case of a relatively coarse-grained rock type, may also enter the rock matrix provided that sufficient capillary pressures are generated.

Parker et al. (1994; 1996) pointed out that due to the porous nature of the matrix surrounding fractures, the DNAPL trapped in fractures may dissolve into the aqueous phase and diffuse into the matrix. The life span of DNAPL in such situations can range from less than a day to hundreds of years depending on the chemical composition of the DNAPL, the physical properties of the matrix, and the fracture aperture.

Ross and Lu (1999) presented an analytical solution to investigate the effects of mass transfer to the matrix on the advancement of DNAPL down a vertical fracture. Using a dimensionless "Nitao" number, Ross and Lu present a method of determining if the effects of matrix diffusion are significant on the rate of advance of a DNAPL front. The analytical formulation, though allowing for dynamic flow behaviour, did not incorporate the effects of relative permeability, or an explicit representation of capillary pressure gradients.

Numerical investigations of DNAPL flow in a single fracture (Slough et al., 1999, Esposito and Thomson, 1999) have examined the effects of porosity, aperture, and spacing on DNAPL migration, and on factors affecting mass removal from a fractured system. Slough et al. (1999) found that increasing the matrix porosity dramatically increased the required time for DNAPL to penetrate a 10m long fracture. Slough et al.'s (1999) use of a constant nonwetting phase flux

boundary condition at the top of the fracture, however, influences the relationship between matrix porosity and nonwetting phase front advancement. Reynolds and Kueper (2000) performed a similar analysis on migration through a 3m fracture embedded in a clay-like matrix, with the incorporation of a constant capillary pressure boundary condition above the fracture to simulate pooled DNAPL, and showed that porosity has less of an impact on DNAPL migration in such a scenario.

The objective of this study is to advance the above works by considering fully the effects of gravity, capillary pressure, relative permeability, viscosity, and matrix diffusion on the rate of DNAPL migration through fractured porous media, and the length of time required for contaminants to "reverse" diffuse back out of the matrix once all DNAPL has been removed from the fractures. This work is focused on a single fracture, as understanding at this scale is a prerequisite to understanding and analysis at the network and field scales.

3.2 Methodology

The numerical model used in this work (QUMPFS, Reynolds and Kueper (2001)) is a fully three-dimensional, multiphase compositional simulator, which allows for explicit simulation of matrix-fracture interactions, non-equilibrium phase partitioning, and hysteresis in the relative permeability and capillary pressure-saturations relationships. The partial differential equations governing isothermal multiphase flow with multicomponent transport in porous media on which the model is based are:

$$\frac{\partial}{\partial t}\left(c_{i\beta}\phi\, S_\beta x_{i\beta}\right)+\nabla\cdot\left(c_{i\beta}x_{i\beta}v_\beta\right)-\nabla\cdot\left[\phi\, S_\beta \vec{D}_{i\beta}\nabla\left(c_{i\beta}x_{i\beta}\right)\right]-q_{i\beta}-I_{i\beta}=0 \qquad [3\text{-}1]$$

$$\beta = 1..n_p, \quad i = 1..n_c$$

where n_p is the number of phases, β is the phase of interest, n_c is the number of components, i is the component of interest, $c_{i\beta}$ is the molar density of phase β, S_β is the fraction of void space occupied by phase β, ϕ is the porosity of the medium, v_β is the flux of phase β, $x_{i\beta}$ is the mole fraction of component i in phase β, $D_{i\beta}$ is the dispersion tensor for component i in phase β, $q_{i\beta}$ is a source or sink of component i in phase β, and $I_{i\beta}$ represents the inter-phase mass transfer of component i to or from phase β. The governing equations are discretized through the finite volume method using a lumped mass time derivative.

The physical system used in this study consists of a single fracture embedded in a porous matrix. The fracture is either 3 m or 10 m long, and is inclined from 30 to 90 degrees below horizontal in various simulations with unit depth into the third dimension. The spatial discretization perpendicular to the fracture grades from 100 microns adjacent to the fracture to over 10 cm at the edge of the domain. This fine discretization is required to handle the steep concentration gradient that exists at early time between the fracture and the matrix, and which greatly affects the behaviour in the system (Slough et al., 1999). The vertical discretization begins with 1 cm at the top (inlet) of the fracture, and grades to 10 cm at the bottom (outlet) of the fracture. Most simulations incorporated between 1500 and 4251 control volumes. All simulation domains were oriented with sides parallel to the horizontal and vertical axes, the differing fracture inclinations being simulated through manipulation of the gravity term in the discretized equations.

Flow boundary conditions on the domain consist of no-flow along all vertical edges, and constant wetting phase pressure along the top and bottom of the domain, such that the pressure distribution is hydrostatic. DNAPL was introduced into the top of the fracture under a constant capillary pressure of 4295 Pa, equal to 0.3 m of pooled TCE situated at the watertable, which is located at the top of the domain. This value was chosen to allow entry into all fracture apertures simulated in this study. All simulations terminated when nonwetting phase appeared in the lowest cell of the fracture. Transport boundary conditions were set such that aqueous phase contaminant was unable to leave the domain except at the fracture outlet. Figure 3-1 illustrates the domain of interest.

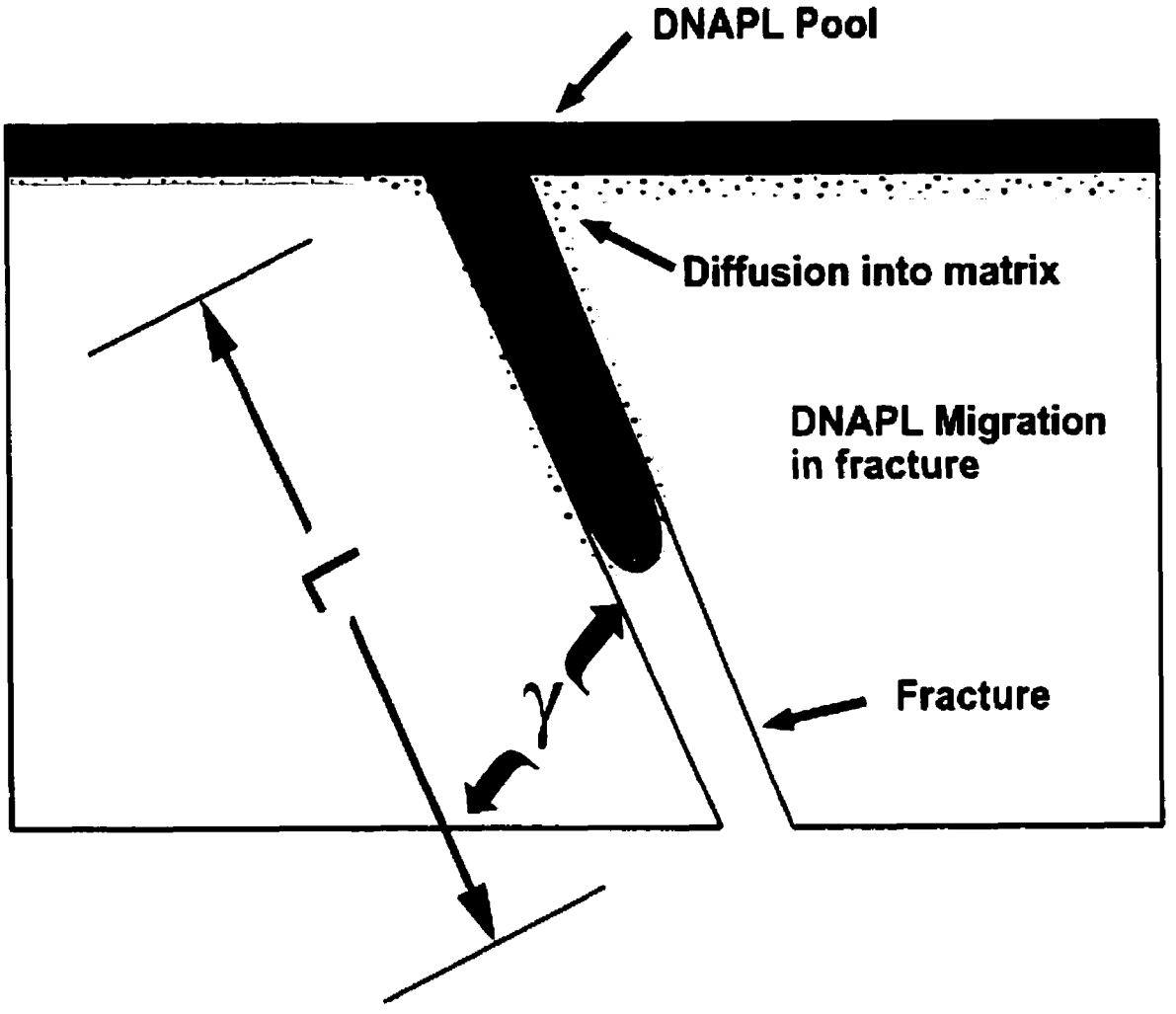

Figure 3-1. Simulation Domain for All Single Fracture Scenarios (L – Fracture Length (m), γ - Fracture Inclination)

Table 3-1 presents the range of parameters used in this study (values in bold denote the base case). The choice of parameters to vary in the study (aperture (e), matrix porosity (ϕ), matrix distribution coefficient (K_d), and fracture inclination (γ)) was based on the work of Kueper and McWhorter (1991) and Pankow and Cherry (1996), who identified these as the key parameters controlling DNAPL migration in fractured clay. In general, the geological parameters were kept within what would be considered appropriate for a clay or silty-clay deposit.

Table 3-1. Physiochemical parameters

Parameter	Value	Parameter	Value
Pore Size Distribution Index	2.0	Longitudinal Dispersivity	0.01 m
Residual Wetting Phase Saturation	0.1	Transverse Dispersivity	0.001 m
Wetting Phase Viscosity	1.0×10^{-3} Pa•s	**Fraction Organic Carbon (f_{oc})**	0.1,**0.01**,0.001
Wetting Phase Density	1000 kg/m^3	**Fracture Aperture**	15, **30**, 50 μm
Interfacial Tension	2.0×10^{-2} N/m	**Matrix Porosity**	0.1, **0.3**, 0.5
Matrix Permeability	1.0×10^{-17} m^2	**Fracture Inclination**	30, **60**, 90 °

The migration of five DNAPLs was investigated in this work: Chlorobenzene (CB), 1,2-dichloroethylene (DCE), Trichloroethylene (TCE), Tetrachloroethylene (PCE), and 1,2-dibromoethane (EDB). The chemical properties of these compounds are presented in Table 3-2. These compounds are commonly occurring DNAPLs and exhibit a wide range of physio-chemical properties.

Table 3-2. Chemical parameters of DNAPLs

Parameter	CB	1,1-DCE	TCE	PCE	EDB
Density (kg/m^3)	1100	1210	1460	1630	2180
K_{oc} (mL/g)	330	64.6	126	263	92
Solubility (mg/L)[1]	500	3350	1100	200	4200
Viscosity (cP)	0.80	0.36	0.57	0.90	1.72
D* (m^2/s)	8.7×10^{-10}	1.01×10^{-9}	1.01×10^{-9}	8.7×10^{-10}	9.6×10^{-10}

1 – Mackenzie 1988
2 – Hayduk and Laudie (1974)

3.3 Results

3.3.1 Rate of Migration

The five DNAPLs chosen in this study vary significantly with respect to solubility and density. TCE is representative of a moderately dense, moderately soluble DNAPL, while EDB can be considered a heavy and very soluble DNAPL. The other three DNAPLs were selected to span the endpoints of the spectrum; PCE as heavy and slightly soluble, CB as light and slightly soluble, and DCE as light and very soluble.

Figure 3-2 presents the breakthrough times (time required for DNAPL to reach bottom of fracture) for each of the five DNAPLs. Note that foc, ϕ, and γ were set to the base case values, and that the fracture permeability is calculated as $e^2/12$. The results presented in Figure 3-2 illustrate the "homogenizing" effect that large apertures have on the DNAPL migration rate. The breakthrough times for the 30 μm and 50 μm aperture fractures are similar, differing by less than a factor of 3.5 for the 10 m fracture, and by less than a factor of 2.5 for the 3 m fracture. This similarity illustrates the difficulty in predicting the results of complex systems without the use of numerical models. Based on consideration of density and solubility alone, it might have been expected that PCE would transit the system most rapidly (high density, low solubility), and DCE the slowest (low density, high solubility). This is only the case, however, in the 15 μm aperture, 10 m long fracture.

In all cases (with the exception of the 15 μm aperture, 10 m long fracture) the slowest migrating DNAPL is the relatively insoluble CB. The explanation for this is found in the other parameters exerting a control on the migration rate, the viscosity and the organic-carbon partition coefficient (K_{oc}). In a comparison between CB and DCE (Table 3-2) it can be seen that CB is more viscous than, and will sorb to a greater degree than, DCE. These parameters exert controlling influences on the migration of the DNAPL in all cases examined, until the DNAPL distribution in the fracture becomes long enough that the large solubility of DCE becomes the controlling influence through matrix diffusion (in the 15 μm, 10 m case). The case of EDB is also of interest, given its high relative density as compared to the other selected DNAPLs. The competing effects of density and solubility are seen in the larger aperture fractures, as breakthrough times are similar to the PCE-TCE-DCE family. In the 15 μm aperture fracture, however, the EDB breakthrough time is approaching that of the previously discussed DCE and CB DNAPLs. The effects of viscosity are quite evident in this case, as given the similar values of K_{oc} and solubility between EDB and DCE it might be expected that EDB's large density would result in more rapid migration through the fracture. This is not the case, the reason being the very large value of viscosity of EDB relative to that of DCE

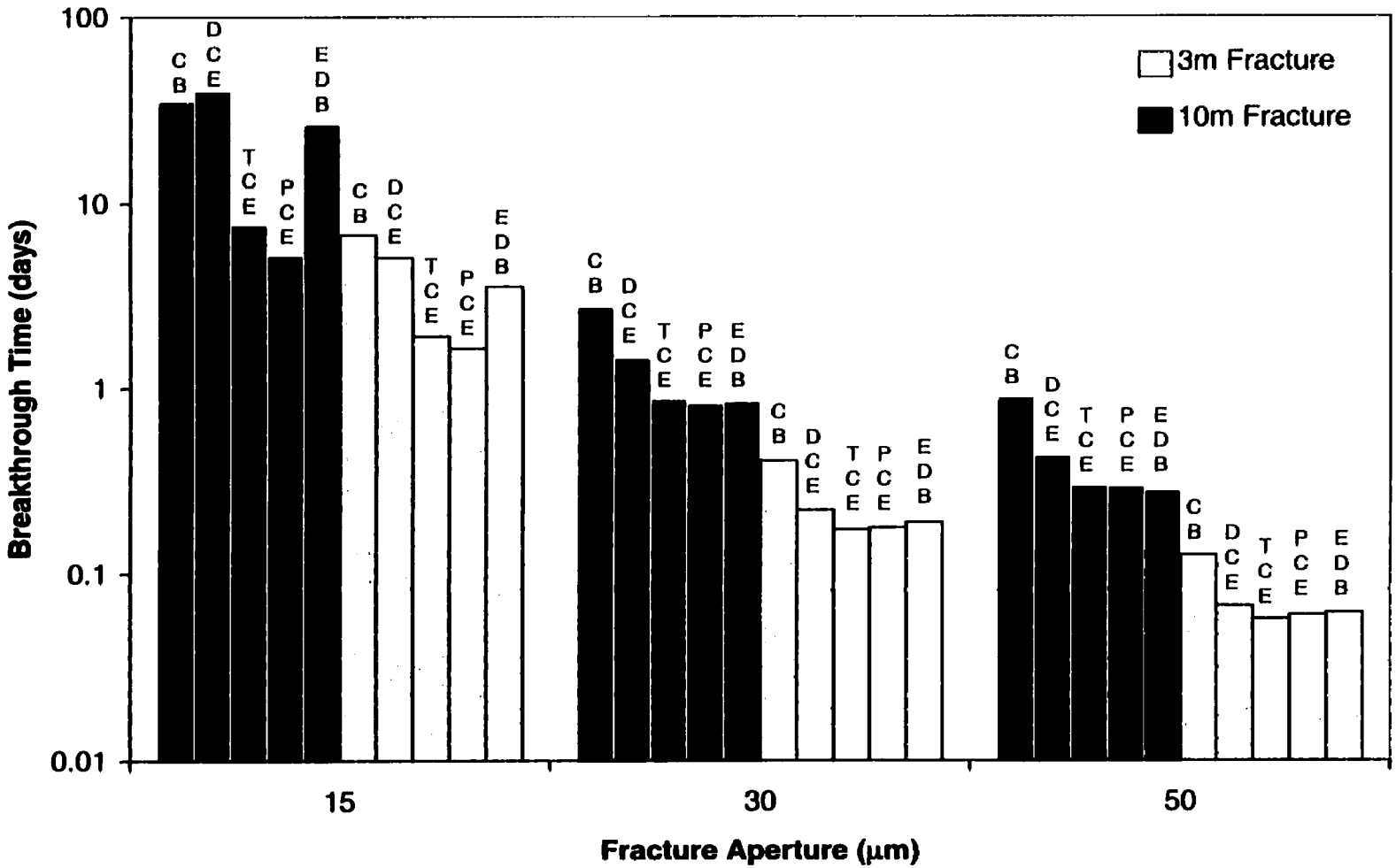

Figure 3-2. Breakthrough Times (First Arrival of DNAPL at Bottom of Fracture) for Various Values of Aperture

Direct comparison of the migration predictions of this work to that of Ross and Lu (1999) is difficult, due to the limitations of the analytical solution of Nitao and Buschek (1991) employed in their derivation. The mathematical formulation of two-phase flow in a fracture used by Ross and Lu (1999) ignores the effects of the reduction in nonwetting phase permeability due to the presence of the wetting phase (and indeed ignores the existence of the wetting phase entirely behind the DNAPL front). In addition, the boundary conditions of their solution are such that the nonwetting phase pressure at the upper boundary of the fracture is set equal to the entry pressure of the fracture, and therefore they cannot consider the effects of capillary over-pressurization.

The reduction in nonwetting phase permeability due to the presence of the wetting phase, and capillary over-pressurization caused by a DNAPL pool above the fracture which exceeds its entry pressure are off-setting phenomena, reducing (relative permeability) and increasing (over-pressurization) the mass flow into the system as compared to Ross and Lu (1999). The relative importance of these factors to an accurate analysis of the migration of DNAPL through a fracture is demonstrated in Figure 3-3, which presents the migration of the PCE and CB fronts through a 3 m fracture for a 60° dip. The effects of relative permeability are clear in the delayed arrival time (more than 100%) of PCE at the terminus of the fracture in this work as compared to that of Ross and Lu (1999). The effects of relative permeability and the resultant increase in travel times increases the mass lost to the matrix over that predicted by Ross and Lu (1999).

It should be noted that the breakthrough times on this graph are at least two orders of magnitude less than the theoretical inflection point used by Ross and Lu (1999) in their calculations, after which the effects of mass loss through matrix diffusion become increasingly important. Based

on this, Ross and Lu (1999) predict that the presence of the matrix will not affect the migration of the DNAPL for all of the cases presented here. As will be discussed further on, matrix diffusion does influence the breakthrough times examined in this study. Slough et al. (1999) found that the migration rate of the DNAPL was also sensitive to the form of the relative permeability function, though comparison is difficult due to their use of a nonwetting phase injection boundary condition at the entrance to the fracture.

The almost co-incident arrival times predicted for CB in Figure 3-3 are an artefact of the particular parameters chosen in this work. Breakthrough time predictions for a 10 m long fracture for CB are significantly longer in this work compared to the work of Ross and Lu (1999) (greater than 60 hours as compared to approximately 31 hours). The CB results presented in Figure 3-3 do show that capillary over-pressurization has some affect on the rate of DNAPL migration, but only at early time. The increased depth of penetration predicted by this work (as compared to Ross and Lu (1999)) at early time is a function of the capillary over-pressurization of the system. The capillary effects are more pronounced for CB as opposed to PCE as the over pressurization forms a larger component of the nonwetting phase driving force due to the lower density of CB.

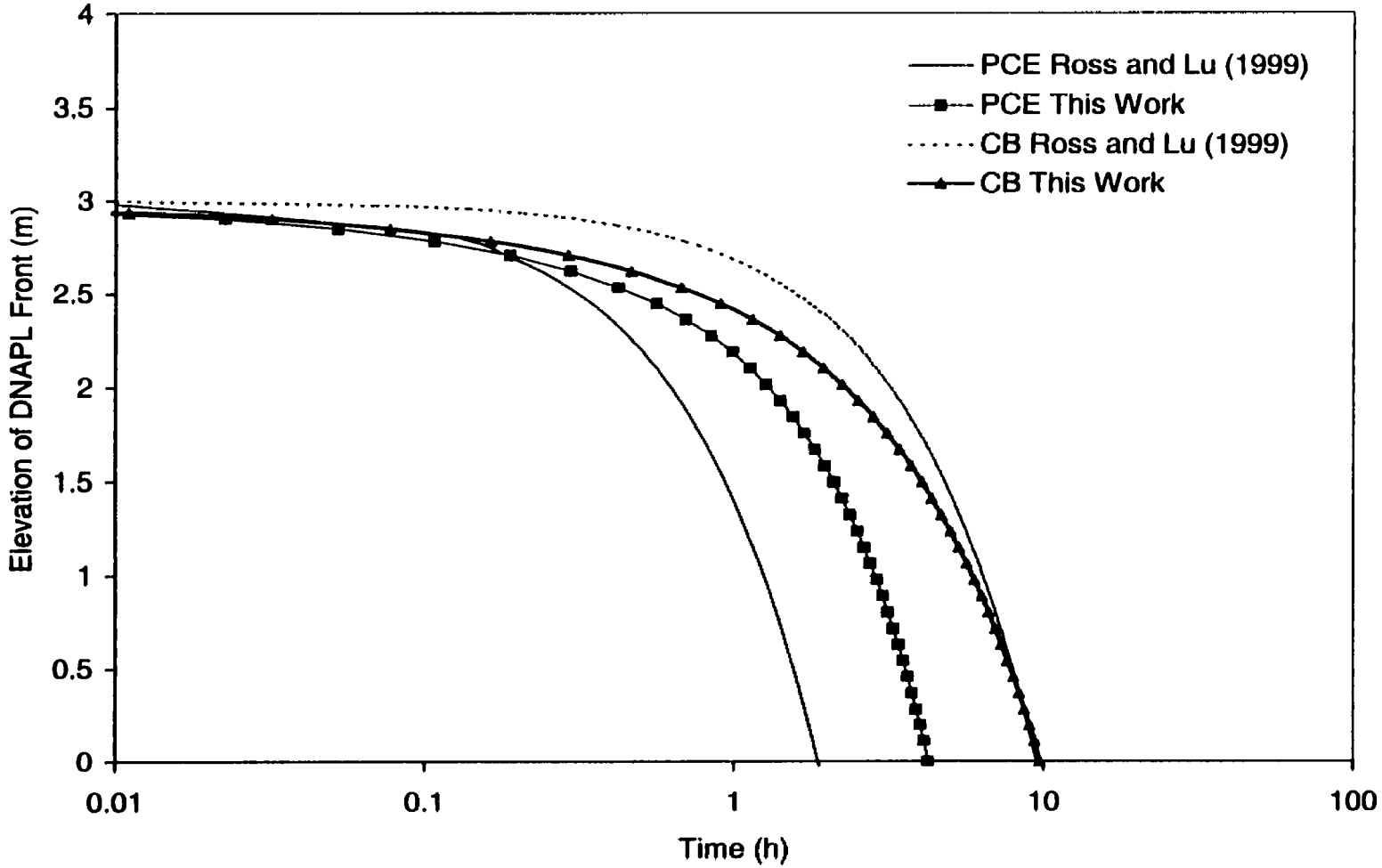

Figure 3-3. Comparison of the Vertical Location of the DNAPL Front vs. Time between the Numerical Model and the Analytical Formulation of Ross and Lu (1999(

Figure 3-4 presents the breakthrough times for the simulations in which the dip of the fracture was varied for each of the DNAPLs (with dip being measured from the horizontal). Physically, a shallower dipping fracture reduces the gravity component of the Darcy flux through the fracture (by 50 percent, for example, for a dip of 30°), thus reducing the volume of DNAPL entering the fracture per unit time. The flux of DNAPL into the fracture is also, however, a function of matrix diffusion. For the 10 m TCE simulations, for example, the flow into the fracture at late time (almost equal to breakthrough time) for the 30° dipping fracture is 58.2 percent of that for the 90° dip. With the ratio of gravity force along the fracture being 0.5, the extra flow in the 30° case is accounted for by more mass loss to the matrix due to the longer residence time in the fracture to that point.

Overall, the effect of dip on the migration rate of the DNAPL is less pronounced than the effect of aperture, as an increase in dip from 30 to 90 degrees resulted in a decrease in breakthrough time of up to 550 percent compared to a decrease of up to 9300 percent for an increase in aperture from 15 to 50 μm. This comparison is somewhat offset when the actual travel distance of the DNAPL is taken into account. Recall that the breakthrough times are defined as the time required for the DNAPL to traverse the 3 m (or 10 m) clay layer. For a fracture with a dip of 30°, this translates into an actual travel distance of 6 m along the fracture in a 3 m thick clay layer, and 20 m in a 10 m thick layer.

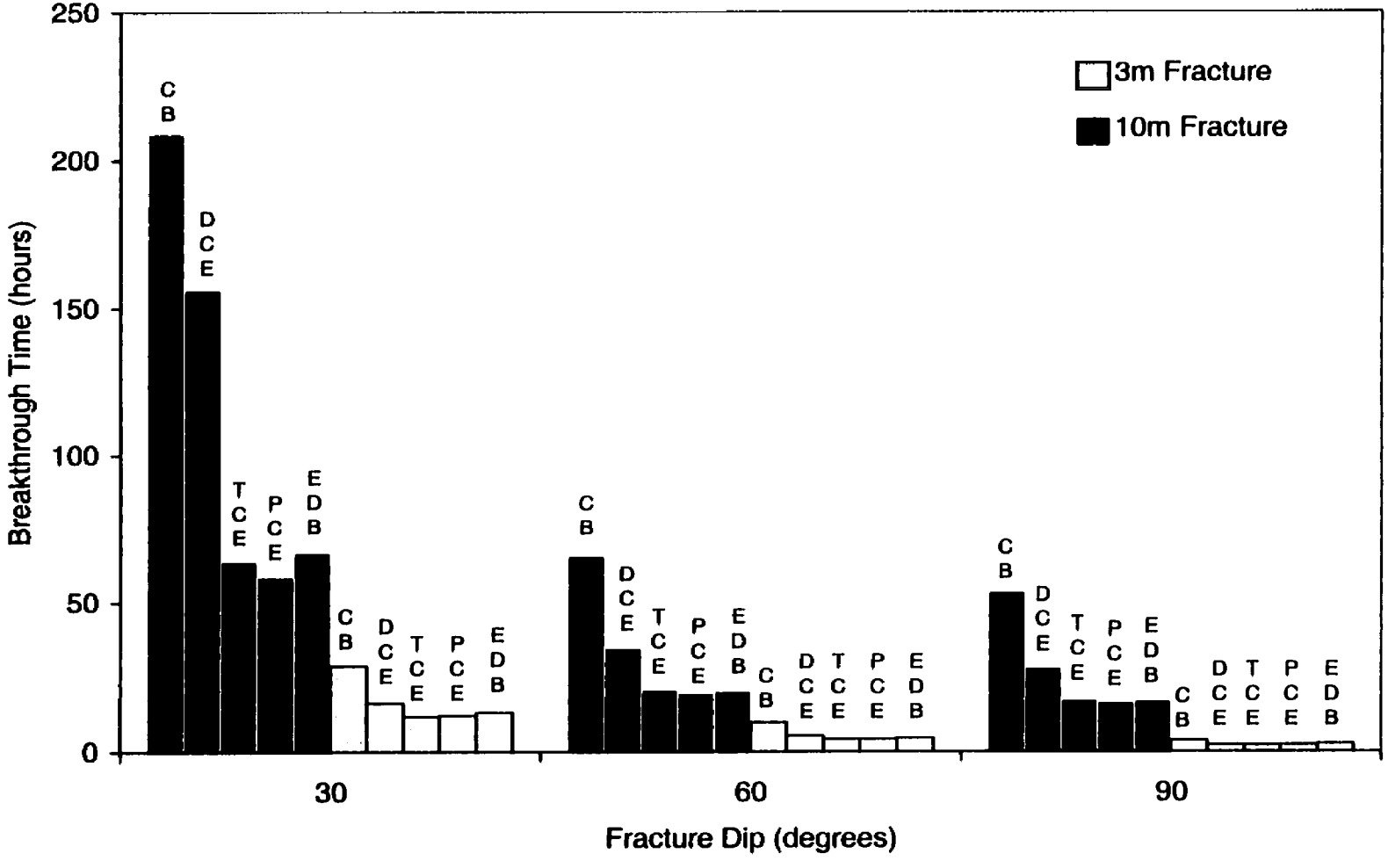

Figure 3-4. Breakthrough Times (First Arrical of DNAPL at Bottom of Fracture) for Various Values of Fracture Inclination

If the migration rate of the DNAPL is assumed constant, the combination of the increase in travel distance and the decrease in gravity driving force should result in an increase in migration time of 400 percent. For DCE in a 30 degree dipping fracture in a 10 m thick clay layer, for example, the additional increase in breakthrough time due to the increase in mass lost to the matrix due to the increased travel time is on the order of 40 percent. In terms of parameter estimation, however, an error in the estimation of aperture by 10 to 15 μm will have a much greater impact on the DNAPL breakthrough time than an error in the estimation of dip by 30 degrees. This illustrates the fundamental importance of being able to estimate fracture aperture when performing travel time calculations.

Figure 3-5 presents the breakthrough times for the simulations in which the fraction of organic carbon contained in the matrix was varied between simulations. The results clearly demonstrate that the effect of increasing the sorptive capacity of the matrix has only a small effect on the migration of the DNAPL through the fracture (with the possible exception of CB). Table 3-3 presents the aqueous phase matrix retardation factors (R) for each DNAPL for each of the f_{oc} values used in this work for a matrix porosity of 0.3 and a dry bulk density of 1.86 g/cc. The relatively large value of R (176.3) for PCE with a f_{oc} of 0.1, for example, would tend to indicate that significant retardation of the DNAPL front might occur due to matrix losses. This is not the case, however, as the low solubility, high density, and low viscosity of PCE mask the effect. The even larger value of R (221.0) for CB with a f_{oc} of 0.1 imparts only slight retardation upon the migration of the DNAPL front, most notably in the 10 m fracture. In comparison to PCE (despite similar viscosities and organic-carbon partition coefficients) the small density of CB results in slower movement of DNAPL through the fracture, and increased relative diffusive (and

therefore sorbed) losses to the matrix. It should be pointed out that this effect is masked in the 3 m fracture, as travel times are rapid enough to minimize matrix losses.

Figure 3-6 presents the breakthrough times for the simulations in which the porosity of the matrix was varied for each of the DNAPLs. The immediate conclusion from these results is the almost complete insensitivity of the DNAPL migration rate to matrix porosity. The lesser sensitivity to porosity as compared to f_{oc} is due to the offsetting effects of increasing porosity from a matrix storage standpoint. The increased porosity results in a lower value of the bulk density of the soil, and thus a smaller amount of sorbed mass per volume. The increased porosity increases the dissolved storage capacity of the matrix, however, by increasing the volume of wetting phase occupying a unit volume of aquifer. An increase in porosity from 0.3 to 0.5, for example, results in an overall net increase in matrix storage capacity (both dissolved and sorbed) for CB of 19.0 percent. In contrast, increasing f_{oc} from 0.01 to 0.1 without changing the matrix porosity increases matrix storage by 166 percent for CB.

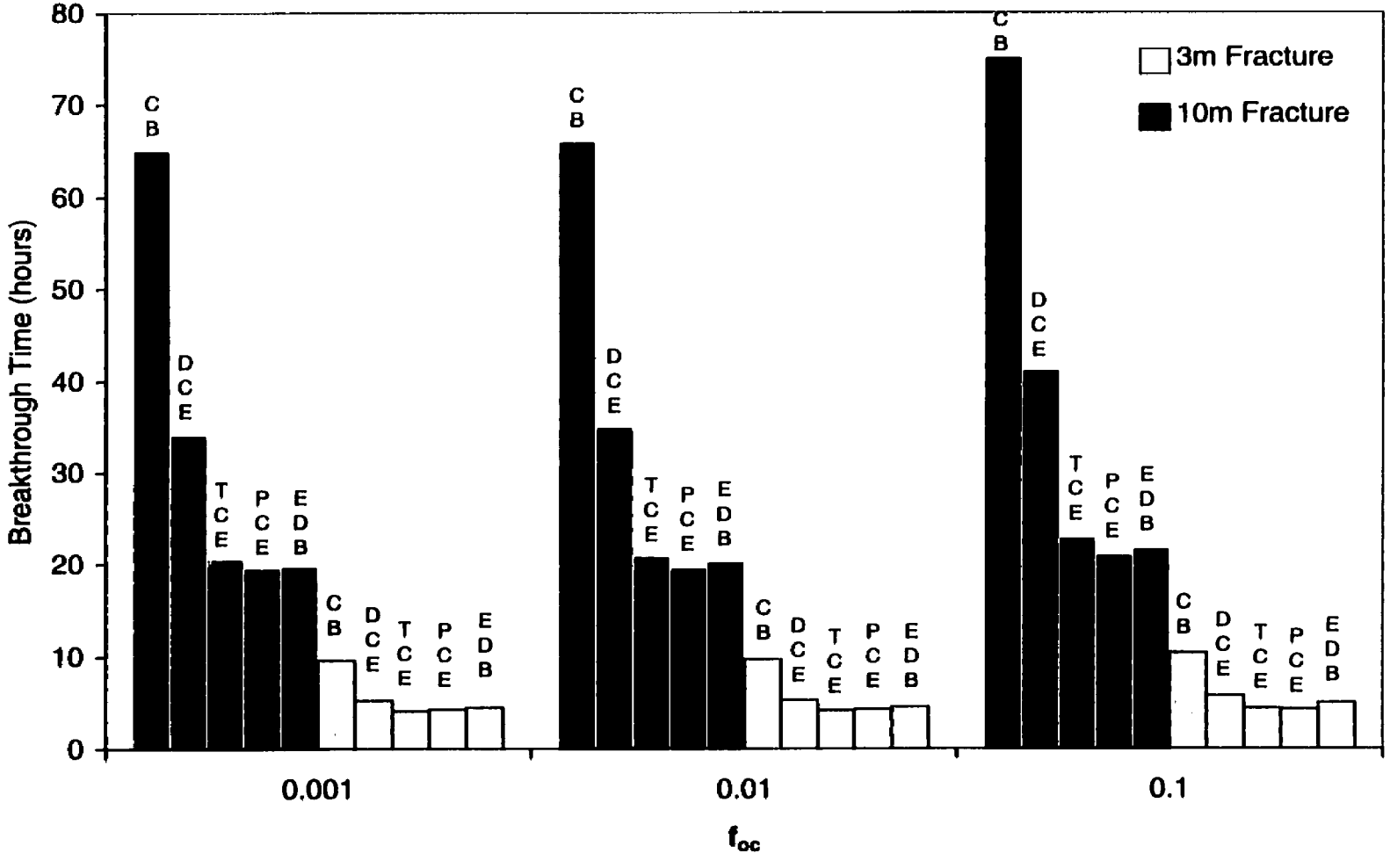

Figure 3-5. Breakthrough Times (First Arrical of DNAPL at Bottom of Fracture) for Various Values of f_{oc}

Table 3-3. Matrix Retardation Factors (ϕ=0.3, ρ_b=1.86 g/cc)

	f_{oc} (percent)		
Compound	0.1	0.01	0.001
CB	221.0	23.0	3.2
DCE	44.1	5.3	1.4
TCE	85.0	9.4	1.8
PCE	176.3	18.5	2.8
EDB	62.3	7.1	1.6

These results for porosity are significantly different than those presented by Slough et al. (1999), who found that increasing the matrix porosity from 0.1 to 0.5 for TCE in a 30 μm aperture, 10 m long fracture significantly increased the breakthrough time for the DNAPL. The apparent contradiction between these findings is explained by an examination of the nonwetting phase boundary conditions applied to the top of the fracture. Slough et al. (1999) used a constant injection rate of DNAPL equal to 0.4 mL/d for their simulations, as opposed to the constant capillary pressure boundary condition employed in this work. The impact of using the constant capillary pressure condition is to allow the physics of the system to determine the amount of DNAPL that enters the fracture. An increased amount of matrix diffusion, for example, would result in an increased amount of DNAPL entering the top of the fracture.

Figure 3-7 presents the percentage of total mass in the system that resides in the matrix (in sorbed and dissolved form) for the base case 3 m TCE run in this work, and an identical simulation in which DNAPL is injected into the top of the fracture at a rate of 0.4 mL/d. After four hours the DNAPL has migrated to within 0.2 m of the bottom of the fracture with the

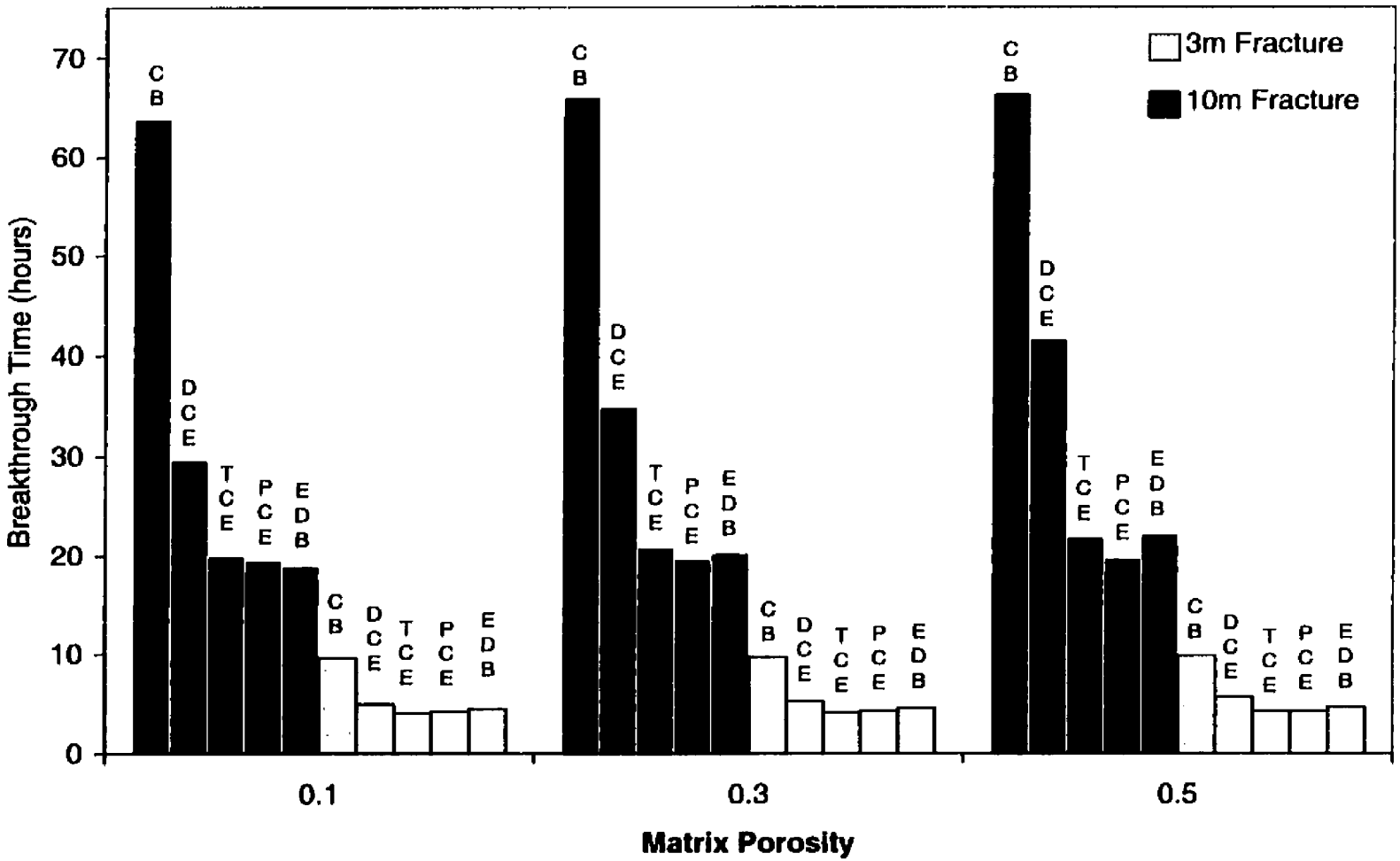

Figure 3-6. Breakthrough Times (First Arrival of DNAPL at Bottom of Fracture) for Various Values of Matrix Porosity

capillary pressure boundary condition, as opposed to only 0.06 m from the top of the fracture in the injection case. The simulation in which the DNAPL is injected at a constant rate results in greater than 40 percent of the mass in the system resident in the matrix after 4 hours, as compared to less than 7 percent for the constant capillary pressure boundary condition. The use of a constant low injection rate in the work of Slough et al. (1999) does not capture the effects of capillary over-pressuring at the top of the fracture.

The controlling factor in the assessment of the effects of matrix diffusion on the rate of DNAPL migration is the amount of mass transferred to the matrix in relation to the amount of mass entering the fracture as replenishment. Figure 3-8 presents the ratio of mass flux (mol/s) into the matrix through diffusion (in dissolved phase) to mass flux (mol/s) entering the fracture (in both the dissolved and nonwetting phases) as a function of time for a 10 m fracture dipping at 60 degrees. The results show that this relationship is primarily a function of solubility, as the order (from bottom to top) is co-incident with the increasing solubility of the DNAPLs. The exception to this is the placement of EDB slightly below DCE despite its greater solubility. This stems from the large difference between the densities of the two DNAPLs, resulting in a larger gravity component of the driving force replenishing EDB to the fracture. The large density difference is countered somewhat by the greater viscosity of EDB which reduces flow-rate along the fracture, the resultant being very similar behaviour between EDB and DCE.

The question of the ability of matrix diffusion to arrest DNAPL migration through a vertical fracture is also addressed through the results presented in Figure 3-8. For the DNAPL to stop migrating, at a minimum, the mass lost to the matrix would have to exceed the mass entering the

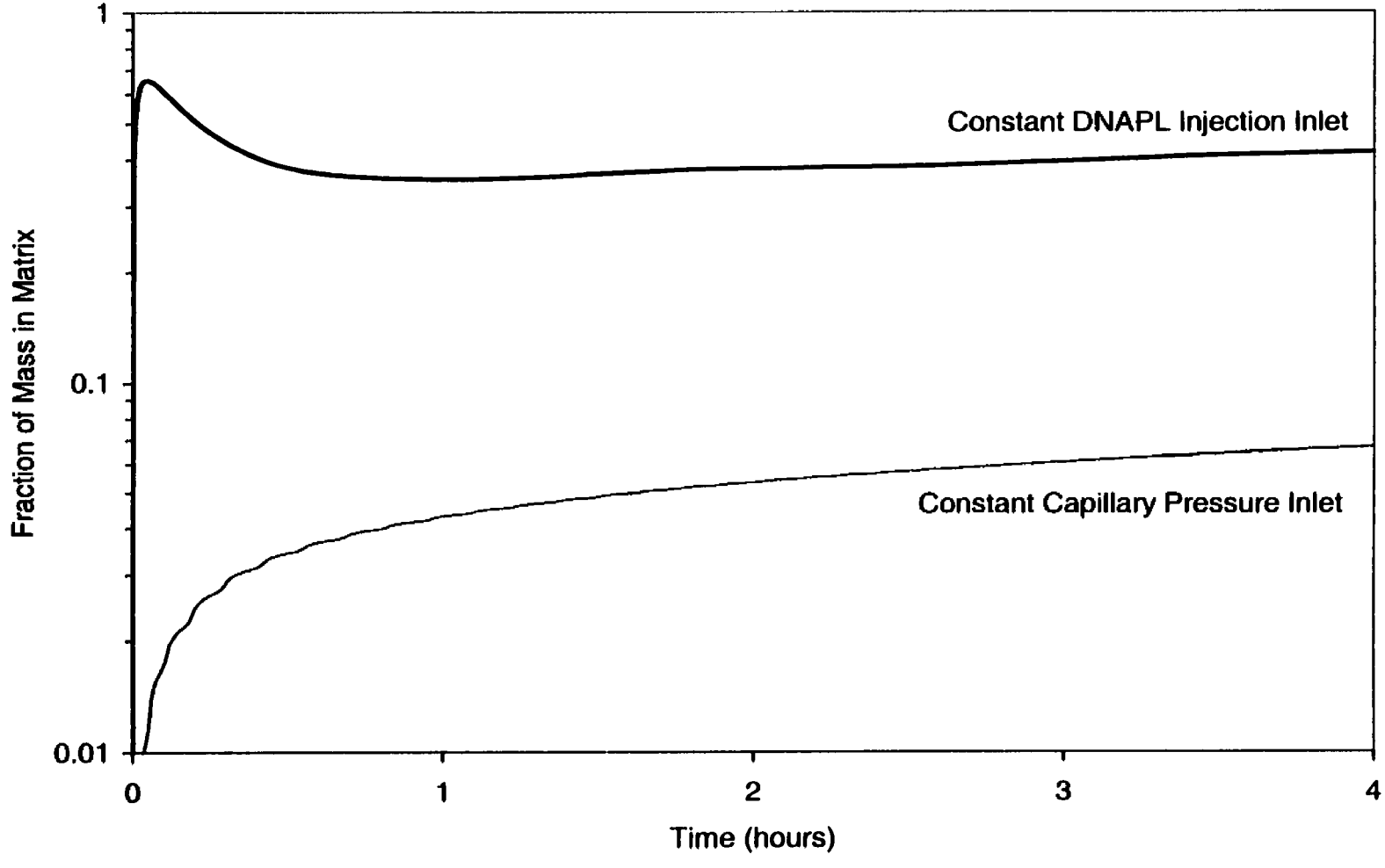

Figure 3-7. Distribution of Contaminant between Matrix and Fracture for Differing Boundary Conditions

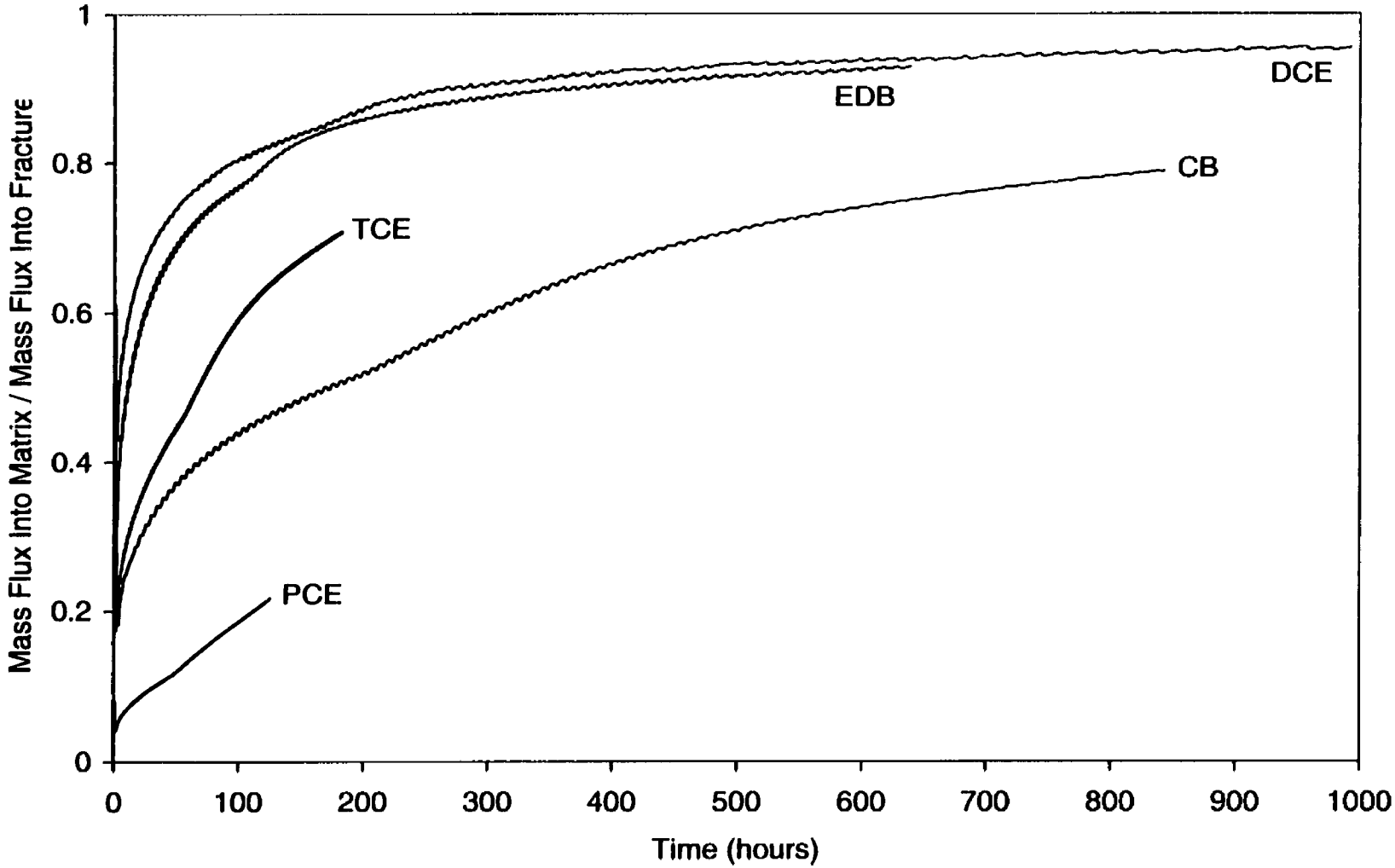

Figure 3-8. Ratio of Mass Flux into Matrix (Aqueous Phase) to Mass Flux Into Fracture (Nonwetting and Aqueous Phases), versus Time

inlet of the fracture. The ratio presented in Figure 3-8 would therefore have to exceed 1.0 for a significant length of time, as even in a temporary net loss scenario the nonwetting phase would continue to flow vertically downward under imbibition conditions due to the effect of gravity until the entire DNAPL mass has exhausted itself to residual. The closest this comes to occurring is for the two high solubility DNAPLs (EDB and DCE), both of which are approaching asymptotic behaviour to a value less than 1.0 when breakthrough is achieved. If the results from Figure 3-8 are extrapolated to a fracture in excess of 10 m in length, when the mass ratio becomes constant, the DNAPL will be migrating at a constant velocity. As can be seen from Figure 3-8, the length of time required to approach the asymptote and hence the length of fracture traversed up to this point in time varies from DNAPL to DNAPL, and will also vary with hydrogeologic setting (aperture, K_d, matrix porosity, etc.). The time and distance required to reach asymptotic behaviour will be larger for heavier, less soluble DNAPLs (e.g. PCE).

3.3.2 Remediation

The results from the previous sections have shown that the mass lost from the nonwetting phase due to dissolution and matrix diffusion is usually not enough to significantly retard the migration of DNAPL through fractures. This lost mass, however, poses a threat to the long-term groundwater quality of the aquifer exclusive of the presence of DNAPL in the fractures. To demonstrate this, five additional simulations were performed in which 5 mL of each of the DNAPLs was allowed to enter a 30 μm aperture, 3 m long fracture subject to the inlet capillary pressure used previously (4295 Pa). After 5 mL had entered (less than 1 hour in each case), the DNAPL source to the fracture was removed and a wetting phase hydraulic gradient of 0.01 was

applied to flush clean water through the fracture (resulting in a groundwater velocity within the fracture of 0.64 m/d). The simulations allowed for DNAPL dissolution into the flowing groundwater (assuming equilibrium partitioning), as well as matrix diffusion. The various stages of interest are illustrated in Figure 3-9.

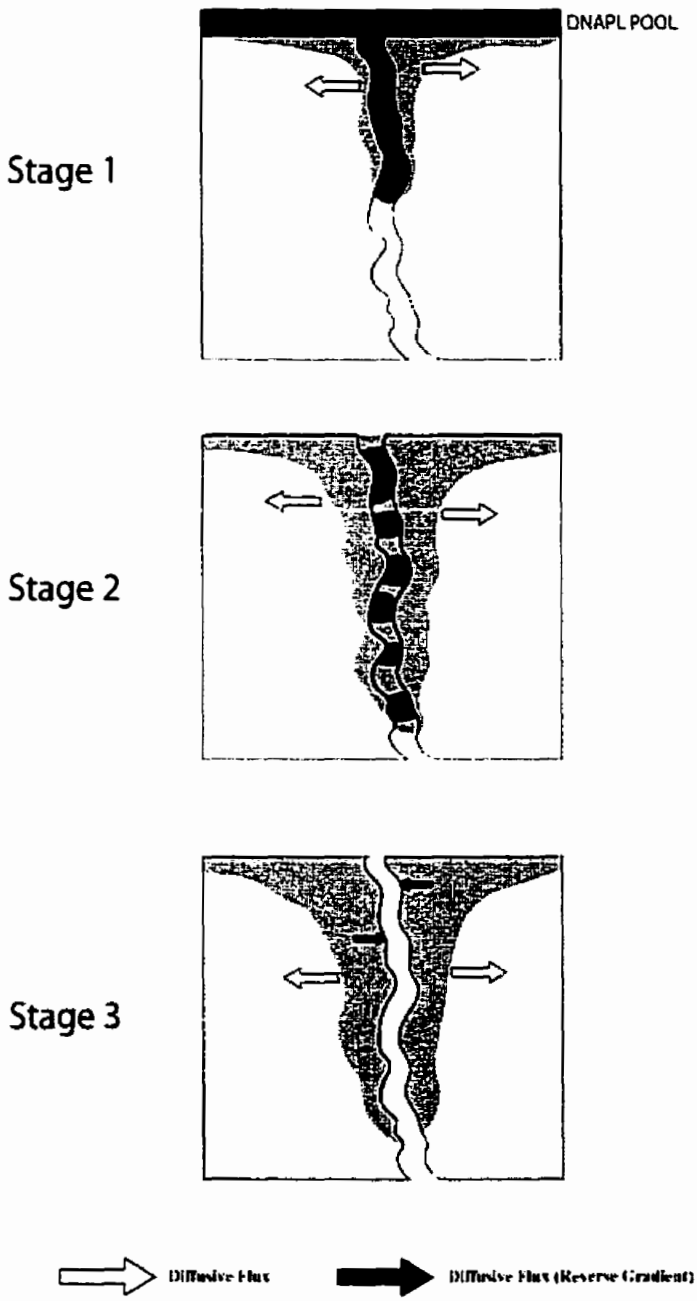

Figure 3-9. Direction of Mass Flux Within the System a) During DNAPL Invasion, b) During DNAPL Redistribution to Residual, c) After DNAPL Disappearance

The small volume of DNAPL that was allowed to enter the fracture was not sufficient to reach the exit of the fracture. The deepest penetrating DNAPL (PCE) reached a maximum depth of 2.1 m into the fracture before becoming immobile under imbibition. In contrast, primarily due to its greater solubility and viscosity, EDB only penetrated 1.4 m into the fracture before depleting itself to residual. In all cases the DNAPL continued to migrate vertically after the source was removed, but at a slower rate due to the reduced capillary driving forces and progressive reduction in nonwetting phase relative permeability that occur under imbibition. After the initiation of the clean water flush, the DNAPL rapidly partitioned itself into the aqueous phase due to the presence of flowing water. The life span of DNAPL in the fracture for these simulations ranged from 15 hours (following the start of injection) for DCE to greater than 140 days for the relatively insoluble and slowly diffusing PCE.

Figure 3-10 displays the dissolved concentrations of each DNAPL at the exit of the fracture as a function of time. Despite the presence of nonwetting phase at early times within the fracture, the exit concentrations never reach more than a fraction of each individual DNAPL's solubility. Under the equilibrium dissolution assumption in this work, concentrations in the invaded portions of the fracture are always at solubility levels while DNAPL exists. Downgradient concentrations, however, are rapidly attenuated by the matrix throughout the portion of the fracture that was not invaded by DNAPL. This is evidenced by the temporal location of the maximum in the effluent curves, which occurs between 275 and 350 days after the disappearance of the nonwetting phase from the system. The line on Figure 3-10 represents a concentration of 5 μg/L (ppb), a typical remediation goal for certain chlorinated compounds. The time required to reach this level is on the order of 500 to 1000 years for the DNAPLs studied, despite the

disappearance of the nonwetting phase in less than a year in each case. This is primarily due to the slow nature of molecular diffusion, the dominant transport process in these simulations once the nonwetting phase disappears from the fractures, and the retardation imparted by sorption phenomena. It is of interest to note that the two low solubility organics (CB and PCE) require the greatest amount of time to reach this 5 µg/L limit (up to 300 years longer than EDB and TCE) due to their affinity for sorption to the clay matrix.

The process of reverse diffusion (from matrix to fracture) during the clean water flush is further retarded by the presence of opposite concentration gradients within the matrix, one towards the fracture, and another away from the fracture towards the centre of each matrix "block". At very early times (when DNAPL is present in the fracture) a uni-directional concentration gradient exists, from the solubility levels within the fracture towards the uncontaminated areas of the matrix farthest away from the fracture. The concentrations at all points within the matrix continue to increase with time, as long as DNAPL is present to maintain the high concentrations within the fracture, and can reach the solubility of the organic in certain cases (Figure 3-11).

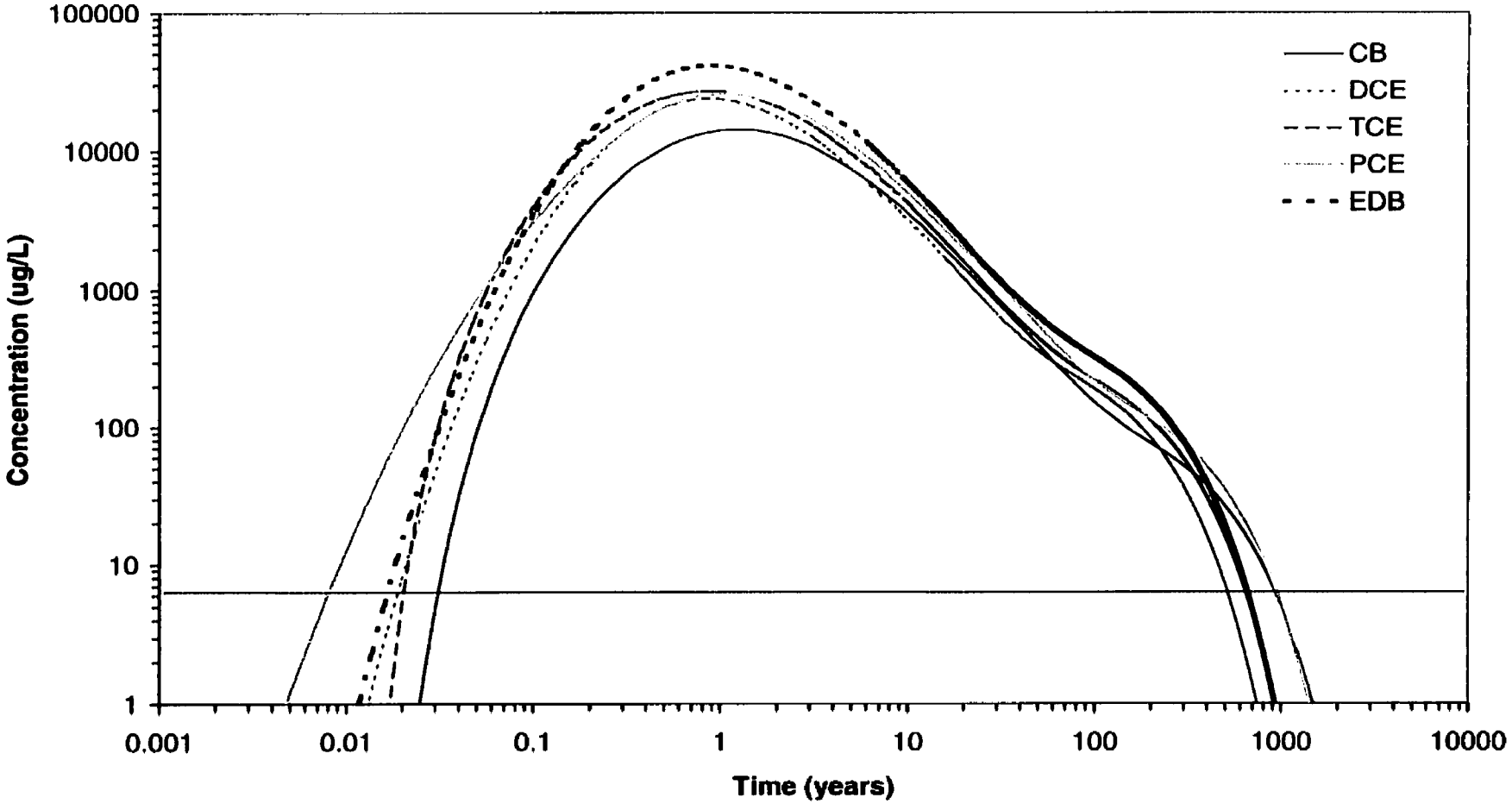

Figure 3-10. Concentrations Exiting Fracture During Clean Water Flush

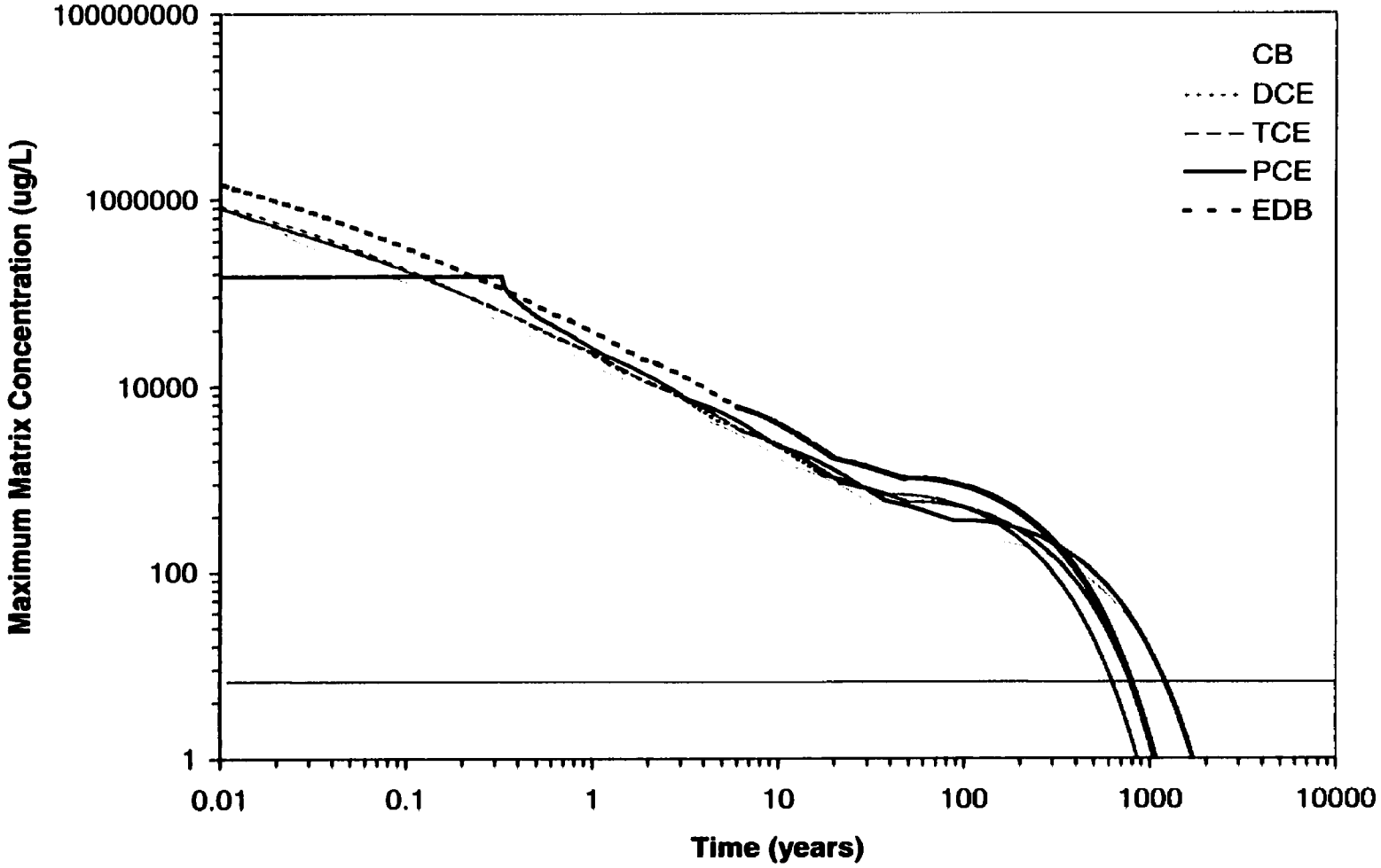

Figure 3-11. Maximum Concentrations in the Matrix During Clean Water Flush

Figure 3-11 shows the maximum concentration achieved in the matrix for each simulation. The two low solubility organics (CB and PCE) achieve solubility limits in the matrix adjacent to the fracture, which are maintained until the DNAPL source in the fracture is exhausted. The three higher solubility DNAPLs, however, never achieve this level within the matrix. The 5 μg/L line is again drawn in Figure 3-11 and shows that concentrations above this level persist for up to 1283 years within the matrix (for PCE), longer than exceedances were observed at the fracture terminus (due to dispersion and dilution within the fracture). After the disappearance of the DNAPL and the instigation of the water flush, the maximum concentration in the system no longer exists in the fracture, but rather some distance into the matrix. As a result, the initial concentration gradient is reversed across the fracture wall. The dissolved contamination is now moving in two directions from the point of highest concentration, towards and away from the fracture.

3.4 Conclusions

The single most important factor controlling the migration rate of DNAPL through a single fracture is the fracture aperture. Increasing the fracture aperture from 15 μm to 50 μm results in an approximately 20-fold increase in the rate of migration. Similar variations in the parameters governing matrix diffusion have a relatively insignificant influence on DNAPL migration rates.

The effect of the inclination of the fracture on the migration rate of the DNAPL is significant, primarily due to the increased length of travel required to traverse the aquitard and the reduced gravity driving force in the direction of flow. The mass lost to the matrix due to the increased

travel time can also retard the migration (up to 40% for DCE in a 10 m fracture). Although the mass lost to the matrix increases with an increase in f_{oc} and matrix porosity the resulting decrease in DNAPL migration rate is negligible. The use of a constant capillary boundary condition ensures that the system is not artificially limited in its ability to replenish the lost DNAPL.

The similarities in breakthrough times predicted in the larger aperture fractures for the five DNAPLs illustrates the difficulty in predicting migration times without the use of numerical models. Based solely on an examination of the solubility and density, the DNAPL with the slowest breakthrough time would be expected to be DCE. This, however, was not the case in the majority of the simulations. In all cases (with the exception of the 15 μm aperture, 10 m long fracture) CB was found to be the slowest migrating DNAPL. The insensitivity of the migration rate to matrix diffusion decreases the importance of solubility, and increases the importance of viscosity and density.

In assessing the decrease in migration rate due to matrix diffusion, the most descriptive indicator is the ratio of mass lost to the matrix to mass replenishment at the fracture entrance. This ratio is primarily dependent upon the solubility of the DNAPL when all other factors remain the same. To arrest downward migration, this ratio would have to exceed 1.0 for a significant length of time. This never occurred in any of the simulations performed in this work. This is due to a limitation in the "contributing length" of the DNAPL body. As the DNAPL penetrates through the aquitard the ratio of mass lost to mass replenished becomes essentially constant, as the matrix adjacent to the upper portions of the fracture becomes saturated with contaminant, and no longer acts as a sink to the DNAPL in the fracture.

The presence of the dissolved and sorbed contaminant within the matrix presents a much longer term impact on groundwater quality than the presence of the DNAPL in the fracture. If the DNAPL source to the fracture is removed, the DNAPL will quickly become entrapped as residual and then disappear due to dissolution and resultant matrix diffusion. Once the fracture is devoid of DNAPL, two concentration gradients exist within the matrix, the first engendering "reverse" diffusion back into the fracture, the second pushing contamination deeper into the matrix. In time this behaviour reverts to the case where a single gradient exists, driving contamination only towards the fracture. These processes can result in aqueous concentrations exiting the fracture above acceptable values for up to 1000 years after the disappearance of DNAPL from the fracture.

3.5 References

Brooks, R.H. and A.T. Corey. 1964. Hydraulic Properties of Porous Media. *Hydrol. Paper 3*, Colorado St. Univ., Fort Collins CO.

Cherry, J.A. Feenstra, S., and D.M. McKay. 1996. Concepts for the Remediation of Sites Contaminated with Dense Nonaqueous Phase Liquids (DNAPLs). In J.F. Pankow and J.A. Cherry (Eds.), Dense Chlorinated Solvents and Other DNAPLs in Groundwater: History, Behaviour, and Remediation, Waterloo Press, Portland, Oregon, p 475-506.

Esposito, S.J., and N.R. Thomson. 1999. Two-phase Flow and Transport in a Single Fracture-porous Media System, *J. Cont. Hyd.*, 37, p 319-341.

Freeze, R.A., and D.B. McWhorter. 1997. A Framework for Assessing Risk Reduction Due to DNAPL Mass Removal from Low Permeability Soils, *Ground Water*, 35(1), p 111-123.

Hayduk, W., and H. Laudie. 1974. Prediction of Diffusion Coefficients for Nonelectrolytes in Dilute Aqueous Solutions, *AIChE J.*, 20, p 611-615.

Kueper, B.H., and D.B. McWhorter. 1991. The Behavior of Dense, Nonaqueous Phase Liquids in Fractured Clay and Rock, *Ground Water*, 29(5), p 716-728.

Pankow, J.F., and J.A. Cherry. 1996. Dense Chlorinated Solvents and other DNAPLs in Groundwater, Waterloo Press, Portland, OR, USA, 522 pgs.

Parker, B.L., Gillham, R.W., and J.A. Cherry. 1994. Diffusive Disappearance of Immiscible-Phase Organic Liquids in Fractured Geologic Media, *Ground Water*, 32(5), p 805-820.

Parker, B.L., McWhorter, D.B., and J.A. Cherry. 1996. Diffusive Loss of Non-Aqueous Phase Organic Solvents from Idealized Fracture Networks in Geologic Media, *Ground Water*, 35(6), p 1077-1088.

Reynolds, D.A., and B.H. Kueper. 2000. DNAPL Flow Through Fractured Porous Media, Treating Dense Nonaqueous-Phase Liquids (DNAPLs), Proc. Sec. Int. Conf. Remedia. Chlorinated and Recalcitrant Compounds, Vol. C2-2, Wickramanayake, G.B., Gavaskar, A.R., and Gupta, N. (Eds.), p 165-172.

Reynolds, D.A., and B.H. Kueper. 2001. Multiphase Flow and Transport in Fractured Clay/Sand Sequences, *J. Cont. Hyd.*, In Press.

Ross, B., and N. Lu. 1999. Dynamics of DNAPL Penetration into Fractured Porous Media, *Ground Water*, 37(1), p 140-147.

Slough, K.J., Sudicky, E.A., and P.A. Forsyth. 1999. Numerical Simulation of Multiphase Flow in Discretely-fractured Geologic Media, *J. Cont. Hyd*, 40(2), p 107-136.

CHAPTER 4 - FACTORS AFFECTING MULTIPHASE FLOW AND TRANSPORT IN FRACTURED GEOLOGIC SEQUENCES[2]

4.1 Introduction

Contamination of groundwater in contact with dense, non-aqueous phase liquids (DNAPLs) such as PCB oils, chlorinated solvents, and creosote has become a major environmental concern over the course of the last two decades. Many sites worldwide have been identified where significant volumes of these chemicals have been released to the subsurface. Given the relatively low solubility and other physio-chemical properties of DNAPLs, they can penetrate to large depths below the watertable. Historically, the existence of low permeability units in the subsurface (clays, silts, etc.) was thought to be an effective barrier to further vertical migration of DNAPLs. Recently, however, it has been shown that the near ubiquitous presence of fractures in these low permeability units (McKay et al., 1993) removes their effectiveness as capillary barriers to DNAPL migration (Kueper and McWhorter, 1991).

Kueper and McWhorter (1991) presented a conceptual model in which DNAPL preferentially enters the higher aperture (lower displacement pressure) fractures in both clay and rock. Given the low storage capacity of the fractures themselves, even small volumes of DNAPL are capable of traveling large distances through interconnected fracture pathways. Longino and Kueper (1999) demonstrated that the residual saturation left behind migrating DNAPL can be as high as

[2] Reynolds, D.A., and B.H. Kueper. 2001. Factors Affecting Multiphase Flow and Transport in Clay/Sand Sequences, Journal of Contaminant Hydrology. In Press.

27% of fracture volume, and is dependent upon factors such as fracture dip, fracture aperture, hydraulic gradient, and maximum capillary pressure attained during drainage. Parker et al. (1994) demonstrated that residual DNAPL has a finite lifespan in fractured porous media as a result of diffusion into the matrix, with timescales on the order of weeks to several hundred years depending on the DNAPL and matrix properties. Although the above studies have significantly advanced our understanding of DNAPL in fractured deposits, they have not considered behaviour in alternating sequences of fractured and granular porous media.

The focus of this work is on numerical simulation of DNAPL movement through layered sequences of fractured and unfractured porous media. Sedimentary deposits of this type are commonly found in shoreline and deltaic depositional environments, and compose a majority of the surface geology along the Gulf Coast of the United States. A typical subsurface environment in this area consists of Pleistocene Age sequences of clays and silty clays with thin, interbedded sand intervals. From a groundwater resource standpoint, the most important feature of these areas is the prevalence of deep sand aquifers (for example the Chicot in Southern Louisiana) that are used as drinking water supplies for many people. The results of this study also have application to shallow sequences of clay aquitards separated by sandy aquifers, characteristic of many settings worldwide.

The complexities of numerically simulating the behaviour of multi-phase flow and transport in fractured media have led to a great deal of research and model development in recent years. Kueper and McWhorter (1991) developed a two-phase model capable of simulating DNAPL flow (without dissolution and aqueous phase transport) through orthogonal fracture systems.

Slough (1997) introduced *CompFlow*, a multi-phase multi-component simulator capable of simulating both DNAPL migration and plume migration. Reitsma and Kueper (1998) developed a complex compositional simulator to investigate non-equilibrium dissolution effects in alcohol flooding of porous media that, however, was limited to one-dimension. Murphy and Thomson (1993) and Esposito and Thomson (1999) developed a numerical model that does not rely on an empirical capillary pressure-saturation relationship, but rather defines phase location explicitly. These models, however, do not include mass transfer or advection of an aqueous phase except under certain restrictive assumptions. To the authors' knowledge, there has not been any published research which utilizes the benefits of compositional simulation to investigate multi-phase flow and transport in fractured, layered geologic sequences containing multiple sand units.

The specific objective of this paper is to systematically study the migration of DNAPLs through layered sand/clay systems below the watertable, with specific emphasis on the effects of hydraulic gradient, displacement pressure ratios between the interbedded sands and the fractures, the importance of dissolution in potentially retarding the rate of DNAPL migration, and the role of DNAPL release volume. These four factors will be assessed by examining their effects on DNAPL first arrival time at the base of the system, and mass flux into the lowermost sand. The first portion of this work introduces QUMPFS (Queen's University Multi-Phase Flow Simulator), a three-dimensional, two- phase, compositional simulator developed to simulate multiphase flow and transport in fractured porous media.

4.2 Numerical Model

A three-dimensional multiphase compositional simulator, with the capabilities of modeling advection, dispersive and diffusive fluxes, equilibrium and non-equilibrium phase partitioning, and capillary hysteresis was developed to investigate the fate of NAPLs in discretely fractured porous geologic media. The model is based on the equations governing isothermal multiphase flow and multicomponent transport in porous media (Abriola and Pinder, 1985):

$$\frac{\partial}{\partial t}\left(c_{i\beta}\phi S_{\beta} x_{i\beta}\right)+\nabla\cdot\left(c_{i\beta} x_{i\beta} v_{\beta}\right)-\nabla\cdot\left[\phi S_{\beta}\vec{D}_{i\beta}\nabla\left(c_{i\beta} x_{i\beta}\right)\right]-q_{i\beta}-I_{i\beta}=0 \qquad [4\text{-}1]$$
$$\beta=1..n_p,\quad i=1..n_c$$

where n_p is the number of phases, n_c is the number of components, β is the particular phase of interest, $c_{i\beta}$ is the molar density of phase β, ϕ is the porosity of the medium, S_β is the saturation of phase β, $x_{i\beta}$ is the mole fraction of component i in phase β, v_β is the Darcy flux of phase β, $D_{i\beta}$ is the dispersion tensor for component i in phase β, $q_{i\beta}$ is the source/sink term for component i in phase β, $I_{i\beta}$ represents the inter-phase mass transfer of component i to or from phase β, and t is time.

The constraints amongst the mole fraction, saturation, and mass transfer terms, as well as the forms of the dispersion tensor, and equilibrium mass transfer are given elsewhere and not repeated here (Unger et al., 1995, Reitsma and Kueper, 1998). The phase flux vector, v_β, is expressed according to Darcy's law (Bear, 1972):

$$v_\beta = -\left[\frac{k' k_{r\beta}}{\mu_\beta}\left(\nabla P_\beta + \rho_\beta g \nabla z\right)\right] \qquad [4\text{-}2]$$

where k' is the intrinsic permeability tensor of the medium, $k_{r\beta}$ is the relative permeability to phase β, μ_β is the viscosity of phase β, P_β is the pressure of phase β, ρ_β is the mass density of phase β, g is the acceleration due to gravity, and z is the elevation.

The Brooks-Corey functional relationship between capillary pressure and saturation (Brooks and Corey, 1964) is adopted in the model for both the fractures and the porous media based on the laboratory work of Reitsma and Kueper (1994):

$$S_e = \left(\frac{P_c}{P_d}\right)^{-\lambda} \qquad [4\text{-}3]$$

where P_c is the capillary pressure defined as the difference between the nonwetting and wetting phase pressures, P_d is the displacement pressure of the medium, λ is the pore size distribution index, and S_e is the effective wetting phase saturation given by:

$$S_e = \frac{S_w - S_{rw}}{1 - S_{rw}} \qquad [4\text{-}4]$$

where S_w is the wetting phase saturation, and S_{rw} the irreducible wetting phase saturation.

Mendoza (1992), using invasion percolation theory, performed a Monte-Carlo analysis and compiled mean capillary pressure and relative permeability curves for multiple realizations of fracture aperture distributions, and also found that the results were adequately represented by the Brooks-Corey model. Mendoza (1992) also pointed out that the capillary pressure-saturation

relationship exhibits hysteretic behaviour at the scale of a single fracture plane, similar to the behaviour of DNAPL/water systems in porous media. Reitsma and Kueper (1994) observed hysteretic behaviour in measuring the relationships between capillary pressure and fluid saturation in a single, rough-walled fracture.

To capture the effects of capillary hysteresis in the model, the technique of Gerhard et al. (1998) was adopted, which uses a linear approximation of the imbibition and secondary wetting curves, based on the initial and residual saturations. Since relative permeability is generally accepted to be weakly influenced by saturation history (Bear, 1972), the non-hysteretic Brooks-Corey saturation-relative permeability relationship is adopted (Brooks and Corey, 1964):

$$k_{rw} = (S_e)^{\frac{2+3\lambda}{\lambda}} \qquad [4\text{-}5]$$

$$k_{rnw} = (1 - S_e)^2 \cdot \left(1 - S_e^{\frac{2+\lambda}{\lambda}}\right) \qquad [4\text{-}6]$$

where k_{rw} is the relative permeability of the wetting phase, and k_{rnw} the relative permeability of the nonwetting phase.

Equation [4-1] is discretized using the finite volume method, incorporating the porous matrix as three-dimensional block cells, and the discrete fractures as two-dimensional planar cells. The discretized form of equation [4-1] is:

$$\left\{\left[\phi S_\beta c_{i\beta} x_{i\beta} + \rho_b K_{di} c_{i\beta} x_{i\beta}\right]_I^{N+1} - \left[\phi S_\beta c_{i\beta} x_{i\beta} + \rho_b K_{di} c_{i\beta} x_{i\beta}\right]_I^{N}\right\}\frac{V_I}{\Delta t}$$
$$-\left[\sum_{J\in\eta_c}\left(\psi_{\beta J}^{N+1} - \psi_{\beta I}^{N+1}\right)\left(c_{i\beta} x_{i\beta}\frac{k_{r\beta}}{\mu_\beta}\right)_{ups(I,J)}^{N+1}\gamma_{IJ}\right] \qquad [4\text{-}7]$$
$$-\left[\sum_{J\in\eta_c}\left(c_{i\beta}\right)_{IJ+1/2}^{N+1}\left(\gamma'_{IJ}\right)_\beta\left(x_{i\beta J} - x_{i\beta I}\right)^{N+1}\right]$$
$$-\left\{q_{i\beta} + I_{i\beta}\right\}^{N+1} V_I = 0 \quad \beta = 1..n_p, \quad i = 1..n_c, \quad I = 1..n_n$$

where I is the node of interest, J represents a node connected to node I, η_c represents the set of all nodes connected to node I, ρ_b is the dry bulk density of the porous medium, K_{di} is the distribution coefficient of component i, V_I is the volume associated with node I, t is time, n_n is the number of nodes, n_c is the number of components, $N+1$ denotes values at the present time step, and N denotes values at the previous time step. The fluid potential of phase β at node I, $\psi_{\beta I}$, is given by:

$$\psi_{\beta I} = P_{\beta I} + \rho_{\beta(IJ+1/2)} g z_I \qquad [4\text{-}8]$$

where subscript $IJ+1/2$ represents the central weighted value between nodes I and J such that:

$$\rho_{\beta(IJ+1/2)} = \frac{\rho_{\beta I} + \rho_{\beta J}}{2} \qquad [4\text{-}9]$$

The molar densities are also centrally weighted:

$$c_{i\beta(IJ+1/2)} = \frac{c_{i\beta I} + c_{i\beta J}}{2} \qquad [4\text{-}10]$$

The advective and dispersive transmissibility terms (γ_{IJ}, γ'_{IJ}) are given by:

$$\gamma_{IJ} = -k_{IJ+1/2}\frac{A_{IJ}}{\Delta x_{ij}} \qquad [4\text{-}11]$$

$$\left(\gamma'_{IJ}\right)_\beta^N = -\left(S_\beta\right)_{IJ+1/2}^{N+1}\left(\frac{\phi D_{i\beta}}{S_\beta}\right)\frac{A_{IJ}}{\Delta x_{IJ}} \qquad [4\text{-}12]$$

where $k_{IJ+1/2}$ is the harmonic mean of the permeability between nodes I and J, A_{IJ} is the cross-sectional area between nodes I and J, and Δx_{IJ} is the distance between nodes I and J.

The advective flux, source/sink, and inter-phase mass transfer terms are treated implicitly within the model, while the non-advective flux term is treated through the combined explicit-implicit formulation expressed in [4-12]. The discretized equations are linearized through a full Newton-Raphson iterative process including optimized under-relaxation, with the resulting matrix equations solved through modified ORTHOMIN (Behie and Forsyth, 1984) acceleration.

The use of mass lumping and fully implicit time-weighting produce a monotone solution regardless of the time step size. Further, all advective flux terms are upstream weighted to ensure monotonicity, a technique that does not introduce significant numerical dispersion of the phase saturation variables due to the self-sharpening nature of the progressing saturation fronts (Aziz and Settari, 1979). The model's use of upstream weighting in terms involving the advective flux of dissolved contaminants will, however, produce numerical dispersion, particularly in regions which are advection dominated and have high wetting phase saturations (Unger et al., 1996). The effects of this induced error are not expected to be significant in this study due to the lack of spatially extensive aqueous phase plumes.

The numerical model was verified against the analytical solution of McWhorter and Sunada (1990), which fully incorporates the effects of capillarity. In addition, a two-dimensional version of QUMPFS was validated against a two-dimensional heterogeneous sand lens experiment (Kueper and Frind, 1991). QUMPFS was also verified against two analytical solutions involving

aqueous phase transport, the one-dimensional advection dispersion solution of Ogata and Banks (1961), and the two-dimensional solution to the problem of transport in a system of parallel fractures (Sudicky and Frind, 1982). These verification and validation procedures provide confidence that, in a two-dimensional cross-section, QUMPFS correctly simulates the physics of multi-phase flow and aqueous phase transport. QUMPFS (as opposed to FRACAS) was required in this work to allow for the transport of the nonwetting phase into the sand lenses.

It has recently been shown that with some approaches, the level of spatial discretization can greatly affect the predictions of phase migration through fracture intersections (Slough et al., 1999). The spatial discretization used in this model incorporates an exact representation of the fracture intersections through the use of a control volume representing the actual intersection (Figure 4-1). To aid in the Newton Raphson procedure, the actual volume of the intersection cell is increased by "borrowing" from the adjacent cells representing the horizontal fracture (Figure 4-1). It has been found that this approach greatly eases Newton Raphson convergence, as the volume of the intersection cell is similar to that of the adjacent fracture cells. This approach introduces a slight approximation into the system during the discretization of the dispersion/diffusion term. The area term in the transmissibility equation [4-12] for the fracture control volumes adjacent to a fracture intersection is the area before "borrowing" occurs. This will cause a slight over- or underestimation of mass transfer if the mole fractions in the intersection control volume is significantly greater than that in the adjacent fracture control volumes. The combination of this discretization approach and the uniform aperture distributions used in the present study circumvents the problems encountered with other approaches.

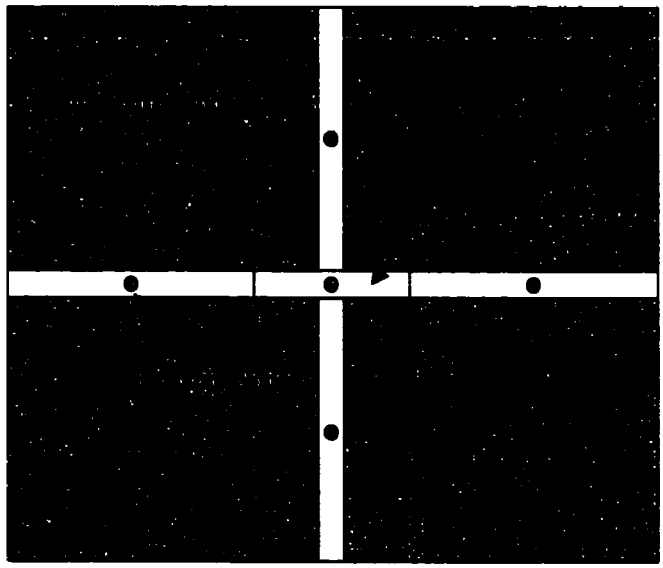

Figure 4-1. Fracture Intersection Discretization Showing "Borrowing" Approach

4.3 Methodology

All simulations presented in this study are carried out in a rectangular two-dimensional, vertical cross section 60 m in width and 33 m in height. The domain is initially 100% water saturated, with a watertable boundary condition along the top of the domain, and constant wetting phase pressure boundary conditions along the vertical sides and bottom of the domain. All porous medium boundaries, with the exception of the top, were assigned a free exit condition for both the nonwetting phase and the dissolved phase. All fracture boundaries were formulated such that contaminant may leave under the process of advection only.

Two different geologic settings were modeled within this framework; the first consisting of a single 30 m thick fractured clay layer overlying a 3m thick lower sand aquifer (Figure 4-2a), and the second identical to the first, with the exception that two horizontal sections of the clay are

replaced with sand lenses (Figure 4-2b). The lenses are referred to as the upper sand lens and the lower sand lens. The fracture patterns within the clay units between the two domains are identical. The porous medium in both domains is discretized into 240 control volumes horizontally (0.25 m spacing) and 264 control volumes vertically (0.125 m spacing), resulting in 63,360 porous media control volumes. The discrete fractures are discretized at an identical scale, resulting in 7,936, and 6,976 fracture control volumes in the first (fractured) and second (lenses) domains, respectively. The discretization incorporated in this work (adjacent to the fractures) is not as refined as was used in Chapter 3 due to computational limitations. The coarser discretization will result in smaller concentration gradients immediately adjacent to the fracture, and result in less mass lost to the matrix, and a corresponding faster predicted migration time for the aqueous phase.

Table 4-1 summarizes the physical parameters used in all simulations. The nonwetting phase has been assigned the properties of trichloroethylene (TCE), a common chlorinated solvent. DNAPL was released into the domain through a 3m wide patch in the middle of the upper boundary. This source allowed DNAPL to access three fractures intersecting the top of the domain. A constant capillary pressure equal to 14,317 Pa was applied to this source in all simulations, and was removed after 10 m^3 had infiltrated the domain in those simulations where the source was terminated. This capillary pressure corresponds to 1.0 m of TCE pooled above the watertable.

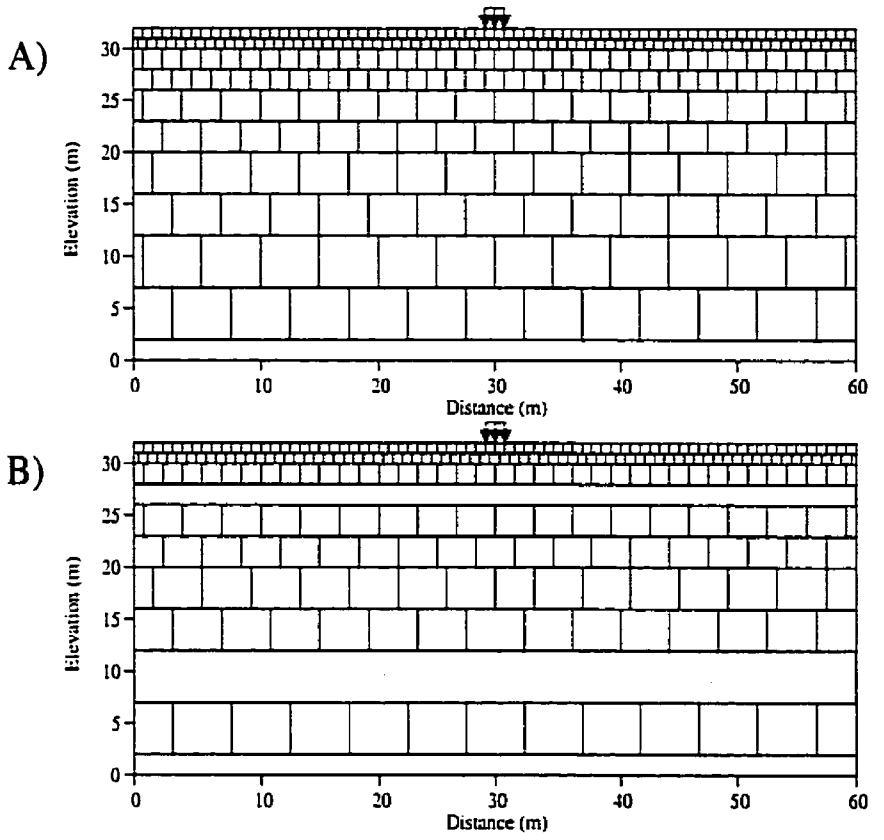

Figure 4-2. Solution Domain A) fractured, B) lens

Table 4-2 summarizes the conditions modelled for each of the simulations that were performed. For clarity and brevity during the presentation of results, each simulation has been given an abbreviation to help place it into one of four broad categories. FD and FND denote the fractured domain, both with dissolution (FD) and with no dissolution (FND). LD and LND denote the lens domain, both with dissolution (LD) and with no dissolution (LND). Each subset is further broken down through the assigning of a simulation number, which pertains to either the applied gradient, the type of release, or the displacement pressure of the sand. Note that a positive gradient in Table 4-2 produces upward groundwater flow.

Table 4-1. Numerical Model Input Parameters

Parameter	Value
Clay permeability	1.0×10^{-17} (m^2)
Sand permeability	1.0×10^{-11} (m^2)
Clay porosity	0.35
Sand porosity	0.25
Pore size distribution index	2.0
Residual wetting phase saturation	0.10
Fracture displacement pressure, Pdf	1145 (Pa)
Clay displacement pressure	30,000 (Pa)
Sand displacement pressure, Pds	326 to 3621 (Pa)
Sand/Clay longitudinal dispersivity	0.1 (m)
Sand/Clay transverse dispersivity	0.03 (m)
Fracture longitudinal dispersivity	0.01 (m)
Fracture transverse dispersivity	0.001 (m)
Fracture aperture	35 (μm)
Fracture permeability	1.02×10^{-10} (m^2)
Wetting phase density	1000 (kg/m^3)
Nonwetting phase density	1460 (kg/m^3)
Wetting phase viscosity	0.001 (Pa s)
Nonwetting phase viscosity	0.00057 (Pa s)
Interfacial tension	0.02 (N/m)
Tortuosity	0.10
Free solution diffusion coefficient	1.01×10^{-9} (m^2/s)
Equilibrium mole fraction in aqueous phase	1.9×10^{-4}
Distribution coefficient	1.26×10^{-4} (m^3/kg)
Dry bulk density clay	1.82×10^{3} (kg/m^3)
Dry bulk density sand	1.95×10^{3} (kg/m^3)
Applied gradient (positive results in upward flow)	-0.25, 0.0, 0.1

Table 4-2. Identification of Simulations

Run	Domain	Gradient	Dissolution	Release [1]	P_{ds} (Pa)
FND1	Fractured	0.0	No	C	NA
FND2	Fractured	-0.25	No	C	NA
FND3	Fractured	0.1	No	C	NA
FD1	Fractured	0.0	Yes	C	NA
FD2	Fractured	-0.25	Yes	C	NA
FD3	Fractured	0.1	Yes	C	NA
LND1	Lenses	0.0	No	C	1145
LND2	Lenses	0.0	No	C	3621
LND3	Lenses	0.0	No	C	362
LND4	Lenses	-0.25	No	C	1145
LND5	Lenses	0.1	No	C	1145
LND6	Lenses	0.0	No	FV	1145
LND7	Lenses	-0.25	No	FV	1145
LND8	Lenses	0.1	No	FV	1145
LD1	Lenses	0.1	Yes	C	1145
LD2	Lenses	-0.25	Yes	C	1145
LD3	Lenses	0.0	Yes	C	1145
LD4	Lenses	0.0	Yes	FV	1145
LD5	Lenses	-0.25	Yes	FV	1145
LD6	Lenses	0.1	Yes	FV	1145

1, C = Continuous, FV = Finite Volume (10 m^3)

4.4 Results and Analysis

4.4.1 First Arrival Time

4.4.1.1 Effect of Incorporating Sand Lenses

The time until the first appearance of DNAPL in the lower aquifer is termed the breakthrough time. Figure 4-3 presents the breakthrough times for all simulations in this work. The most striking conclusion that can be drawn from the data is the large increase in breakthrough times when sand lenses are incorporated into the domain (Figure 4-3a). The DNAPL reached the lower aquifer in less than 5 days in the six simulations performed in the fractured domain, with times increasing between the negative, neutral, and positive gradients.

The average breakthrough time for the eight lens domain scenarios that eventually reached the lower aquifer was 857 days (2.3 years) (ranging from 120 days for LND4 to 2345 days (6.4 years) for LND2), as compared to an average of 3.0 days for the fractures-only domain. The most significant factor controlling this behaviour is the large retention capacity of the sand as compared to the fractures. Although the DNAPL velocity is high in the fractures, the DNAPL flow rate is exceedingly small. A significant period of time must pass before the fractures have supplied sufficient DNAPL to exceed the retention capacity of the sand units. This is depicted graphically in Figure 4-4, which shows the location of the leading edge of the DNAPL as a function of time for several scenarios. Comparing FND1 and LND1 (both having a neutral gradient), it can be seen that the time required to reach the lower aquifer increases from 0.5 days to over 200 days with the presence of interspersed sand lenses.

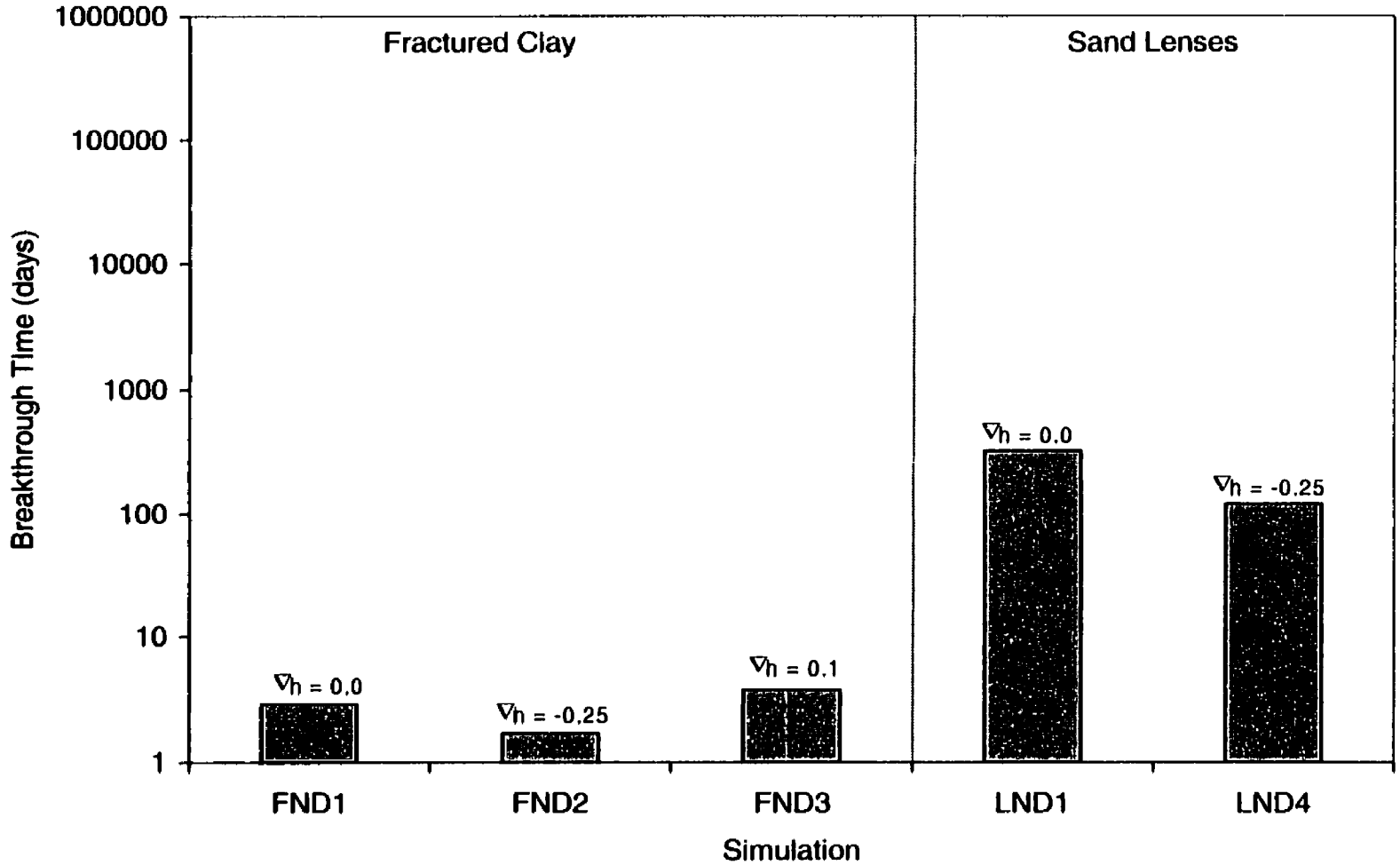

Figure 4-3a. Factors Influencing First Arrival Time of Nonwetting Phase at Lower Aquifer: Influence of Sand Lenses

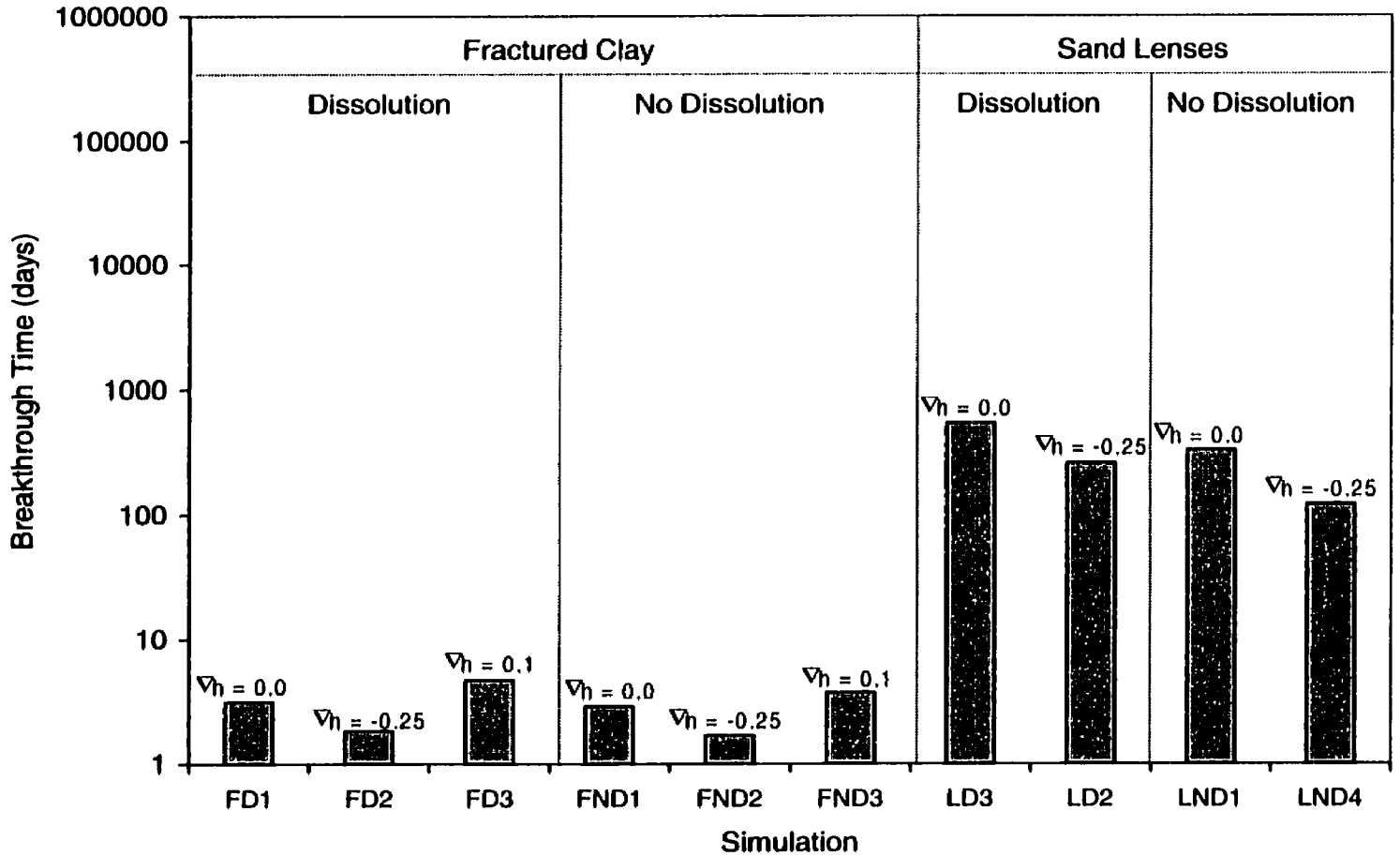

Figure 4-3b. Factors Influencing First Arrival Time of Nonwetting Phase at Lower Aquifer: Influence of Hydraulic Gradient and dissolution

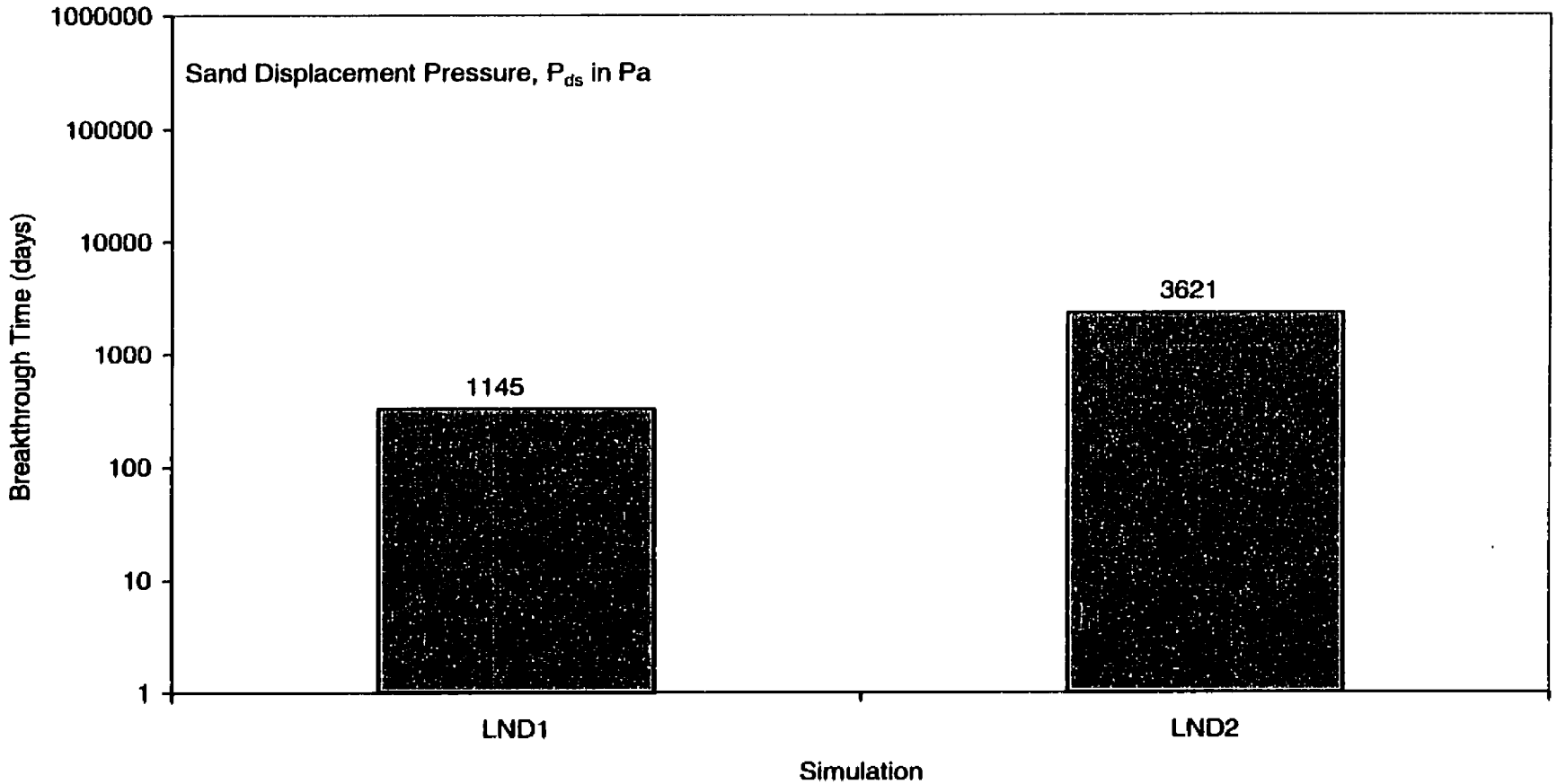

Figure 4-3c. Factors Influencing First Arrival Time of Nonwetting Phase at Lower Aquifer: Influence of Displacement Pressure

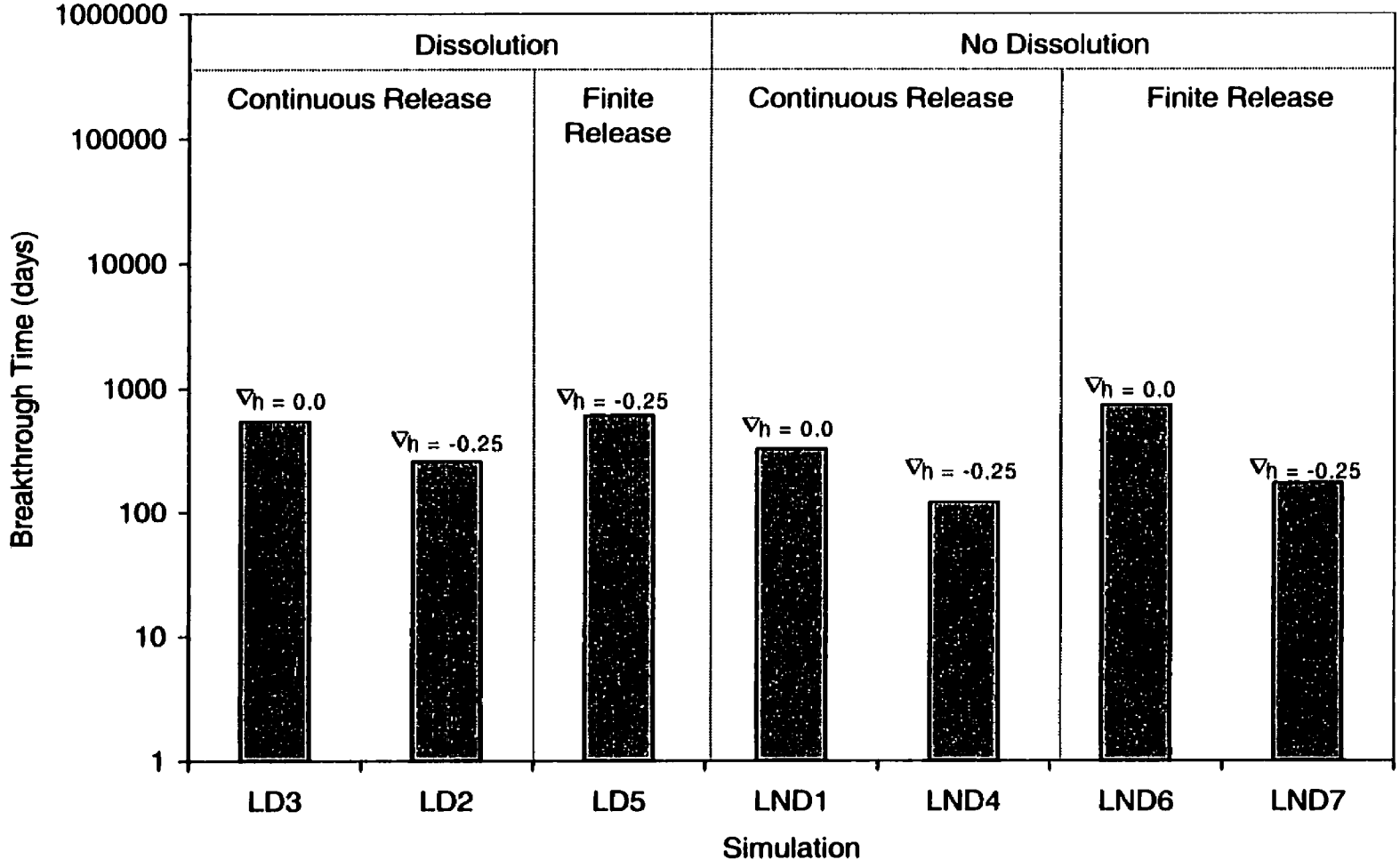

Figure 4-3d. Factors Influencing First Arrival Time of Nonwetting Phase at Lower Aquifer: Influence of Release Volume

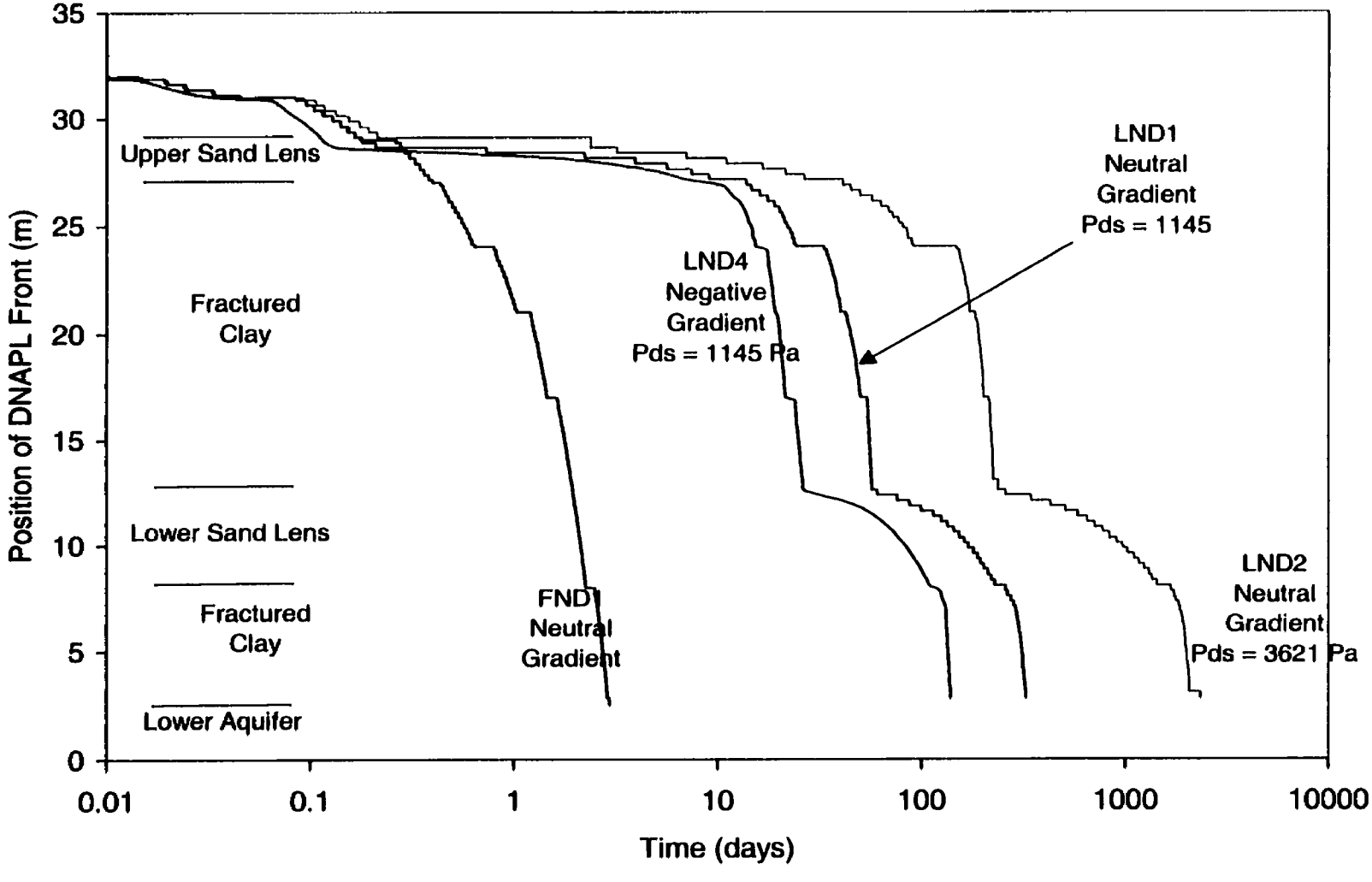

Figure 4-4. Nonwetting Phase Penetration Depth vs. Time for Selected Simulations

4.4.1.2 Effect of Hydraulic Gradient

The DNAPL failed to reach the lower aquifer in five simulations in this work (maximum simulation time was 150 years). Specifically, breakthrough was never achieved for any of the upward groundwater flow scenarios in the lens domain (4 simulations), nor for the case where the displacement pressure of the sand was less than that of the fractures (1 simulation). In the fractured domain, upward groundwater flow did not prevent the DNAPL from reaching the lower aquifer, but did slow it by 28.5 to 49.9 percent (FND3 and FD3 respectively) compared to the neutral gradient simulation (FND1). The effect of hydraulic gradient on the penetration rate through the system is also depicted in Figure 4-4. The applied negative gradient (LND4) creates downward groundwater flow and therefore increases the penetration rate through the upper fractured layer, and slightly increases the rate through the upper sand lens.

The influence of a vertical gradient in the wetting phase on the rate of DNAPL migration is best illustrated using the following one-dimensional form of Darcy's Law:

$$q_{nw} = -\frac{k k_{rnw}}{\mu_{nw}} \left(\frac{\partial (P_w + P_c)}{\partial z} + \rho_{nw} g \right) \qquad [4\text{-}13]$$

where q_{nw} is the nonwetting phase (DNAPL) flux, k is the intrinsic permeability of the medium (porous or fractured), k_{rnw} is the nonwetting phase relative permeability, μ_{nw} is the nonwetting phase viscosity, P_w is the wetting phase pressure, P_c is the capillary pressure, z is the elevation, ρ_{nw} is the nonwetting phase density, and g is the gravitational constant.

Equation (13) clearly shows that the wetting phase hydraulic gradient can oppose both the capillary pressure and gravitational gradients, and that downward DNAPL migration will be arrested in a one-dimensional system where:

$$\frac{\partial P_w}{\partial z} + \frac{\partial P_c}{\partial z} + \rho_{nw} g = 0 \qquad [4\text{-}14]$$

Although the applied gradients in this study do not appear to satisfy (14) across the entire domain, the condition is met locally within the domain for some simulations. In particular, it should be noted that $\partial P_w/\partial z$ can reach relatively high values locally where the medium permeability is low, and where high DNAPL saturations exist (promoting low values of k_{rw} which in turn promote high values of $\partial P_w/\partial z$).

4.4.1.3 Effect of Displacement Pressure

The effect of increasing the displacement pressure of the sand lenses relative to that of the fractures (run LND2 vs. LND1, Figure 4-3b) manifests itself as an increased time for DNAPL to penetrate the sand lenses and exit the overlying fractures. The long horizontal plateau in Figure 4-4 for LND2 near 1 day, for example, is the result of the capillary pressures requiring time to build up at the base of the fractures prior to overcoming the entry pressure of the upper sand lens. The logarithmic time scale in Figure 4-4 obscures this behaviour when the DNAPL reaches the top of the lower sand lens (around 350 days). Approximately 85 days elapse in run LND2 while the capillary pressures at the base of the fractures build to overcome the entry pressure of the lower sand lens. Figure 4-5 illustrates the saturation distribution for runs LND1 and LND2 when DNAPL first reaches the lower aquifer. It is clear that there is increased lateral spreading of DNAPL in the fractures at the upper elevations as a result of the increased capillary resistance exhibited by the sand.

The simulation in which the displacement pressure of the sand was lowered relative to that of the fractures (run LND3 vs. LND1, Figure 4-3b) did not achieve breakthrough into the lower aquifer. The relatively lower capillary resistance of the sand units promoted lateral flow of DNAPL out the side boundaries of the solution domain, and prevented the build-up of high capillary pressures. Simulation LND3 resulted in capillary pressures less than 1145 Pa in the lower sand lens. As a result, DNAPL could not penetrate the underlying fractures since the capillary pressure never exceeded the fracture entry pressure.

4.4.1.4 Effects of Dissolution

Of the six pairs of simulations performed in the lens domain to investigate the effects of dissolution and matrix diffusion on the penetration rate of the nonwetting phase through the system (continuous and finite volume releases, three gradients each), three pairs reached the lower aquifer allowing for comparison. The upward gradient scenarios, as was mentioned earlier, did not reach the lower aquifer within the simulation period, nor did the neutral gradient finite volume release with dissolution simulated.

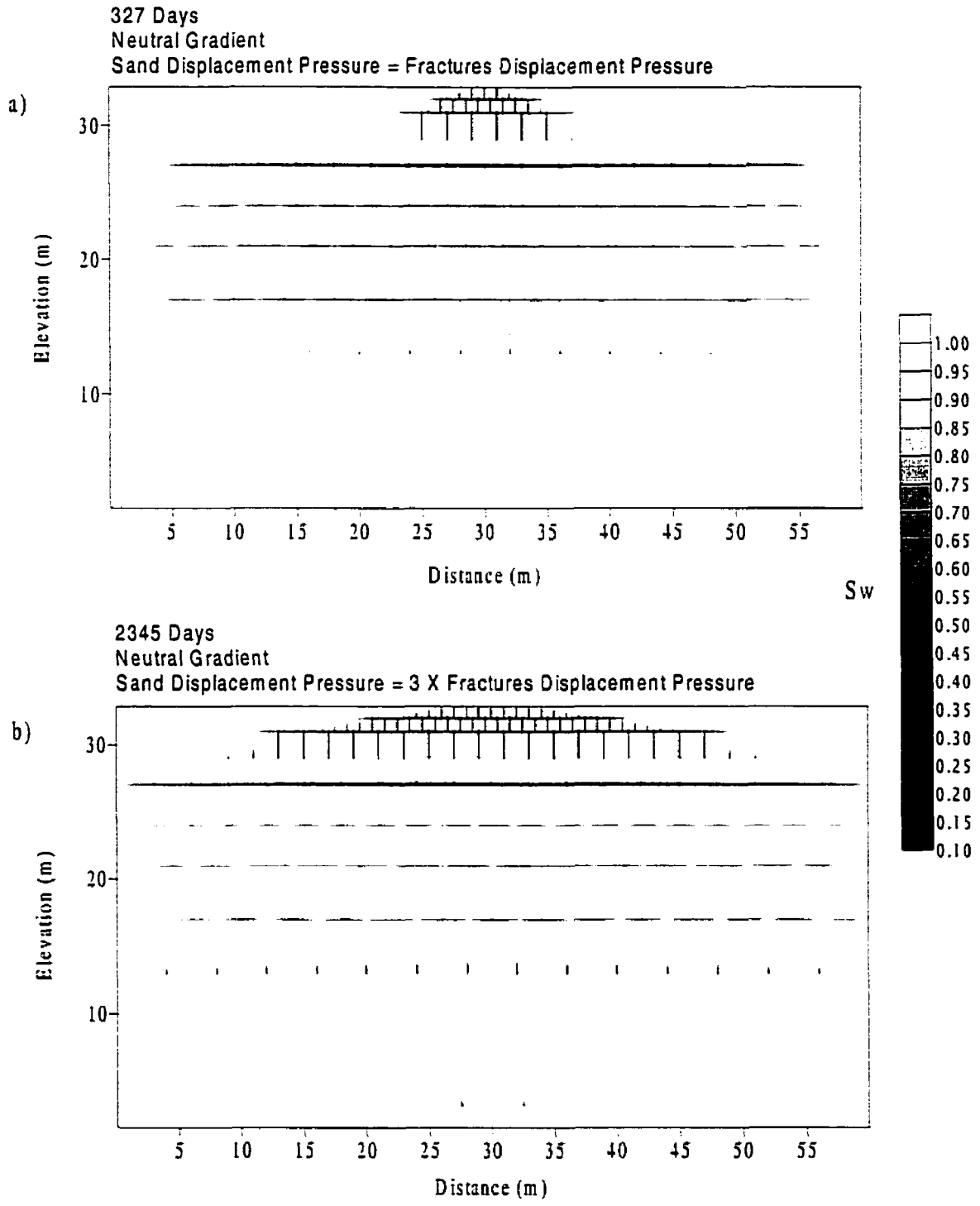

Figure 4-5. Nonwetting Phase Saturations at Two Breakthroughs into Lower Aquifer

The increase in breakthrough time as a result of incorporating dissolution into the sand lens domain ranged from 67 percent (LND1 vs. LD3), to over 254 percent (LND7 vs. LD5). The incorporation of dissolution in the fractured domain increased breakthrough time to a smaller degree; 9.1 percent (FND2 vs. FD2) to 25.6 percent (FND3 vs. FD3). These relatively small increases are similar to those found by Reynolds and Kueper (2000) in a study on the effects of diffusive losses to the matrix on the migration rate of DNAPL through a single fracture. The larger timescales that the nonwetting phase requires to reach the lower aquifer in the lens domain allows for increased mass lost to the clay matrix through diffusion. In addition, significant mass is lost from the DNAPL within the sand lenses themselves due to dissolution and subsequent sorption.

4.4.1.5 Effect of Release Volume

An interesting phenomenon occurs in regards to the finite volume releases with dissolution incorporated. As was explained in the previous section, the nonwetting phase in the negative gradient simulation managed to reach the lower aquifer for both dissolution cases. The neutral gradient simulation, however, reached the lower aquifer for the no-dissolution case, but not for the dissolution case (Figure 4-3d). The mass lost from the nonwetting phase through the various processes described above was sufficient to halt the penetration through the lower sand lens above the contact with the clay unit separating it from the lower aquifer. The reduced driving forces in the system (lower capillary pressures due to mass lost to the matrix in conjunction with imbibition behaviour) resulted in an extremely low volume flux to the lower sand lens, which was completely cut-off when the fractures entering from the top entered a residual nonwetting phase saturation state. This behaviour was not evident in the downward gradient simulation as

the increased rate of advance (and decreased spreading) allowed a DNAPL flux to the lower sand lens that was sufficient to ensure complete penetration to the lower clay unit.

Figure 4-6 compares the breakthrough times of the DNAPL and aqueous phases for all of the dissolution simulations that reached the lower aquifer. The high levels of attenuation of the aqueous phase by diffusive losses to the matrix, even under downward flowing conditions, are evident by the relatively small lag of the DNAPL behind the dissolved phase.

4.4.1.6 Long-term Migration of DNAPL

A pertinent question is raised by this work, concerning the time required for DNAPL to stop moving in the subsurface. An exact and detailed study of such is far beyond the scope of this work, but some observations of interest concerning vertical migration can be made. DNAPL did not penetrate to the lower aquifer (within the 150 year timeframe simulated) in six simulations performed in this work. Three of the simulations involved a continuous DNAPL source for the entire 150 years (LD1, LND3, LND5). Excluding the unlikelihood of such a source occurring, what was seen in these simulations was a cessation of vertical migration due to the presence of a positive gradient, or a capillary barrier. In the cases where the presence of the positive gradient was preventing entry into the fractures underlying a sand lens and causing lateral spreading, the DNAPL saturations in the sand immediately above the fractures were still slowly increasing after 150 years. Given this source condition, this slow buildup will eventually cause entry into the underlying fractures.

A more realistic examination of the timescales of vertical migration in the system can be conducted on the three finite volume release simulations that did not reach the lower aquifer

(LD4, LD6, LND8). Simulation LD6 and LND8 are the finite volume equivalents of the two positive gradient continuous release simulations discussed in the previous paragraph. The depth of penetration of these is significantly less than their continuous release counterparts (do not penetrate through the upper sand lens) and all DNAPL migration has ceased by the end of the simulations (all DNAPL has either exited the domain laterally, decreased to residual, or is in stable pools). Simulation LD4 (finite volume release, neutral gradient) did not reach the lower aquifer, but was stopped in the fractured clay immediately above it, due to a combination of mass lost to dissolution and reduced driving forces (as compared to the continuous release simulation). After 150 years vertical penetration of the DNAPL front has ceased, but slow imbibition is still occurring within the main DNAPL body. It should be noted that capillary behaviour within the DNAPL body is governed by the linearized representation of the imbibition functional relationship in the numerical model discussed earlier. Different formulations of these functions could lead to different predicted behaviour in the system.

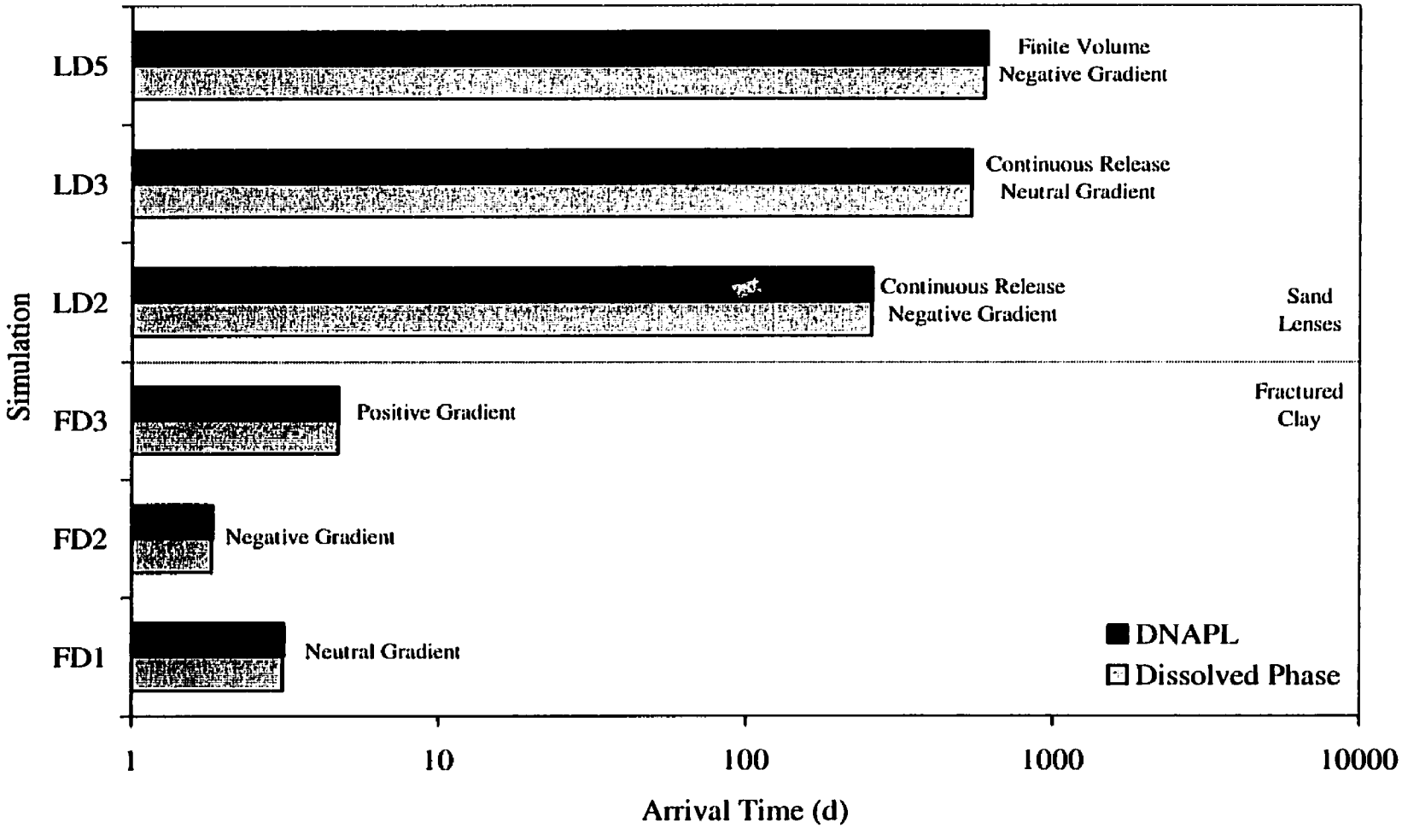

Figure 4-6. Arrival Times of DNAPL and Aqueous Phases at Lower Aquifer

4.4.2 Mass Loading

A second important facet of multi-phase flow and transport through these fractured layered sequences, from a groundwater quality perspective, are the volumes of contaminant that are capable of reaching the lower aquifer. If even a small volume of DNAPL enters the lower aquifer, it has the capability of contaminating large volumes of water due to low regulatory limits, and the low solubility of common chlorinated solvents.

4.4.2.1 Nonwetting Phase

Figure 4-7 presents the fraction of DNAPL entering the lower aquifer relative to the amount of DNAPL entering the system along the top boundary at steady-state for a variety of simulations. The steady-state values for flow into the fractured system are hydraulic gradient dependent, and were approximately 1.4 m^3/yr, 1.2 m^3/yr, and 0.9 m^3/yr for the negative (FND2), neutral, and positive (FND3) gradients respectively. Steady-state is defined here as equal masses of DNAPL entering and exiting the simulation domain. The six different scenarios in the fractured domain showed very little storage or loss of nonwetting phase within the system. The negative and neutral gradient simulations both transferred greater than 99 percent of the DNAPL flow entering the system to the lower aquifer. The positive gradient scenarios sustained some degree of mass loss out the sides of the domains through the horizontal fractures, but still transferred greater than 90 percent of the nonwetting phase through the system.

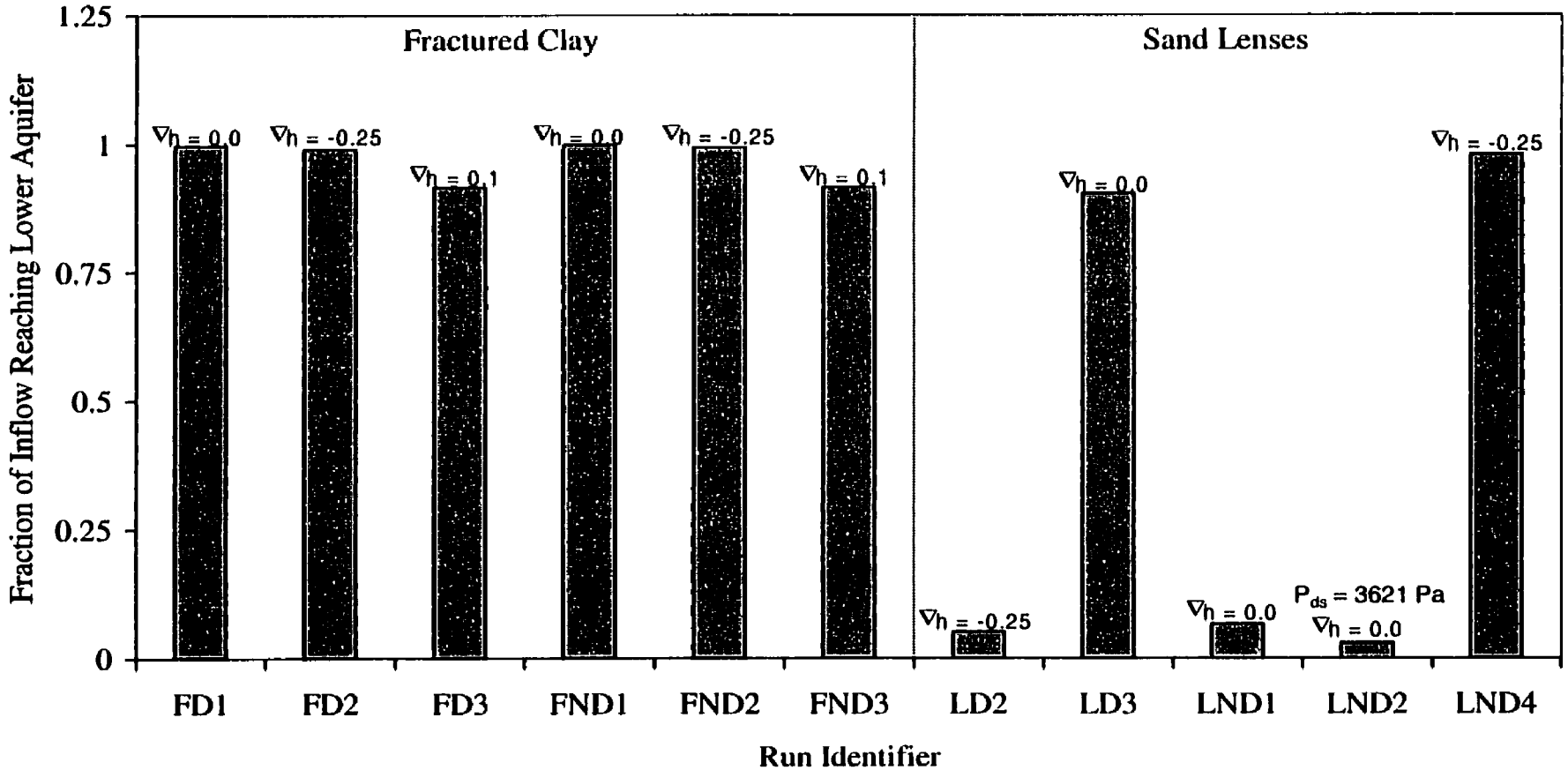

Figure 4-7. Fraction of Nonwetting Phase Entering System Reaching Lower Aquifer

The simulations carried out in the lens domain presented different trends with respect to mass loading into the lower aquifer. Figure 4-7 also presents the steady-state loading fractions for the five lens domain continuous release scenarios that reached the lower aquifer. The behaviours of the two negative gradient scenarios (LD2 and LND4) are somewhat similar to that of the fractured domain, transferring 90 and 98 percent, respectively, of the nonwetting phase entering the domain to the lower aquifer. The difference in loading fraction between the dissolution (LD2) and non-dissolution (LND4) scenarios is greater than the difference between the equivalent simulations in the fractured domain (8 percent vs. 0.3 percent) due to the increased time required to traverse the system, and the resultant greater mass lost to dissolution/matrix diffusion.

The most striking data presented in Figure 4-7 are the very small fractions of the DNAPL flux that reached the lower aquifer for the neutral gradient simulations (LD3 and LND1). Less than 7 percent enters the lower aquifer for the non-dissolution scenario, and less than 5 percent for the dissolution scenario. Without the downward driving force of an applied gradient, the DNAPL tends to pool at the bottom of the sand lenses, and spread laterally. For each sand lens, there are a greater number of fractures acting as a source of DNAPL (entering the top) than there are acting as a sink (leaving the bottom). The lateral spreading of the DNAPL eventually reaches the side boundaries of the domain and is lost from the system. This occurs in each of the sand lenses for the equal displacement pressure scenarios discussed previously, but only in the upper sand lens for the simulation in which the displacement pressure of the sand is greater than that of the fractures (LND2). In this simulation, significant mass is lost through the horizontal fractures intersecting the domain boundaries as capillary pressures build in the fractures to overcome the

displacement pressure of the underlying sand lenses. This, combined with a much larger lateral loss from the upper sand lens, equates to less than 3 percent of the entering nonwetting phase reaching the lower aquifer.

The mass lost from the system through the side boundaries of the domain would not, in fact, be lost from a real system. The lateral spreading which is occurring under neutral and positive gradient conditions would, in an infinite domain, give access to additional vertical migration pathways which may eventually reach the lower aquifer, and, therefore, increase the percentage of total mass reaching the lower aquifer. Compositional simulation at this scale requires significant computing resources and extensive run times. The domains chosen for this work were a balance between available computing resources, and spatial extents required to demonstrate the physical processes.

4.4.2.2 Aqueous Phase

Table 4-3 presents the steady-state aqueous phase mass loading rates into the lower aquifer for each of the dissolution simulations where DNAPL reached the lower aquifer. The largest value in the fractured system (FD2) represents less than 5 g/yr of dissolved phase contaminant entering the lower aquifer. This is clearly of secondary importance as compared to the volumes of DNAPL entering the aquifer. It should be pointed out that in the case of a finite volume release (LD5), the maximum dissolved phase loading into the lower aquifer does not occur when the system is at steady state, but rather somewhat earlier as DNAPL is entering the lower aquifer (Figure 4-8).

Table 4-3. Aqueous Phase Mass Loadings to Lower Aquifer

Run	Gradient	Mass Loading (g/yr)
FD1	0.0	6.897×10^{-1}
FD2	-0.25	4.179
FD3	0.1	1.30×10^{-3}
LD2	-0.25	0.347
LD3	0.0	8.87×10^{-7}
LD5[1]	-0.25	31.25

1 – Not a Steady-state Loading

The previous discussion has focused on the simulations in which the nonwetting phase was released continuously into the system. These are the only simulations in which steady-state flow conditions are approached, allowing for a standard basis for comparison. The six simulations conducted for the finite volume releases obviously do not achieve a steady-state flow condition, but some observations can be made. The largest volume of DNAPL entered the lower aquifer for the negative gradient simulation without dissolution (2.5 m^3). Conversely, the volume entering the lower aquifer for the negative gradient simulation with dissolution was only 0.2 L. In this case, not only has dissolution significantly retarded the arrival of the DNAPL at the lower aquifer, but it has also greatly reduced the volume of DNAPL in the aquifer. The aqueous phase mass loading to the lower aquifer for the negative gradient dissolution scenario and a finite volume release was the largest recorded in these simulations (31 g/yr). This high value is due to the fact that only two of the fractures entering the lower aquifer were invaded with DNAPL, allowing unobstructed pathways for the aqueous phase (at high concentrations) to enter the lower aquifer.

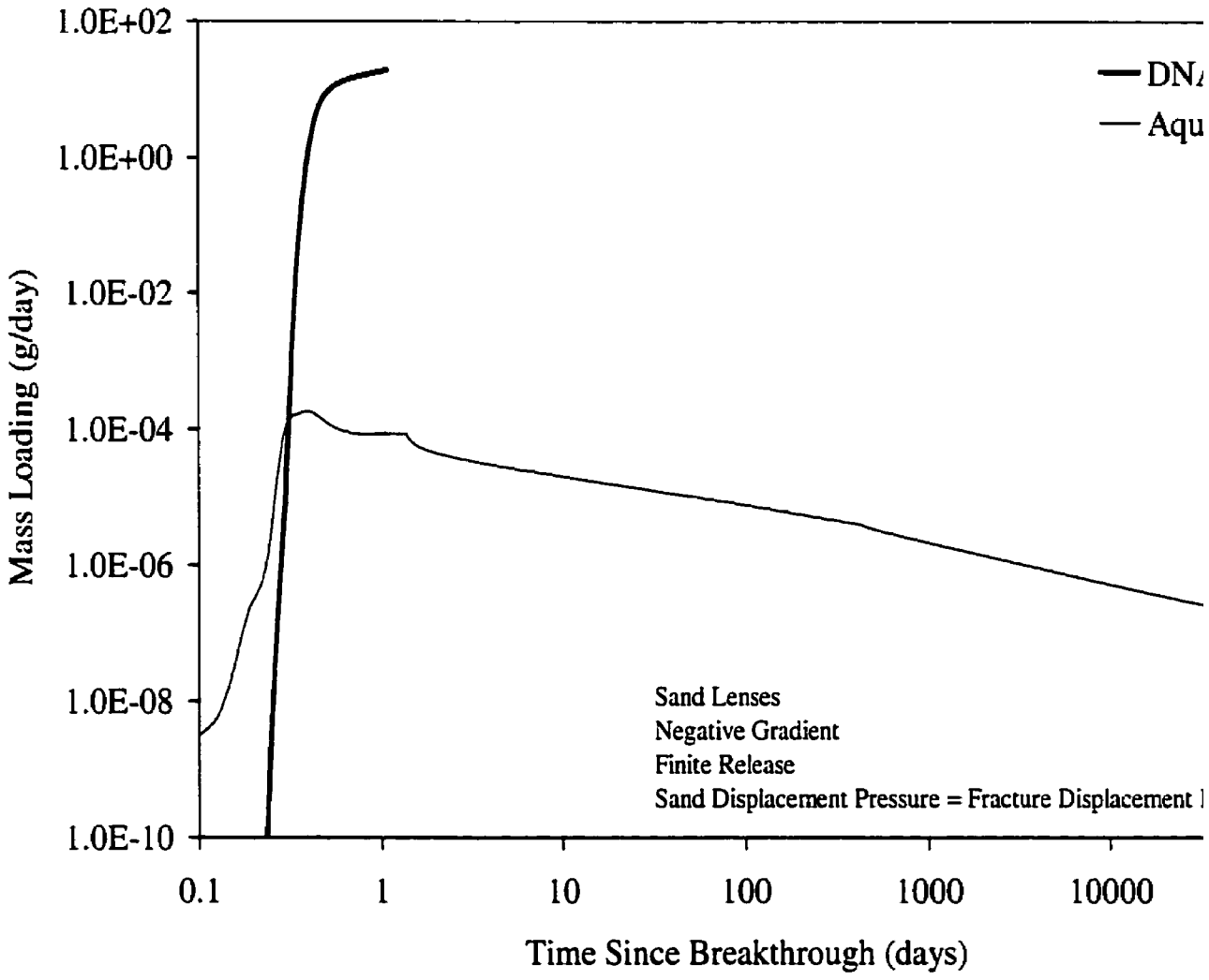

Figure 4-8. Mass Loading to Lower Aquifer Versus Time (Run LD5)

This finding (in addition to the results presented in Figure 4-8) shows that the nature of the contaminant penetrating fractured layered systems changes over time (assuming that the source is depleted at some point) from predominantly DNAPL to predominantly aqueous phase. The timescales and relative amounts transferred during theses different stages will vary with the hydrogeology of the system, and the nature and volume of the contaminant.

4.5 Conclusions

The rate of vertical penetration of DNAPL through fractured clay aquitards void of sand lenses can be extremely rapid, on the order of days for a 30 m sequence containing 35 μm fractures. The presence of vertical gradients can enhance or retard this rate, depending on whether groundwater flow is downwards or upwards. The loss of mass to the matrix through dissolution and diffusion has relatively little effect on the penetration rate, given the rapid rate of DNAPL migration.

The ratio of displacement pressures between the fractures and the sand lenses is another major controlling factor in the migration time of the DNAPL through the system. Increasing the displacement pressure of the sand relative to that of the fractures (by a factor of approximately three) resulted in more than a ten-fold increase in the DNAPL breakthrough time. Conversely, decreasing the displacement pressure of the sand relative to that of the fractures (by a factor of approximately three) prevented the nonwetting phase from reaching the lower aquifer.

The existence of sand lenses interbedded with fractured clay, as commonly found in deltaic depositional environments, significantly influences the migration times of the nonwetting phase vertically through the system. The presence of a 2 m and a 5 m thick sand lens within the 30 m clay layer can increase the time required to traverse the system from a few days to several years. The presence of vertical gradients in the layered sequence caused significant changes in the DNAPL breakthrough times. A downward gradient of 0.25 decreased the breakthrough time from over 300 days to less than 150 days, while an applied upward gradient of 0.1 completely arrested the nonwetting phase within the lower sand lens.

The retardation of the arrival of the nonwetting phase in the lower aquifer, due to the presence of matrix diffusion, was more pronounced with the inclusion of sand lenses into the domain as opposed to the fractures-only system. The quantities of aqueous phase flux penetrating the system are, however, significantly less than that of the nonwetting phase in almost all possible scenarios. The exception to this occurs in the case of a limited volume release, in which, on occasion, no nonwetting phase reaches the underlying aquifer, or the nonwetting phase flow is cut-off as the source is depleted.

4.6 References

Aziz, K. and A. Settari. 1979. Petroleum Reservoir Simulation. Applied Science, London.

Bear, J. 1972. Dynamics of Fluids in Porous Media. Dover Publications Inc., New York.

Abriola, L.M. and G.F. Pinder. 1985. A Multiphase Approach to the Modeling of Porous Media Contamination by Organic Compounds, 1. Equation Development, *Water Res. Res.*, 27(6), p 11-18.

Behie, G.A. and P.A. Forsyth. 1984. Incomplete Factorization Methods for Fully Implicit Simulation of Enhanced Oil Recovery, *SIAM J. Scientific and Statistical Computing*, 5(3), p 543-561.

Brooks, R.H. and A.T. Corey. 1964. Hydraulic Properties of Porous Media, Civ. Eng. Depart., Colorado State Univ., Fort Collins, Hydrology Paper No. 3.

Esposito, S.J. and N.R. Thomson. 1999. Two-phase Flow and Transport in a Single Fracture-porous Medium System, *J. Cont. Hyd.*, 37, p 319-341.

Gerhard, J.I., Kueper, B.H., and G.R. Hecox. 1998. The Influence of Waterflood Design on the Recovery of Mobile DNAPLs, *Ground Water*, 36(2), p 283-292.

Kueper, B.H. and E.O. Frind. 1991. Two-phase Flow in Heterogeneous Porous Media: 2. Model Application, *Water Res. Res.*, 27(6), p 1049-1057.

Kueper, B.H. and D.B. McWhorter. 1991. The Behaviour of Dense, Nonaqueous Phase Liquids in Fractured Clay and Rock, *Ground Water*, 29, p 716-728.

McKay, L.D., Cherry, J.A., and R.W. Gillham. 1993. Field Experiments in a Fractured Clay Till: 1. Hydraulic Conductivity and Fracture Aperture, *Water Res. Res.*, 29(4), p 1149-1162.

McWhorter, D.B. and D.K. Sunada. 1990. Exact Integral Solutions for Two-phase Flow, *Water Res. Res.*, 26(3), p 399-413.

Mendoza, C.A. 1992. Capillary Pressure and Relative Transmissivity Relationships Describing Two-phase Flow Through Rough Walled Fractures in Geologic Media, Ph.D. thesis, Univ. of Waterloo, Waterloo, Ontario, Canada.

Murphy, J.R. and N.R. Thomson. 1993. Two-phase Flow in a Variable Aperture Fracture, *Water Res. Res.*, 29(10), p 3453-3476.

Ogata, A. and R.B. Banks. 1961. A Solution of the Differential Equation of Longitudinal Dispersion in Porous Media. U.S. Geological Survey Professional Paper 411-A.

Parker, B.L., Gillham, R.W., and J.A. Cherry. 1994. Diffusive Disappearance of Immiscible Phase Organic Liquids in Fractured Geologic Media, *Ground Water*, 32(5), p 805-820.

Slough, K.J. 1997. A Numerical Simulation of Multiphase Flow and Phase Partitioning in Discretely-fractured Geologic Media, M.Sc. thesis, Earth Sciences, Univ. of Waterloo, Waterloo, Ontario, Canada.

Slough, K.J., Forsyth, P.A., and E.A. Sudicky. 1999. Numerical Simulation of Multiphase Flow and Phase Partitioning in Discretely-fractured Geologic Media, *J. Cont. Hyd.*, 40 p107-136.

Sudicky, E.A. and E.O. Frind. 1982. Contaminant Transport in Fractured Porous Media: Analytical Solutions for a System of Parallel Fractures, *Water Res. Res.*, 18, p 1634-1642.

Reitsma, S. and B.H. Kueper. 1994. Laboratory Measurement of Capillary Pressure-saturation Relationships in a Rock Fracture, *Water Res. Res.*, 30(4), p 865-878.

Reitsma, S. and B.H. Kueper. 1998. Non-equilibrium Alcohol Flooding Model for Immiscible Phase Remediation: 1. Equation Development, *Adv. Water Res.*, 21(8), p 663-678.

Reynolds, D.A., and B.H. Kueper. 2000. DNAPL Flow Through Fractured Porous Media, *Proceedings, Second Int. Conf. on Remediation of Chlorinated and Recalcitrant Compounds*, Monterey, CA, USA, May 22-25, 2000, Vol. C2-2, Battelle Press, Columbus, OH, p 165-172.

Unger, A.J.A., Forsyth, P.A., and E.A. Sudicky. 1995. Mechanisms Controlling Vacuum Eextraction Coupled with Air Sparging for Remediation of Heterogeneous Formations Contaminated by Dense Nonaqueous Phase Liquids, *Water Res. Res.*, 31(8), p 1913-1925.

Unger, A.J.A., Forsyth, P.A., and E.A. Sudicky. 1996. Variable Spatial and Temporal Weighting Schemes for use in Multi-phase Compositional Problems, *Adv. Water Res.*, 19(1), p 1-27.

CHAPTER 5 – DNAPL MIGRATION IN FRACTURED HETEROGENEOUS POROUS MEDIA[3]

5.1 Introduction

The presence of DNAPL (Dense, Non-Aqueous Phase Liquid) in the subsurface is recognized as a significant source of long-term groundwater contamination at many sites throughout North America and Europe (Cherry et al., 1996; Freeze and McWhorter, 1997). DNAPLs of environmental concern include PCB oils, chlorinated solvents, coal tar, and creosote. The migration of DNAPL through the subsurface will depend upon many factors, such as the permeability of the porous medium, the physical and chemical properties of the DNAPL (density, viscosity, etc.), and the volume and intensity of the release itself. Schwille (1988), for example, performed extensive laboratory studies examining the migration of several DNAPLs through a variety of porous media, showing that they may pool above lower permeability layers below the watertable, and may also become trapped as immobile residual. Field experiments have shown that DNAPL migration pathways through the subsurface can be strongly influenced by even minor variations in permeability (Poulson and Kueper, 1991; Kueper et al., 1993).

Several authors have investigated the effects of subsurface heterogeneity on the migration of DNAPL through the subsurface with the use of numerical models (e.g. Kueper and Frind, 1991; Kueper and Gerhard, 1995; Dekker and Abriola, 2000). Dekker and Abriola (2000) performed a

[3] Submitted to Journal of Contaminant Hydrology

modelling study investigating the effects of spill release rate, hydraulic gradient, and the statistical descriptions of the permeability field in multiple realization studies incorporating random spatially correlated fields. Results showed that the mean, variance, and vertical correlation length of the permeability field, along with the spill rate, exerted the most influence on the distribution of the DNAPL in the subsurface. Gerhard and Kueper (1995) investigated the influence of source strength and size on the infiltration rate and lateral spreading of DNAPL in a water saturated heterogeneous porous medium. The infiltration rates in twenty-five realizations of a spatially correlated random field were found to be log-normally distributed and with a variance that mimicked the underlying variation in the permeability field. Gerhard and Kueper (1995) also found that increasing the size of the source in relation to the horizontal correlation length decreased the variability of the infiltration rate. Neither the degree of lateral spreading of the DNAPL body, nor the infiltration rate showed any tendency to converge to an ensemble average. Bradford et al. (1998) used a numerical approach similar to that of Dekker and Abriola (2000) to show that, if the wettability characteristics of a porous medium are correlated with permeability, spatial variations in wettability can have a dramatic impact on DNAPL distributions, resulting in higher nonwetting phase saturations and increased lateral spreading.

Significant work has also been undertaken involving the numerical simulation of the migration of DNAPL in fractured environments, based on the conceptual model of Kueper and McWhorter (1991) which showed that the underlying physics controlling DNAPL migration in porous media are identical to that for fractures. The majority of studies to date (Murphy and Thompson, 1993; Slough et al., 1999a) have only dealt with the migration of DNAPL through a single fracture, or through a fractured clay aquitard overlying a higher permeability aquifer. Reynolds and Kueper

(2001) studied the migration of Trichloroethylene (TCE) through an idealized layered system consisting of 30 m of fractured clay containing two thin interbedded sand lenses. It was found that the presence of the sand lenses retarded the migration rate of the DNAPL through the system by orders of magnitude, as compared to a 30 m sequence of fractured clay without interspersed sand beds. In addition, Reynolds and Kueper (2001) found that the presence of vertical hydraulic gradients and the ratio of displacement pressures between the fractures and the sand lenses also affected the migration rate. Slough et al. (1999b) found that the magnitude of the displacement pressure of the rock matrix surrounding a fracture network exerted significant control on the migration pattern of a DNAPL release.

The presence of fractures in clay environments has been well documented (e.g. McKay, 1995), and recent evidence has pointed to the existence of fractures in silts and silty-clays (e.g. Pankow et al., 1984). Based on this evidence it is logical to assume that in extremely heterogeneous environments, where the permeability ranges over several orders of magnitude, fractures may exist across low permeability lenses linking higher permeability lenses, resulting in a combination of fracture and porous media flow within the system. To date, no investigation has focused on the role of fractures in the migration of DNAPL in heterogeneous porous media. The objective of this study, therefore, is to investigate the migration and entrapment of DNAPL in a heterogeneous permeability environment, containing fractures in the lowest permeability lenses. To this end, a series of multiphase flow and transport simulations are undertaken to investigate the importance of various key parameters in the distribution of the DNAPL in the subsurface. The influence of the mean and variance of the random permeability field, as well as the degree of fracturing within the simulation domain, are studied.

5.2 Model and Domain Development

The numerical model used in this study (QUMPFS), developed by Reynolds and Kueper (2001), has been tested against analytical solutions for multiphase flow and mass transport under advection and dispersion. In addition, the model has been verified against other published numerical simulators (Kueper and Frind, 1991a,b; Gerhard and Kueper, 1995). QUMPFS is a three-dimensional multiphase compositional simulator, with the capabilities of modeling advection, dispersive and diffusive fluxes, equilibrium and non-equilibrium phase partitioning, and capillary hysteresis. The model utilizes a finite volume approach to solve the partial differential equations governing isothermal multiphase flow and multicomponent transport in porous media (Abriola and Pinder, 1985):

$$\frac{\partial}{\partial t}\left(c_{i\beta}\phi S_\beta x_{i\beta}\right)+\nabla\cdot\left(c_{i\beta}x_{i\beta}v_\beta\right)-\nabla\cdot\left[\phi S_\beta \vec{D}_{i\beta}\nabla\left(c_{i\beta}x_{i\beta}\right)\right]-q_{i\beta}-I_{i\beta}=0 \qquad [5\text{-}1]$$
$$\beta=1..n_p,\quad i=1..n_c$$

where n_p is the number of phases, n_c is the number of components, β is the particular phase of interest, $c_{i\beta}$ is the molar density of phase β, ϕ is the porosity of the medium, S_β is the saturation of phase β, $x_{i\beta}$ is the mole fraction of component i in phase β, v_β is the Darcy flux of phase β, $\vec{D}_{i\beta}$ is the dispersion tensor for component i in phase β, $q_{i\beta}$ is the source/sink term for component i in phase β, $I_{i\beta}$ represents the inter-phase mass transfer of component i to or from phase β, and t is time.

Equation set [5-1] is closed by assuming the phase saturations and the mole fractions of each component comprising a phase both sum to unity. The model employs the constitutive relationships of Brooks and Corey (1964) relating capillary pressure, saturation, and relative permeability, with the modifications proposed by Gerhard et al. (1995) to simulate hysteresis. The use of Brooks-Corey functions to represent two-phase flow in fractures is supported by the work of Reitsma and Kueper (1994). The model is formulated using a fully implicit approach, and utilizes full Newton-Raphson iteration with upstream weighting of the relative permeabilities.

All simulations conducted in this study are carried out in a two-dimensional, vertical section 120 m wide by 40 m high. The upper boundary is specified as the watertable, and all other boundaries are specified as to impose an upward gradient of 0.05 (resulting in downward wetting phase flow). The nonwetting phase is introduced into the domain at a constant capillary pressure of 7158.4 Pa (equal to 0.5 m of TCE pooled above the watertable) along a 20 m wide patch centred along the top of the domain. The domain is discretized into 38,400 regularly spaced control volumes comprising 240 nodes in the horizontal direction by 160 nodes in the vertical direction. A horizontal nodal spacing of 0.5 m and a vertical spacing of 0.25 m is employed in all cases. A spatially correlated random permeability field was generated assuming an exponential autocorrelation function (Robin et al., 1991). The variance of the correlated permeability fields was set high (>5.5 for the log of permeability) to assure that the generated permeabilities encompassed values ranging from a coarse sand (1.0×10^{-9} m^2) to a lacustrine clay (1.0×10^{-18} m^2). The horizontal and vertical correlation lengths were assigned values of 8.75 m

and 0.92 m, respectively. The nodal discretization ensured that 12 and 40 correlation lengths were included in the horizontal and vertical directions, respectively.

The use of a typical capillary pressure-saturation scaling relationship (e.g., Leverett, 1941) is not appropriate given the wide variation in the permeabilities in the generated fields. The relationship employed in this work was, therefore, developed from values of displacement pressure reported in the literature for various porous media. Results reported by Brooks and Corey (1964), Thomas et al. (1968), Schowalter (1979), and Kueper and Frind (1991b) were used to develop a relationship between displacement pressure and permeability (Figure 5-1). The values of displacement pressure reported in these studies were scaled to an interfacial tension of 0.04 N/m before being plotted. The best-fit log-log linear relationship between permeability and displacement pressure was found to be:

$$P_d = 10^{(-0.227 \log(k) + 0.889)} \qquad [5\text{-}2]$$

where P_d is the displacement pressure (Pa) and k is the intrinsic permeability (m^2). The sole dependence of the displacement pressure on permeability is satisfactory in this study, as only a single fluid pair is considered, and the porosity in the system is kept constant. The entry pressure of the fractures in the system is based upon Kueper and McWhorter (1991):

$$P_e = \frac{2\sigma \cos(\theta)}{e} \qquad [5\text{-}3]$$

where σ is the interfacial tension (N/m), e is the aperture of the fracture giving rise to the first connected pathway of the nonwetting phase (m), and θ is the contact angle.

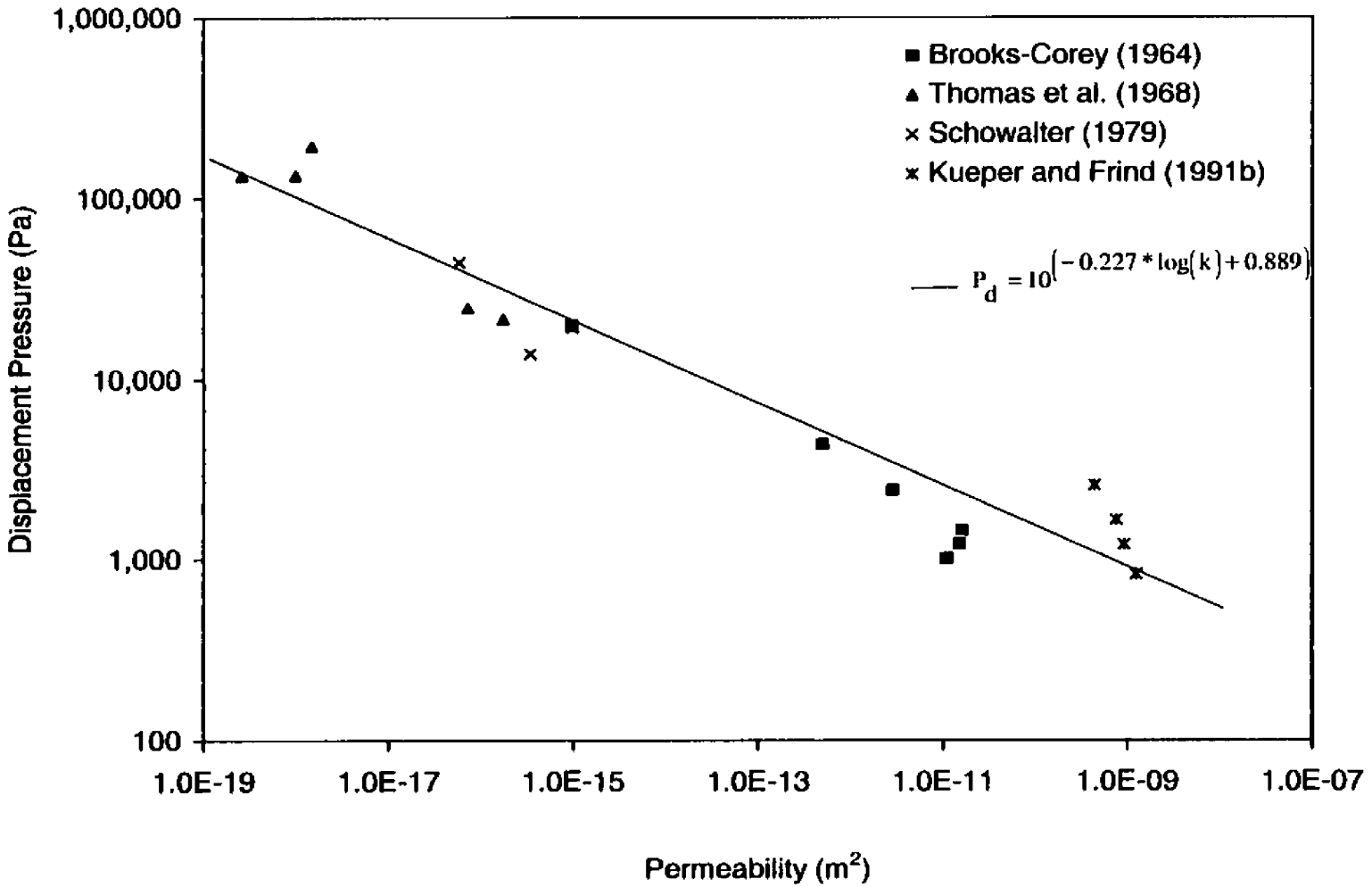

Figure 5-1. Correlation Between Displacement Pressure and Porous Media Permeability Employed in Modelling. The Illustrated Straight Line is Characterized by $P_d = 10^{(-0.227 \log(k) + 0.889)}$.

The placement of the fractures within the domain was based on the intrinsic permeability. For the majority of the simulations, it was assumed that all lenses with permeabilities less than or equal to that of a typical silt (1×10^{-13} m^2) contained fractures. This was based on Pankow et al. (1984) which reports fractures occurring naturally in a lacustrine silt deposit, and represents the highest permeability fractured deposit reported in the literature. Horizontal spacing of the vertical fractures within the low permeability lenses was constant and equal to 2 m. No horizontal fractures were simulated given the small vertical correlation lengths in the generated fields. The apertures of the generated fractures were correlated to the permeability of the lenses surrounding them. Figure 5-2 presents literature values of aperture in terms of the reported matrix permeability of the fractured unit. The majority of these studies used modelling to determine "hydraulic" apertures for the medium in question, and no differentiation is made between "hydraulic" and mechanical apertures. The best-fit line to the presented data is given by:

$$e = (759{,}098 + 45{,}455 \log(k))^{0.43} \qquad [5\text{-}4]$$

where e is the aperture (μm) and k is the intrinsic permeability (m^2) of the porous medium.

The primary focus of this work is on the geologic controls on nonwetting and dissolved phase migration through fractured heterogeneous environments. Three key geologic parameters were investigated, the mean permeability of the generated field, the variance in permeability, and the maximum permeability of units that were assigned fractures. The base case domain used in the simulations is displayed in Figure 5-3a, showing the random permeability field in greyscale (with the fractures portrayed by the vertical white lines).

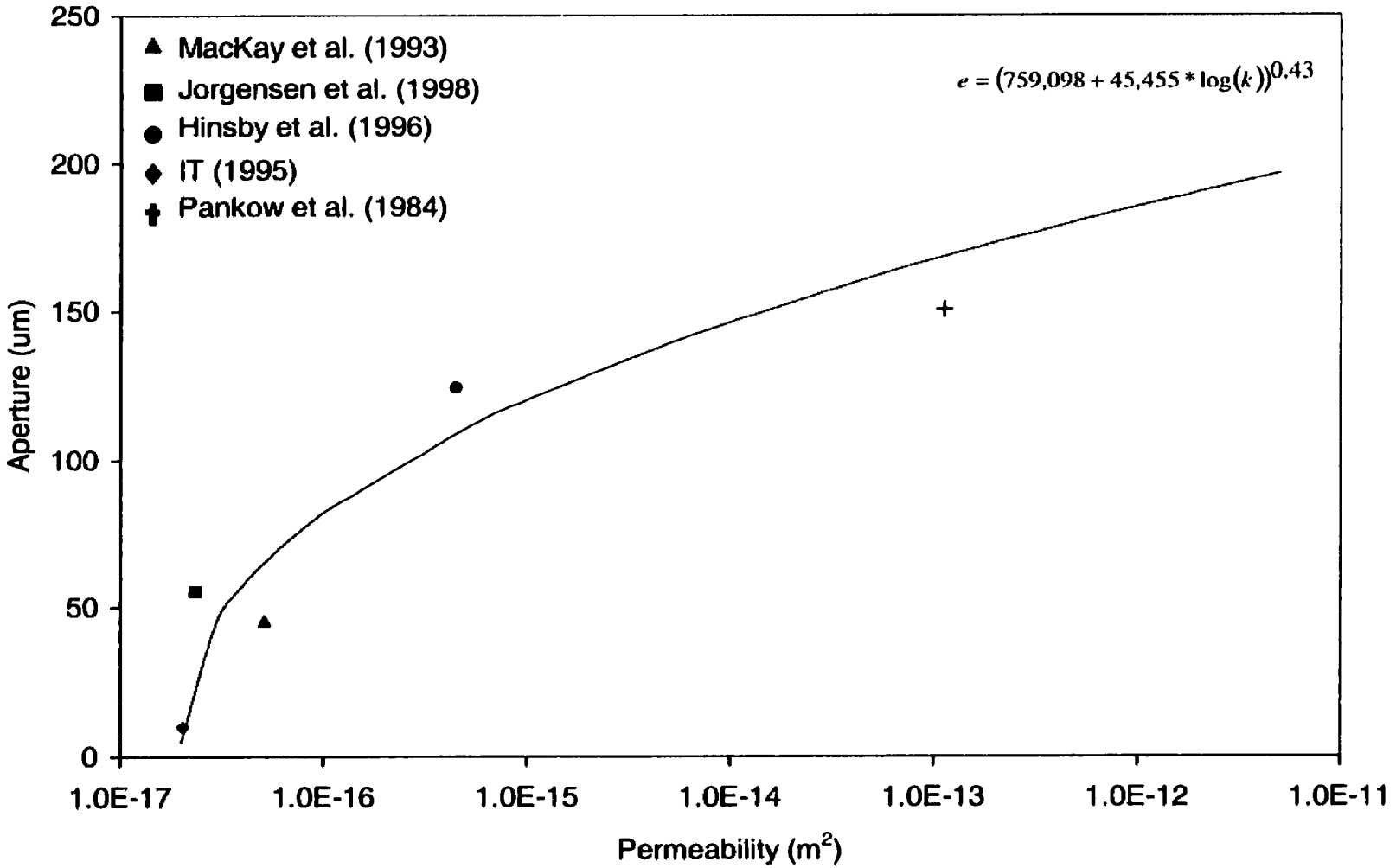

Figure 5-2. Correlation Between Aperture and Porous Media Permeability. The fit Line is Characterized by $e = (759{,}098 + 45{,}455 \log(k))^{0.43}$

The values of the relevant parameters used in the base-case simulation are listed in Table 5-1, with the chemical parameters chosen to be representative of TCE. A total of 30 m^3 of TCE was released into the domain in each simulation, with an applied upward wetting phase gradient of 0.05. A summary of all simulations is provided in Table 5-2. The sensitivity of the migration to the statistical parameters governing the generated permeability field was evaluated by performing identical release simulations with the mean equal to ten times and one tenth of its base value, and the variance equal to twice and one half its base value (four simulations in addition to base case). The generation of the permeability fields with different means was performed with the same random seed, thus ensuring that the location and size of the lenses was identical, the only difference being the magnitude of the permeability. The fracturing procedure was not varied between simulations, however, which resulted in different fracture patterns between the fields. As described earlier, the fracturing algorithm located all lenses with permeabilities less than 1.0×10^{-13} m^2, and produced vertical fractures within the lenses at a spacing of 2 metres. For the simulation with the increased mean permeability, this procedure results in significantly less fracturing in the system as compared to the base scenario (e.g. Figure 5-3b vs. Figure 5-3a). The fracture patterns and locations in the permeability fields with differing variances are not as altered from the base scenario as for the increased mean permeability case (e.g. Figure 5-3c vs. Figure 5-3a). The final geologic control varied in this work was the cut-off permeability below which fractures were created (two simulations). Figure 5-3d presents the permeability field for the case where the cut-off permeability was increased by an order of magnitude (to 1.0×10^{-12} m^2). This results in significantly more fracturing in the system, as more lenses fall under the cut-off, as well as increasing the lengths of the existing fractures through the higher permeability gradations surrounding the previously fractured lenses.

The reverse behaviour applies to the above discussion when the varied parameter is less than the base parameter (Figure 5-4 a through d).

Table 5-1. Base Case Numerical Model Input Parameters

Parameter	Value
Mean porous media permeability	1.02×10^{-13} (m^2)
Variance of log of permeability	5.5
Porous media permeability horizontal correlation length	20.0 m
Porous media permeability vertical correlation length	1.0 m
Maximum porous media permeability fractured	1.02×10^{-13} (m^2)
Porous Media porosity	0.30
Pore size distribution index (porous media and fractures)	2.0
Residual wetting phase saturation (porous media and fractures)	0.10
Porous media longitudinal dispersivity	1.0 (m)
Porous media transverse dispersivity	0.10 (m)
Fracture longitudinal dispersivity	0.01 (m)
Fracture transverse dispersivity	0.001 (m)
Wetting phase density	1000 (kg/m^3)
Nonwetting phase density	1460 (kg/m^3)
Wetting phase viscosity	0.001 (Pa s)
Nonwetting phase viscosity	0.00057 (Pa s)
Interfacial tension	0.01 (N/m)
Tortuosity	0.10
Free solution diffusion coefficient (porous media and fractures)	1.01×10^{-9} (m^2/s)
Equilibrium mole fraction in aqueous phase	1.9×10^{-4}
Distribution coefficient (porous media and fractures)	1.26×10^{-4} (m^3/kg)
Porous media dry bulk density	1.82×10^{3} (kg/m^3)
Applied wetting phase gradient	0.05 Upwards

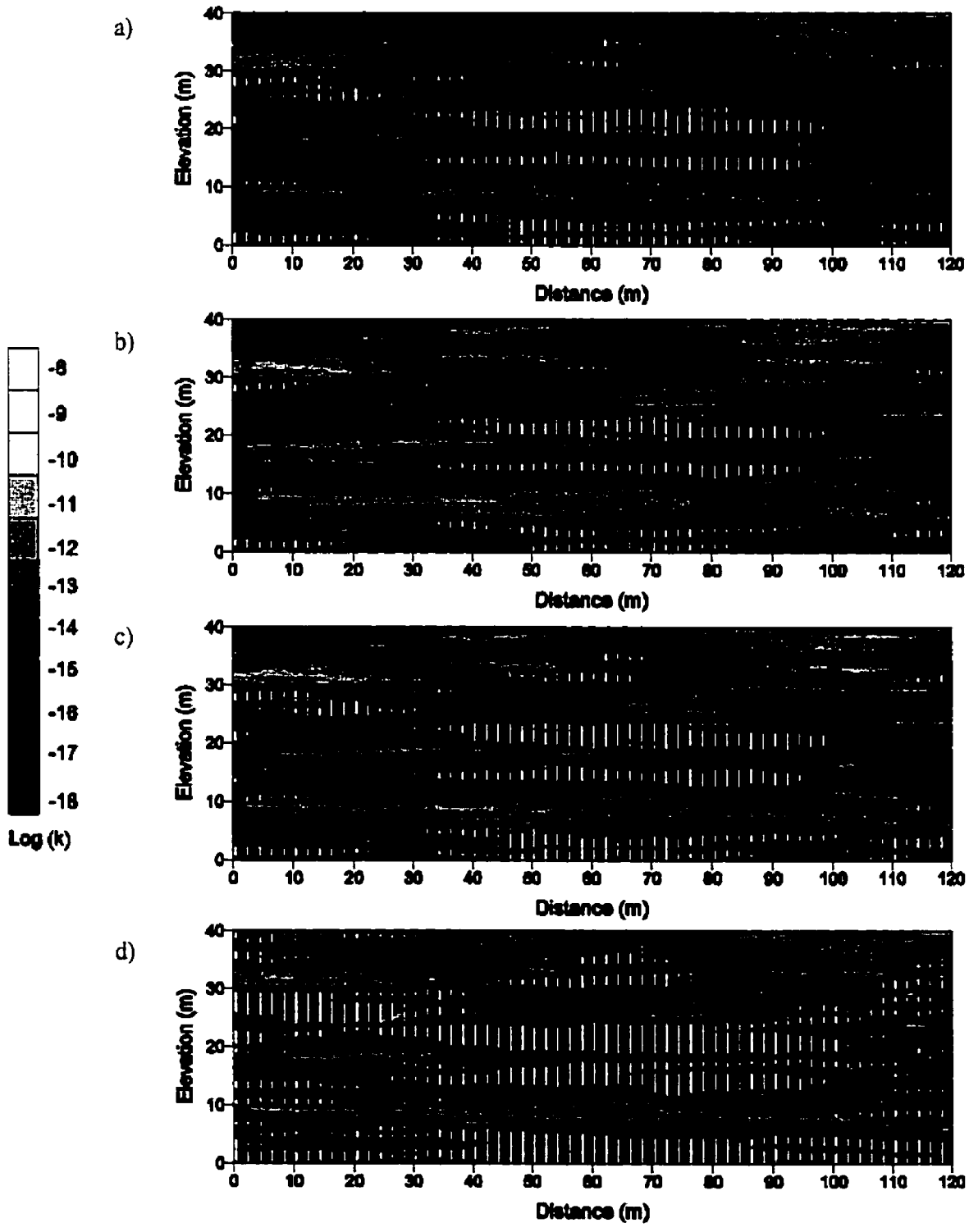

Figure 5-3. Generated Permeability Fields (a) Base Case, (b) Increased Mean Permeability, (c) Increased Permeability Variance, (d) Increased Cut-off Permeability for Fractures

Table 5-2. Parameters Varied in Sensitivity Simulations

Simulation	Mean Permeability (m^2)	Variance of log Permeability	Maximum Fractured Lens Permeability (m^2)
Low-k	1.02×10^{-14}	5.5	1.02×10^{-13}
Hi-k	1.02×10^{-12}	5.5	1.02×10^{-13}
Low-Var	1.02×10^{-13}	4.5	1.02×10^{-13}
Hi-Var	1.02×10^{-13}	6.5	1.02×10^{-13}
Cut-Low	1.02×10^{-13}	5.5	1.02×10^{-14}
Cut-Hi	1.02×10^{-13}	5.5	1.02×10^{-12}

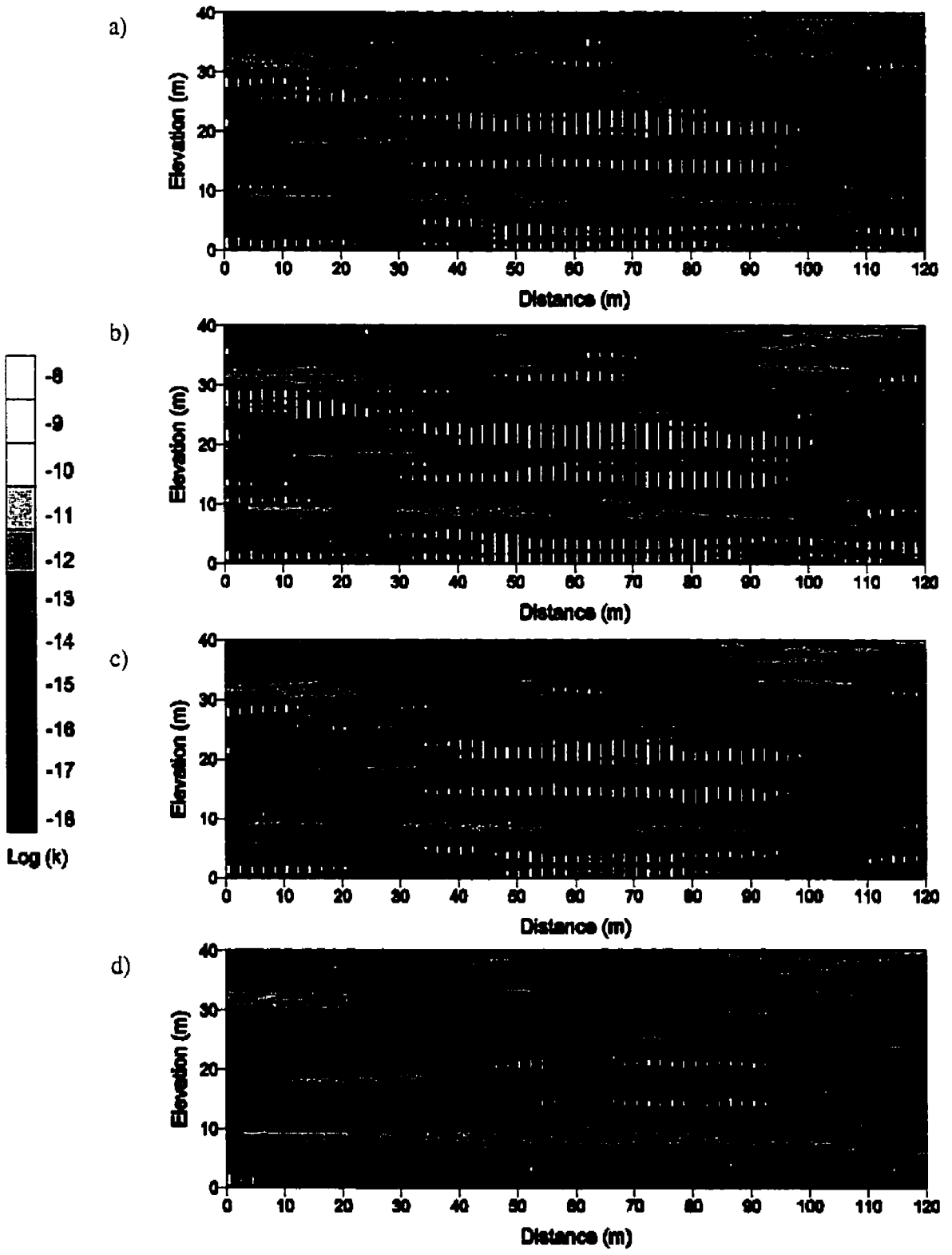

Figure 5-4. Generated Permeability Fields (a) Base Case, (b) Decreased Mean Permeability, (c) Decreased Permeability Variance, (d) Decreased Cut-off Permeability for Fractures

5.3 Results and Discussion

5.3.1 Depth of Migration

One of the most critical questions asked in a DNAPL release scenario is the maximum depth of penetration of the nonwetting phase in the system. It is well established that the migration pathway of the DNAPL is controlled by subtle permeability variations in the subsurface (Kueper et al., 1993) whose locations cannot be predicted by common field methods. The presence of high permeability fractures in the path of the migrating DNAPL opens the possibility of significant "short-circuiting" of the DNAPL across otherwise impenetrable lenses.

Table 5-3 presents the total length of fractures in the seven simulations conducted in this work. Given the algorithm used to produce the fractures, the maximum length possible for a domain consisting entirely of fractured media would be 2,400 m, with the simulations conducted in this work ranging between 1.5 and 30 percent of the maximum. Figure 5-5 compares the lowest elevation of the DNAPL front versus time for the seven different scenarios. The most obvious trend in the data is the importance of the mean porous media permeability of the domain. The increased permeability simulation exhibits DNAPL migrating quickly through the system, due to the lower entry pressures and higher permeabilities encountered.

Figure 5-6 reports the time required for the 30 m^3 of DNAPL to enter the domain for each simulation. As expected, the low permeability and high permeability fields exhibit the lowest and highest rates of infiltration, respectively. It is of interest to note the behaviour of the infiltration rates for the different cut-off permeability simulations as compared to the base case

scenario. The rate is almost identical to the base for the situation where only lenses of permeability less than $1.0x10^{-14}$ m^2 are fractured, implying that during the "source-on" portion of the simulations, the geology encountered by the migrating DNAPL is similar and fractures have little influence on the infiltration rate (this is supported by the results presented in Figure 5-5). The infiltration rate is greater than that of the base case for the simulation, however, where lenses of permeability less than $1.0x10^{-12}$ m^2 are fractured, implying that the increased presence of fractures in the system is providing some control over the migration process.

Table 5-3. Total Length of Fractures Present in Simulations

Simulation	Total Linear Length of Fractures (m)
Decreased Cut-off Permeability	65.0
Increased Mean Permeability	245.5
Decreased Variance of Permeability	276.3
Base	351.5
Increased Variance of Permeability	406.0
Decreased Mean Permeability	481.5
Increased Cut-off Permeability	728.5

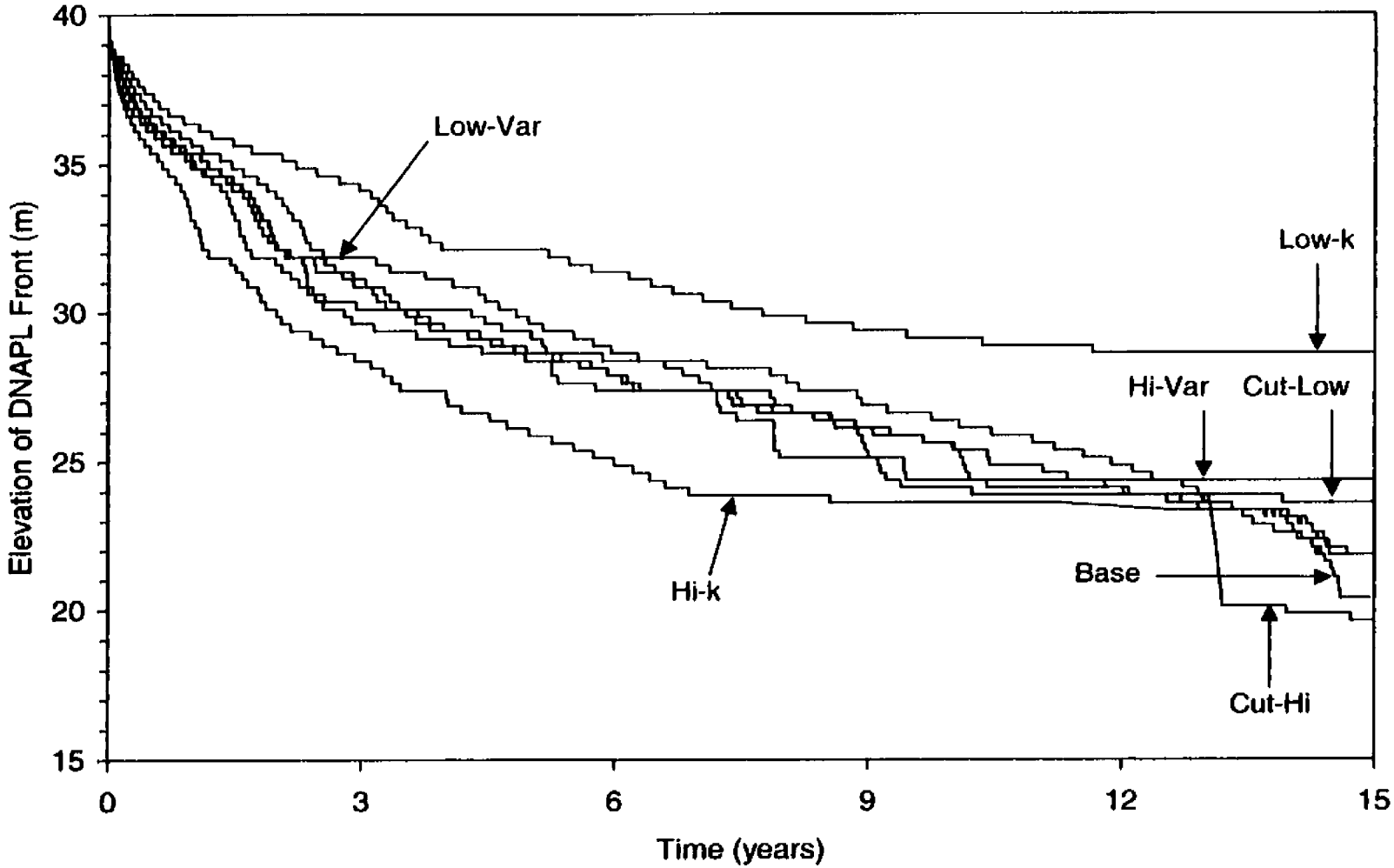

Figure 5-5. Elevation of DNAPL Front (Farthest Penetration into the System) versus Time

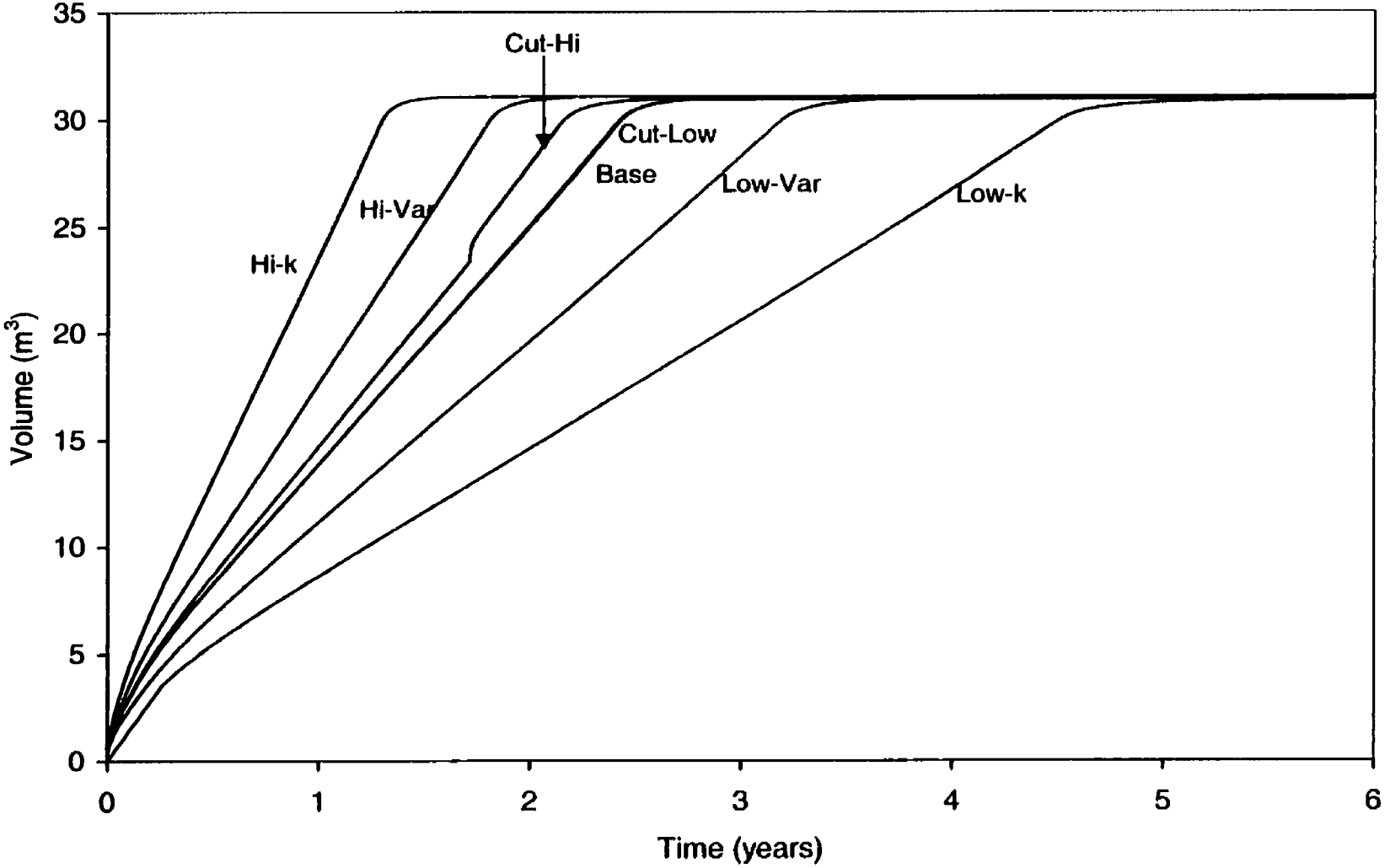

Figure 5-6. Volume of DNAPL Entering Domain versus Time

The importance of the fractures in the system is highlighted by examining the behaviour of the DNAPL front as it arrives at a low permeability feature that is present in all simulations. The silt lens, located at an elevation of approximately 32 m and spanning from 50 m to 70 m horizontally is present in some form in each of the seven domains. Three ways exist to penetrate beyond this barrier; by-passing it through porous media flow, penetrating into it through porous media flow, and short-circuiting through it via fractures. The determination of which process has occurred requires examination of the global pattern of migration, as the presence of the DNAPL at an elevation equal to that of the bottom of the lens does not necessarily signify breakthrough, since this could be occurring elsewhere in the domain. Comparisons for four simulations are presented after 15 years of migration in Figure 5-7. In the four scenarios presented, the low permeability lens under consideration has been by-passed in the base case, increased mean permeability, and increased variance of permeability simulations. The increased fracturing present in the increased permeability cut-off simulation has allowed the DNAPL to both by-pass and short-circuit across the lens. The short-circuiting is the quicker mechanism in this particular circumstance, as evidenced by the rapid decrease in elevation of the DNAPL front shortly after reaching the capillary barrier (Figure 5-5). This pattern is signatory of flow through fractures and its occurrence can be noted elsewhere in Figure 5-5.

The time required for the bypassing of the capillary barrier in the increased mean permeability scenario is similar to that of the increased permeability cut-off scenario, but is entirely through by-passing, as evidenced in Figure 5-7b. The decreased mean permeability simulation requires greater than twice the time to by-pass the barrier due to a combination of the decreased infiltration rate providing reduced driving forces, a greater lateral extent of the lens, and a "skin"

effect which occurs as the permeability of the lens and it's surroundings is decreased requiring higher capillary pressures to be invaded, yet is not low enough to be fractured and provide high permeability pathways. A second, more significant (both from a capillary and size standpoint) barrier exists in every domain centred at an elevation of approximately 21 m and a horizontal distance of 65 m. The upper surface of the lens is variable between domains, due to the different controlling statistics underlying their generation, but is located at approximately 24 m. After 15 years, four of the seven simulations have resulted in the occurrence of DNAPL below this barrier. The three simulations that do not exhibit DNAPL below this barrier (decreased mean permeability, increased variance of permeability, and decreased cut-off permeability) have essentially stopped migration after 15 years.

The near-vertical section of the migration vs. time data for the increased cut-off permeability scenario at approximately 13 years in Figure 5-5 is the rapid crossing of the lens through the extensive fracturing in this domain. The slow vertical migration that occurs in this simulation after breaking through the lens is a function of the small volumes which fractures are capable of transmitting. Reynolds and Kueper (2001) found similar behaviours in homogeneous domains, where the presence of porous media underlying fractured formations resulted in significant increases in vertical migration times. At the 15 year point in the migration the only other simulation to breach the lower capillary barrier is the base case, and this has occurred in a single fracture only (Figure 5-7a)

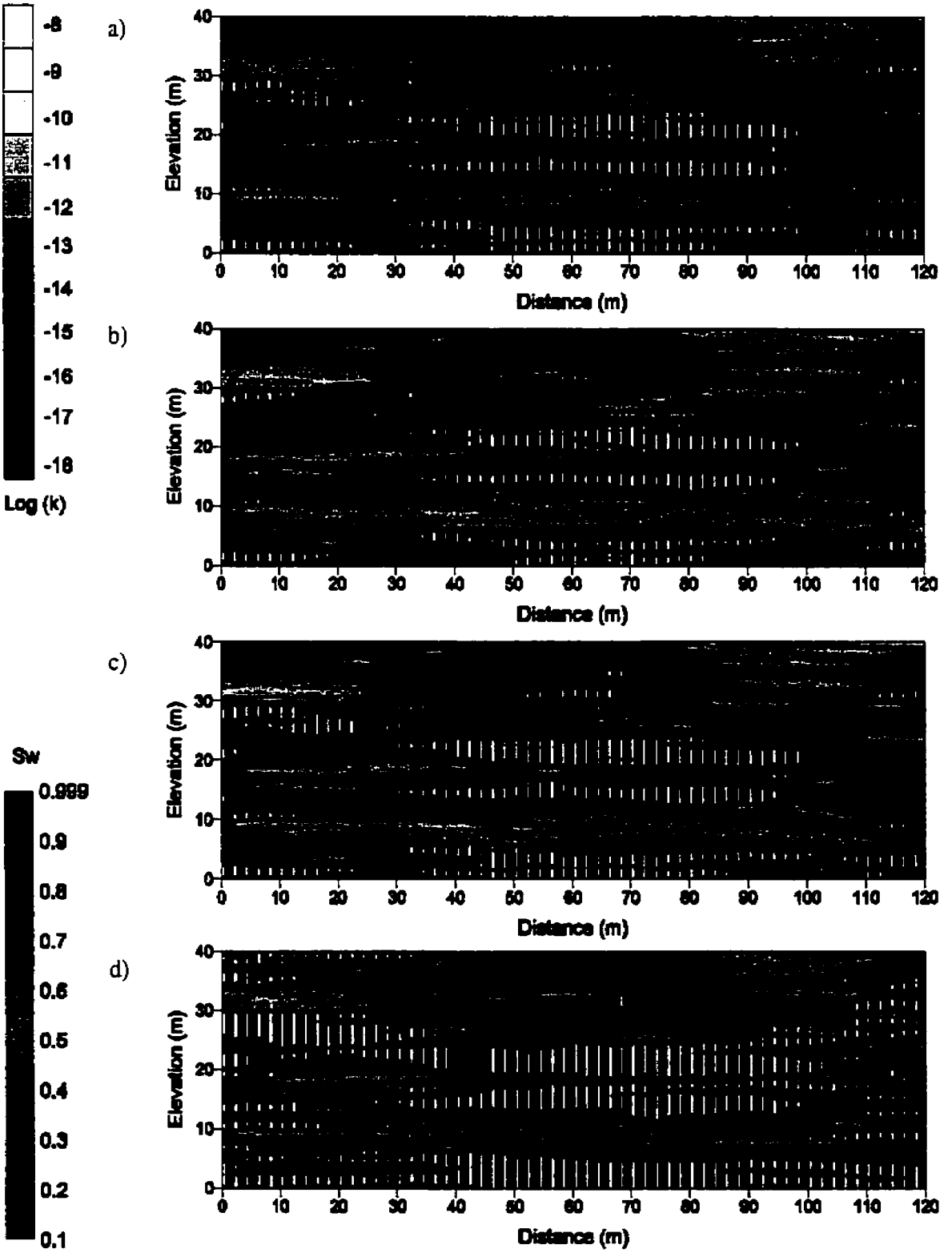

Figure 5-7. Wetting Phase Saturations After 15 Years (a) Base, (b) Increased Mean Permeability, (c) Increased Permeability Variance, (d) Increased Cut-off Permeability for Fractures

5.3.2 Lateral and Vertical Spreading

The depth of penetration into the domain is only one indicator of the spatial extent of the contamination that has occurred. Nonwetting phase moments can be used as an indicator of the vertical and horizontal spreading that has occurred (Kueper and Frind, 1991b):

$$M_{ij} = \int_{-\infty}^{\infty}\int_{-\infty}^{\infty} x^i z^j V_{nw}\, dx dz \qquad [5\text{-}5]$$

where V_{nw} is the volume of the nonwetting fluid (m^3). Figure 5-8 presents a plot of the nonwetting phase second moment about a horizontal axis through the centre of mass for each simulation according to:

$$\sigma_z^2 = M_{02}/M_{00} - Z_c^2 \qquad [5\text{-}6]$$

where Z_c is the position of the z coordinate of the centre of mass (m). A higher second moment as defined by [5-6] is indicative of a higher degree of vertical spreading in the system. The same procedure is also adopted to determine the second moment about a vertical axis through the centre of mass, which corresponds to a measure of the degree of lateral spreading (i.e., along horizontal lenses) within the system. The second moments about a vertical axis through the centre of mass for all simulations are presented in Figure 5-9.

The moments presented in Figure 5-8 and 5-9 in general "level-off" after approximately 9 years, as the source has re-distributed itself into a residual configuration. Vertical movement is still occurring in all simulations, but at a generally lesser rate than at early time. This is consistent with the leading-edge vertical migration results presented in Figure 5-5. The DNAPL in the exceptions to this case (base case, increased permeability cut-off, decreased permeability

variance) is still migrating vertically, but has essentially ceased spreading horizontally (Figure 5-9).

The maximum depth of penetration into a system, however, does not provide a complete picture of the extents of DNAPL contamination. The maximum vertical penetration portrayed in Figure 5-5 could be the result of DNAPL travelling down a single fracture, while the bulk of the DNAPL resides higher in the system. Combining the results of Figure 5-5 with those of Figure 5-8 (vertical second moments) produces a more accurate view of the vertical extent of the DNAPL contamination in the system. Based on Figure 5-5, after 12 years the maximum penetration into the system for all the scenarios (with the exception of the reduced mean permeability simulation) is between elevations of 23 and 25 m. Comparing the degree of vertical spreading between simulations (Figure 5-8) shows that only the base case, decreased variance of permeability and low permeability cut-off simulations have similar vertical second moments, and therefore similar vertical DNAPL distributions in the subsurface. Coupled with this, the similarities in horizontal second moments (Figure 5-9) in these simulations indicates that the DNAPL body is migrating in a similar manner in these three domains. It is of interest to note that the lower infiltration rate exhibited by the reduced variance of permeability simulation does not affect the vertical migration pattern of the DNAPL, but rather the extents of the horizontal migration.

The general trends exhibited in regards to the vertical spreading of the DNAPL body are expected, based on the underlying permeability distributions. The increased mean permeability domain exhibits the largest degree of vertical spreading, as the boundary capillary pressures

force the body through the horizontal lenses. Conversely, the reduced mean permeability simulation exhibits the least degree of vertical spreading. The decreased variance of permeability simulation migrates vertically at a slower rate than the increased scenario, but penetrates deeper into the system. These results are mimicked by the vertical second moments, which show the increased variance of permeability simulation spreading to a greater degree at early time, and to a lesser degree at late time. This is likely a function of the generated distribution allowing for migration along a high permeability pathway at early time in the more heterogeneous domain.

Figure 5-10 presents the arithmetic average wetting phase saturations in each domain as a function of time (all nodes are included in this calculation, whether invaded by DNAPL or not). The reduced spreading in the reduced mean permeability domain is accounted for in the increased average wetting phase saturations. The DNAPL has tended to remain trapped in lenses at greater saturations than in the other simulations. The general increasing trends exhibited by all simulations in Figure 5-10 (after the abrupt inflection point) represents the redistribution of the DNAPL after the source has been turned "off".

The presence of fractures in the porous media domains studied here has not influenced the vertical migration of the DNAPL body to a significant degree, but has affected the horizontal spreading. The increased cut-off permeability scenario has managed to avoid the high permeability "sink" located at the left side of the domain at an elevation of 30 m (Figure 5-3). This simulation (as well as the decreased mean permeability) was the only one to display this behaviour. The increased density of fracturing in the system allowed the DNAPL to by-pass the

"sink" by migrating vertically through a lower permeability layer. Similar behaviour (to a lesser degree) can be seen to occur on the right hand edge of the DNAPL body.

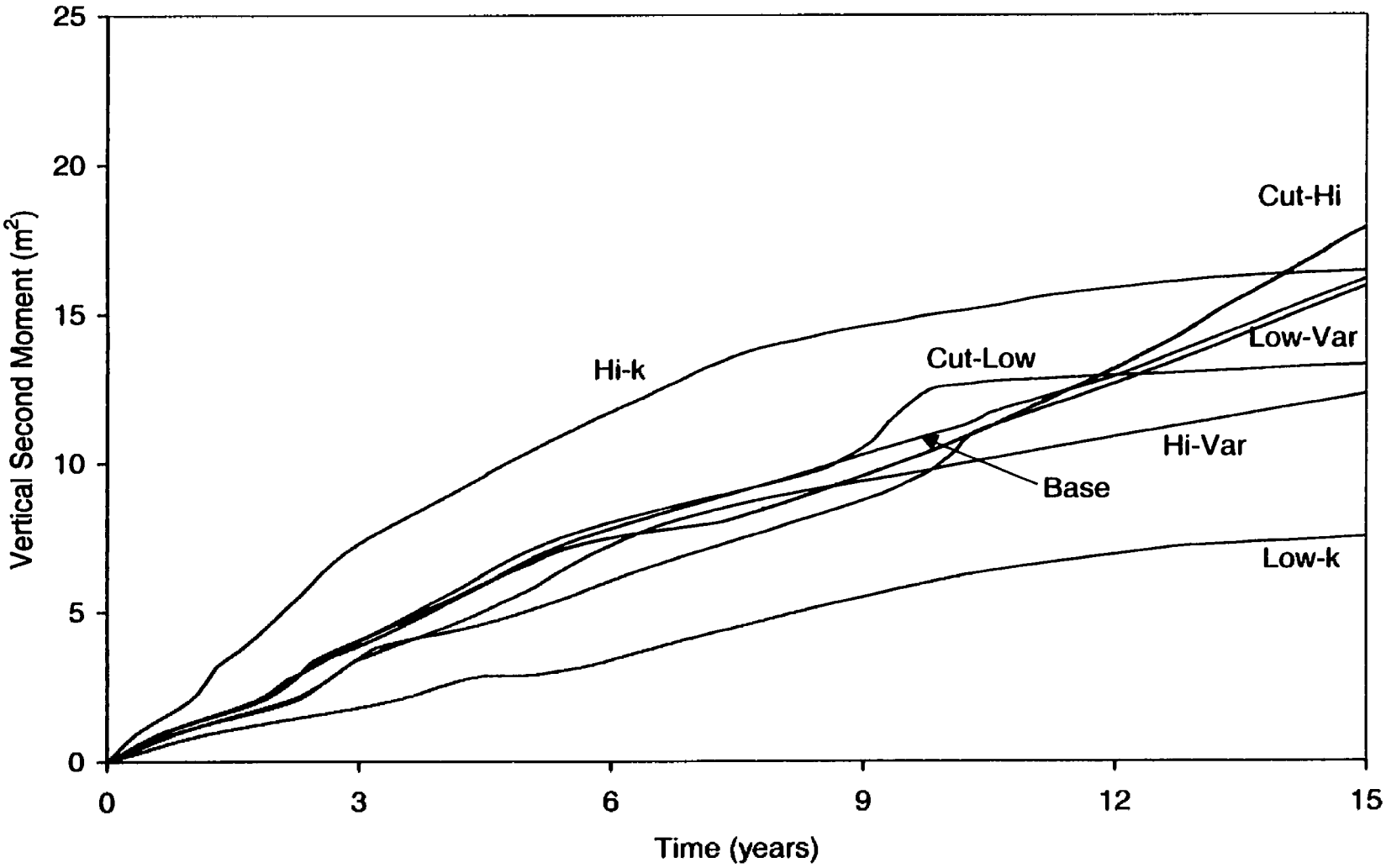

Figure 5-8. Nonwetting Phase Second Moment about Horizontal Axis versus Time

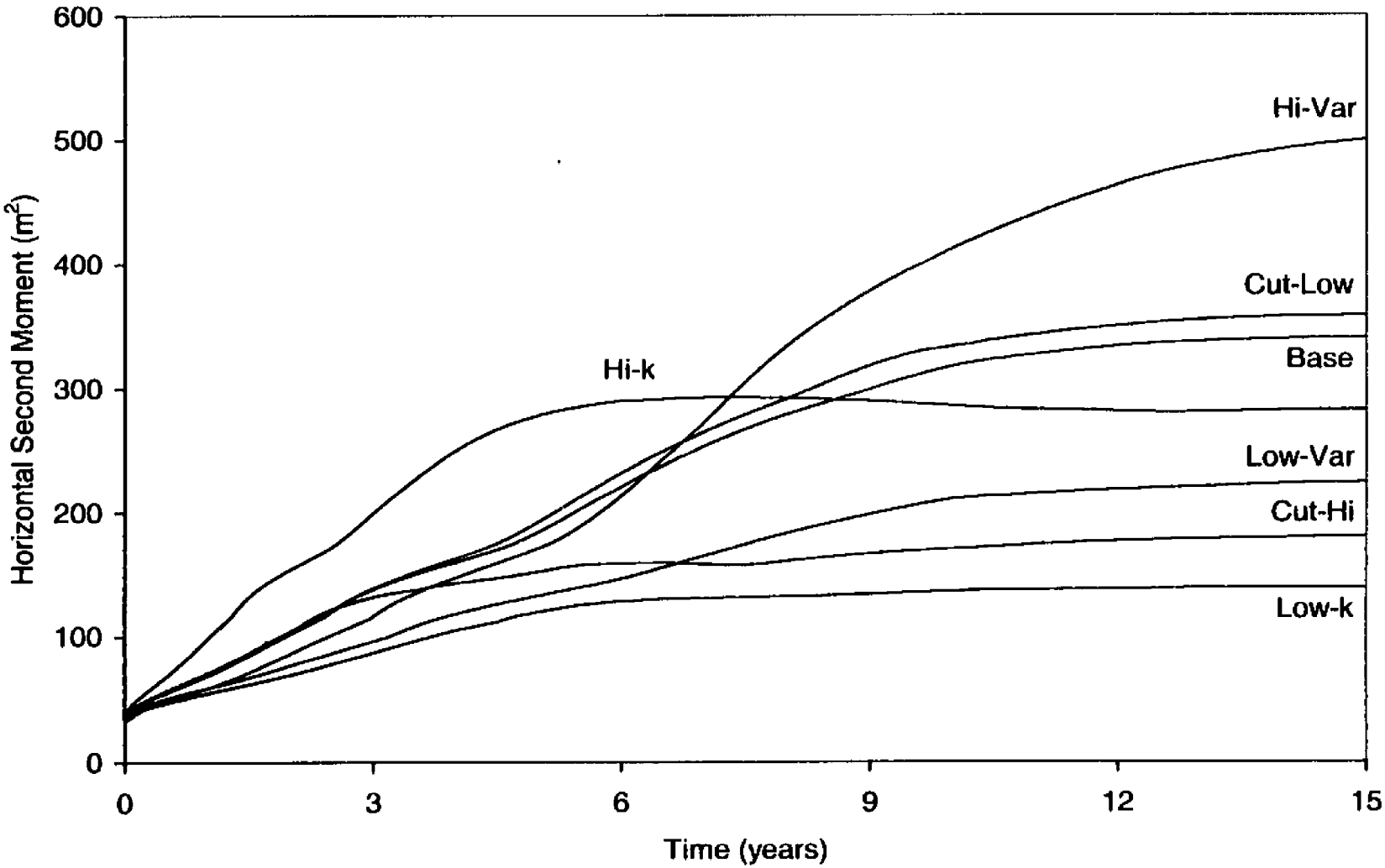

Figure 5-9. Nonwetting Phase Second Moment about Vertical Axis versus Time

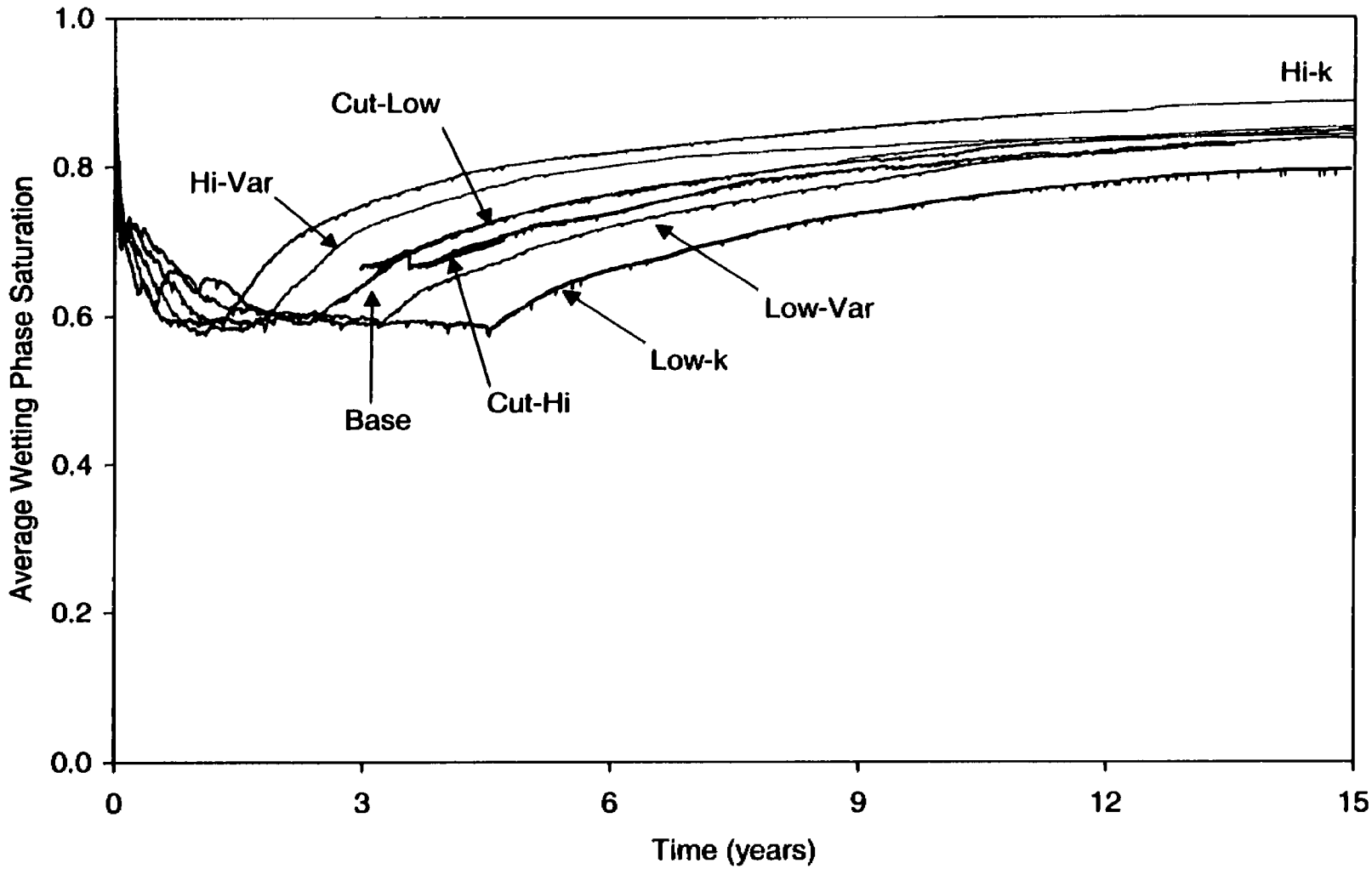

Figure 5-10. Average Wetting Phase Saturation (Includes all Nodes in Domain) versus Time

The changing nature of the DNAPL body with time is evidenced by comparing the second moments of the increased mean permeability simulation. The DNAPL in this domain spreads laterally and vertically faster than any other simulation, due to the high capillary pressure to displacement pressure ratio as compared to the other simulations. Examination of Figure 5-9 shows the degree of horizontal spreading decreases after 6 years, however. This is not indicative of the edges of the DNAPL body receding, but could be due to the mobile DNAPL mass draining slowly back towards the middle of the domain and vertically downwards, or a migration of the centre of mass.

5.3.3 Timescales of DNAPL Movement

Another important aspect concerning the migration of a DNAPL through the subsurface is the timeframe during which movement occurs. The incorporation of hysteresis and trapping in the constitutive relationships within the model allows for simulation of the production of residual DNAPL upon re-distribution. It should be pointed out that the particular formulation of the hysteretic relationship used, as well as the employed parameters, will influence the time of migration. The results presented here, therefore, are an attempt to determine the relative effects of the altered permeability fields, rather than an attempt to produce a general statement on the migration times of DNAPL spills.

In the process of assessing the migration of a DNAPL body after its release to the subsurface, differentiation must be made between migration and re-distribution and the parameters used to indicate each. The results presented in Figure 5-5 represent the migration of the DNAPL

vertically through the subsurface, resulting in further contamination as the front drops. From these results, it can be concluded that in the majority of the simulations, DNAPL has stopped rapid large-scale migration after 15 years (with the possible exception of the increased permeability for fracturing scenario). The use of moment analysis, however, does not necessarily indicate that a larger volume of the subsurface is being contaminated with increasing moments. The DNAPL may be re-distributing within the body after the source has been removed (as is evidenced in Figure 5-10), and not increasing in volume.

The second moment results presented in Figures 5-8 and 5-9 allow for some indication of the continuing movement of the DNAPL body. If the second moments are stabilizing with time, it can be inferred (in this work) that the DNAPL body has, at least temporarily, slowed in its large-scale migration. Of the seven simulations presented in Figure 5-9 it would appear that the increased variance of permeability simulation is the only one exhibiting lateral DNAPL migration to any great extent after 15 years. The 15 year "snap-shot" presented in Figure 5-7 shows that the high permeability lens located in the upper left hand side of the domain contains high nonwetting phase saturations, and is exiting the side of the domain (this is the only simulation in which this occurred). Slow migration laterally is also occurring above the centrally located low permeability barrier.

The moments presented in Figure 5-8, however, indicate that vertical redistribution of the DNAPL after 15 years is still occurring in all but three scenarios (reduced mean permeability, increased mean permeability, and increased variance of permeability). This is an indication that while the presence of fractures does not exhibit a controlling influence on the extent of vertical

DNAPL migration in the systems studied, they do allow for extended periods of movement. The two altered mean permeability simulations (which are no longer migrating vertically) have the least amount of fracture length contaminated by DNAPL, due to the few fractures present in the increased mean permeability scenario, and the lack of fractures encountered in the decreased mean permeability scenario. The remaining scenarios have significant flow occurring in the fractures, as well as in the porous media underlying the fractures. The base case scenario was extended to 30 years simulation time, and had yet to reach asymptotic behaviour (data not shown).

5.3.4 Aqueous Phase Contamination

The main focus of this work has been on the migration of the nonwetting phase through the seven simulated systems. All simulations conducted in this work also included equilibrium dissolution as well as advective/dispersive transport of the dissolved phase. The upward gradient applied (0.05) resulted in an average downward retarded solute velocity of 0.61 m/year. This is locally variable due to the combined effects of local-scale permeability and the reduced relative permeability due to the presence of DNAPL.

Figure 5-11 presents "snap-shots" of the contaminant plume after 15 years of simulation for the base case, decreased mean of permeability, decreased variance of permeability, and decreased cut-off permeability for fracturing scenarios. In general, the arrival times of the dissolved phase are not significantly in advance of the nonwetting phase. In certain cases the DNAPL source has become exhausted, and the vertical migration has stopped slightly above a fractured unit (for example the protrusion on the right hand side of the main DNAPL body in the base and

increased variance of permeability simulations at 80 m in Figure 5-7). The wetting phase flow is being funnelled around this area due to the reduced permeability caused by the presence of the DNAPL and the high permeability pathway below represented by the fractures. This causes the dissolved phase to migrate through the fractures and appear "ahead" of the DNAPL. Due to the discretization limitations imposed by the available computational resources, this migration is not as retarded due to matrix diffusion as might be the case in an analytical formulation. An analysis of the migration of TCE through a 1 m long 130 μm aperture fracture (equivalent to a silty sand in this work) within a similar hydrological setting using the analytical method of Sudicky and Frind (1982), however, showed arrival of the solute at levels greater than 1 ppm after less than 10 days. The presence of these large fractures allows for the vertical migration of the dissolved phase ahead of the DNAPL phase (a 30 μm fracture in the same setting would require more than 150 years to transmit equivalent concentrations).

The second situation in which the dissolved phase occurs in advance of the DNAPL also involves the deviation of the flowlines due to increased permeability zones in the domain that are not due to fractures. An examination of the dissolved phase in the reduced variance of permeability simulation (Figure 5-11c) shows the migration of the aqueous phase out the left side of the domain through the high permeability lens at 30 m elevation discussed earlier. In general, however, the vertical aqueous phase migration is not significantly in advance of the DNAPL, under the moderate gradients applied in this work.

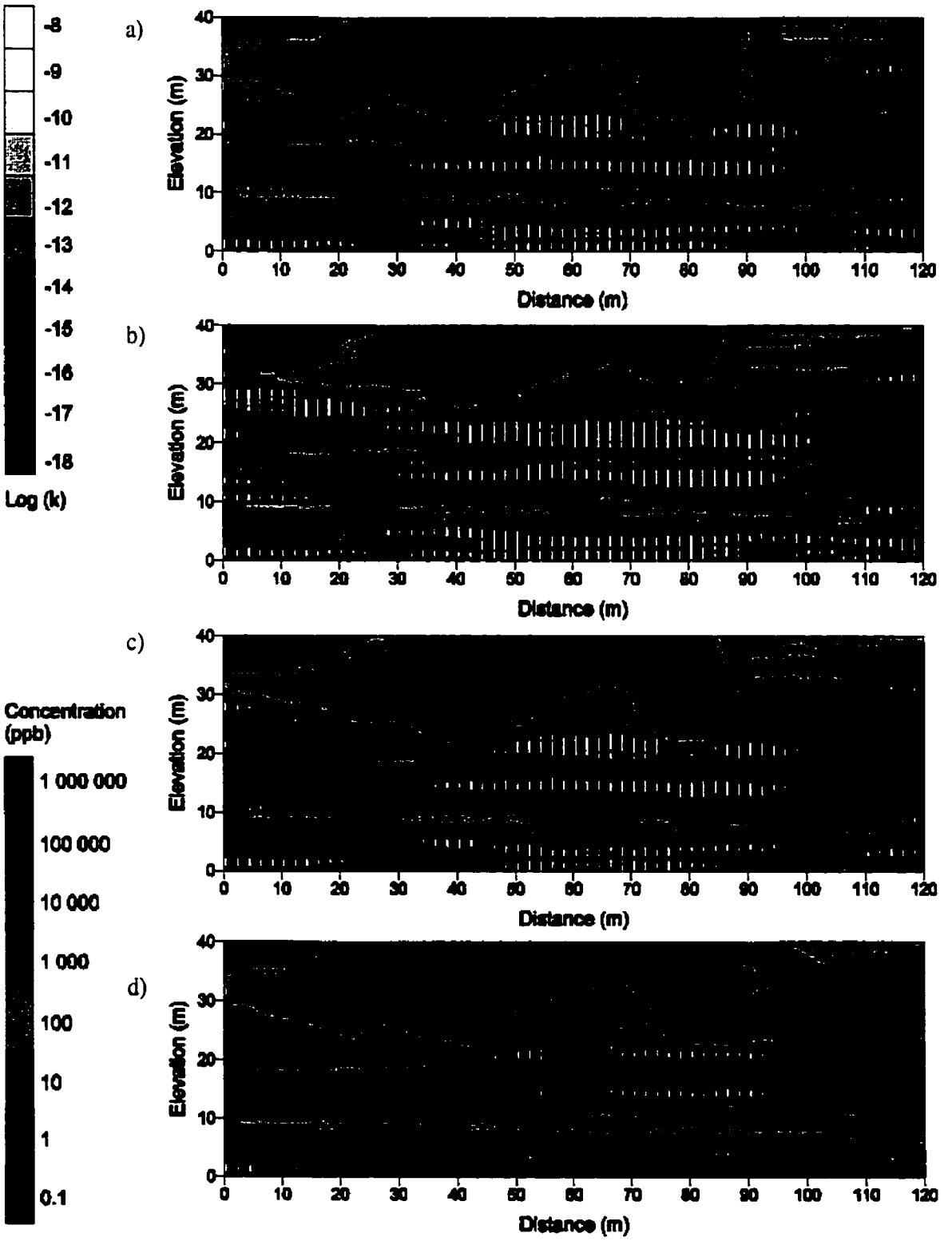

Figure 5-11. TCE Concentrations After 15 Years (a) Base, (b) Decreased Mean Permeability, (c) Decreased Permeability Variance, (d) Decreased Cut-off Permeability for Fractures

5.4 Conclusions

The migration of DNAPL and dissolved phase contamination through a fractured heterogeneous porous medium has been investigated through the use of a multiphase compositional model. The sensitivity to the mean permeability, the variance of the permeability, and the degree of fracturing of the domain were examined. A release of 30 m^3 of TCE was allowed to migrate for 15 years, and the resultant distribution of the nonwetting and dissolved phases was examined. The investigation used relationships between the permeability of a lens and fracture aperture, and between the permeability and displacement pressure that were developed from published values.

The first focus was to the sensitivity of the maximum depth of DNAPL penetration to the varied parameters. It was found that increasing the mean permeability of the domain allowed the DNAPL to penetrate deeper into the subsurface, while decreasing the mean permeability caused the DNAPL to pool at shallower depths. The infiltration rates of these two simulations were found to be the highest and lowest respectively, indicating that the order of lenses encountered in the migration determined the overall rates of migration. The presence of fractures within the system was found to control the infiltration only for the case where lenses with a permeability of less than $1.0x10^{-12}$ m^2 were fractured. The importance of fractures in the system was seen when examining the time required to penetrate through low permeability features present in all simulated domains. In simulations with extensive fracturing, the DNAPL was able to "short-circuit" rapidly across low permeability layers and penetrate deeper into the subsurface. In most cases where the DNAPL encountered a low permeability barrier during the "source-on"

condition, DNAPL eventually migrated below the barriers, either through by-passing, invasion, or a combination of the two.

The extent of DNAPL contamination within the system was also evaluated through the use of moments about the centre of mass of the DNAPL body. The moments, which indicate the degree of lateral and vertical spreading of the DNAPL, tended to level off after approximately nine years (maximum duration of the source-on condition was approximately 4.5 years). This tended to be due to a redistribution of the DNAPL towards a residual configuration, as was evidenced by the gradual trending of average nonwetting phase saturations within the domain to a static value. The increased presence of fracturing within the domain was, in general, found to allow for deeper DNAPL penetration into the subsurface. The exception to this was found when the mean of the permeability field was reduced. Reducing the mean produced more fractures in the domain (as the permeability of more lenses fell below the cut-off value for fracturing) but the higher degree of lateral spreading prevented the DNAPL from encountering significant numbers of fractures.

The dissolved phase plume was found to migrate at essentially the same rate as the nonwetting phase, due to the reduced relative permeability of lenses containing DNAPL, and due to diffusive losses of mass to the matrix of fractured clay and silty-clay lenses. Some exceptions to this were found when the DNAPL could not overcome the displacement pressure of a lens, and could not bypass the lens due to the lack of available driving force after the source had been shut off.

5.5 References

Abriola, L.M. and G.F. Pinder. 1985. A Multiphase Approach to the Modeling of Porous Media Contamination by Organic Compounds, 1. Equation Development, *Water Res. Res.*, 27(6), p 11-18.

Bradford, S.A., Abriola, L.M., and K. Rathfelder. 1998. Flow and Entrapment of Dense Nonaqueous Phase Liquids in Physically and Chemically Heterogeneous Formations, *Adv. Water Res.*, 22(2), p 117-132.

Brooks, R.H. and A.T. Corey. 1964. Hydraulic Properties of Porous Media. *Hydrol. Paper 3*, Colorado St. Univ., Fort Collins CO.

Cherry, J.A. Feenstra, S., and D.M. MacKay. 1996. Concepts for the Remediation of Sites Contaminated with Dense Nonaqueous Phase Liquids (DNAPLs). In J.F. Pankow and J.A. Cherry (Eds.), *Dense Chlorinated Solvents and Other DNAPLs in Groundwater: History, Behaviour, and Remediation*, Waterloo Press, Portland, Oregon, p 475-506.

Dekker, T.J. and L.M. Abriola. 2000. The Influence of Field-scale Heterogeneity on the Infiltration and Entrapment of Dense Non-aqueous Phase Liquids in Saturated Formations, *J. Cont. Hyd.*, 42, p 187-218.

Freeze, R.A., and D.B. McWhorter. 1997. A Framework for Assessing Risk Reduction Due to DNAPL Mass Removal from Low Permeability Soils, *Ground Water*, 35(1), p 111-123.

Gerhard, J.I., B.H. Kueper, and G.R. Hecox. 1998. The influence of waterflood design on the recovery of mobile DNAPLs, *Ground Water*, 36(2), p 283-292.

Hinsby, K., McKay, L.D., Jorgensen, P., Lenczewski, M., and C.P. Gerba. 1996. Fracture Aperture Measurements and Migration of Solutes, Viruses, and Immiscible Creosote in a Column of Clay-Rich Till, *Ground Water*, 34(6), p 1065-1075.

International Technology Corporation. 1995. Base Clay Characterization Report, Phase II Draft Sitewide RFI Report, 3(1).

Jorgensen, P.R., McKay, L.D., and N.H.Spliid. 1998. Evaluation of Chloride and Pesticide Transport in a Fractured Clayey Till Using Large Undisturbed Columns and Numerical Modeling, *Water Res. Res.*, 34(4), p 539-553.

Kueper, B.H. and E.O. Frind. 1991a. Two-phase Flow in Heterogeneous Porous Media: 2. Model Development, *Water Res. Res.*, 27(6), p 1049-1057.

Kueper, B.H. and E.O. Frind. 1991b. Two-phase Flow in Heterogeneous Porous Media: 2. Model Application, *Water Res. Res.*, 27(6), p 1058-1070.

Kueper, B.H. and D.B. McWhorter. 1991. The Behaviour of Dense, Nonaqueous Phase Liquids in Fractured Clay and Rock, *Ground Water*, 29(5), p 716-728.

Kueper, B.H., Redmond, D., Starr, R.C., Reitsma, S., and M. Mah. 1993. A Field Experiment to Study the Behaviour of Tetrachloroethylene Below the Water Table: Spatial Distribution of Residual and Pooled DNAPL, *Ground Water*, 31(5), p 756-778.

Kueper, B.H. and J.I. Gerhard. 1995. Variability of Point Source Infiltration Rates for Two-phase Flow in Heterogeneous Porous Media, *Water Res. Res.*, 31(12), p 2971-2980.

Leverett, M.C. 1941. Capillary Behaviour in Porous Solids, *AIME Transactions*, 142, p 152-169.

McKay, L.D., Cherry, J.A., and R.W. Gillham. 1993. Field Experiments in a Fractured Clay Till 1. Hydraulic Conductivity and Fracture Aperture, *Water Res. Res.*, 29(4), p 1149-1162.

Murphy, J.R. and N.R. Thomson. 1993. Two-Phase Flow in a Variable Aperture Fracture, *Water Res. Res.*, 29(10), p 3453-3476.

Pankow, J.F., Johnson, R.L., Houck, J.E., Brillante, S.M., and W.J. Bryan. 1984. Migration of Chlorophenolic Compounds at the Chemical Waste Disposal Site at Alkali Lake, Oregon – 1. Site Description and Ground-Water Flow, *Ground Water*, 22(5), p 593-601.

Poulsen. M., and B.H. Kueper. 1992. A Field Experiment to Study the Behaviour of Tetrachloroethylene in Unsaturated Porous Media, *Environ. Sci. Technol.*, 26(5), p 889-895.

Reynolds, D.A. and B.H. Kueper. 2001. Multiphase Flow and Transport in Fractured Clay/Sand Sequences, *J. Cont. Hyd.*, In press.

Reitsma, S.R. and B.H. Kueper. 1994. Laboratory Measurement of Capillary Pressure-Saturation Relationships in a Rock Fracture, *Water Res. Res.*, 30(4), p 856-878.

Robin, M.J.L., Sudicky, E.A., Gillham, R.W., and R.G. Kachanowski. 1991. Spatial Variability of Strontium Distribution Coefficients and Their Correlation with Hydraulic Conductivity in the Candian Forces Base Borden Aquifer, *Water Res. Res.*, 27(10), p 2619-2632.

Schowalter, T.T. 1979. Mechanics of Secondary Hydrocarbon Migration and Entrapment, *Amer. Ass. of Pet. Geol. Bull.*, 63(5), p 723-760.

Schwille, F. 1988. Dense Chlorinated Solvents in Porous and Fractured Media, Trans. by J.F. Pankow, Lewis, Chelsea, MI.

Slough, K.J., Sudicky, E.A., and P.A. Forsyth. 1999a. Numerical Simulation of Multiphase Flow and Phase Partitioning in Discretely Fractured Geologic Media, *J. Cont. Hyd.*, 40, p 107-136.

Slough, K. J., Sudicky, E.A., and P.A. Forsyth. 1999b. Importance of Rock Matrix Entry Pressure on DNAPL Migration in Fractured Geologic Materials, *Ground Water*, 37(2), p 237-244.

Sudicky, E.A. and E.O. Frind. 1982. Contaminant Transport in Fractured Porous Media: Analytical Solutions for a System of Parallel Fractures, *Water Res. Res.*, 18, p 1634-1642.

Thomas, L.K., Katz, D.L., and M.R. Tek. 1968. Threshold Pressure Phenomenon in Porous Media, *SPE Journal*, 243, p 174-184.

CHAPTER 6 – LARGE-SCALE CAPILLARY PRESSURE RELATIONSHIPS IN FRACTURED ROCK

6.1 Introduction

The numerical simulation of subsurface flow and transport can incorporate relatively well understood concepts and simple geologic environments (such as single phase flow through homogeneous porous media), as well as significantly more complex scenarios such as multiphase flow through discretely fractured rock masses. The flow of fluids through the subsurface can be strongly influenced by spatial variability that may exist at the centimetre or smaller scale. It is currently computationally challenging to simulate large-scale problems with this level of detail, and as a result some scaling must occur to translate this information to a practicable scale. In addition to the computational infeasibility, the acquisition of data at a fine scale can be difficult given existing field methods. Significant work has been undertaken to investigate the scaling of the hydraulic conductivity of porous and fractured media (e.g., Long et al., 1982; Zhang et al., 1996, Zhang and Sanderson, 1999), but relatively little work has been performed (in the context of simulating environmental contamination) on the scaling of the constitutive relationships (such as relative permeability-saturation and capillary pressure-saturation) required in the modelling of multiphase flows.

Given the non-linearity of many constitutive relationships, their scaling is significantly more complex than the single-phase permeability tensor. Petroleum reservoir characterization studies

have dominated the literature concerning the scaling of multiphase flow behaviours (see Christie (1996) for a review) in an attempt to convert detailed geologic models to their numerical equivalents. The focus of the literature, however, has been on the scaling of porosity and permeability, where the total flows through coarse homogeneous grid blocks are matched to finer heterogeneous grid blocks. For example, King et al. (1993) used renormalization procedures (where small subsets of the fine grid are extracted and used to produce an average) to produce effective relative permeabilities. A different approach was undertaken by Durlofsky et al. (1997) who used an adaptable grid technique to scale the intrinsic permeability alone, while retaining a single pair of constitutive relations for the entire medium.

In general, there are three approaches to the scaling of the constitutive relations; averaging methods, stochastic methods, and deterministic methods. In addition, Hassanizadeh and Gray (1990), and Gray (2000) formulated a system of equations describing two-phase flow in porous media based on macro-scale thermodynamic concepts. The equations developed for describing the movement and appearance/disappearance of interfaces are the macroscopic versions of microscopic interfacial tension concepts. The resulting formulation of capillary pressure as a function of mass density, porosity, saturation, temperature, and specific surface, though thermodynamically correct, complicates the determination of the large-scale relationships, and has yet to be fully tested (Miller et al., 1998).

A second approach to the scaling of multiphase flow parameters is the utilization of large-scale volume averaging. With this approach, the flow equations and effective properties at a large-scale are calculated by averaging over the equations corresponding to a finer scale. Darcy's

Law, for example, may be thought of as a large-scale averaging process of Stokes Law at the pore scale to the local-scale. Quintard and Whitaker (1988) found that the large-scale equations in a quasi-static case are similar to the local-scale versions (based on Darcy's Law), and the constitutive relationships are functions of the large-scale saturation only. The use of this approach on dynamic problems (i.e. where pressure gradients and transient effects result in saturation changes over the averaging volume) is limited by poorly defined closure equations (Quintard and Whitaker, 1990). Ahmadi and Quintard (1996) performed a large-scale averaging analysis of multiphase flow in random porous media, using correlations between the physical properties (such as porosity and permeability), and determined that the use of local-scale correlations is not justified in either two or three dimensions. Desbarats (1995), however, found that upscaled capillary pressure (scaled as a function of permeability, porosity, and irreducible water saturations) accurately reproduced vertical saturation profiles in layered unsaturated systems.

Stochastic approaches to the scaling of multiphase flows in porous media have mostly concentrated on the unsaturated zone (Dagan and Bresler, 1983; Mantoglou and Gelhar, 1987a, b, c). Mantoglou and Gelhar (1987a, b, c) averaged the local unsaturated flow equations over repeated realizations of a statistically homogeneous random field. The permeability, specific moisture capacity, and a relative permeability fitting parameter were separated into mean and variation components as functions of the mean capillary tension head and mean hydraulic gradient, as well as the statistical parameters of the permeability field. Yeh et al. (1985) found excellent agreement between their stochastic results and laboratory data, and found that the

anisotropy ratio of the large-scale hydraulic permeability increased when the large-scale capillary pressure increases, or the large-scale moisture content decreases.

The use of a deterministic approach to the scaling of multiphase flow in porous media involves the numerical simulation of fine scale domains, and the creation of averaged macro-scale properties based on the results from the local-scale. The use of re-normalization in the simulation of petroleum reservoirs (King, 1989; King, et al., 1993) where a large problem is reduced to a series of smaller, tractable problems is an example of a deterministic approach. Percolation theory was first applied to the deterministic production of large-scale capillary pressure curves in heterogeneous porous media by Kueper and McWhorter (1992) and Ferrand and Celia (1992). Kueper and McWhorter (1992) used a macroscopic percolation approach, in which the classical pore and pore throat dimensions were replaced with local-scale porosity, permeability, and capillary pressure-saturation relationships. This approach allowed for the construction of large-scale hysteretic pressure relationships, but did not allow for the determination of large-scale saturation-relative permeability functions, and cannot account fully for gravitational and viscous forces. Ioannidis et al. (1996) also used macroscopic percolation to investigate quasi-static drainage and imbibition in three-dimensional spatially correlated permeability fields. Their results, which included the effects of buoancy and gravity, showed that large-scale capillary pressure and relative permeability curves are strongly influenced by spatial correlation.

The homogenization approach to the large-scale representation of multiphase flow in porous media was developed by Amazine et al. (1991), where a representative elementary volume

(REV) for periodic heterogeneous media is determined, and the large-scale saturation-relative permeability relationship found through numerical simulation. Desbarats (1995) performed similar studies on the capillary pressure-saturation relationship in layered soils under capillary gravity equilibrium. Ataie-Ashtiani et al. (2001) performed a homogenization study on periodic heterogeneous porous media through upscaling of both the relative permeability and capillary pressure relationships. The general findings of these studies was that the underlying heterogeneity exerted significant control on the large-scale flow behaviours, and that no single method exist which is tractable and applicable in all situations.

The majority of the work detailed above has been performed in porous media, and not in a discretely fractured rock setting. The focus in rock settings to date has been upon the scaling of the intrinsic permeability tensor for single-phase flow (e.g., Long et al., 1982; Cravero and Fidelibus, 1999; Zhang and Sanderson, 1999), or large-scale averaging approaches in dual-porosity systems (e.g., Chen, 1995). The petroleum literature contains numerous studies on the use of pseudorelative permeabilities in the upscaling of reservoir simulation (see Barker and Thibeau (1997) for a review), but their focus tends to be on imbibition processes, and high oil saturations, as opposed to drainage behaviour and low nonwetting phase saturations often encountered in environmental applications.

The work presented here utilizes FRACAS (FRActure Compositional Simulator), a newly developed numerical model, to investigate the deterministic production of large-scale constitutive relationships ($P_c(S_w)$ and two-phase $kkr_{nw}(S_w)$) for flow in a two-dimensional section of fractured granite developed from published field data. The sensitivity of the large-scale

properties to the statistics underlying the aperture distribution is presented, as well as the importance of fracture terminations, a phenomenon not encountered in porous media work. The conducted simulations are posed such that the off-diagonal terms in the tensor representation of the combined intrinsic and nonwetting relative permeabilities (kkr_{nw}, which is defined in this work as the effective permeability) can be calculated, and the difficulties of producing the entries representative of a gradient in the direction orthogonal to gravity are discussed.

6.2 Domain Development

The production of representative three-dimensional discrete fracture networks is a difficult task, primarily due to the limited availability of data, and the difficulties associated with collecting such data. The synthesis of outcrop mapping, borehole logging/hydraulic testing, and down-hole geophysics can, however, produce reasonably accurate stochastic or combined stochastic/deterministic models of the distribution of fractures in the subsurface. A discrete fracture network can be characterized by the statistical distributions describing all aspects of the network, from the broad classification of fractures into similar sets and the determination of intensity, to distributions describing the orientation of the fracture poles, the areal size of the fractures, and the fracture aperture (e.g., Dershowitz and Miller, 1995b). The two-dimensional fracture network used as the basis for this work was extracted from a numerically generated three-dimensional network based on the properties of various granitic sequences reported in the literature.

The ASPO Hard Rock laboratory in Sweden formed the basis for the majority of the data used in the development of the three-dimensional network. The fracture orientation distribution was simulated with the bootstrap method, based on Uchida et al. (1997). The distribution of fracture radii was also taken from Uchida et al. (1997) and was simulated as lognormal with a mean of 6.85 m and a variance of 6.35 m^2. In order to keep the size of the domain tractable, the intensity $P_{32}$of the fractures within the domain was increased from that reported at the ASPO site, from 0.02 to 1.0, a value consistent with the results of Ehlan (1999) who performed extensive lineament and outcrop analysis of weathered and unweathered granites in Southeast Asia. The selection of statistics covering the aperture distribution within the domain was the least rigorous, as little information is available on the mechanical apertures of fractures at large scales. Consistent with the results of Bianchi (1968), however, a lognormal distribution was chosen, with a mean of 50 μm, and a variance of 25 μm^2. The apertures were assigned to the network on the basis of fracture number, meaning that within a given fracture the apertures were homogeneous and aperture varied from fracture to fracture. The exception to this case occurs at the intersection of two fractures, in which case the aperture of the node representing the intersection is consistently set equal to the larger of the two apertures. This approach will allow for nonwetting phase migrating through a large aperture fracture to cross a smaller aperture fracture without invasion necessarily occurring. Conversely, nonwetting phase migrating along a small aperture fracture will enter an intersecting larger aperture fracture, and not cross the higher aperture fracture until sufficient nonwetting phase saturations have built to overcome the entry pressure of the low aperture fracture (based on the local displacement pressure of the higher aperture fracture).

The three-dimensional fracture network was generated using FRACMAN®, a discrete fracture generator and analysis tool (Dershowitz et al., 1995a), in a cube measuring 250 m per side. The three-dimensional network was sampled by taking a vertical slice 100 m by 100 m, centred in the middle of the cube. This approach ensured that edge effects resulting from the generation procedure were not included. The fractures in the domain were therefore represented by a Planar Straight Line Graph (Figure 6-1), used as input to TRIANGLE (Shewchuk, 1986) which performed a Delaunay triangulation, resulting in a finite element mesh containing triangular elements representing the rock matrix and line elements representing the fracture traces. The discretization was performed such that at least two line elements occurred between each fracture intersection, and between each boundary node and each fracture intersection. The domain contained 1440 fracture traces, which were discretized into 113 516 nodes representing both fracture and matrix, and 22 542 nodes representing the matrix alone. The use of a two-dimensional plane cutting through the three-dimensional network means that the statistics of the three-dimensional field are not necessarily retained. The fracture traces in Figure 6-1 were therefore quantified based on their dips, measured from a horizontal axis in the positive x direction. To give an estimate of the anisotropy of the system, the total length of all traces with dips falling within four brackets was calculated. The total lengths of all traces with dips between 0° and 45°, 45° and 90°, 90° and 135°, and 135° and 180° were 3534 m, 5855 m, 4924 m, and 2867 m respectively. This shows an anisotropy biased towards flow in the vertical direction.

6.3 Model Development and Numerical Approach

6.3.1 Governing Equations

Abriola and Pinder (1985) developed the partial differential equations governing multiphase flow and multicomponent transport in porous media as follows:

$$\frac{\partial}{\partial t}\left(c_{t\beta}\phi S_\beta x_{i\beta}\right)+\nabla\cdot\left(c_{t\beta}x_{i\beta}v_\beta\right)-\nabla\cdot\left[\phi S_\beta D_{i\beta}\nabla\left(c_{t\beta}x_{i\beta}\right)\right]-q_{i\beta}-I_{i\beta}=0 \qquad [6\text{-}1]$$
$$\beta=1..n_p, i=1..n_c$$

where $c_{t\beta}$ is the molar density of phase β, ϕ is the porosity of the medium, S_β is the saturation of phase β expressed as a fraction of void space, $x_{i\beta}$ is the mole fraction of component i in phase β, v_β is the Darcy flux of phase β, $D_{i\beta}$ is the dispersion tensor for component i in phase β, $q_{i\beta}$ is a source or sink of component i to or from phase β, and $I_{i\beta}$ is the interphase mass transfer of component i to or from phase β.

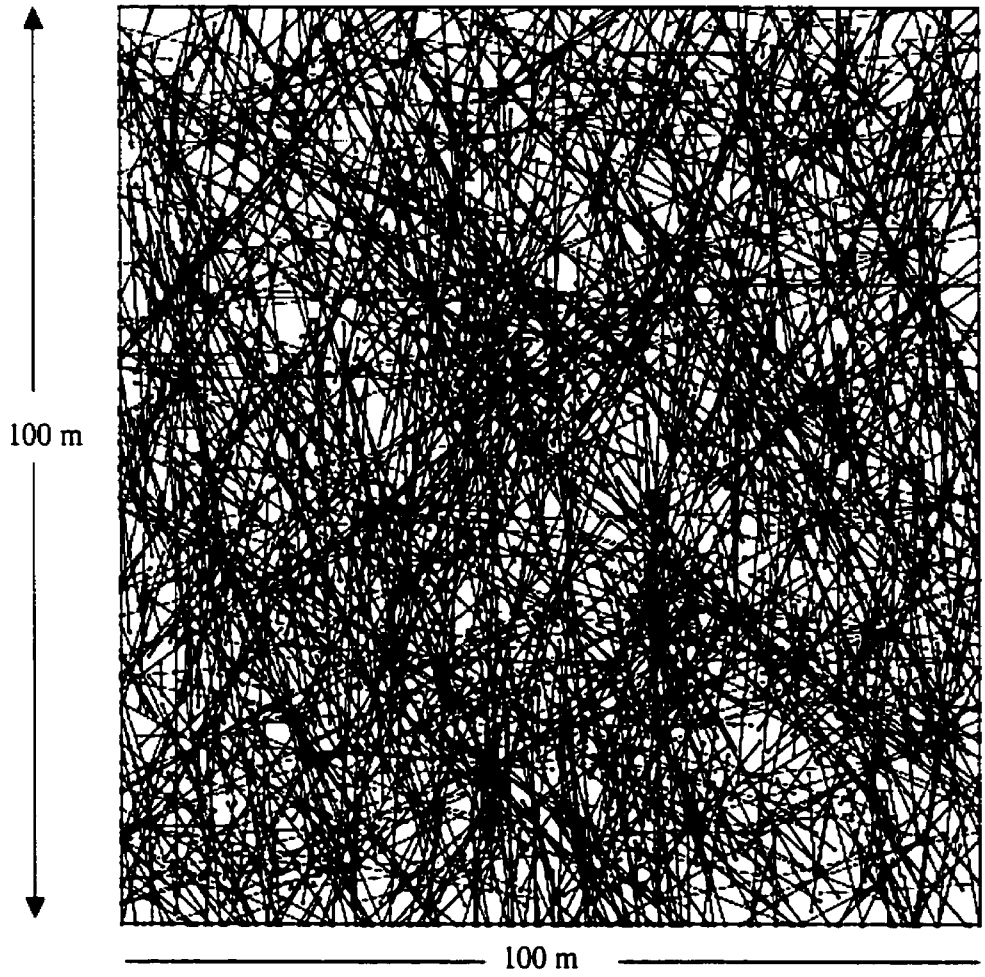

Figure 6-1. Fracture Network in Simulation Domain (Extracted from 3-D Network)

The governing equations described above were discretized through the use of the Control Volume Finite Element method (CVFE) of Forsyth (1991), through the use of overlapping continua representing the fractures and the matrix:

$$R_{i,I}^{\beta} \equiv \left\{\left[\phi c_{i\beta} x_{i\beta} + \rho_b K_d c_{i\beta} x_{i\beta}\right]_I^{N+1} - \left[\phi c_{i\beta} x_{i\beta} + \rho_b K_d c_{i\beta} x_{i\beta}\right]_I^{N}\right\}_m \frac{V_{I_m}}{\Delta t}$$

$$+ \left\{\left[\phi S_\beta c_{i\beta} x_{i\beta} + \rho_b K_d c_{i\beta} x_{i\beta}\right]_I^{N+1} - \left[\phi S_\beta c_{i\beta} x_{i\beta} + \rho_b K_d c_{i\beta} x_{i\beta}\right]_I^{N}\right\}_f \frac{V_{I_f}}{\Delta t}$$

$$- \left[\sum_{J \in n_{c_m}} \left(\psi_{\beta J}^{N+1} - \psi_{\beta I}^{N+1}\right) \left(\frac{c_{i\beta} x_{i\beta}}{\mu_\beta}\right)_{ups(I,J)}^{N+1} \gamma_{IJ_m}\right]$$

$$- \left[\sum_{J \in n_{c_f}} \left(\psi_{\beta J}^{N+1} - \psi_{\beta I}^{N+1}\right) \left(c_{i\beta} x_{i\beta} \frac{k_{r\beta}}{\mu_\beta}\right)_{ups(I,J)}^{N+1} \gamma_{IJ_f}\right]$$

$$- \left[\sum_{J \in n_{c_m}} \left(c_{i\beta}\right)_{IJ+1/2}^{N+1} \left(\gamma'_{IJ_m}\right)_\beta \left(x_{i\beta_J} - x_{i\beta_I}\right)^{N+1}\right]$$

$$- \left[\sum_{J \in n_{c_f}} \left(c_{i\beta}\right)_{IJ+1/2}^{N+1} \left(\gamma'_{IJ_f}\right)_\beta \left(x_{i\beta_J} - x_{i\beta_I}\right)^{N+1}\right]$$

$$- \left\{q_{i\beta} - I_{i\beta}\right\}^{N+1} V_I = 0$$

[6-2]

where ρ_b is the dry bulk density of the medium, K_d is the distribution coefficient, V_I is the elemental volume, μ is the dynamic viscosity, γ_{IJ} is the cross-sectional area available for flux divided by the distance between nodes and multiplied by the permeability, ψ is the fluid potential, and γ'_{ij} is the cross-sectional area available for flux divided by the distance between the nodes and multiplied by a dispersion term. The subscripts *f* and *m* refer to the contributions of the fractures and matrix, respectively. Equation [6-2] was solved in a fully implicit manner utilizing wetting phase pressure and wetting phase saturation as dependent variables, with full Newton-Raphson iteration. The model was verified against the analytical solution of McWhorter and Sunada (1990) for one-dimensional two-phase flow in the absence of mass transfer. Nodes representing the fractures were always co-incident with nodes representing the matrix, ensuring continuity of wetting phase pressures between the two continua.

Equation set [6-2] is closed by assuming the phase saturations and the mole fractions of each component comprising a phase both sum to unity. The model employs the constitutive relationships of Brooks and Corey (1964) relating capillary pressure, saturation, and relative permeability, with the modifications proposed by Gerhard et al. (1998) to simulate hysteresis. The use of Brooks-Corey functions to represent two-phase flow in fractures is supported by the work of Reitsma and Kueper (1994). The effects of mass transfer from the nonwetting to the wetting phase were not included in this study.

6.3.2 Large-scale Capillary Pressure and Relative Permeability

The definition of large-scale capillary pressure can take various forms, depending on the process being considered. Kueper and McWhorter (1992) define the macroscopic capillary pressure in a heterogeneous medium as:

$$\overline{P}_c = \frac{1}{V_{nw}} \int_{V_{nw}} P_{nw} dV_{nw} - \frac{1}{V_w} \int_{V_w} P_w dV_w \qquad [6\text{-}3]$$

where $\overline{P}_c$ is the macroscopic average capillary pressure, V_{nw} is the total volume of nonwetting fluid in the region, P_{nw} is the local-scale nonwetting phase pressure, V_w is the total volume of wetting fluid in the region, and P_w the local-scale wetting phase pressure. The macroscopic wetting phase saturation, $\overline{S}_w$, corresponding to this capillary pressure is given by:

$$\overline{S}_w = \frac{\int V_w dV}{V \int \phi \, dV} \qquad [6\text{-}4]$$

where ϕ is the local-scale porosity and V the total volume of the region of interest. In this formulation, negative large-scale capillary pressure may result when small percentages of the volume are invaded by the nonwetting phase.

Ataie-Ashtiani et al. (2001) presented large-scale capillary pressure-saturation curves in terms of the applied boundary capillary pressure (thus not incorporating the capillary pressures within the domain) and an arithmetic average of the nodal wetting phase saturations. Desbarats (1995) used volume averaging to define large-scale water saturations and porosities, with the incorporation of a characteristic pore length defined by the ratio of intrinsic permeability to porosity.

Four approaches for the calculation of the large-scale capillary pressures are calculated in this work. The first utilizes the method presented in [6-3]. The second considers a volume averaged capillary pressure of the invaded nodes (inv) only:

$$\overline{P}_c = \frac{1}{V_{inv}} \int_{Vinv} P_c dV_{inv} \qquad [6\text{-}5]$$

where P_c is the local capillary pressure, and V_{inv} is the volume of the domain containing two fluids. The third method considers a volume average of all nodes, where un-invaded nodes (*univ*) are assigned a capillary pressure equal to their local-scale displacement pressure:

$$\overline{P}_c = \frac{1}{V_{inv}} \int_{V_{inv}} P_{c_i} dV_{inv} + \frac{1}{V_{univ}} \int_{V_{univ}} P_{di} dV_{univ} \qquad [6\text{-}6]$$

where P_{di} is the local displacement pressure. The fourth method utilizes the volume average of all nodes, where un-invaded nodes are assigned the applied boundary capillary pressure:

$$\overline{P}_c = \frac{1}{V_{inv}} \int_{V_{inv}} P_{c_i} dV_{inv} + \frac{1}{V_{univ}} \int_{V_{univ}} P_c^b dV_{univ} \qquad [6\text{-}7]$$

where P_c^b is equal to the applied boundary capillary pressure.

Figure 6-2 presents three formulations of the large-scale capillary pressure curves for the domain described in section 6.2. The curves for the method presented in [6-3] are not included, as they produced negative values. The shifting of the curve produced by including only the nodes invaded by the nonwetting phase towards higher nonwetting phase saturations is simply a result of its definition (as the effects of areas where the nonwetting saturation is equal to zero are not considered). Similarly, the higher capillary pressures exhibited at intermediate wetting phase saturations through the utilization of [6-6] (as compared to calculations based on [6-7]), are due to the inclusion of the displacement pressures of un-invaded nodes, which are necessarily greater than the applied boundary pressure. The boundary pressure approach was adopted for the remaining simulations in this work, as it represents behaviour between the other two approaches.

The calculation of the large-scale constitutive relationships relating the nonwetting phase permeability of the system to the average wetting phase saturation are arrived at through application of the two-phase formulation of Darcy's Law for the nonwetting phase:

$$\overline{q}_{i,nw} = \frac{-k_{ij}k_{rnw}}{\mu_{nw}}\left(\frac{\partial P_c}{\partial x_j} + \frac{\partial P_w}{\partial x_j} + \rho_{nw} g \frac{\partial z}{\partial x_j}\right); \qquad i, j = x, z \qquad [6\text{-}8]$$

where $\overline{q}_{i,nw}$ is the large-scale flux of the nonwetting phase, k_{ij} is the large-scale intrinsic permeability tensor, kr_{nw} is the large-scale relative permeability of the nonwetting phase, μ_{nw} is the viscosity of the nonwetting phase, ρ_{nw} is the density of the nonwetting phase, and z is the elevation above the datum. If the steady-state volumetric fluxes through the boundaries are recorded from the numerical model, and the large-scale gradients are known, the elements of the

effective permeability (kkr_{nw}) tensor can be calculated. The off-diagonal terms of the effective permeability tensor are posed such that the flow through both boundaries perpendicular to the gradient are additive.

6.3.3 Representative Elementary Volumes

Implicit in the formulations presented for the calculation of the large-scale capillary pressure and effective permeability relationships is that the volume considered is large enough such that small changes in its value do not have a significant effect on $\overline{P}_c$ and $\overline{S}_w$. This requires that the volume of interest be considered as a representative elementary volume (REV), with the physical meaning that the averaging process has encompassed enough fractures such that increases in the size of the domain do not affect the macro-scale parameter of interest. Neuman (1990) proposed that, as opposed to an REV, fractured rock be treated as multiscale stochastic continua for single-phase flow and transport. Margolin et al. (1998) performed a percolation study on three-dimensional networks of fractures and found that the macroscopic permeability became invariant with scale above a block size of approximately 100 m. It is felt that given the relative density (P_{21}) of conducting fractures within our domain, and he fact that the fracture generation process is stationary, an REV that is small enough in size to be numerically tractable is attainable.

One method of determining the existence of an REV is to examine the fracture network statistics versus domain size. Figure 6-3 presents the average fracture length, average fracture aperture, and the trace-plane fracture density (P_{21}) which is defined as the length of fracture traces divided by the cross-sectional area of the domain. The variation in all three statistical descriptions is

decreasing with domain size, and approaches constant behaviour after a domain size of approximately 60 m to70 m. The relatively small variation in P_{21} is due to the nature of the fracture generation process, which is formulated such that the density of the fractures are the controlling statistic, whereas the length and apertures are "randomly" assigned.

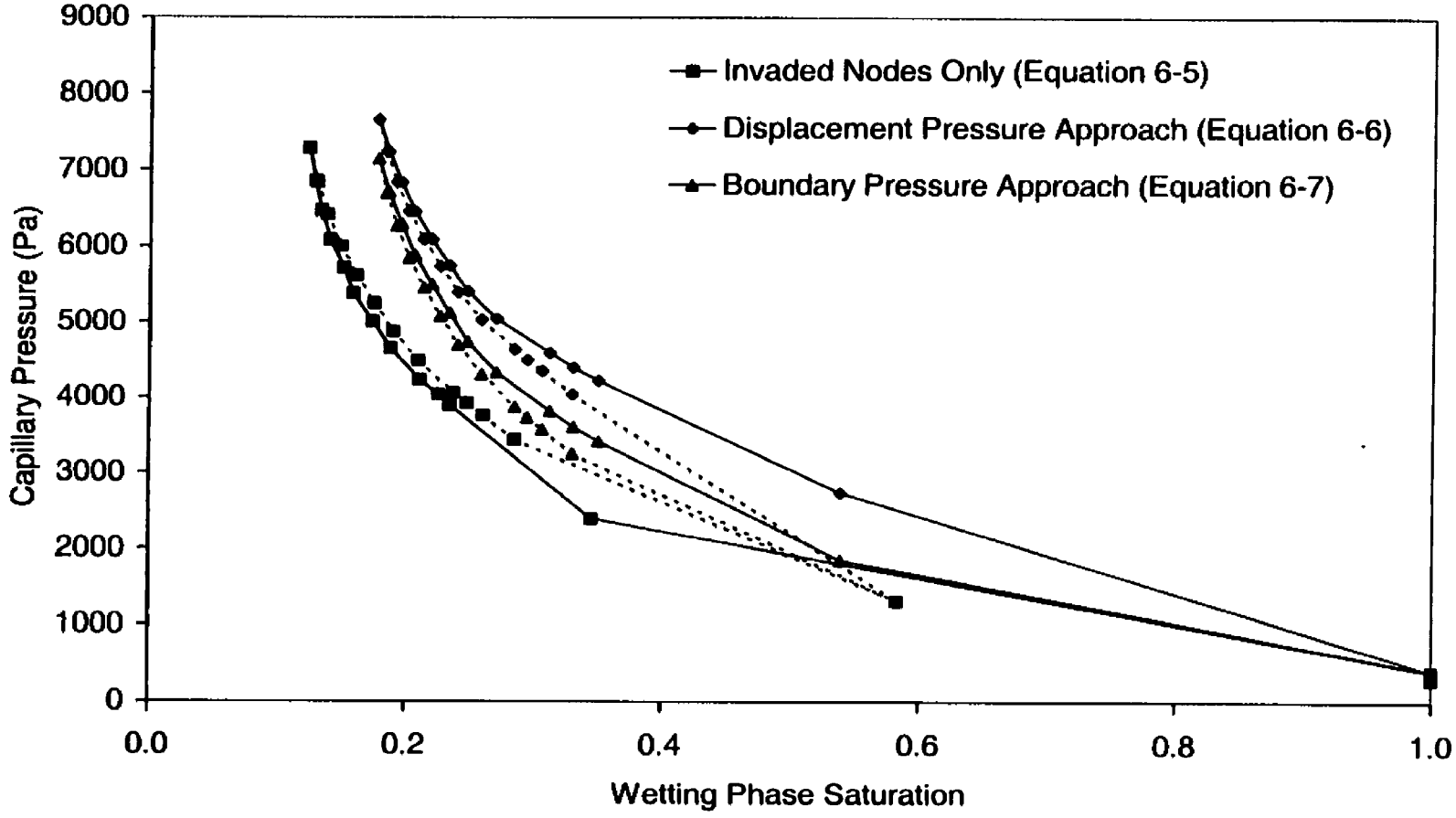

Figure 6-2. Alternate Approaches to the Calculation of Large-scale Capillary Pressure Curves

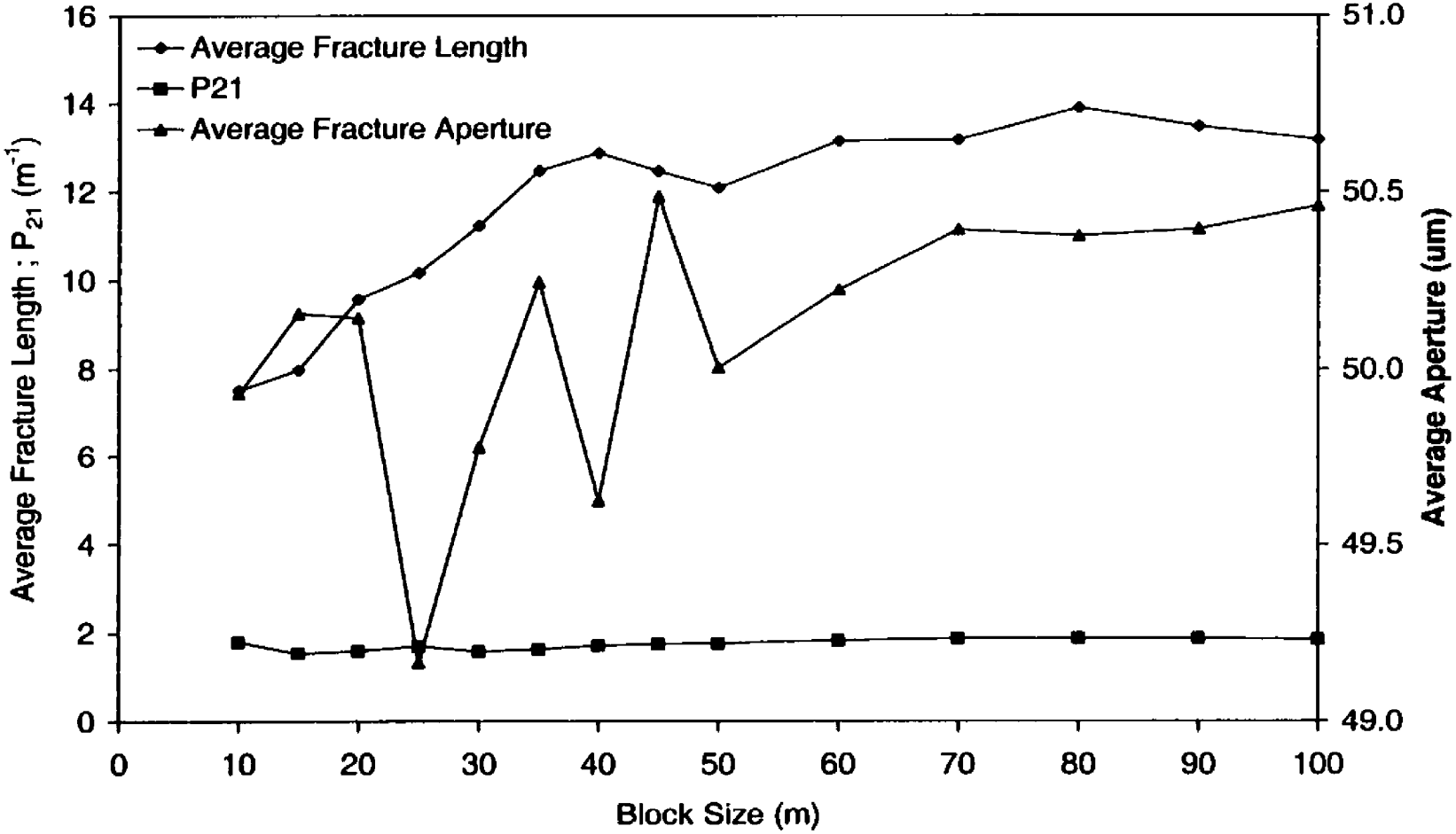

Figure 6-3. Average fracture Length, Aperture, and P21 (length of trace divide by Area of Domain) vs. Block Size

The generated fracture network was also tested for REV behaviour by examining the single phase hydraulic conductivity in both the x and z directions, and the average capillary pressure within the domain given the boundary condition approach represented by [6-7]. The investigation of the existence of an REV was deterministic, accomplished by performing single and multiphase flow simulations on subsets of the 100 m by 100 m domain. Concentric "squares" aligned on the Cartesian centre of the large domain were extracted, starting at 5 m by 5 m in size and increasing until the entire domain was tested. The boundary conditions for the hydraulic conductivity evaluation consisted of applying a hydraulic gradient of 0.1 across the domain, and setting the opposing sides to a no-flow condition. This was carried out in both directions to yield the large-scale hydraulic conductivity in both the x and z directions. Darcy's Law was used to back-calculate the large-scale hydraulic conductivity of the fracture network given the calculated steady-state boundary fluxes and the imposed large-scale hydraulic gradient. Figure 6-4 presents the results of the hydraulic REV analysis, and it can be seen that the behaviour begins to become independent of size after approximately 50 m in both the x and z directions. The general anisotropy of permeability in the fracture network, imparted by the larger density of sub-vertical fractures, is captured in this analysis.

The determination of an REV for capillary pressure was more computationally demanding, given the extra difficulties inherent in the simulation of multiphase flow. A boundary capillary pressure of 1000 Pa was applied to all sides of the sub-domains extracted for the hydraulic conductivity REV determination, resulting in a vertical gradient driving flow. The wetting phase pressures on the boundary were hydrostatic. The simulations were allowed to run until a steady-state condition for flow in/out of the domain was reached. The nonwetting phase was assigned a

density of 1460 kg/m^3, a viscosity of 5.0×10^{-4} Pa s, and an interfacial tension of 20 dynes/cm. Figure 6-5 presents the results of this analysis, and it can be seen that the REV found in the hydraulic case is also satisfactory for the determination of the macroscopic capillary pressure and saturation. Given the similarities in the length scales of the REVs for hydraulic conductivity and macroscopic capillary pressure, a block size of 50 m was selected for the remainder of this study. The PSLG depicted in Figure 6-1 represents a very well fractured rock mass, and accounts for all fractures present regardless of their ability to transmit fluid.

6.3.4 Boundary Conditions

The selection of boundary conditions for the simulations was critical, as the stresses applied to the system were required to be consistent with the goal of producing an effective permeability tensor relation, as opposed to two scalar representations based on direction. This issue is of significant importance, as the boundary conditions will influence the outcome of the simulations. Several options exist for the specification of the boundary conditions, including sequences (e.g., White and Horn, 1987), and periodicity (e.g., Durlofsky, 1991). The specification of periodicity is numerically attractive, as it guarantees a symmetric, positive definite scaled permeability tensor (Durlofsky, 1991). The work to date incorporating periodic boundary conditions (which entails the specification of correspondences between boundary pressures and fluxes, as opposed to specification of boundary values) has been focused on the production of homogenized relative permeability curves, not large-scale capillary pressure curves. Kueper and McWhorter (1992) successfully applied the sequence approach in the production of large-scale capillary pressure curves through percolation theory.

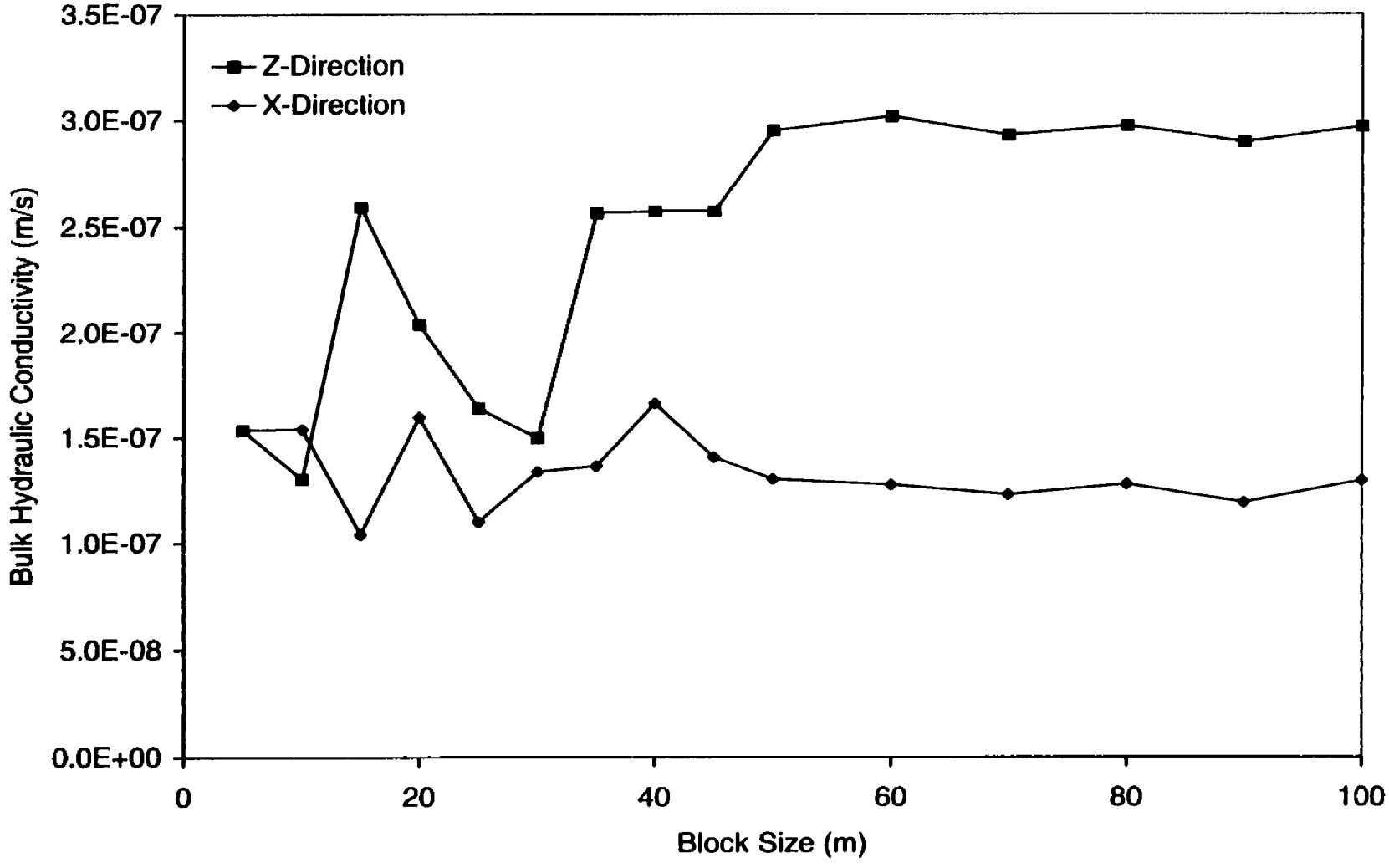

Figure 6-4. Average Hydraulic Conductivity vs. Block Size for 2-D Cross-section

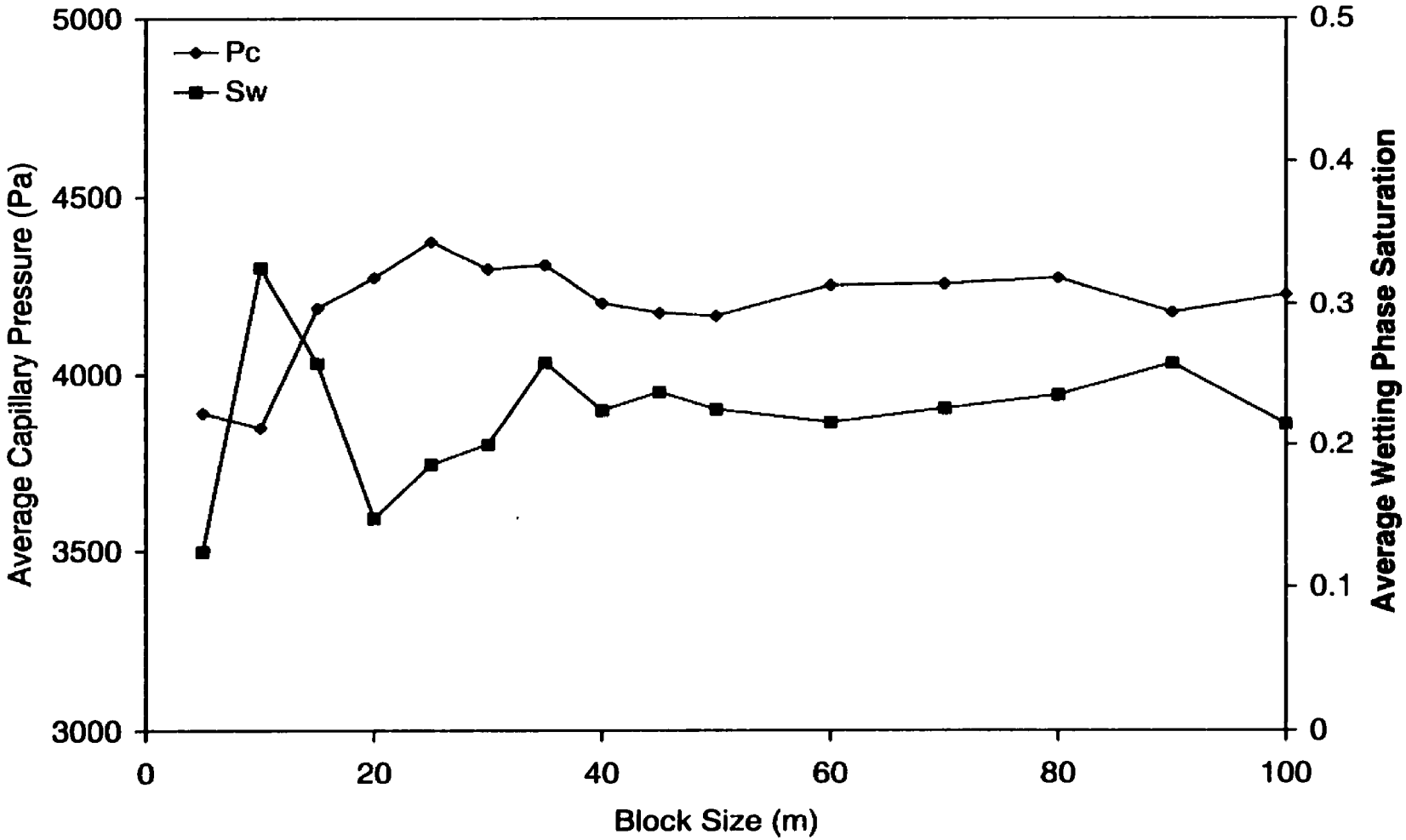

Figure 6-5. Average Capillary Pressure and Wetting Phase Saturation for 2-D Cross-section vs. Block Size

Considering the two-dimensional, two-phase formulation of Darcy's Law for the nonwetting phase [6-8], if a constant capillary pressure boundary condition is applied to all four exterior edges of the domain, and the wetting phase pressure distribution is set to hydrostatic, then only the gravity term in [6-8] acts as a large-scale driving force vertically across the domain. This allows for straightforward determination of the entries in the right column of the tensor:

$$kk_{r,nw_{ij}} = \begin{bmatrix} kk_{r,nw_{xx}} & kk_{r,nw_{xz}} \\ kk_{r,nw_{zx}} & kk_{r,nw_{zz}} \end{bmatrix} \qquad [6\text{-}9]$$

Determination of the two entries in the tensor representing flow due to a large-scale gradient applied in the x (or horizontal) direction (left column) requires that simulation be performed without the incorporation of a large-scale gravity gradient ($\rho g\, \partial z/\partial x_j$) in the direction of large-scale flow. As discussed previously, calculation of the left-hand column in [6-9] is beyond the scope of the current study.

For flow in the vertical direction, it is not intuitive that the $\partial P_c/\partial z$, $\partial P_w/\partial z$, and $\rho_{nw} g\, \partial z/\partial z$ terms can be assigned arbitrary values to arrive at a specified total pressure gradient across the domain. In an effort to assess this, three simulations were performed in the 50 m square domain. The first simulation was conducted with the large-scale vertical gradient generated only as a result of the gravity term (i.e. large-scale $\partial P_w/\partial z$ and $\partial P_c/\partial z$ equal to zero). The second simulation was conducted with a less dense nonwetting liquid, resulting in a lower gravity driving force. In order to produce the same large-scale total driving force as in the first simulation, the large-scale wetting phase pressure gradient was increased to offset the loss of gradient due to the reduced density. Given the two densities used in this test (1460 kg/m^3 and 1100 kg/m^3), the total required increase in wetting phase gradient was 3530.16 Pa/m. This was applied between the top and

bottom boundaries of the domain. The constant wetting phase pressures along the vertical sides of the domain were also adjusted to exactly replicate the nonwetting phase potentials between the different gradient formulations everywhere on the boundaries. The third simulation was identical to the first, with the exception that a lower density nonwetting phase was employed, resulting in a lower large-scale vertical driving force.

Figure 6-6 presents the main drainage and main wetting limbs of the large-scale capillary pressure curves generated from the three simulations. These curves were created by starting with an initially wetting fluid saturated domain, and increasing the macroscopic capillary pressure (along the boundaries) in small (<500 Pa) increments to a maximum of 5,000 Pa. At that point, the boundary capillary pressure was incrementally reduced to create a wetting curve (dotted line). The effects of manipulating the density and wetting phase gradient to match the gravity driven case are evident, with a shifting of the macroscopic curve to higher nonwetting phase saturations and lower capillary pressures. The third curve, which represents the case where the wetting phase gradient is not altered to match the gravity driven case is similar to the altered wetting phase gradient case, implying that the density of the nonwetting phase may be the controlling factor in these systems. The results of this analysis indicate that the large-scale $P_c(S_w)$ relationship is not simply a function of the total gradient applied across the system, but is dependent on fluid density.

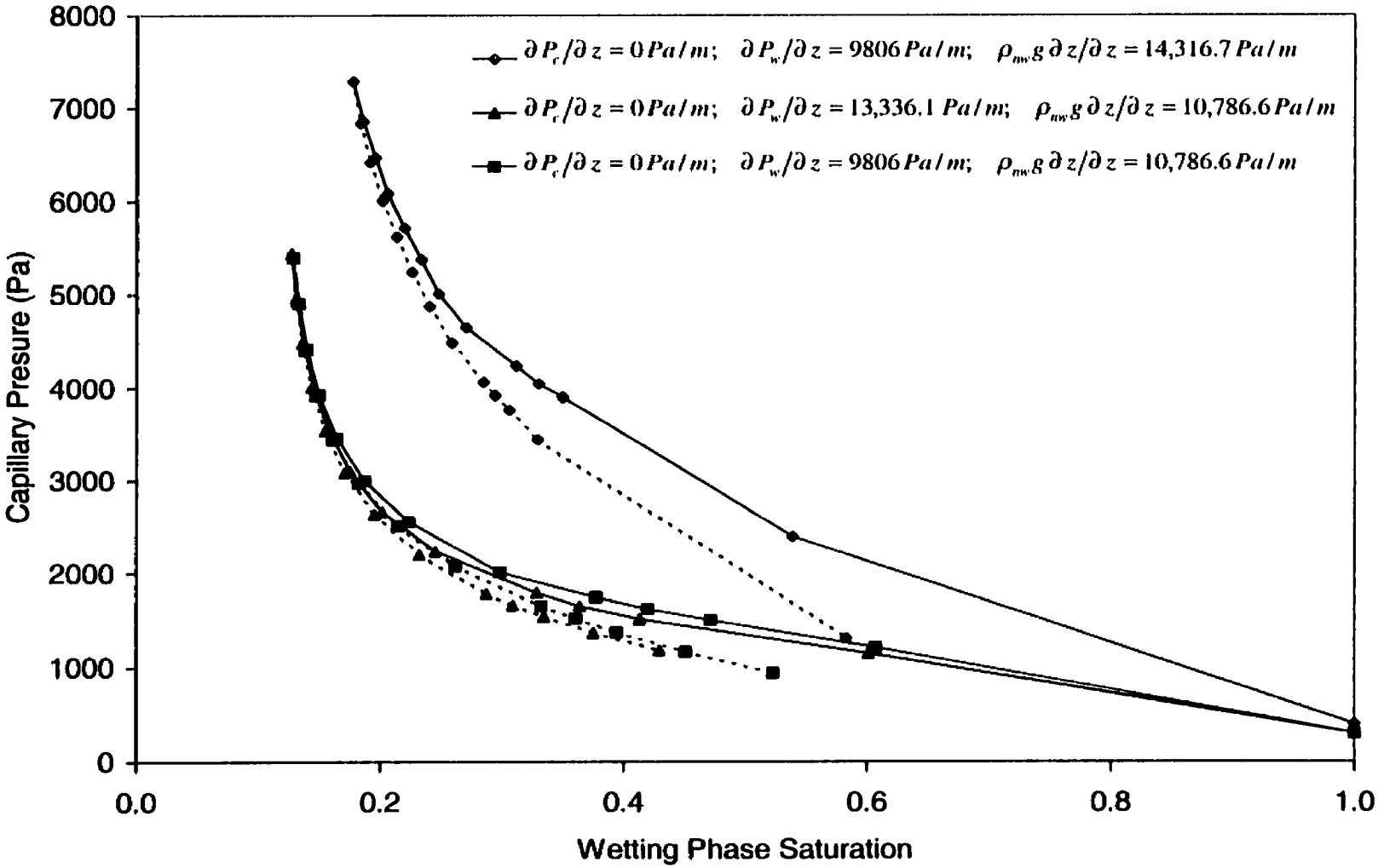

Figure 6-6. Large-scale Capillary Pressure Curves for Different Boundary Condition Formulations

Figures 6-7 through 6-9 present the three components of the total gradient (capillary pressure, wetting phase pressure, and gravity) on a local-scale basis. The vertical component of each of the three total gradient components in each linear fracture element for each of the simulations was calculated and plotted as histograms. Close examination of the local-scale gradient behaviours shows that each of the gradients translates to a more positive state with the application of the lower density, increased wetting phase pressure boundary condition. Of particular interest is the change in the distribution of the wetting phase gradients. The implementation of the gradient requires that the wetting phase is no longer in a hydrostatic condition, and results in flow through the system. The resulting energy losses in the flowing system disperse the distribution of local-scale wetting phase gradients from the uniform distribution of the static case (Figure 6-8). This is mimicked in the distribution of capillary gradients (Figure 6-7). The overall effects of the change in wetting phase pressure gradients is not significant, however, as evidenced by the similarities in the large-scale curves between the reduced density and equal total gradient simulations (Figure 6-6).

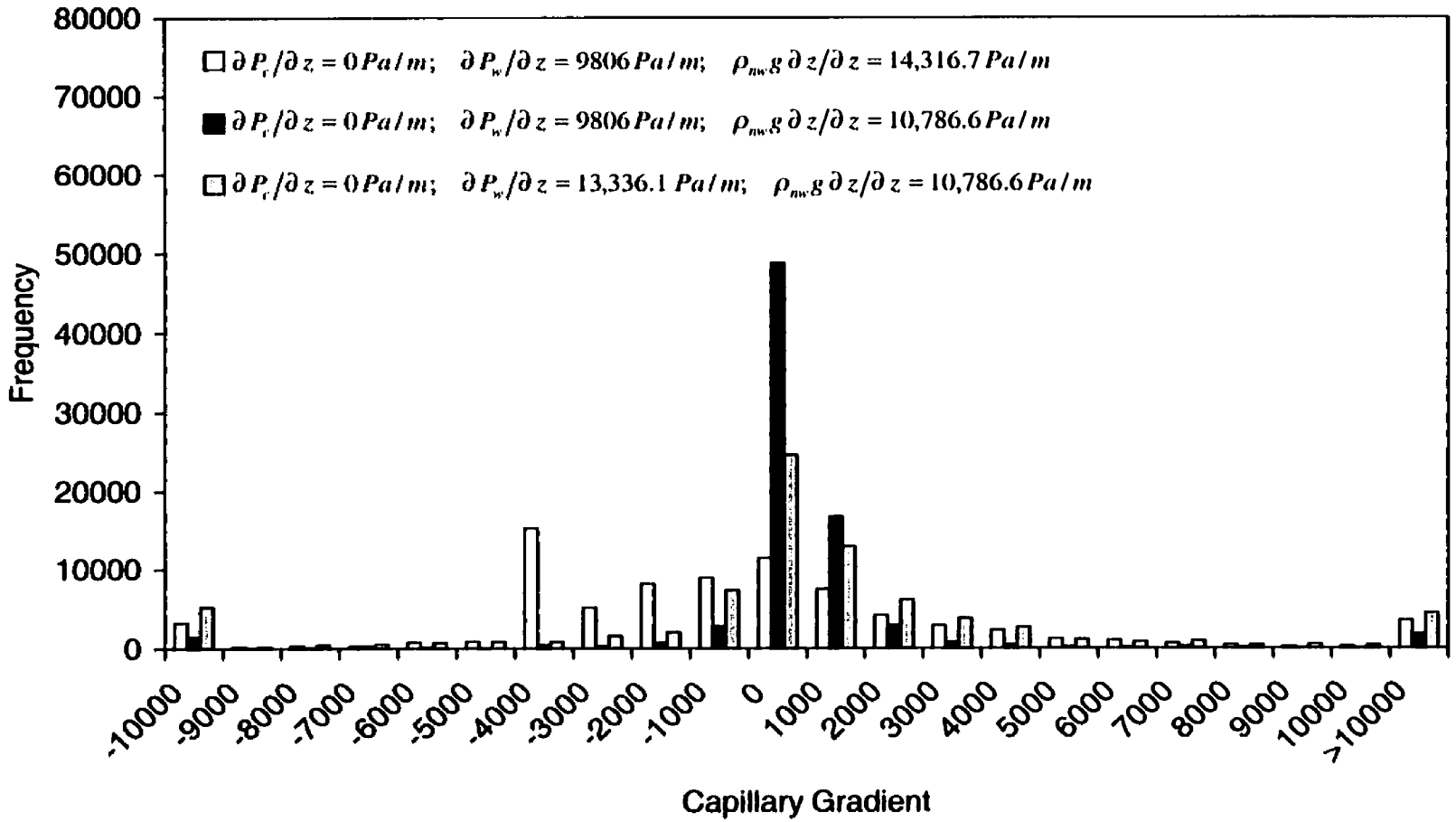

Figure 6-7. Distribution of Capillary Gradients Between Alternate Boundary Condition Formulations. The Frequency Represents Nodal Values from Fractures Only (not Matrix)

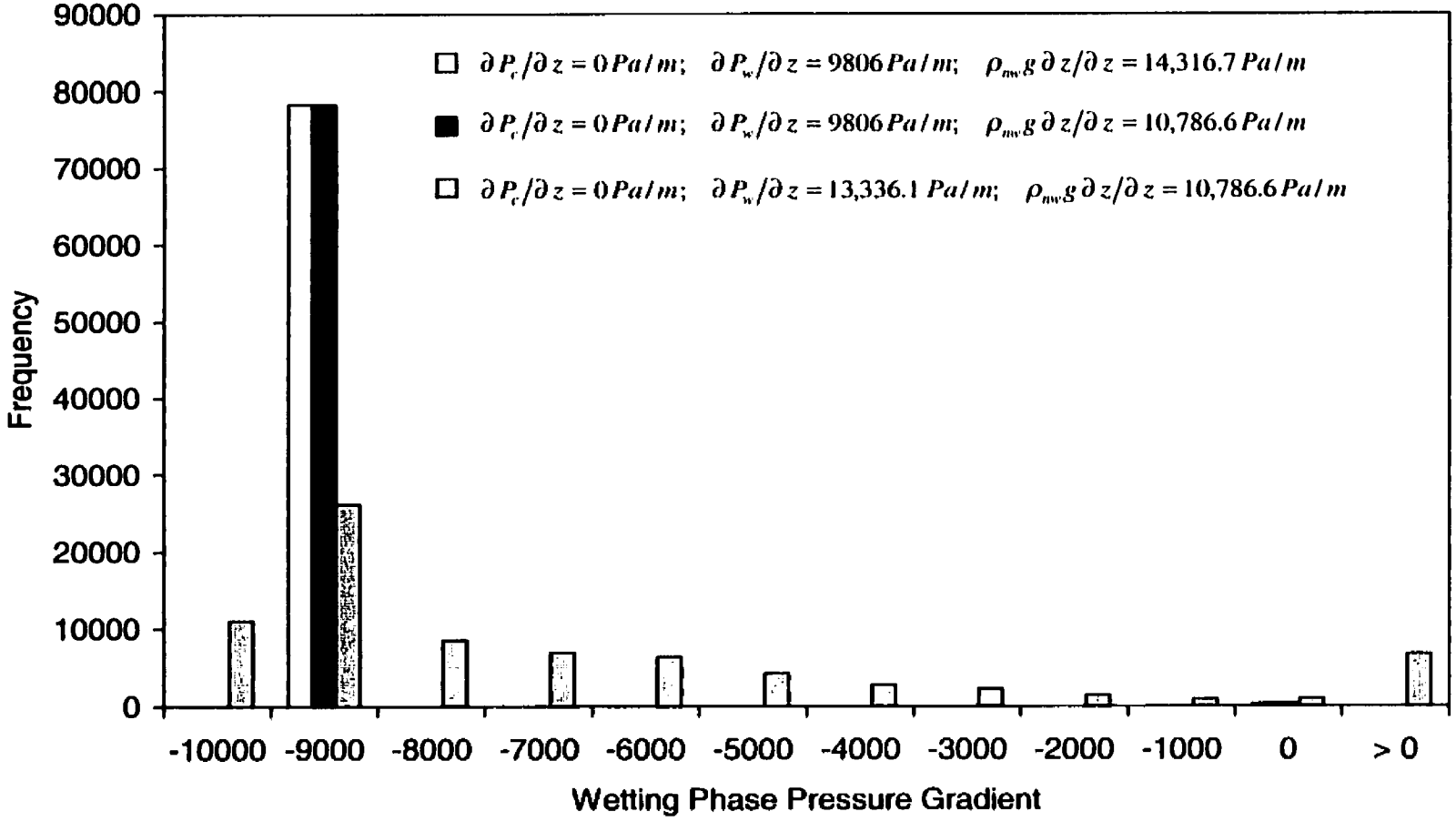

Figure 6-8. Distribution of Wetting Phase Gradients Between Alternate Boundary Condition Formulations. The Frequency Represents Nodal Values from Fractures Only (not Matrix)

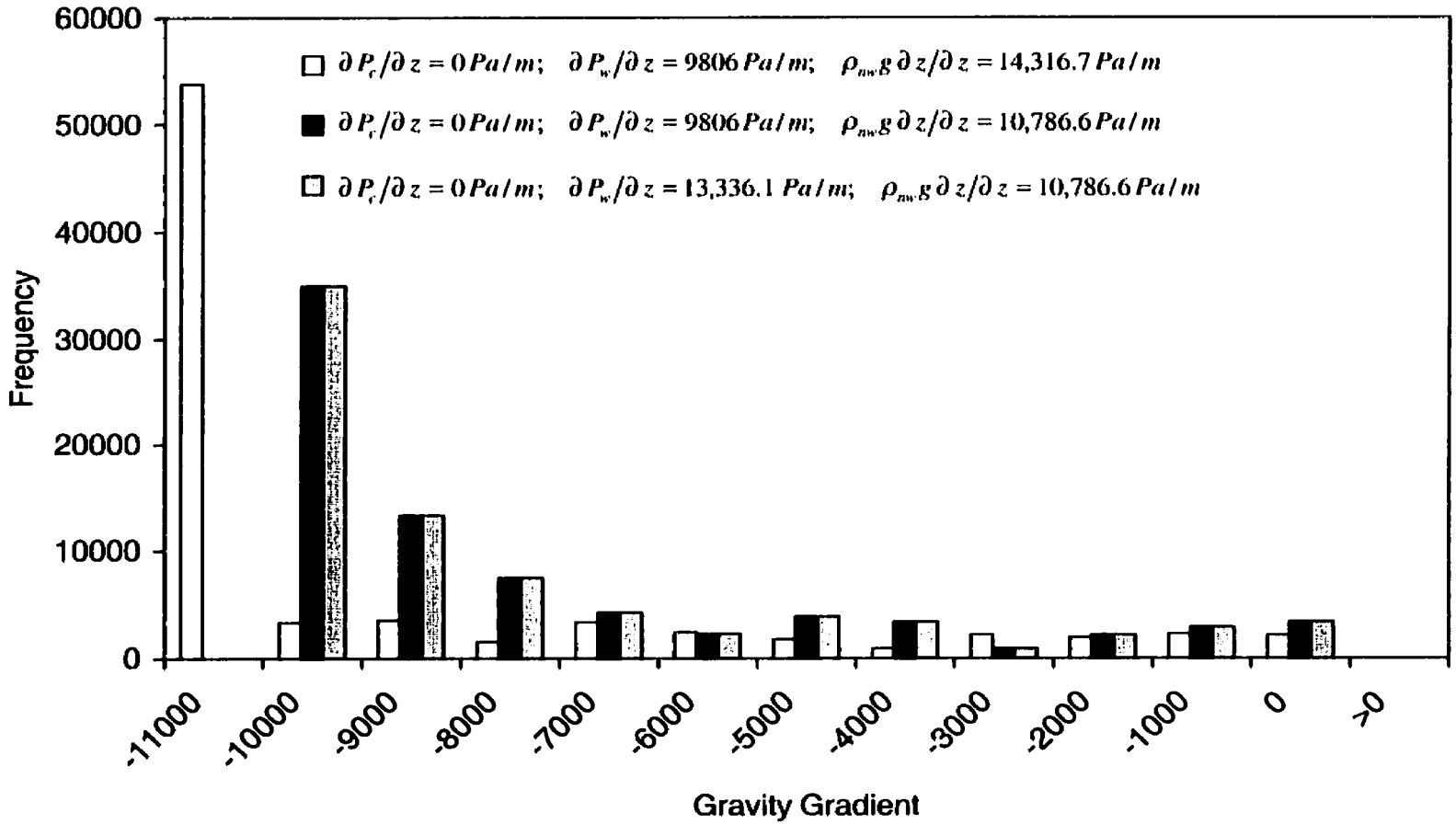

Figure 6-9. Distribution of Gravity Gradients Between Alternate Boundary Condition Formulations. The Frequency Represents Nodal Values from Fractures Only (not Matrix)

The local-scale gradient distributions of the density and wetting phase pressure (Figures 6-9 and 6-8) globally shift to match the changes at the boundaries (shift to a more positive average). Given this behaviour, the local-scale capillary gradients should remain unchanged if the large-scale capillary pressure curves remained unchanged. Given the observed changes in the large-scale capillary pressure curves, it is therefore not surprising that the local-scale capillary behaviour is dramatically different between the simulations. The drastic shift in capillary behaviour exhibited at the local-scale between the base and reduced density simulations is indicative of the density dependent behaviour discussed earlier. There is less of a force driving the nonwetting phase through the system, therefore nonwetting phase saturations increase at low permeability features. The shift in local-scale capillary behaviour between the reduced density and equal total gradient simulations is significantly less, resulting in similar behaviour. Work is currently on-going to develop the appropriate methodologies which will allow for a determination of all the elements of the effective permeability tensor.

6.4 Results and Discussion

Table 6-1 lists the parameters used in the production of each of the 11 large-scale relationships discussed in this study. The base case scenario for the simulations consisted of the 50 m by 50 m section arrived at through the REV study discussed in 6.3.3. The pattern of fractures within the domain was not varied, as it was produced from a three-dimensional network generated with a given set of statistics. The average length of the fractures in the domain is 12.1 m, and the fracture intensity on the trace plane is 3.21 m^{-1}. The nonwetting phase density was 1460 kg/m^3, the nonwetting phase viscosity was $5.0x10^{-4}$ Pa s, and the interfacial tension was 0.02 N/m.

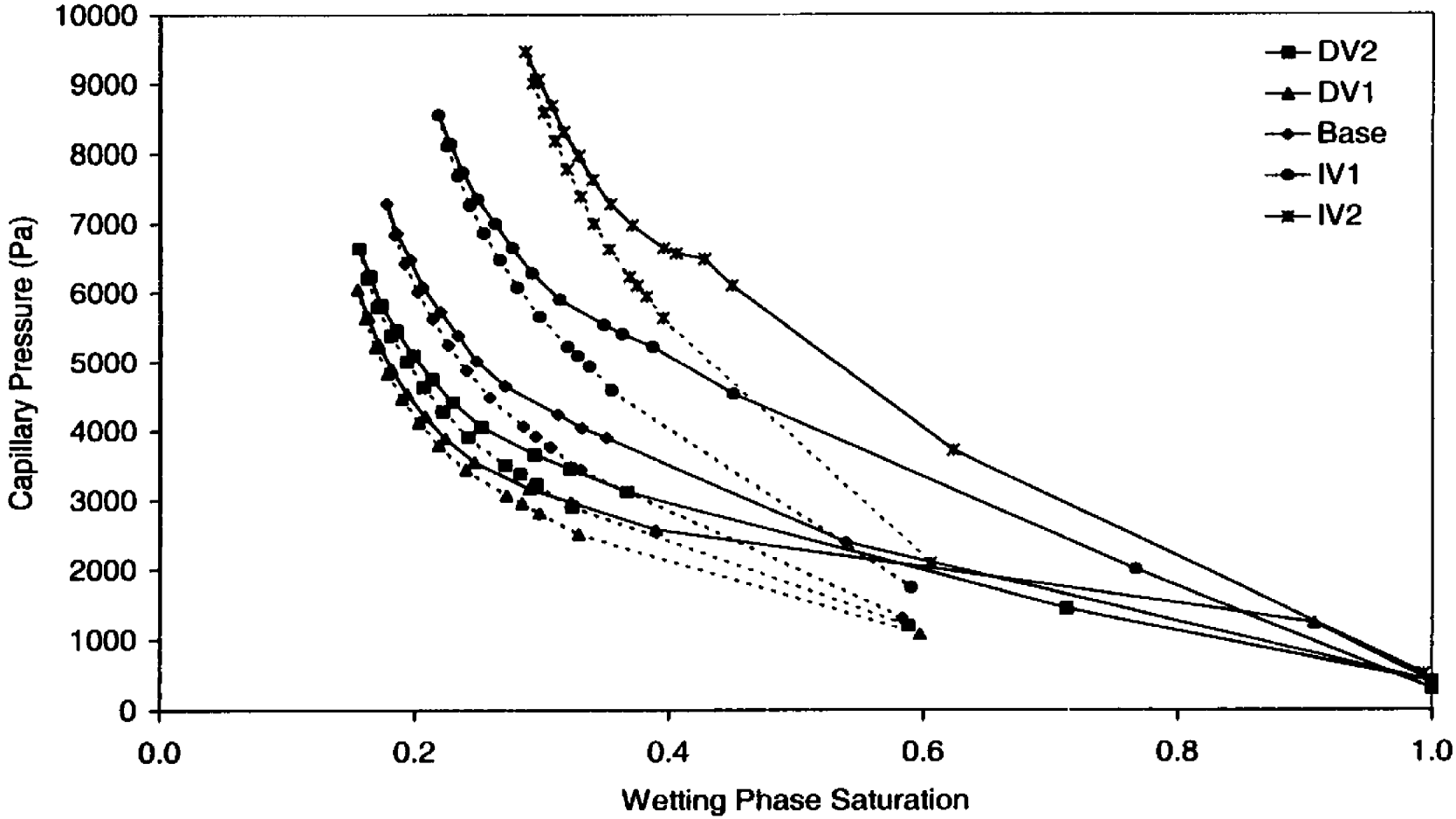

Figure 6-10. Sensitivity of Large-scale Capillary Pressure Curves to a Variance in Aperture

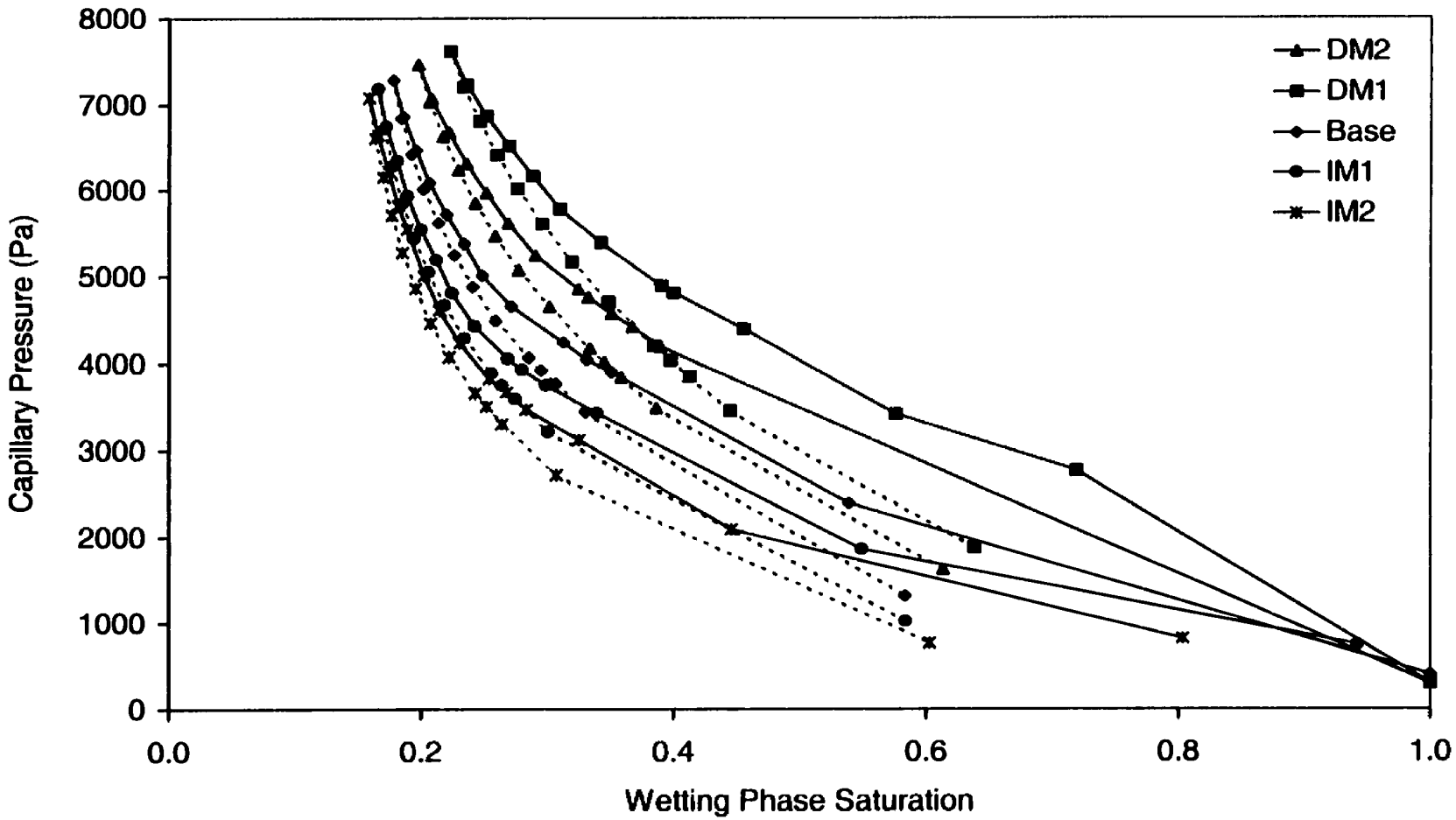

Figure 6-11. Sensitivity of Large-scale Capillary Pressure Curves to Aperture Mean

6.4.1 Large-Scale Capillary Pressure Behaviour

The results presented in Figure 6-10 illustrate the sensitivity of the large-scale capillary pressure curves to the variance of the lognormal aperture distribution amongst the fractures. A reduction in the variance of the aperture distribution results in a shallower slope of the curve, analogous to a porous media scenario where the grain size distribution is less heterogeneous. Similar behaviour is seen in the simulations representative of an increase in the variance of the lognormal aperture distribution where the slope of the curves increases with increasing variance. These results are markedly similar to those presented by Ferrand and Celia (1992), Kueper and McWhorter (1992), and Girgrah (1994) for macroscopic behaviour in correlated and uncorrelated random permeability fields. It is important to point out that the distributions are not exactly scaled at the smallest apertures. For the case where the variance of the aperture distribution was increased to 40 μm, some apertures became negative, and in these cases the apertures were arbitrarily set equal to 1 μm. This procedure did not affect the results, as these fractures were not invaded at any of the applied boundary capillary pressures.

The curve representative of the largest variance in aperture also displays the lowest entry pressure, indicative of the first entrance into the network. This occurred at a boundary capillary pressure of 300 Pa (as opposed to greater than 500 Pa for all other simulations) due to the appearance of a high permeability feature intersecting a boundary. The definition of the entry pressure for this domain tends to be sharper than that of a porous medium, given that less than 1000 fractures intersect the boundary, and the lateral extensiveness of the fractures tends to blur the difference between entry and displacement pressure.

Table 6-1. Parameters Used in the Production of Large-scale Curves[1]

Simulation	Mean Aperture (μm)	Variance of Aperture (μm^2)	Termination Percentage
Base	50	25	0
DM1	**25**	25	0
DM2	**33**	25	0
IM1	**75**	25	0
IM2	**100**	25	0
DV1	50	**10**	0
DV2	50	**15**	0
IV1	50	**30**	0
IV2	50	**40**	0
IT1	50	25	**50**
IT2	50	25	**100**

1 – Nonwetting phase density = 1460 kg/m^3, IFT = 0.02 N/m, Pore Size Distribution Index = 2.5, Nonwetting phase viscosity = 5.0×10^{-4} Pa s

It is also of interest to note that the performance of the chosen block size, in regards to being an REV, is satisfactory (as indicated by the smoothness of curves) for all cases with the exception of the curve representing the largest variance in the lognormal aperture field. The inflection point in the drainage curve corresponding to a wetting phase saturation of 0.43 is indicative of a significant increase in the volume of the domain invaded, an increase which is significantly more abrupt than at any other incremental increase in any of the lower variance simulations. This is an

indication that the REV for capillary behaviour is likely a function of the statistics describing the local-scale aperture distribution.

A comparison of the differences in capillary pressure at a given wetting phase saturation between the drainage and wetting limbs of the large-scale curves, shows the effects of trapping of the nonwetting fluid as the variance in the aperture distribution increases. The distribution of local-scale nonwetting saturations at residual is also correlated to the aperture distribution, resulting in more trapped nonwetting phase at a given capillary pressure with increasing variance in the aperture distribution.

The sensitivity of the large-scale capillary curves to changes in the mean of the lognormal aperture distribution is shown in Figure 6-11, where the mean aperture is increased and decreased by factors of 1.5 and 2, respectfully. The results are again similar to what would be expected from a porous medium, with the curves shifting vertically upwards and downwards with an increase and decrease in the mean aperture, respectively. Unlike the curves determined for the changes in the variance of the aperture distribution, the slopes of the large-scale curves remain relatively constant, as do the magnitudes of the differences between the drainage and wetting limbs. These results are consistent with the local-scale physics, requiring higher capillary pressures to produce the same wetting phase saturations in a lower permeability (smaller aperture) feature.

The concept of directionality or anisotropy in large-scale capillary pressure curves is a poorly studied concept, and the differences between porous and fractured media are expected to be

significant, given the highly structured and linear pathways available for flow in a fractured environment. Girgrah (1994) found that the capillary pressure curve was shifted vertically upwards when the bedding of a correlated random permeability field was rotated 90 degrees, in addition to an alteration of the slope of the large-scale curve.

6.4.2 Large-Scale Relative Permeability Behaviour

The second focus of this study, the production of large-scale relative permeability curves for the simulated fracture network, also assessed the sensitivity of the permeability behaviour to the statistics of the applied aperture distribution. The reader is reminded that the results presented here are not, strictly speaking, relative permeability curves. They are more properly identified as effective permeability curves, combining the large-scale intrinsic permeability of the network with the effects of the reduced permeability imparted by the presence of a second fluid phase.

Figures 6-12 and 6-13 present the effective permeability term (kkr_{nw}) for the decreased and increased variance of the lognormal aperture distribution, respectively. The curves representing the effective permeability of the nonwetting phase in the vertical direction (kkr_{zz}) are similar in form to the underlying Brooks-Corey constitutive relationship, and relatively invariant with changes in the variance of the aperture distribution. The exception to this is for the largest variance simulated (40 μm) which plots significantly shifted towards higher wetting phase saturations. It should be noted that the relative horizontal location of the curve is a function of the underlying large-scale capillary curve. The maximum value of effective permeability achieved on drainage is the important factor in analyzing these curves. It can be seen that the

overall vertical effective permeability of the system, and thus the overall vertical flow through the system, increases with decreasing variance of the aperture distribution. The only exception to this case again involves the simulation with the largest variance in the aperture distribution. This is most likely due to the existence of a high permeability pathway developing within the system, and again points to the possible dependence of the REV on the aperture distribution. The maximum value attained on the effective permeability curves compares well with the unidirectional hydraulic conductivity found during the REV study.

The curves representing the effective permeability of the nonwetting phase in the horizontal direction (due to an applied gradient in the vertical direction, kkr_{xz}) are significantly different than the vertical cases. The behaviour in respect to absolute effective permeability versus the variance of the aperture is in agreement with the results for vertical case, in that the absolute value of effective permeability decreases with decreasing variance of the aperture distribution. This behaviour is expected, as the total flow through the system is dependent upon the macroscopic gradient and should be invariant with a given variance in the aperture distribution.

The shape of the horizontal effective permeability curves is not similar to that of the underlying Brooks-Corey relationship, as the curves invariably reach a maximum value at an intermediate value of wetting phase saturation. The underlying orientation distribution of the fracture network exerts a controlling effect in terms of effective permeability. The large-scale intrinsic permeability of the network exhibits anisotropy (Figure 6-4) with a higher value in the vertical direction than the horizontal direction. This results in the saturation dependent effective permeability exhibited by the large-scale curves in Figures 6-12 and 6-13, where the horizontal

component of flow is close to the vertical at low nonwetting phase saturations, when the local-scale nonwetting phase relative permeabilities are small. As the local-scale nonwetting phase permeabilities increase, the total vertical effective permeability of the system increases relative to that of the horizontal due to the gravity gradient that exists in the vertical direction. It is also of interest to note that the reversal of the slope on the kkr_{xz} terms occurs at similar wetting phase saturations as a subtle change in slope of the large-scale capillary pressure curves (Figure 6-12 vs. Figure 6-10).

The relative magnitudes of the effective permeability terms in the simulation with the largest variance in the aperture distribution are inverted from all other simulations, with the horizontal effective permeability consistently higher than the vertical effective permeability. This is a general trend that can be seen with increasing variance in the aperture distribution, as the difference between vertical and horizontal effective permeability values at the highest applied boundary capillary pressure is decreasing with increasing variance. In the simulation with a variance of 40 μm, the values of the effective permeability terms are essentially equal at the top of the drainage curve, corresponding to an essentially isotropic medium with respect to flow in the nonwetting phase.

Figures 6-14 And 6-15 present the effective permeability curves for the increased and decreased mean of the lognormal aperture distribution, respectively. The large-scale saturation dependent anisotropy occurs in these cases as well, identically to that for the previous simulations.

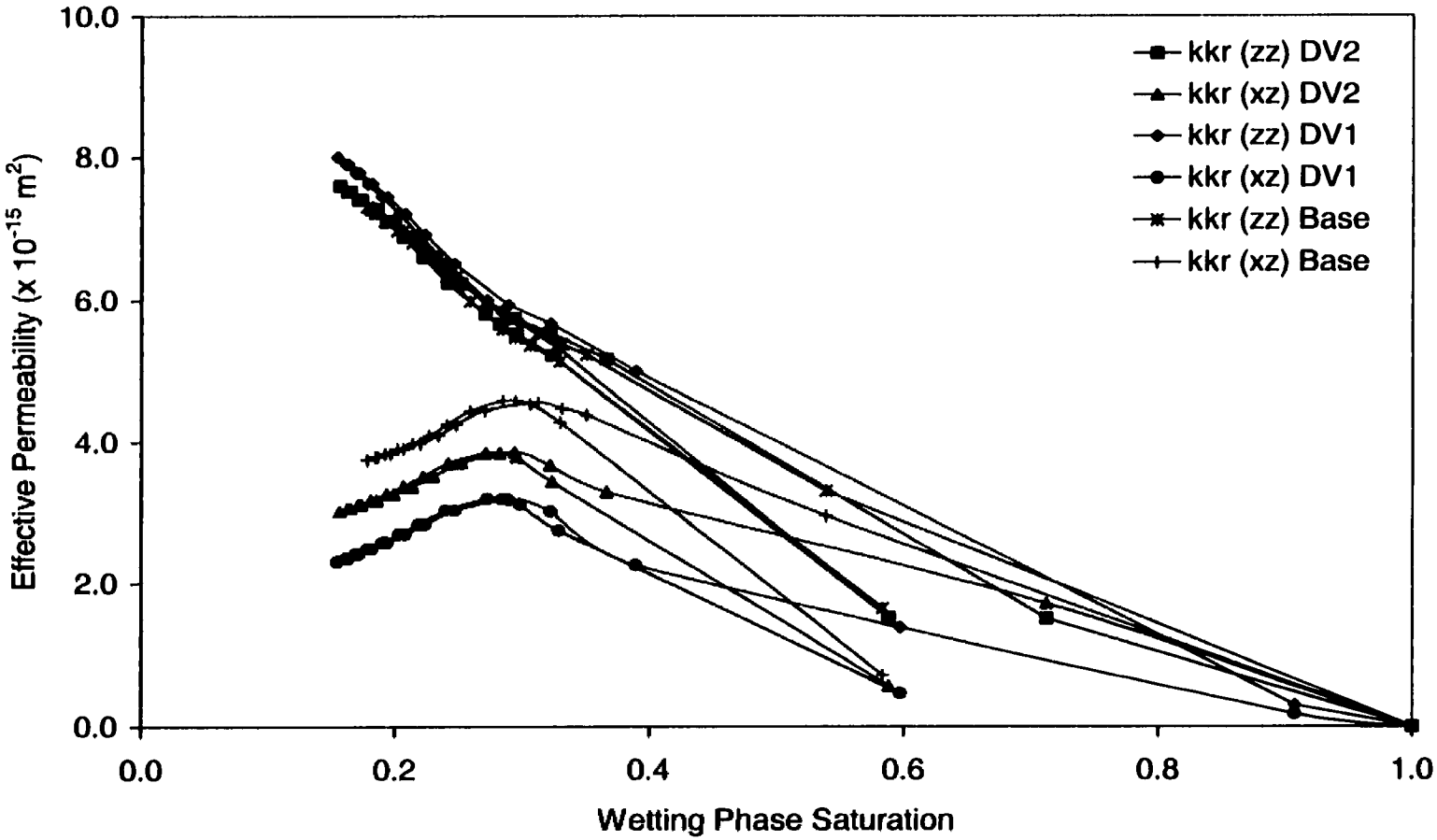

Figure 6-12. Large-scale Effective Permeability Curves for Decreased Aperture Variance

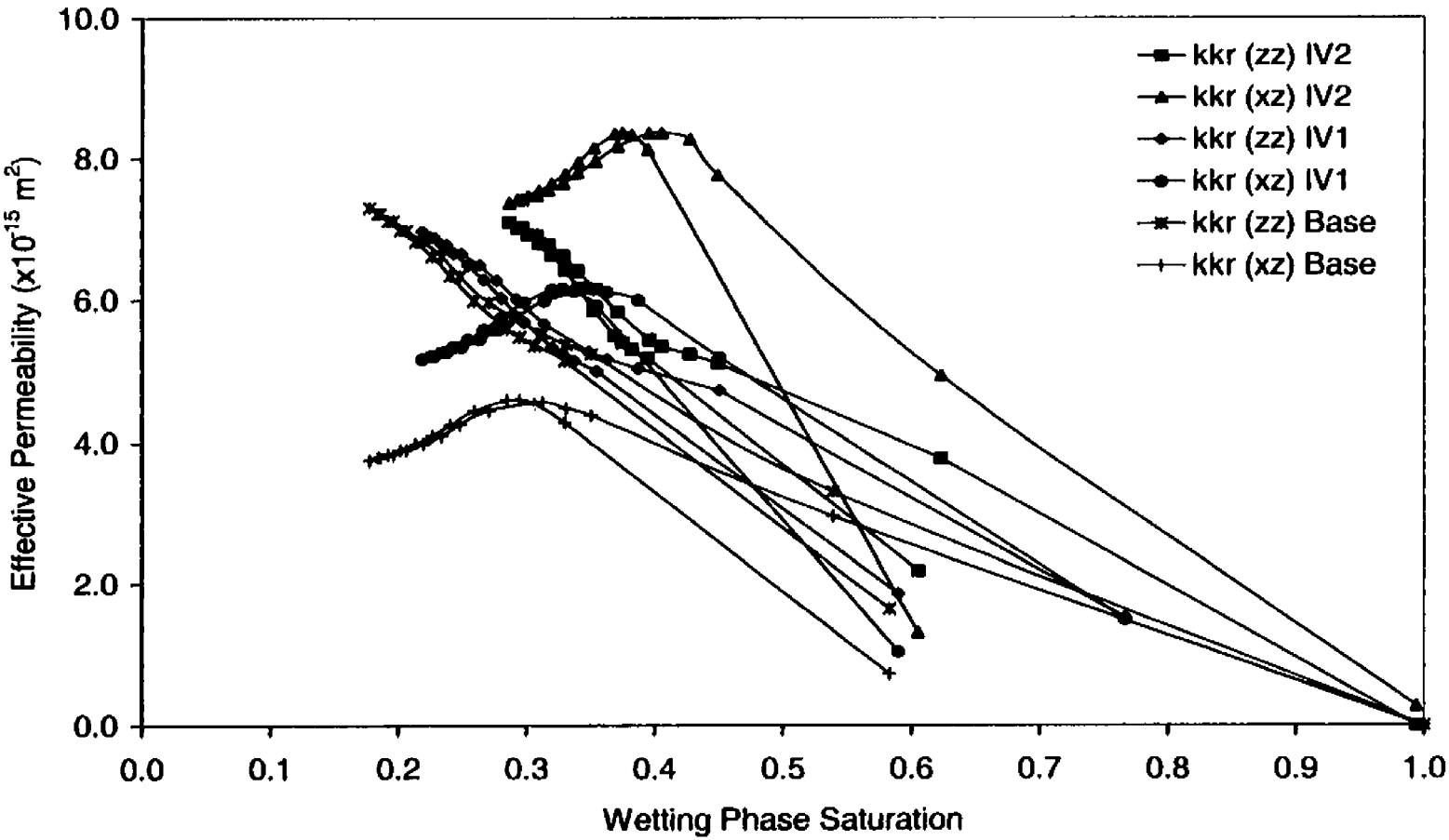

Figure 6-13. Relative Permeability Curves for Increased Aperture Variance

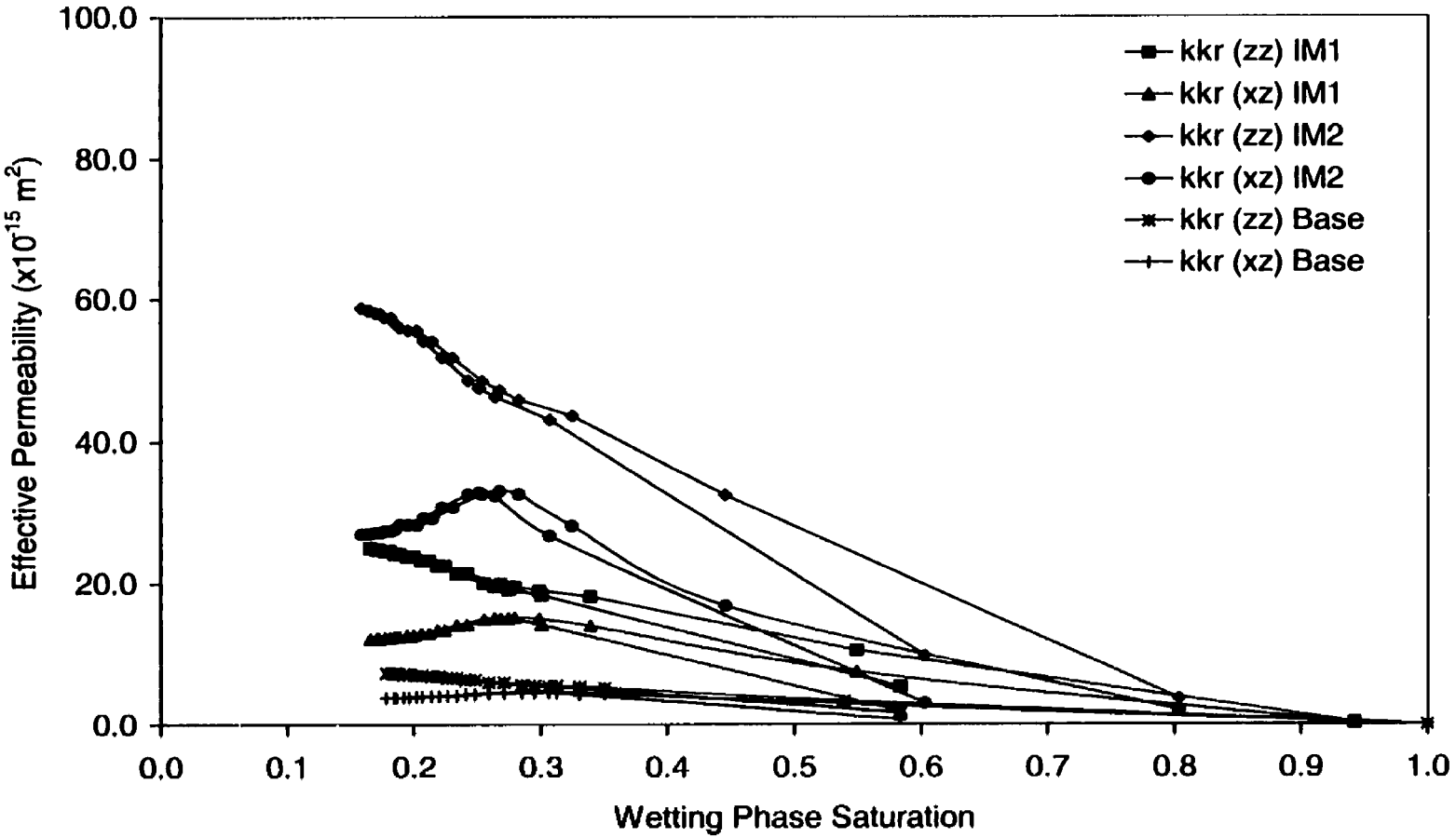

Figure 6-14. Large-scale Effective Permeability Curves for Increased Mean Aperture

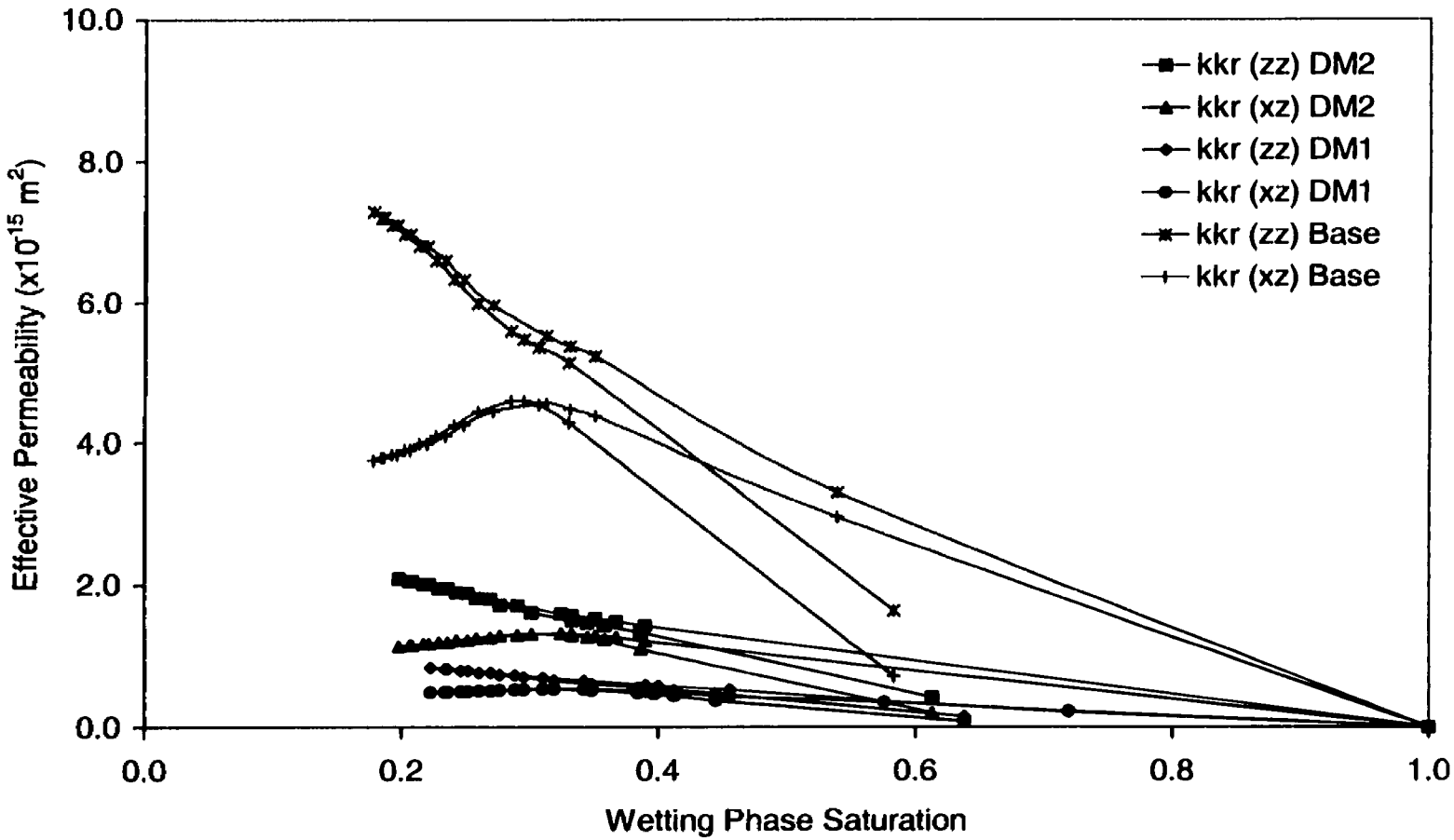

Figure 6-15. Large-scale Effective Permeability Curves for Decreased Mean Aperture

The curves for these cases, however, scale almost exactly as a function of mean aperture, with little differences occurring except for the relative values. In fact the ratio of the vertical to horizontal terms is essentially unchanged between simulations, the apparent differences being due to the scales used on the dependent axes.

In general, the results of the sensitivity study for the large-scale effective permeability terms shows that there are two competing factors underlying the results, the saturation dependent nature of the horizontal effective permeability term, and the non-scalar nature of the relative permeability term itself. These results have shown that the common representation of relative permeability as a scalar is not correct when considering large-scale averaged approximations to the constitutive relationships. These results are consistent with porous media work, both the stochastic results of Yeh et al. (1985) and the deterministic approach of Ataie-Ashtiani et al. (2001).

6.4.3 Effects of Fracture Terminations

A significant difference in the conceptualization of flow through porous versus fractured media exists in the form of dead-end fractures in a network. In correlated porous media, lateral flow paths are essentially ubiquitous throughout any realization, meaning that flow is rarely permanently "trapped" in any region during a drainage process. The occurrence of vertical dead-end fractures provide regions of a fractured network that accept nonwetting phase due to density effects, yet do not contribute to the global flow within the network. As the boundary capillary pressures in the simulated network increase, more nonwetting phase enters these dead-end

pathways, and is essentially unable to exit as the boundary capillary pressures are reduced (some vertical migration will occur when the capillary gradient exceeds the gravity gradient at the local-scale, however).

The importance of this phenomenon was examined by sequentially eliminating the number of vertical dead-end fractures within the domain. This was performed by identifying the locations of the fractures, and rendering them essentially impermeable by increasing their displacement pressure to infinity. Only those fractures that terminate vertically downward were eliminated, thus flow vertically upwards into a dead-end fracture was still allowed. The procedure was performed randomly, first by removing 50 percent of the dead-end fractures (50 percent termination), and then 100 percent (100 percent termination).

Figure 6-16 presents the large-scale capillary pressure curves for the base scenario (0 percent termination) and the two new cases. The results clearly show that the presence of the dead-end fractures bias the curves towards higher nonwetting phase saturations, due to the aforementioned build-up of the nonwetting phase due to density effects. The overall decrease in large-scale capillary pressure with increasing termination results from an identical process. The overall hysteresis between the drainage and wetting limbs also results from the existence of high nonwetting phase saturations in the termini, as the nodes within the dead-ends are still on the drainage curve. The effects of the termination percentage on the effective permeability of the nonwetting phase is essentially nonexistent (Figure 6-17), as the dead-end fractures do not contribute to flow through the network.

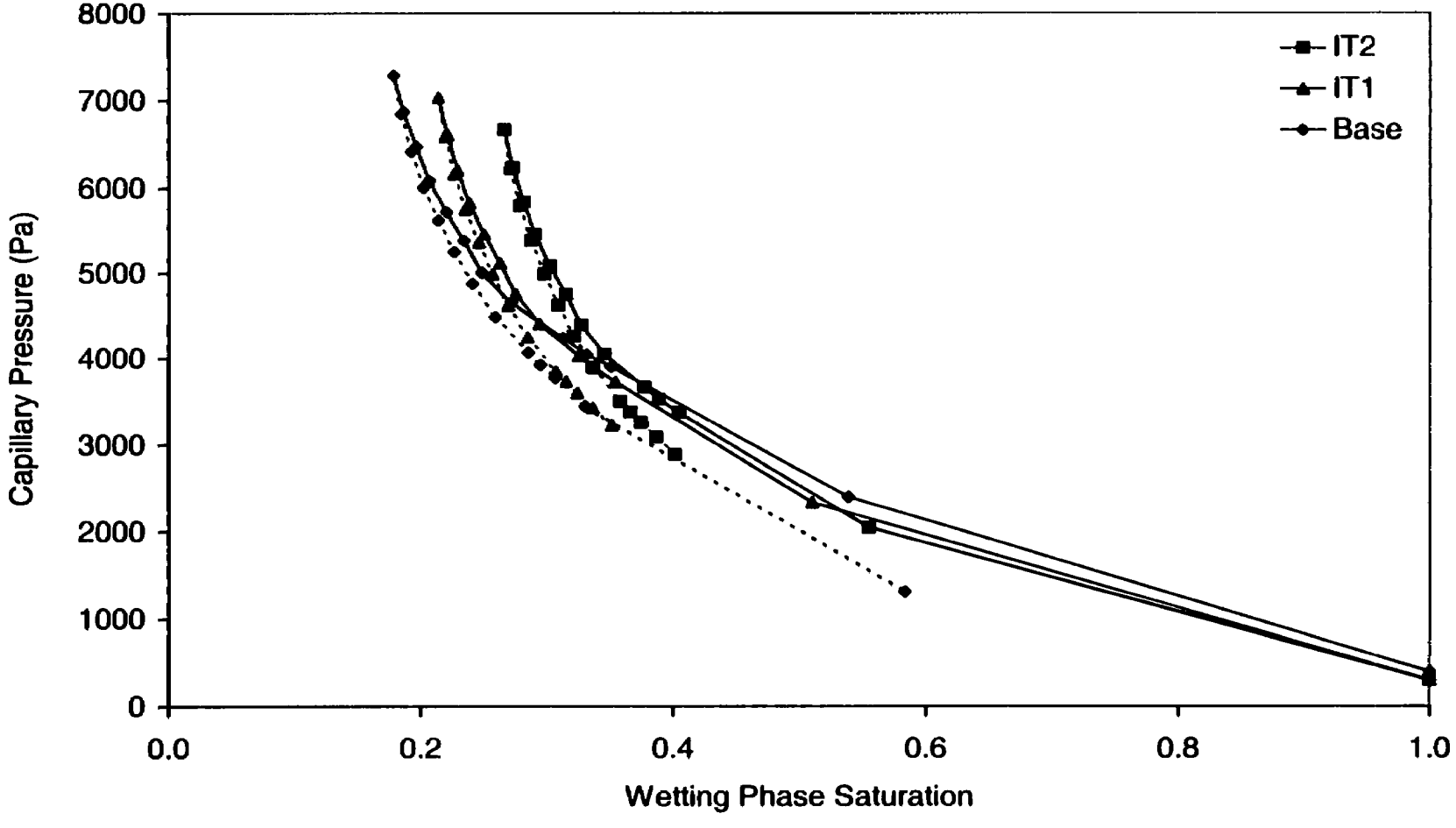

Figure 6-16. Large-scale Capillary Pressure Curves for Differing Degrees of Fracture Termination Percentages

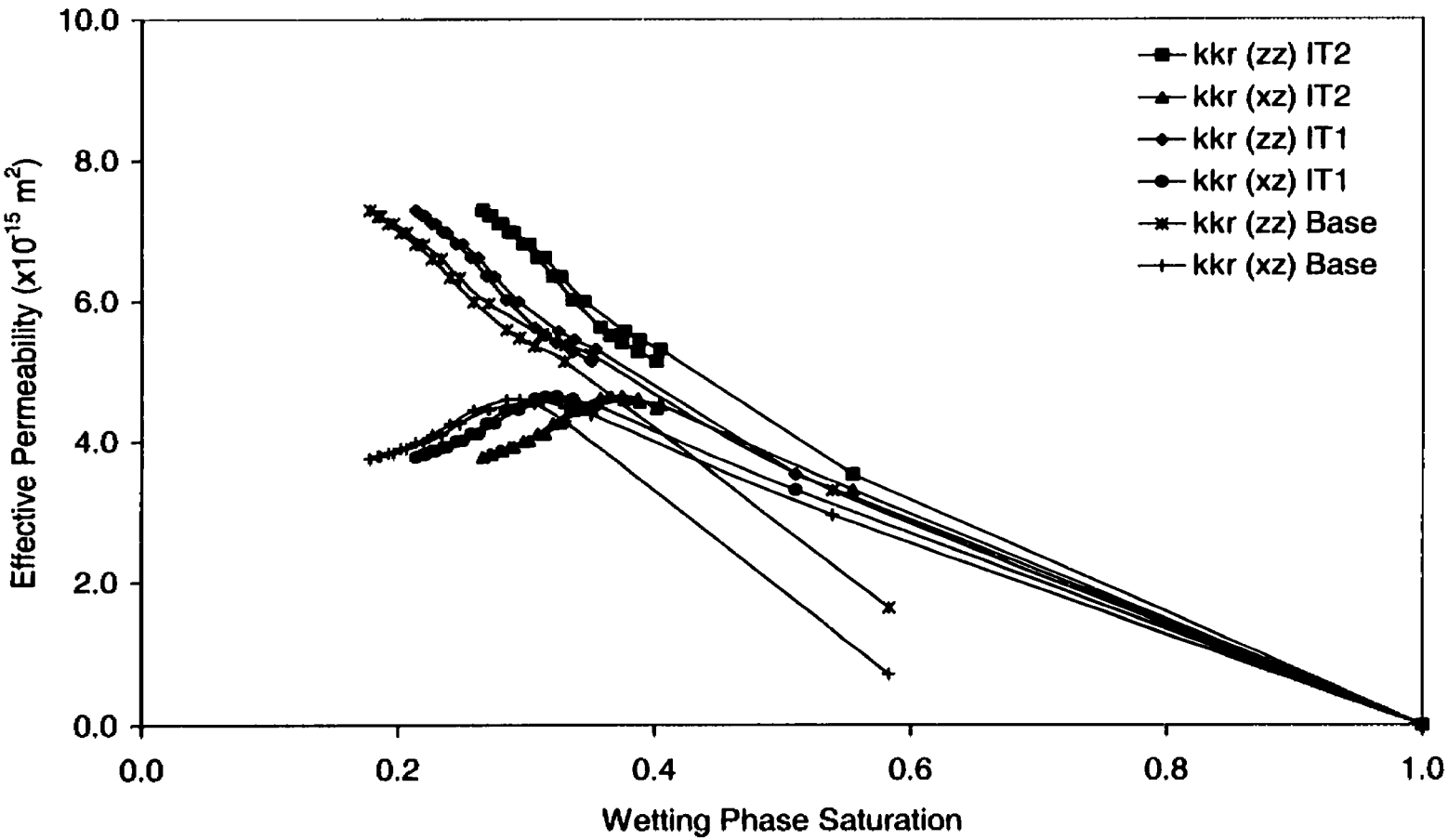

Figure 6-17. Large-scale Effective Permeability for Differing Degrees of Fracture Termination Percentages

6.5 Conclusions

The development of large-scale formulations of capillary pressure-saturation and saturation-relative permeability relationships has been performed for a two-dimensional representation of a discretely fractured granite. The effective properties of such a domain are often of more interest than the local-scale behaviour, given the computational resources required to simulate multiphase flow in large discretely fractured rock masses, and the difficulties inherent in the acquisition of accurate statistical descriptions of the fracture network. In this work the large-scale relationships for a fracture network produced from a composite of site data are found through a deterministic approach using numerical simulation.

Successive determination of the bulk hydraulic conductivity and average capillary properties in increasing block sizes showed that an REV exists for the fracture network simulated, and the results of the study supported this conclusion. The effective large-scale relations were found by incrementally increasing the applied capillary pressure on the boundaries of the domain, and allowing the system to achieve steady-state flow. The use of a constant capillary pressure boundary condition on all boundaries of the domain allowed for a determination of the effective permeability in both the vertical and horizontal directions (combined intrinsic and relative permeability) resulting from a gradient applied in the vertical direction. The density dependent nature of multiphase flow presented conceptual difficulties for the determination of the remaining terms in the effective permeability tensor, and would require artificial manipulation of the gravity vector to become tractable. It is of interest to note that the use of equal equivalent

total gradients (capillary plus wetting phase plus gravity) does not result in equivalent large-scale relationships.

The large-scale capillary pressure-saturation relationship was found to be sensitive to the statistics governing the underlying aperture distribution. The overall effects on the relationships were found to be analogous to porous media, in that reducing or increasing the variance of the aperture distribution resulted in a corresponding shallowing or steepening of the curve, respectively. Altering the mean of the aperture distribution again resulted in behaviour similar to that for porous media, by vertically shifting the curves upwards (increase in the mean) or downwards (decrease in the mean).

The large-scale effective permeability curves representative of flow in the vertical direction produced in this work followed the general form of the underlying local-scale Brooks-Corey constitutive relationship and were relatively invariant with changing variance of the aperture distribution. The large-scale curves representing flow in the horizontal direction due to an imposed gradient in the vertical direction, however, are significantly different from the Brooks-Corey relationship. The maximum value of effective permeability achieved during the incremental steps of the procedure occurred at an intermediate wetting phase saturation corresponding to an applied boundary capillary pressure less then the maximum applied value. The anisotropy of the fracture network was also replicated in the large-scale effective permeability relationships.

The presence of dead-end vertical fractures in the network is a significant conceptual difference from a porous media. The existence of these allows for nonwetting phase to become removed from the connected flow-path of the domain due to density-driven migration into the dead-ends. The importance of these features was examined by successively removing them from the domain, without altering the fracture pattern. The presence of these hydraulically inactive features biases the large-scale relationships towards higher nonwetting phase saturations and less hysteresis between the drainage and wetting limbs.

6.6 References

Abriola, L.M. and G.F. Pinder. 1985. A Multiphase approach to the modeling of porous media contamination by organic compounds. 1. Equation development, *Water Res. Res.*, 27(6), p 11-18.

Ahmadi, A., and M. Quintard. 1996. Large-scale Properties for Two-phase Flow in Random Porous Media, *J. Hyd.*, 183, p 69-99.

Amazine, B., Bourgeat, A., and J. Koebbe. 1991. Numerical Simulations and Homogenization of Two-phase Flow in Heterogeneous Porous Media, *Tran. Por. Media*, 6, p 519-547.

Ataie-Ashtiani, B., Hassanizadeh, S.M., Oostrom, M., Celia, M.A., and M.D. White. 2001. Effective Parameters for Two-phase Flow in a Porous Medium with Periodic Heterogeneities, *J. Cont. Hyd.*, 49, p 87-109.

Barker, J.W., and S. Thibeau. 1997. A Critical Review of the Use of Psuedorelative Permeabilities for Upscaling, SPE Res. Eng., 5, p 138-143.

Bear, J. 1972. Dynamics of Fluids in Porous Media. Dover Publications Inc., New York.

Brooks, R.H. and A.T. Corey. 1964. Hydraulic properties of porous media. Civ. Eng. Depart., Colorado. State Univ., Fort Collins. Hydrology. Paper No. 3.

Chen, Z. 1995. Large-scale Averaging Analysis of Multiphase Flow in Fractured Reservoirs, *Tran. Por. Media*, 21, p 269-295.

Christie, M.A. 1996. Upscaling for Reservoir Simulation, *J. Pet. Tech.*, Novenber, p 1005-1010.

Cravero, M., and C. Fidelibus. 1999. A Code for Scaled Flow Simulations on Generated Fracture Networks, *Comp. Geosci.*, 25, p 191-195.

Dagan, G., and E. Bresler. 1983. Unsaturated Flow in Spatially Variable Fields I. Derivation of Models of Infiltration and Redistribution, *Water Res. Res.*, 19(2), p 413-420.

Dershowitz, W., Lee, G., Geier, J., Foxford, T., LaPointe, P., and A. Thmoas. 1995a. FRACMAN: Interactive Discrete Feature Data Analysis, Geometric Modelling, and Exploration Simulation, User Documentation, Version 2.5, Golder Ass., Redmond, WA, USA.

Dershowitz, W., and I. Miller. 19995b. Dual Porosity Fracture Flow and Transport, *Geo. Res. Lett.*, 22(11), p 1441-1444.

Desbarats, A.J. 1995. Upscaling Capillary Pressure-Saturation Curves in Heterogeneous Porous Media, *Water Res. Res.*, 31(2), p 281-288.

Durlofsky, L.J. 1991. Numerical Calculations of Equivalent Grid Block Permeability Tensors for Heterogeneous Porous Media, *Water Res. Res.*, 27, p 699-708.

Durlofsky, L.J., Jones, R.C., and W.J. Milliken. 1997. A Nonuniform Coarsening Approach for the Scale-up of Displacement Processes in Heterogeneous Porous Media, *Adv. Water Res.*, 20(5), p 335-347.

Ehlan, J. 1999. Fracture Characteristics in Weathered Granites, *Geomorphology*, 31, p 29-45.

Ferrand, L.A., and M.A. Celia. 1992. The Effect of Heterogeneity on the Drainage Capillary Pressure-Saturation Relation, *Water Res. Res.*, 28(3), p 859-870.

Forsyth, P.A. 1991. A Control Volume Finite Element Approach to NAPL Groundwater Contamination, *SIAM J. Sci. Stat. Comput.*, 12(5), p 1029-1057.

Gerhard, J.I., B.H. Kueper, and G.R. Hecox. 1998. The Influence of Waterflood Design on the Rrecovery of Mobile DNAPLs, *Ground Water*, 36(2), p 283-292.

Girgrah, B. 1994. Effective Large-Scale Parameters for Two-Phase Flow in Heterogeneous Porous Media, M.Sc. (Eng.) Thesis, Department of Civil Engineering, Queens University, ingston, Ontario, Canada, 121 pgs.

Gray, W.G. 2000. Macroscale Equilibrium Conditions for Two-Phase Flow in Porous Media, *Int. J. Multi. Flow*, 26, p 467-501.

Hassanizadeh, S.M., and W.G. Gray. 1990. Mechanics and Thermodynamics of Multiphase Flow in Porous Media Including Interphase Boundaries, *Adv. Water Res.*, 13(4), p 169-186.

Ioannidis, S.M., Chatzis, I., and F.A.L. Dullien. 1996. Macroscopic Percolation Model of Immiscible Displacement: Effects of Buoyancy and Spatial Structure, Water Res. Res., 32(11), p 3297-3310.

King, P.R. 1989. The use of Renormalization for Calculating Effective Permeability, *Tran. Por. Media*, 4, p 37-58.

King, P.R., Muggeridge, A.H., and W.G. Price. 1993. Renormilization Calculations of Immiscible Flow, *Tran. Por. Media*, 12, p 237-260.

Kueper, B.H. and E.O. Frind. 1991. Two-phase flow in heterogeneous porous media: 2. Model Development, *Water Res. Res.*, 27(6), p 1049-1057.

Kueper, B.H., and D.B. McWhorter. 1992. The Use of Macrscopic Percolation Theory to Construct Large-scale Capillary pressure Curves, *Water Res. Res.*, 28(9), p 2425-2436.

Long, J.C.S., Wilson, C.R., and P.A. Witherspoon. 1982. Porous Media Equivalents for Networks of Discontinuous Fractures, *Water Res. Res.*, 18, p 645-658.

Long, J.S., and D.M. Billaux. 1987. From Field Data to Fracture Network Modelling: An Example Incorporating Spatial Structure, *Water Res. Res.*, 23(7), p 1201-1216.

Mantoglou, A., and L.W. Gelhar. 1987a. Stochastic Modeling of Large-Scale Transient Unsaturated Flow Systems, *Water Res. Res.*, 23(1), p 37-46.

Mantoglou, A., and L.W. Gelhar. 1987b. Capillary Tension Head Variance, Mean Soil Moisture Content, and Effective Specific Soil Moisture Capacity of Transient Unsaturated Flow in Stratified Soils, *Water Res. Res.*, 23(1), p 47-56.

Mantoglou, A., and L.W. Gelhar. 1987c. Effective Hydraulic Conductivities of Transient Unsaturated Flow in Stratified Soils, *Water Res. Res.*, 23(1), p 57-67.

Margolin, G., Berkowitz, B., and H. Scher. 1998. Structure, Flow, and Generalized Conductivity Scaling in Fracture Networks, *Water Res. Res.*, 34(9), p 2103-2121.

McWhorter, D.B., and D.K. Sunada. 1990. Exact Integral Solutions for Two-phase Flow, *Water Res. Res.*, 26(3), p 399-413.

Miller, C.T., Christakos, G., Imhoff, P.T., McBride, J.F., Pedit, J.A., and J.A. Trangenstein. 1998. Multiphase Flow and Transport Modeling in Heterogeneous Porous Media: Challenges and Approaches, *Adv. Water Res.*, 21(2), p 77-120.

Neuman, S.P. 1990. Universal Scaling of Hydraulic Conductivities, *Water Res. Res.*, 26(8), p 1749-1758.

Neuman, S.P., Illman, W.A., Hyun, Y., Vesselinov, V.V., Di Federico, V., Tartakovsky, D.M. 2001. Observation and Analysis of a Pronounced Permeability and Porosity Scale Effect in Unsaturated Fractured Tuff, *Proceedings, Fractured Rock 2001*, March 26-28, Toronto, Ontario, Canada.

Quintard, M., and S. Whitaker. 1988. Two-phase Flow in Heterogeneous Porous Media, the Method of Large-scale Averaging, *Tran. Por. Media*, 3, p 357-413.

Quintard, M., and S. Whitaker. 1990. Two-phase Flow in Heterogeneous Porous Media I. The Influence of Large Spatial and Temporal Gradients, *Tran. Por. Media*, 5, p 341-379.

Reitsma, S.R. and B.H. Kueper. 1994. Laboratory Measurement of Capillary Pressure-Saturation Relationships in a Rock Fracture, *Water Res. Res.*, 30(4), p 856-878.

Shewchuk, J.R. 1986. Triangle – A Two-dimensional Delaunay Triangulator, Carnegie Melon University, Pitt. PA.

Uchida, M., Dershowitz, W., Sawada, A., Wallman, P., and A. Thomas. 1997. Fracman Discrete Fracture Modelling for the ASPO Tunnel Drawdown Experiment, SKB International Cooperation Report 97-03, SKB, Stockholm, Sweden.

White, C.D., and R.N. Horne. 1987. Computing Absolute Transmissibility in the Presence of Fine-scale Heterogeneity, *SPE Paper 16011*, SPE Sym. Res. Simul., San Antonio.

Yeh, T-C.J., Gelhar, L.W., and A.L. Gutjahr. 1985. Stochastic Analysis of Unsaturated Flow in Heterogeneous Soils 3. Observations and Applications, *Water Res. Res.*, 21(4), p 465-471.

Zhang, X., Sanderson, D.J., Harkness, R.M., and N.C. Last. 1996. Evaluation of the 2-D Permeability Tensor of Fractured Rock, *Int. J. Rock Mech. Min. Sci.*, 33, p 17-37.

Zhang, X., and D.J. Sanderson. 1999. Scale up of Two-dimensional Conductivity Tensor for Heterogeneous Fracture Networks, *Eng. Geol.*, 53, p 83-99.

CHAPTER 7 – SUMMARY AND CONCLUSIONS

The prediction of the migration of DNAPLs and their associated dissolved phase plumes through the subsurface is a complex and numerically intensive proposition. The level of complexity increases as such factors as heterogeneity, capillary hysteresis, and the presence of fractures operating as high permeability pathways through otherwise impermeable barriers are considered. This work has studied the physics underlying migration through the subsurface, beginning with a simple single fracture scenario, and then increasing in complexity to networks of fractures in clay sequences containing interspersed sand units, through to a realistic scenario containing correlated random permeability fields and various fracture configurations. The production of large-scale constitutive relationships in non-orthogonally fractured consolidated media forms the final step of complexity investigated. Two numerical models, FRACAS and QUMPFS, were developed as tools to perform this work. Both are multiphase multi-component compositional simulators, capable of accurately simulating advection, dispersion, sorption, and non-equilibrium dissolution in the subsurface.

The building block for the understanding of flow through a fractured environment is the single fracture scale. The single most important factor controlling the migration rate of DNAPL through a single fracture is the fracture aperture. Increasing the fracture aperture from 15 μm to 50 μm results in an approximately 20-fold increase in the rate of migration. Similar variations in the parameters governing matrix diffusion, however, have a relatively insignificant influence on DNAPL migration rates. The effect of the inclination of the fracture on the migration rate of the

DNAPL is also significant, primarily due to the increased length of travel involved to migrate the same vertical distance.

An analysis of the migration of five common DNAPLs through a single fracture was performed and the similarities in breakthrough times predicted in large aperture fractures for the five DNAPLs illustrates the difficulty in predicting migration times without the use of numerical models. Based solely on an examination of the solubility and density, a DNAPL with the lowest density and highest solubility may be expected to have the slowest breakthrough time. This, however, was not the case in the majority of the simulations conducted. In all cases (with the exception of the smallest aperture aperture/longest fracture combination) Chlorobenzene (low solubility/low density) was found to be the slowest migrating DNAPL. The insensitivity of the migration rate to matrix diffusion decreases the importance of solubility, and increases the importance of viscosity and density.

In assessing the decrease in migration rate due to matrix diffusion, the most descriptive indicator is the ratio of mass lost to the matrix to mass replenishment at the fracture entrance. This ratio is primarily dependent upon the solubility of the DNAPL when all other factors remain the same. To arrest downward migration, this ratio would have to exceed 1.0 for a significant length of time. This never occurred in any of the simulations performed in this work. This is due to a limitation in the "contributing length" of the DNAPL body. As the DNAPL penetrates through the aquitard the ratio of mass lost to mass replenished becomes essentially constant, as the matrix adjacent to the upper portions of the fracture becomes saturated with contaminant, and no longer acts as a sink to the DNAPL in the fracture.

Given the insensitivity of the migration rate of a DNAPL to mass lost to the matrix, the rate of vertical penetration of DNAPL through fractured clay aquitards void of sand lenses can be extremely rapid, on the order of days for a 30 m sequence containing 35 μm fractures. The presence of vertical gradients can enhance or retard this rate, depending on whether groundwater flow is downwards or upwards.

The existence of sand lenses interbedded with fractured clay, as commonly found in deltaic depositional environments, significantly influences the migration times of the nonwetting phase vertically through the system. The presence of a 2 m and a 5 m thick sand lens within the aforementioned 30 m clay layer can increase the time required to traverse the system from a few days to several years. The presence of vertical gradients in a layered sequence caused significant changes in the DNAPL breakthrough times, in some cases completely arresting the vertical migration after the source had been removed.

The ratio of displacement pressures between fractures and the sand lenses into which they exit is also a controlling factor in the migration of DNAPL. Increasing the displacement pressure of the sand relative to that of the fractures (by a factor of approximately three) resulted in more than a ten-fold increase in the DNAPL breakthrough time. Conversely, decreasing the displacement pressure of the sand relative to that of the fractures (by a factor of approximately three) prevented the nonwetting phase from reaching the lower aquifer.

The retardation of the arrival of the nonwetting phase in the lower aquifer, due to the presence of matrix diffusion, began to be noticeable with the inclusion of sand lenses into the domain as opposed to a system consisting only of fractured clay. The quantities of aqueous phase flux penetrating the system are, however, significantly less than that of the nonwetting phase in almost all possible scenarios. The exception to this occurs in the case of a limited volume release, in which, on occasion, no nonwetting phase reaches the underlying aquifer, or the nonwetting phase flow is cut-off as the source is depleted. The presence of the matrix as a dissolved phase sink was evident, however, in that the arrival times of the nonwetting and dissolved phases at the bottom of the system were essentially coincidental.

The migration of DNAPL and dissolved phase contamination through a fractured heterogeneous porous medium represents the most physically realistic scenario, as flow can occur both through (in fractures) and around (through higher permeability lenses) low permeability capillary barriers. It was found that the mean permeability of the domain controlled the depth of migration below the surface to a large degree, and the presence of fractures was less important than in the previous homogeneous/layered scenarios. The presence of fractures within the system was found to control the infiltration of the nonwetting phase only for the case where lenses with a permeability of less than 1.0×10^{-12} m^2 were fractured.

The importance of fractures in the system, however, was highlighted when examining the time required to penetrate through low permeability features. In simulations with extensive fracturing, the DNAPL was able to "short-circuit" rapidly across low permeability layers and penetrate deeper into the subsurface. In most cases where the DNAPL encountered a low

permeability barrier during the "source-on" condition, DNAPL eventually migrated below the barriers, either through by-passing, invasion, or a combination of the two.

The extent of DNAPL contamination within the heterogeneous system was also evaluated through the use of moments about the centre of mass of the DNAPL body. The moments, which indicate the degree of lateral and vertical spreading of the DNAPL, tended to level off after approximately nine years (maximum duration of the source-on condition was approximately 4.5 years). This tended to be due to a redistribution of the DNAPL towards a residual configuration, as was evidenced by the gradual trending of average nonwetting phase saturations within the domain to a static value. The increased presence of fracturing within the domain was, in general, found to allow for deeper DNAPL penetration into the subsurface.

The final investigation conducted in this work departed from the consideration of multiphase flow and transport in unconsolidated media, and looked at the production of large-scale effective constitutive relationships for two-dimensional fractured rock domains. Successive determination of the bulk hydraulic conductivity and average capillary properties in increasing block sizes showed that an REV exists for the fracture network simulated, and the large-scale capillary pressure-saturation curves produced supported this conclusion.

The large-scale capillary pressure-saturation relationship was found to be sensitive to the statistics governing the underlying aperture distribution. The overall effects on the relationships were found to be analogous to porous media, in that reducing or increasing the variance of the aperture distribution resulted in a corresponding shallowing or steepening of the curve,

respectively. Altering the mean of the aperture distribution again resulted in behaviour similar to that for porous media, by vertically shifting the curves upwards (increase in the mean) or downwards (decrease in the mean).

The large-scale effective permeability curves (combined intrinsic and relative permeability) representative of flow in the vertical direction produced in this work followed the general form of the underlying local-scale Brooks-Corey constitutive relationship and were relatively invariant with changing variance of the aperture distribution. The large-scale curves representing flow in the horizontal direction due to an imposed gradient in the vertical direction, however, are significantly different from the Brooks-Corey relationship. The maximum value of effective permeability achieved during the incremental steps of the procedure occurred at an intermediate wetting phase saturation corresponding to an applied boundary capillary pressure less then the maximum applied value.

The use of numerical simulators to investigate multiphase flow and aqueous phase transport in fractured geologic media has been shown to be a powerful tool, allowing insights into the controlling physics at both the local and macro scales. Further work is necessary in the production of large-scale constitutive relationships for fractured rock masses, looking at the importance of other fracture parameters (such as the distribution of lengths, orientation, etc.) as well as the applicability of the results presented here, from two-dimensional simulations, to three-dimensional domains. The migration from two to three dimensions requires the development of new mathematical approaches to the representation of discrete randomly oriented fractures within a porous rock matrix.

The large-scale implications of this work, especially in regards to remediation of contaminated sites, are many and diverse. The migration of DNAPL through extensively fractured geology is quite rapid, and given the tortuous pathways represented by the fractures (as primary conduits for DNAPL migration) is exceptionally difficult to predict or, in a field setting, locate. Aperture variations within individual fractures are expected to be the dominant control on large-scale migration, and will result in isolated areas of high contamination as well as large uncontaminated volumes of the subsurface. The transfer of mass from the nonwetting phase to the aqueous phase and its subsequent diffusion into the porous matrix surrounding a fracture represents a contamination source that can exist for decades above allowable limits.

Historically, the presence of clay layers in the subsurface has been viewed as a barrier to the vertical migration of DNAPL. The greater importance of interbedded sand lenses found in this work, however, shows that remediation (in the form of mass removal) can be attained through some mechanism which operates on the sand. The presence of fractures in the case where permeable porous media is the dominant component of the subsurface has fewer implications in regards to remediation, as the majority of the mass is contained in the permeable units and can be treated with agresive and passive remediation methods. The work performed in this thesis has shown that, in all cases studied, the existence of detectable concentrations of contaminant in permeable porous media overlain by fractured impermeable porous media effectively points to the existence of DNAPL in the permeable media.

APPENDIX A - ONE-DIMENSIONAL CONTROL VOLUME FINITE ELEMENT MODEL DEVELOPMENT AND VERIFICATION

Model Description

The one-dimensional model developed in this appendix is solved through the use of a control volume, finite element approach, and can handle the advection of the wetting and nonwetting phases, as well as the dispersion and diffusion of the aqueous phase. The formulation is limited to line elements, and can simulate equilibrium and non-equilibrium mass transfer.

A.1 Discretization of the Governing Equations

Abriola and Pinder (1985) developed the partial differential equations governing multiphase flow and multicomponent transport in a porous media:

$$\frac{\partial}{\partial t}\left(c_{i\beta}\phi S_\beta x_{i\beta}\right)+\nabla\cdot\left(c_{i\beta}x_{i\beta}v_\beta\right)-\nabla\cdot\left[\phi S_\beta D_{i\beta}\nabla\left(c_{i\beta}x_{i\beta}\right)\right]-q_{i\beta}-I_{i\beta}=0 \qquad \beta=1..n_p, i=1..n_c \qquad \text{[A-1]}$$

where $c_{i\beta}$ is the molar density of phase β, ϕ is the porosity of the medium, S_β is the saturation of phase β expressed as a fraction of void space, $x_{i\beta}$ is the mole fraction of component i in phase β, v_β is the Darcy flux of phase β, $D_{i\beta}$ is the dispersion tensor for component i in phase β, $q_{i\beta}$ is a

source or sink of component i to or from phase β, and $I_{i\beta}$ is the interphase mass transfer of component i to or from phase β.

The governing equations described above were solved through the use of the Control Volume Finite Element method (CVFE) of Forsyth (1991). The development that follows hereafter is taken from Therrien (1992) and Letniowski (1989).

The first step is to adapt the Lagrange C^o polynomial basis functions:

$$\begin{aligned} &N_I = 1 \quad \textit{at node } I \\ &N_I = 0 \quad \textit{at node } J \\ &\sum_J N_J = 1 \end{aligned} \qquad \text{[A-2]}$$

The pressure in the domain is represented by:

$$\overline{P}(x,t) \approx P(x_I,t) = \sum_J P_J N_J \qquad \text{[A-3]}$$

where $P(X,t)$ is the actual pressure at point x at time t, and $P(x_I,t)$ is the pressure at a node in the domain. In addition, the fluid potential (ψ_β)is:

$$\psi_\beta = \sum_J \psi_{\beta J} N_J = \sum_J \left(P_{\beta J} + \rho_{\beta J} g z_J\right) N_J \qquad \text{[A-4]}$$

the saturation is:

$$S_\beta = \sum_J S_{\beta J} N_J \qquad \text{[A-5]}$$

and the mole fraction is:

$$x_{i\beta} = \sum_{J} x_{i\beta J} N_J \qquad \text{[A-6]}$$

At this stage, the Galerkin approach is used to discretize the governing equation over a region of space of volume V. This leads to:

$$\int \left(\begin{array}{l} \dfrac{\partial}{\partial t}\left[\phi S_\beta C_{i\beta} x_{i\beta}\right] - \dfrac{\partial}{\partial x_j}\left[c_{i\beta} x_{i\beta} \dfrac{k_{kj} k_{r\beta}}{\mu_\beta} \dfrac{\partial \psi_\beta}{\partial X_k} \right] \\ - \dfrac{\partial}{\partial X_j}\left[\phi S_\beta D_{i\beta_{jk}} \dfrac{\partial}{\partial X_k}\left(c_{i\beta} x_{i\beta}\right) \right] - q_{i\beta} - I_{i\beta} \end{array} \right) \cdot N_I dV = 0 \qquad \text{[A-7]}$$

for $j,k=1,2,3$, and $i=1,n$ where n is the total number of nodes in a domain. The time derivative is handled using a lumped mass approach, as are the source/sink and mass transfer terms:

$$\int_V \left(\frac{\partial}{\partial t}\left[\phi S_\beta c_{i\beta} x_{i\beta}\right] \right) \cdot N_I dV = \left\{ \left[\phi S_\beta c_{i\beta} x_{i\beta}\right]_t^{N+1} - \left[\phi S_\beta c_{i\beta} x_{i\beta}\right]_t^{N} \right\} \frac{1}{\Delta t} \int_V N_I dV \qquad \text{[A-8]}$$

$$\int_V \left\{ q_{i\beta} + I_{i\beta} \right\} \cdot N_I dV = \left\{ q_{i\beta} + I_{i\beta} \right\} \cdot \int_V N_I dV \qquad \text{[A-9]}$$

The term in equation A7 representing advective flux in the domain can be manipulated to:

$$-\int_V \left\{ \frac{\partial}{\partial X_J} \left(c_{i\beta} x_{i\beta} \frac{k_{jk} k_{r\beta}}{\mu_\beta} \frac{\partial \psi_\beta}{\partial X_k} \right) \right\} \cdot N_I dV = \int_V \left(c_{i\beta} x_{i\beta} \frac{k_{jk} k_{r\beta}}{\mu_\beta} \frac{\partial \psi_\beta}{\partial X_k} \right) \cdot \frac{\partial N_I}{\partial X_J} dV + \int_B q_{i\beta} N_I dB \qquad \text{[A-10]}$$

where the last term represents the fluid flux normal to the boundary (B) of volume V, which, for simplicity, will be set equal to zero.

Further manipulation of this expression leads to:

$$\frac{\partial \psi_\beta}{\partial X_k}\frac{\partial N_I}{\partial X_J} = \frac{\partial}{\partial X_k}\left(\sum_J \psi_{\beta J} N_J\right)\frac{\partial N_I}{\partial X_J} \qquad \text{[A-11]}$$

rewriting N_I:

$$N_I = 1 - \sum_{J \neq I} N_J \qquad \text{[A-12]}$$

so that the derivative of N_I with respect to X_k is:

$$\frac{\partial N_I}{\partial X_k} = -\frac{\partial}{\partial X_k}\sum_{J \neq I} N_J \qquad \text{[A-13]}$$

With these two results, the right hand side of A11 can be written as:

$$\begin{aligned}
&\frac{\partial}{\partial X_k}\left(\sum_J \psi_{\beta J} N_J\right)\frac{\partial N_I}{\partial X_J} \\
&= \left[\frac{\partial}{\partial X_k}\sum_{J \neq I} \psi_{\beta J} N_J + \frac{\partial \psi_{\beta I} N_I}{\partial X_k}\right]\frac{\partial N_I}{\partial X_J} \\
&= \left[\frac{\partial}{\partial X_k}\sum_{J \neq I} \psi_{\beta J} N_J - \psi_{\beta I}\frac{\partial}{\partial X_k}\sum_{J \neq I} N_J\right]\frac{\partial N_I}{\partial X_J} \\
&= \left(\psi_{\beta J} - \psi_{\beta I}\right)\frac{\partial}{\partial X_k}\left(\sum_{J \neq I} N_J\right)\frac{\partial N_I}{\partial X_J}
\end{aligned} \qquad \text{[A-14]}$$

Substituting this result into the advective flux equation A10 gives:

$$\int_V \left\{ c_{i\beta} x_{i\beta} \frac{k_{jk} k_r}{\mu_\beta} \frac{\partial \psi_\beta}{\partial X_k} \right\} \cdot \frac{\partial N_I}{\partial X_J} dV$$
$$= \int_V \left(c_{i\beta} x_{i\beta} \frac{k_{jk} k_r}{\mu_\beta} \left(\psi_{\beta J} - \psi_{\beta I} \right) \frac{\partial}{\partial X_k} \left(\sum_{J \neq I} N_J \right) \right) \cdot \frac{\partial N_I}{\partial X_J} dV \qquad \text{[A-15]}$$

and discretization of the domain will determine nodal connectivity. Only those nodes connected to i ($\in n_c$), will contribute to flow or storage at node i. Therefore:

$$\int_V \left(c_{i\beta} x_{i\beta} \frac{k_{jk} k_r}{\mu_\beta} \left(\psi_{\beta J} - \psi_{\beta I} \right) \frac{\partial}{\partial X_k} \left(\sum_{J \neq I} N_J \right) \right) \cdot \frac{\partial N_I}{\partial X_J} dV$$
$$= \sum_{J \in n_c} \left(\psi_{\beta J} - \psi_{\beta I} \right) \int_V \left\{ c_{i\beta} x_{i\beta} \frac{k_{jk} k_{r\beta}}{\mu_\beta} \frac{\partial N_J}{\partial X_k} \frac{\partial N_I}{\partial X_J} \right\} dV \qquad \text{[A-16]}$$

The permeability used in this expression is taken as the harmonic mean of the permeabilities of nodes i and j, whereas the flux term is always taken as the upstream value. This is due to the hyperbolic nature of the governing equations. The molecular density and mass density terms are not upstream weighted, but are centrally weighted between nodes i and j. With this, equation A16 becomes:

$$\sum_{J \in n_c} \left(\psi_{\beta J} - \psi_{\beta I} \right) \int_V \left\{ c_{i\beta} x_{i\beta} \frac{k_{jk} k_r}{\mu_\beta} \frac{\partial N_J}{\partial X_k} \frac{\partial N_I}{\partial X_J} \right\} dV$$
$$= -\left[\sum_{J \in n_c} \left(\psi_{\beta J} - \psi_{\beta I} \right) \left(c_{i\beta} x_{i\beta} \frac{k_{jk} k_r}{\mu_\beta} \right)_{UPS(I,J)} \gamma_{IJ} \right] \qquad \text{[A-17]}$$

where:

$$\psi_{\beta I} = P_{\beta I} + \rho_{(\beta,IJ+1/2)} g z_I$$

$$\rho_{(\beta,IJ+1/2)} = \frac{\left(\rho_{\beta I} + \rho_{\beta J}\right)}{2} \qquad \text{[A-18],[A-19],[A-20]}$$

$$\left(c_{i\beta} x_{i\beta} \frac{k_{r\beta}}{\mu_\beta}\right)_{upst(I,J)} = \begin{cases} \left(c_{i\beta} x_{i\beta} \frac{k_{r\beta}}{\mu_\beta}\right)_I & if\, \gamma_{IJ}\left(\psi_{\beta J} - \psi_{\beta I}\right) \succ 0 \\ \left(c_{i\beta} x_{i\beta} \frac{k_{r\beta}}{\mu_\beta}\right)_J & if\, \gamma_{IJ}\left(\psi_{\beta J} - \psi_{\beta I}\right) \prec 0 \end{cases}$$

The term γ_{IJ} is given by:

$$\gamma_{IJ} = -\int_V \frac{\partial N_I}{\partial X_j} \cdot \tilde{k}_{jk} \cdot \frac{\partial N_J}{\partial X_k} dV \qquad \text{[A-21]}$$

where the harmonic permeability is given as:

$$\tilde{k}_{jk} = \frac{2 k_{I_{jk}} k_{J_{jk}}}{k_{I_{jk}} + k_{J_{jk}}} \qquad \text{[A-22]}$$

The preceding procedure has only looked at the advective flux components of the governing equations. The non-advective flux terms in A7 can be manipulated in the same way as the advective terms to give:

$$-\int_V \frac{\partial}{\partial X_j}\left[\phi S_\beta D_{i\beta_{jk}} \frac{\partial}{\partial X_k}\left(c_{i\beta} x_{i\beta}\right)\right] \cdot N_I dV = -\sum_{J \in n_c} \left(c_{i\beta}\right)_{IJ+1/2} \left(\gamma'_{IJ}\right)_\beta \left(x_{i\beta_J} - x_{i\beta_I}\right) \qquad \text{[A-23]}$$

The term γ'_{IJ} is given by:

$$\gamma'_{IJ} = -\left(S_\beta\right)^{N+1}_{IJ+1/2} \cdot \int_V \frac{\partial N_I}{\partial X_j} \cdot \left(\phi D_{i\beta_{jk}}\right)^N \cdot \frac{\partial N_J}{\partial X_j} \qquad \text{[A-24]}$$

where the $ij_{+1/2}$ terms are evaluated as for the advective terms. Combination of the discretized terms for the time derivative, the advective and non-advective fluxes and the sink/source and mass transfer terms yields the final discretized equation obtained through the CVFE method:

$$\begin{aligned} R^\beta_{i,I} \equiv & \left\{\left[\phi S_\beta c_{i\beta} x_{i\beta}\right]^{N+1}_I - \left[\phi S_\beta c_{i\beta} x_{i\beta}\right]^N_I\right\}\frac{V_I}{\Delta t} \\ & - \left[\sum_{J\in n_e}\left(\psi^{N+1}_{\beta J} - \psi^{N+1}_{\beta I}\right)\left(c_{i\beta} x_{i\beta}\frac{k_{r\beta}}{\mu_\beta}\right)^{N+1}_{ups(I,J)}\gamma_{IJ}\right] \\ & - \left[\sum_{J\in n_e}\left(c_{i\beta}\right)^{N+1}_{IJ+1/2}\left(\gamma'_{IJ}\right)_\beta\left(x_{i\beta_J} - x_{i\beta_I}\right)^{N+1}\right] \\ & - \left\{q_{i\beta} - I_{i\beta}\right\}^{N+1} V_I = 0 \end{aligned} \qquad \text{[A-25]}$$

where V_I is the volume associated with node i and is given by:

$$V_I = \int_V N_I dV \qquad \text{[A-26]}$$

The basis functions used in the formulation must first be evaluated. Using the method proposed by Huyakorn and Pinder (1983), the basis functions N_I are defined as:

$$N_I = \frac{1}{L_e}\left(a_I + b_I X\right) \qquad \text{[A-27]}$$

where:

$$a_I = X_I^{m+1}$$
$$b_I = -1 \qquad \text{[A-28]}$$
$$L_e = \left| X_I^m - X_I^{m+1} \right|$$

where L_e is the length of the element, and m corresponds to node i and $m+1$ to node j. The γ_{IJ} term is obtained by replacing the derivative of N_I such that:

$$\gamma_{IJ} = -\int_V \frac{\partial N_I}{\partial X_j} \cdot \tilde{k}_{jk} \cdot \frac{\partial N_J}{\partial X_k} dV$$
$$= -\frac{1}{L_e^2} \int_x b_I \cdot \tilde{k} \cdot b_J dx \qquad \text{[A-29]}$$
$$= \frac{\tilde{k}}{L_e}$$

The nodal volume used in the formulation for one-dimension, which represents the contribution of volume from node i to node j of element e, is given by:

$$V_I^J = \frac{\gamma_{IJ}}{2} \left[(X_I - X_J)^2 \frac{1}{\tilde{k}} \right] \qquad \text{[A-30]}$$

which reduces to $L_e/2$. The volume associated with node i is:

$$V_I = \sum_{J \in n_e} V_I^J \qquad \text{[A-31]}$$

which reduces to L_e in one dimension.

A.2 Solution Technique

Given the non-linearity of the governing equations, full Newton-Raphson iteration was required. The resulting matrix equation has the form:

$$F'\left(X^k\right)\cdot\left(X^{k+1}-X^k\right)=-F\left(X^k\right) \qquad \text{[A-32]}$$

where X^k is the known solution at the last iterative level, $F'(X^k)$ is the Jacobian evaluated at X^k, and $F(X^k)$ is the vector of equation A25 at X^k. For a two-phase, two-component system, this results in a 4n by 4n matrix. For the special case where only one component is soluble in the other, this produces a 3n by 3n matrix.

The form of the Jacobian is a block tri-diagonal matrix, with each entry consisting of a 3 by 3 sub-matrix. The independent equations A25 are ordered into a vector:

$$(F)^T=\left(R^w_{1,1},R^w_{2,1},R^{nw}_{2,1},.....,R^w_{1,nn},R^w_{2,nn},R^{nv}_{2,nn}\right) \qquad \text{[A-33]}$$

as are the unknowns for these equations:

$$(\chi)^T=\left(P_{w,1},x_{2w,1},S_{w,1},.....,P_{w,nn},x_{2w,nn},S_{w,nn}\right) \qquad \text{[A-34]}$$

With this formulation, each row of the matrix for a one-dimensional problem consists of:

$$\begin{array}{ccc|ccc|ccc}
\frac{\partial R^{w}_{1,I}}{\partial P_{w,I-1}} & \frac{\partial R^{w}_{1,I}}{\partial x_{2w,I-1}} & \frac{\partial R^{w}_{1,I}}{\partial S_{w,I-1}} & \frac{\partial R^{w}_{1,I}}{\partial P_{w,I}} & \frac{\partial R^{w}_{1,I}}{\partial x_{2w,I}} & \frac{\partial R^{w}_{1,I}}{\partial S_{w,I}} & \frac{\partial R^{w}_{1,I}}{\partial P_{w,I+1}} & \frac{\partial R^{w}_{1,I}}{\partial x_{2w,I+1}} & \frac{\partial R^{w}_{1,I}}{\partial S_{w,I+1}} \\
\frac{\partial R^{w}_{2,I}}{\partial P_{w,I-1}} & \frac{\partial R^{w}_{2,I}}{\partial x_{2w,I-1}} & \frac{\partial R^{w}_{2,I}}{\partial S_{w,I-1}} & \frac{\partial R^{w}_{2,I}}{\partial P_{w,I}} & \frac{\partial R^{w}_{2,I}}{\partial x_{2w,I}} & \frac{\partial R^{w}_{2,I}}{\partial S_{w,I}} & \frac{\partial R^{w}_{2,I}}{\partial P_{w,I+1}} & \frac{\partial R^{w}_{2,I}}{\partial x_{2w,I+1}} & \frac{\partial R^{w}_{2,I}}{\partial S_{w,I+1}} \\
\frac{\partial R^{nw}_{2,nw}}{\partial P_{w,I-1}} & \frac{\partial R^{nw}_{2,nw}}{\partial x_{2w,I-1}} & \frac{\partial R^{nw}_{2,nw}}{\partial S_{w,I-1}} & \frac{\partial R^{nw}_{2,nw}}{\partial P_{w,I}} & \frac{\partial R^{nw}_{2,nw}}{\partial x_{2w,I}} & \frac{\partial R^{nw}_{2,nw}}{\partial S_{w,I}} & \frac{\partial R^{nw}_{2,nw}}{\partial P_{w,I+1}} & \frac{\partial R^{nw}_{2,nw}}{\partial x_{2w,I+1}} & \frac{\partial R^{nw}_{2,nw}}{\partial S_{w,I+1}}
\end{array}$$

The Jacobian matrix can be developed through either numerical or analytical methods. Given that the constitutive relationships are known and fixed for this work, the analytical approach was used.

The resulting set of linearized equations is solved using a direct Gaussian elimination procedure. This procedure, though slow, is adequate for one-dimensional simulations and extremely robust (as long as care is taken to avoid a zero pivot), and accurate to the precision of the machine.

A.3 Boundary Conditions

In addition to the discretized governing equations and a set of initial conditions, every numerical model requires a set of boundary conditions to make it tractable. The incorporation of boundary conditions was done via a method similar to that of Forsyth (1988), in which the sink/source terms in equation A25 are modified at each boundary node to simulate any possible condition.

For Dirchlet type conditions, the source sink terms are set to:

$$q_{i\beta,B} = W_I\left(A^{*} - A_B\right) \qquad \text{[A-35]}$$

where A^* is the fixed value of the condition (be it pressure, saturation, or mole fraction), A_B is the value at the boundary node, and W_I is a very large number (i.e. 10^{20}). The result of this manipulation is a very large number on the diagonal of the Jacobian for that variable. This forces the solution $\Delta A \cong 0$.

For free-exit boundary conditions, the source/sink term is modified at the boundary nodes by:

$$q_{iw,B} = -Q_{w,B} c_{nw,B} x_{iw,B} \qquad \text{[A-36]}$$

where $Q_{w,B}$ is the volume flux of wetting phase leaving the domain at the boundary node. In the case where two phases are present in the boundary node, and the effective permeability of one phase is restricted in some form (i.e. cannot enter or exit) the calculation of $Q_{w,B}$ must take into account the direction of the nonwetting phase flux (Reitsma, 1996). For example, when the flux of the nonwetting phase is from the boundary node into the domain, $Q_{w,B}$ is the sum of the wetting and nonwetting phase fluxes from the domain to the boundary. When the nonwetting phase flux is from the domain to the boundary, $Q_{w,B}$ is the flux of the wetting phase only from the domain to the boundary.

The source/sink terms for the nonwetting phase equations at the boundary node given a free exit boundary condition are:

$$q_{inw,B} = \begin{cases} -Q_{nw,B} C_{inw,B} x_{inw,B} & Q_{nw,B} > 0 \\ 0 & Q_{nw,B} < 0 \end{cases} \qquad \text{[A-37]}$$

where $Q_{nw,B}$ is the nonwetting phase flux from the domain to the boundary. The formulation of the free exit boundary condition only allows for advective flux to leave the domain.

For Cauchy type boundary conditions, the source/sink term for the wetting phase is:

$$q_{iw,B} = -Q_{w,B} c^{\bullet}_{nw,B} x^{\bullet}_{iw,B} \qquad \text{[A-38]}$$

where $c^{\bullet}_{nw,B}$ is the molar density of the entering fluid, and $x^{\bullet}_{iw,B}$ is the mole fraction of component i in the entering fluid.

It should be noted that the numerical procedures for the free-exit and Cauchy boundary conditions require modification of off-diagonal terms in the Jacobian matrix. This is due to the fact that changes in primary variables away from the boundary nodes will have an effect on the fluxes to the boundary nodes and thus on the boundary conditions. The formulation of the Cauchy and free-exit boundary conditions is identical, the difference in terminology being used to differentiate between inlet and outlet conditions.

A.4 Model Verification - Two Phase Flow

The model developed in this work cannot be fully verified against an analytical solution, due to the large numbers of complexities involved in the various underlying processes. Two specific aspects of the model can, however, be checked against analytical solutions to ensure they are converging to the correct solution. The first check is for two-phase flow in a porous medium

with capillary effects. The analytical solution by McWhorter and Sunada (1990) was used, and consisted of a one-dimensional horizontal column containing a non-deforming homogeneous porous medium initially saturated with wetting phase throughout.

The boundary conditions imposed upon the analytical solution are; a constant wetting phase saturation at the injection end, a no-flow boundary (for the wetting phase) at the injection end, and a constant wetting phase pressure at the outlet. The analytical solution is valid so long as the nonwetting phase never reaches the exit boundary. A Brooks-Corey type capillary pressure curve (Brooks and Corey, 1966) was used in both the analytical and numerical formulations.

The porous medium in the column was assigned a permeability of $1x10^{-11}$ m^2, a porosity of 0.35, a pore size distribution index of 2.0, a residual wetting phase saturation of 0.1, and a displacement pressure of 3000 Pa. The wetting and nonwetting phase viscosities were $8.9x10^{-4}$ Pa-s, the length of the column was 0.625 m, the inlet wetting phase saturation was 0.5, and the outlet pressure was 0.0 Pa. Figure A-1 presents the wetting phase saturation profiles with distance along the column at three different times for both the analytical and numerical simulations. The numerical model is in agreement with the analytical solution and all mass balance errors were less than $1.0x10^{-7}$ moles.

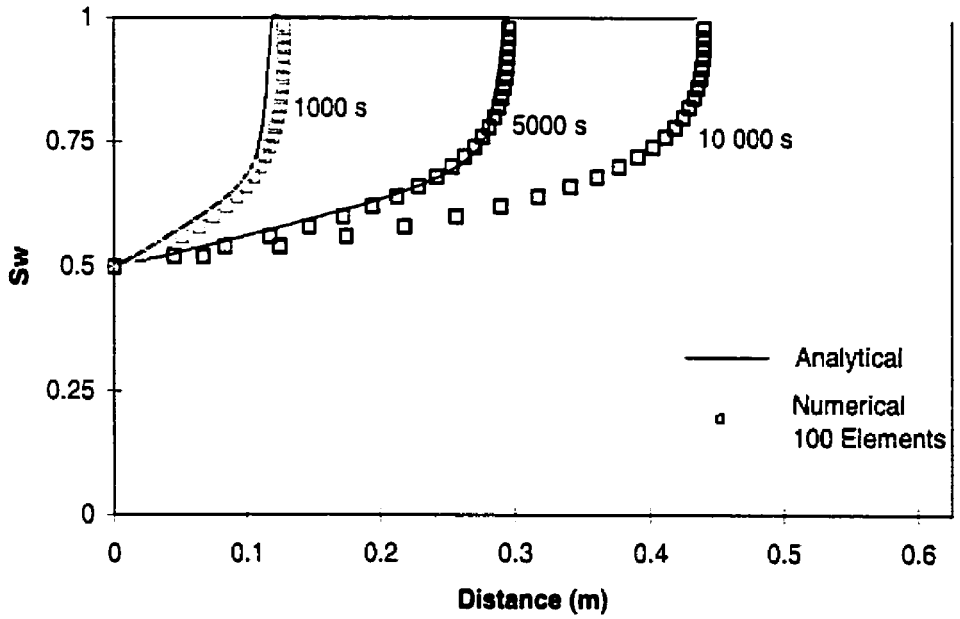

Figure A-1. Model Comparison to Analytical Solution for Two-Phase Flow

A.5 Model Verification - Mass Transport

The second facet of the numerical model that could be verified against an analytical solution is advection-dispersion mass transport. The analytical solution used was the Ogata and Banks (1961) formulation, modified by Gershon and Nir (1969) to include Cauchy boundary conditions. The physical setting was once again a horizontal one-dimensional column initially saturated with wetting phase, in a homogeneous incompressible porous medium. The flow was single phase, constant and steady state.

Boundary conditions for the simulations were:

$$C(\infty,t)=0 \qquad t\geq 0 \qquad \text{[A-39]}$$

$$vC(0,t) - D\frac{\partial C(0,t)}{\partial x} = vC_o \qquad t \geq 0 \qquad \text{[A-40]}$$

where C is the solute concentration, x is the distance from the inlet of the column, t is the elapsed time, v is the average linear velocity in the column, D is the dispersion coefficient, and C_o is the concentration of the solute in the injected fluid. The initial conditions were:

$$C(x,t) = 0 \qquad \text{[A-41]}$$

The analytical solution is:

$$\frac{C}{C_o} = \frac{1}{2}\left(erfc\left(\frac{x-vt}{2\sqrt{Dt}} \right) - \exp\left(\frac{vx}{D} \right) erfc\left(\frac{x+vt}{2\sqrt{Dt}} \right)\left(1 + \frac{vx+v^2t}{D} \right)\right) + \frac{v\sqrt{t}}{\sqrt{\pi D}} \exp\left(-\frac{(x-vt)^2}{4Dt} \right) \qquad \text{[A-42]}$$

where *erfc* is the complimentary error function. The outlet boundary condition in the numerical model was free exit, and the dispersion coefficient was defined as:

$$D = \alpha_L v + \tau D_i^* \qquad \text{[A-43]}$$

where α_L is the longitudinal dispersivity, τ is the tortuosity of the medium, and D_i^* is the free-liquid diffusivity of the solute in water. The value of the dispersivity was 0.1m while the tortuosity was set to 0.0. The porous medium was assigned physical parameters identical to that of the two-phase simulations with the exception that the column was 1.0 m in length. The gradient across the column was specified such that the average linear velocity in the column was constant at $1.405 \times 10^{-3} m \cdot s^{-1}$.

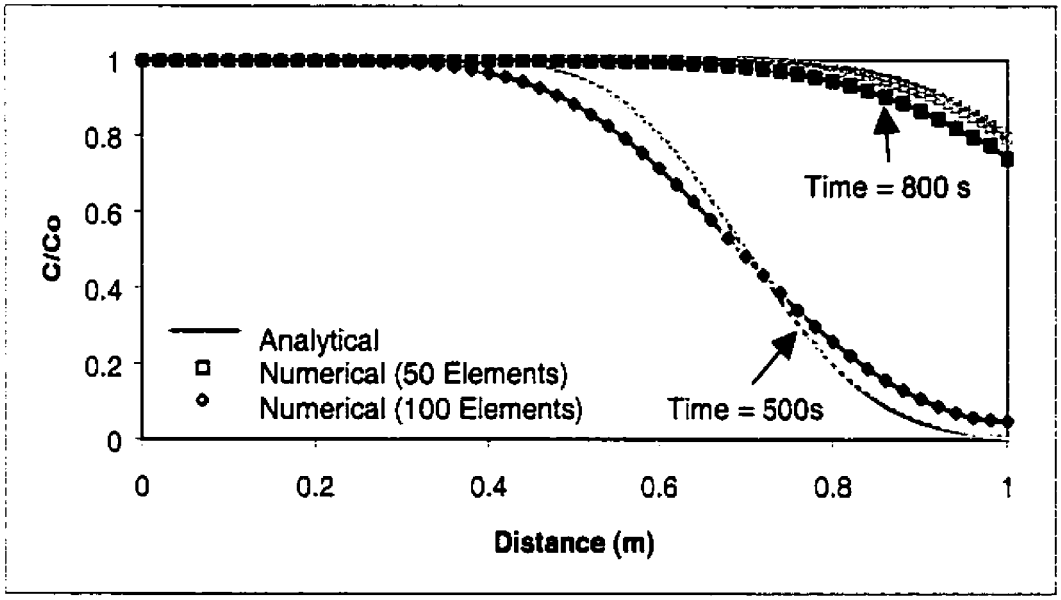

Figure A-2. Model Comparison to Analytical Solution for Mass Transport

Figure A-2 depicts the verification results for the advection-dispersion simulations. The smearing introduced through numerical dispersion due to coarse griding is evident, however the greater accuracy of finer griding produces a reasonable approximation.

A.6 Model Testing - Heterogeneous Media

The third stage in the verification and validation procedure is to test the models performance on physical scenarios that are more realistic. No exact solutions exist for the simulations carried out in this section and comparison to laboratory data is beyond the scope of this work. Despite these problems, it was felt that some basic one-dimensional studies could be undertaken, given that one-dimensional two-phase flow is a relatively well-understood concept, and validated models do exist for this phenomenon.

The scenarios used in this stage of the testing were quite similar to those used in the analytical comparison. The properties used are summarized in Table A-1. The only significant conceptual variations between these runs and the analytical comparison is that the column was oriented vertically to ensure the model could accurately simulate the effects of gravity, and various lenses of differing permeabilities were introduced to evaluate the effects of heterogeneity.

Figure A-3 displays the evolving wetting phase profiles for the four scenarios simulated. Part A depicts a homogeneous column similar to that of the analytical comparison. Unlike the horizontal runs, however, the nonwetting phase is not retarded with time, due to the presence of gravity, and flows through the column in a relatively uniform manner, first reaching the exit at 2766 s. The typical "s" shape of vertical two-phase profiles (Aziz and Settari, 1979) is evident in the developing profile.

Part B of Figure A-3 is identical to Part A with the exception that a high permeability (5.0×10^{-10} m^2) lens is located in the centre of the column. The evolving wetting phase profile shows that the nonwetting fluid quickly imbibes into the high permeability lens immediately upon encountering it. The lens continues to fill while the nonwetting phase attempts to enter the low permeability sand beneath it. Once the capillary pressure in the lens has exceeded the entry pressure of the general sand, the nonwetting phase quickly traverses the remainder of the column, first exiting at 3291 s.

Table A-1. Physical Properties of Column Used in Verification

Porosity	0.35
Length	1.0 m
Residual Wetting Phase Saturation	0.05
Permeability	5.0×10^{-11} m^2
Pore Size Distribution Index	2.5
Displacement Pressure	2000.0 Pa
Wetting Phase Viscosity	1.0×10^{-3} Pa·s
Nonwetting Phase Viscosity	0.5×10^{-3} Pa·s
Inflow Boundary Saturation	0.5
Outflow Boundary Pressure	9.806×10^{3} Pa

Part C of Figure A-3 is showing the results of a simulation identical to that of Part B with the exception that the high permeability lens has been replaced with a low permeability lens (5.0×10^{-12} m^2). Unlike the previous scenario, the nonwetting fluid initially cannot penetrate the lens, and pools above it until the 2209.4 Pa entry pressure of the lens is exceeded. This results in an extremely low wetting phase saturation above the lens and an inverse "s" saturation profile. Once the displacement pressure of the lens has been exceeded, the nonwetting phase continues towards the terminus of the column and first reaches it at 44 041 s.

The final portion of Figure A-3 (Part D) is for a column composed of completely heterogeneous media. Each node in the domain was randomly assigned permeability values from a log-normal distribution with a mean of 1.03×10^{-11} m^2 and a variance large enough to ensure that the maximum and minimum permeabilities were separated by three orders of magnitude. The

profile shown is for a time of 100 000 s, showing the large times required for the nonwetting front to traverse completely heterogeneous media. This is considered an extremely demanding test of the model, to ensure that fluid saturations are discontinuous between nodes, and pressures are continuous.

A.7 Model Testing - Mass Transfer

The verification of the model's ability to simulate mass transfer was the most difficult to develop a foundation for. Similar to the heterogeneous simulations, no exact analytical solution exists for this scenario. Increasing the difficulties is that at this point in the model development process, the actual form of the mass transfer constitutive relationship is unknown. A relatively simple check could be made, however, to ensure that the model is fulfilling its conservation of mass formulation and that it can converge when all aspects of its formulation (two-phase flow, mass transport, and mass transfer) are considered.

To check on mass conservation, the one-dimensional column from the mass transport scenarios was modified by eliminating the Cauchy inflow condition, and trapping a small amount of nonwetting phase in an element surrounded by elements of lower permeability. This ensured that the nonwetting phase was immobile, and would disappear only through dissolution. A single node, 0.1m from the outflow boundary was set at an initial wetting saturation of 0.95. The two nodes on either side were assigned a permeability of 1.0×10^{-12} m^2. The gradient across the column was set at $\partial h/\partial x = 0.1$, the exit boundary was free exit, and the inflow boundary was modified to prevent diffusion out of the column.

The mass transfer term in the discretized equation was simulated through:

$$I_{2,w} = K'\left(x_{2w} - x_{2w}^{sat}\right)\varepsilon_{in}\Delta t \qquad \text{[A-44]}$$

$$I_{2,nw} = -I_{2w} \qquad \text{[A-45]}$$

where K' is the mass transfer coefficient, and x^{sat}_{iw} is the saturation concentration of component i (nonwetting) in the wetting phase as a mole fraction. Three forms of the mass transfer coefficient were used, a constant value of $2.5\text{x}10^{-3}$, and two forms which were dependent upon the saturation of the node:

$$K' = \left(1 - \left(S_w\right)^a\right)^b_n \qquad \text{[A-46]}$$

The first simulation with this method used coefficients of $a=1.0$ and $b=2.0$. This gave an initial value for K' of $2.5\text{x}10^{-3}$ identical to the constant formulation. The second scenario used coefficients of $a=3.0$ and $b=1.0$.

It should be noted at this point that the formulation for the mass transfer terms is entirely explicit, and involves only the values of wetting phase saturation and mole fraction of component i in the wetting phase. Figures A-4, A-5, and A-6 display the results of the three simulations described above. The initial amount of nonwetting phase trapped in the system is 1.215 moles, and the mass balance in each system is less than $1.0\text{x}10^{-7}$ moles. The effects of the different mass transfer formulations are distinct, the major difference being in the rate at which the nonwetting phase is dissolved from the "trapped" node. In the constant K' case the effect is similar to that of equilibrium mass transfer, as the system is at quasi-steady state until the non-aqueous phase is fully dissolved.

The variable mass transfer coefficient formulations are more truly non-equilibrium, in that after several thousand seconds the dissolved values in the "trapped" node are no longer at the original levels. The differences in behaviour between the two representations of mass transfer indicate the wide variety of possibilities that exist to parameterize the phenomenon.

The final scenario in the one-dimensional validation and verification is the "everything" simulation. The column from the analytical two-phase flow scenario was used, with the addition of the variable *K'* mass transfer formulation. Figure A-7 displays the wetting phase saturation profile, and the dissolved plume mole fraction profile. Conceptually, everything is as would be expected, the inclusion of the mass transfer term has not slowed or accelerated the invading nonwetting phase appreciably, the maximum concentration in the system does not exceed the saturation concentration of component *i* in the wetting phase, and the dissolved plume is migrating ahead of the nonwetting phase front.

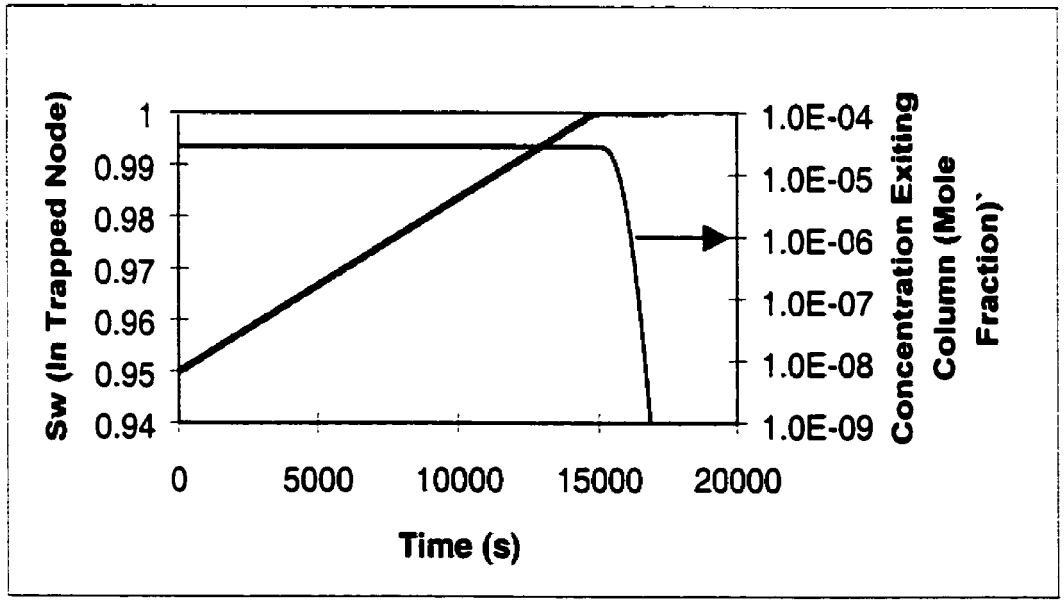

Figure A-4. Mass Transfer Validation, Constant K'

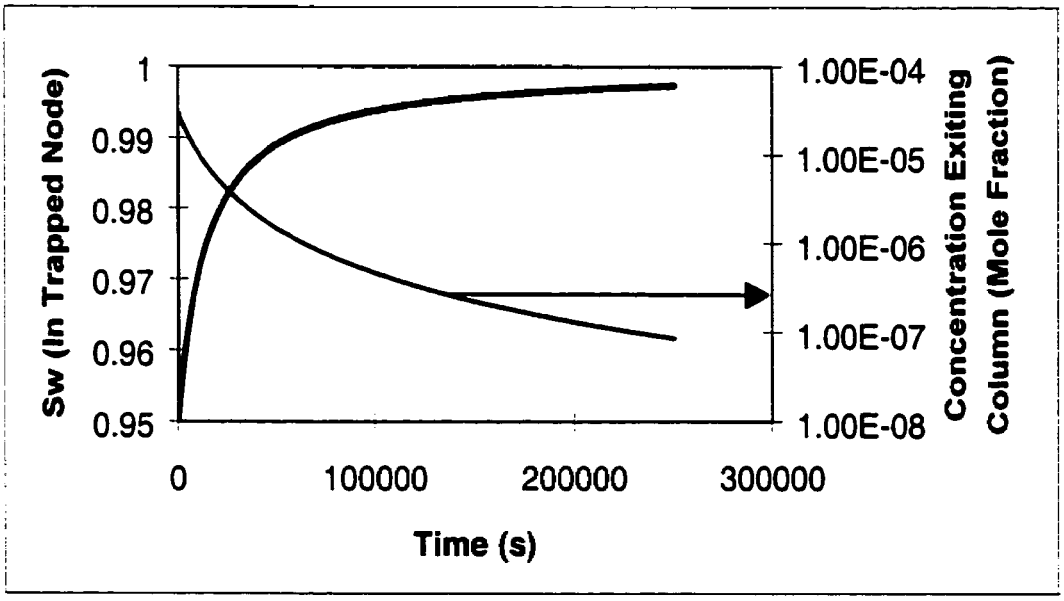

Figure A-5. Mass Transfer Validation, a=2.0, b=1.0

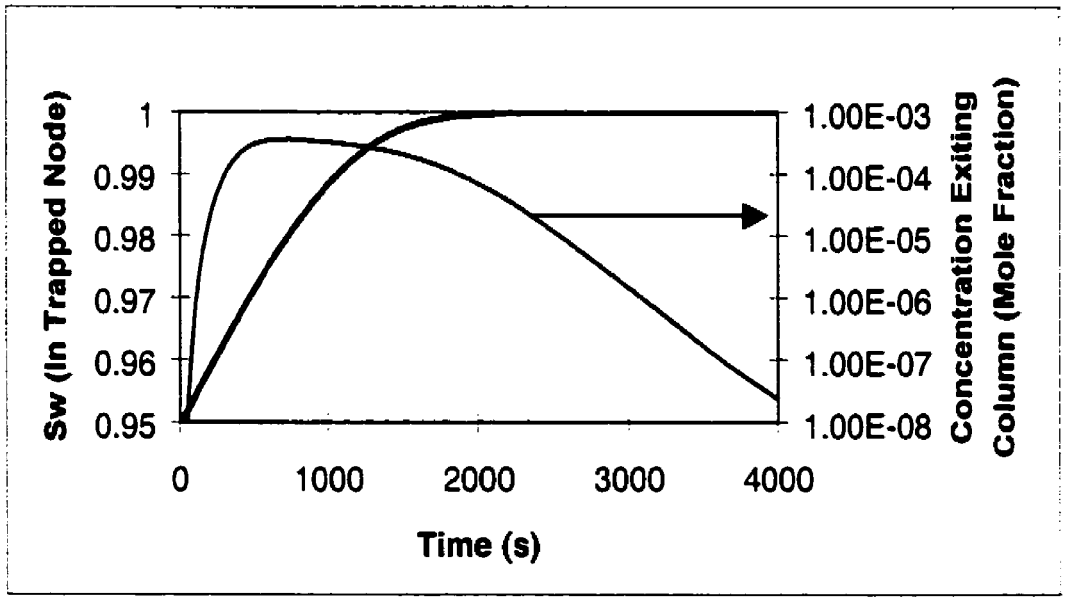

Figure A-6. Mass Transfer Validation, a=3.0, b=1.0

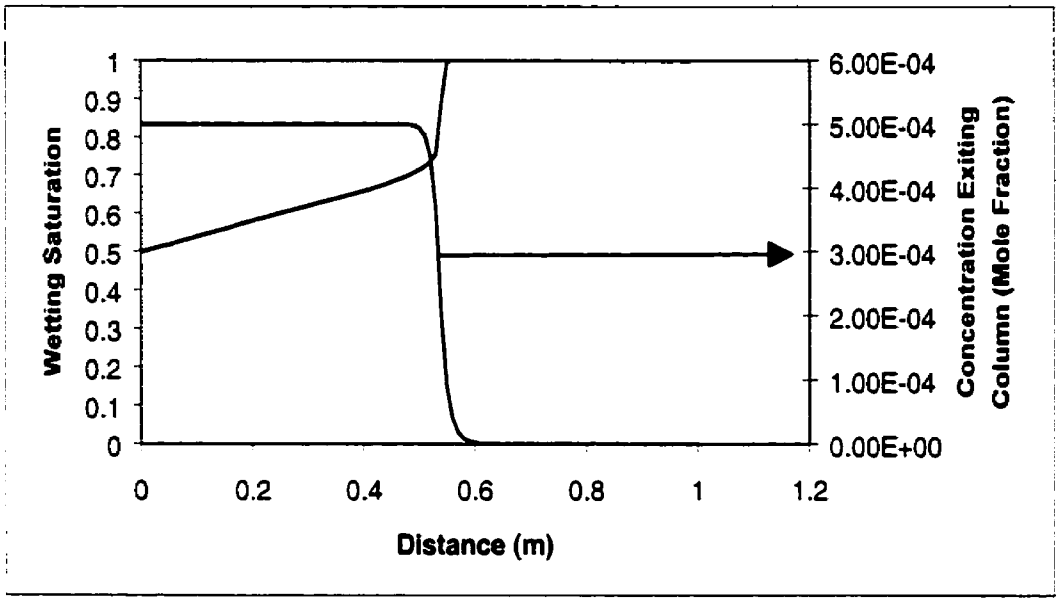

Figure A-7. Wetting Phase Saturations and Mole Fractions Predicted by One-dimensional Model Run

A.8 References

Abriola, L.M., and G.F. Pinder. 1985. A Multiphase Approach to the Modelling of Porous Media Contamination by Organic Compounds; Numerical Simulation, *Water Res. Res.*, 21(1), p 19-26.

Aziz, K., and A. Settari. 1979. Petroleum Reservoir Simulation, Applied Science, London

Brooks, R.H., and A.T. Corey. 1964. Hydraulic Properties of Porous Media, Hydrol. Pap. 3, Colorado State University, Fort Collins, Co.

Forsyth, P.A. 1988. Comparison of the Single-phase and Two-phase Numerical Formulation for Saturated-unsaturated Groundwater Flow, *Comput. Methods Appl. Mech. Engr.*, 69, p 243-259.

Forsyth, P.A. 1991. A Control Volume Finite Element Approach to NAPL Groundwater Contamination, *SIAM J. Sci. Stat. Comput.*, 2(5), p 1029-1057.

Gershon, N. and A. Nir. 1969. Effects of Boundary Conditions of Models on Tracer Distribution in Flow Through Porous Media, *Water Res. Res.*, 5, p 830-839.

Huyakorn, P.S., and G.F. Pinder. 1983. Computational Methods in Subsurface Flow, Academic Press, New York, NY, 473 pgs.

Letniowski, F.W. 1989. Numerical Methods for Nonaqueous Phase Liquid Groundwater Contamination in Three Dimensions, M.Math. Thesis, University of Waterloo, Waterloo, Ontario, 98 pgs.

McWhorter, D.B., and D.K. Sunada. 1990. Exact Integral Solutions for Two-phase Flow, *Water Res. Res.*, 26(3), p 399-413.

Ogata, A., and R.B. Banks. 1961. A Solution of the Differential Equation of Longitudinal Dispersion in Porous Media, U.S.G.S. Prof. Paper 411-A.

Reitsma, S. 1996. Equilibrium and Non-equilibrium Compositional Alcohol Flooding Models for Recovery of Immiscible Liquids from Porous Media, Ph.D. Thesis, Department of Civil Engineering, Queen's University, Kingston, Ontario, Canada, 192 pgs.

Therrien, R. 1992. Three-Dimensional Analysis of Variably-saturated Flow and Solute Transport in Discretely-fractured Porous Media, Ph.D. Thesis, University of Waterloo, Waterloo, Ontario.

APPENDIX B - TWO-DIMENSIONAL CONTROL VOLUME FINITE ELEMENT MODEL DEVELOPMENT AND VERIFICATION

Model Description

The two-dimensional model developed in this appendix is solved through the use of a control volume, finite element approach, and can handle the advection of the wetting and nonwetting phases, as well as the dispersion, diffusion, and sorption of the aqueous phase. The formulation is a superposition of triangular elements representing the matrix, and line elements representing fracture traces. The nonwetting phase cannot enter the matrix in the present formulation.

B.1 Solution of the Governing Equations

The solution procedure for the governing differential equations is unchanged from the one-dimensional model described in Appendix A. The CVFE approach is again used, with the exception that linear triangular elements are used in place of line elements. The most significant change involved in the solution of the equations involves the use of a new method to solve the resultant sparse Jacobian matrix.

In the one-dimensional model the resultant set of linearized equations was solved with direct Gaussian elimination. Though entirely adequate for simple dense matrices, the cost of that

procedure is extremely prohibitive for the large sparse matrices that will be encountered in this work. To overcome this, a specially designed sparse matrix solver was required which could operate on non-symmetrical matrices. Using methods outlined by Barrett et al. (1994) two different preconditioned solvers (GMRES and BCGStab) were added to the model. GMRES (Saad and Schultz, 1986) is a Generalized Minimal Residual method that minimizes the norm of the residual vector at every iteration over a Krylov subspace. BCGStab (Van der Vorst, 1992) is similar to the standard conjugate gradient method, with the exception that the orthogonal sequence of residuals generated through the Conjugate Gradient method is replaced by two mutually orthogonal vectors.

B.2 Two-dimensional Basis Functions and Influence Coefficients

The extension of the model to two-dimensions required the adaptation of the element basis functions and the resultant changes to the influence coefficients. For two-dimensional triangular elements, the linear basis functions can be given by:

$$N_i = \frac{1}{2A_e}(a_i + b_i X + c_i Y) \qquad \text{[B-1]}$$

where:

$$b_i = -\begin{vmatrix} 1 & Y_i^{m+1} \\ 1 & Y_i^{m+2} \end{vmatrix} \qquad c_i = -\begin{vmatrix} X_i^{m+1} & 1 \\ X_i^{m+2} & 1 \end{vmatrix} \qquad a_i = \begin{vmatrix} X_i^{m+1} & Y_i^{m+1} \\ X_i^{m+2} & Y_i^{m+2} \end{vmatrix} \qquad \text{[B-2]}$$

and the area of the triangular element (A_e) is:

$$A_e = \frac{1}{2}\begin{vmatrix} 1 & X_i^m & Y_i^m \\ 1 & X_i^{m+1} & Y_i^{m+1} \\ 1 & X_i^{m+2} & Y_i^{m+2} \end{vmatrix} \qquad \text{[B-3]}$$

The node number of the element at the local-scale (m) corresponds to node *i* of the *ij* pair, and the subsequent nodes are identified by the sequential index (*m+1*, *m+2*) in a counter-clockwise fashion around the element. In addition, the incremental volume, V_I^J, representing the volume contribution to node *i* from node *j* is:

$$V_I^J = \frac{\gamma_{IJ}}{4}\left[(X_I - X_J)^2 \frac{1}{\tilde{k}_x} + (Y_I - Y_J)^2 \frac{1}{\tilde{k}_y}\right] \qquad \text{[B-4]}$$

The influence coefficients for the advective (γ_{IJ}) and non-advective (γ'_{IJ}) flux terms are found through the substitution of the derivative of the two-dimensional representation of N_I into:

$$\gamma_{IJ} = -\int \frac{\partial N_I}{\partial X_j} \tilde{k}_{jk} \frac{\partial N_J}{\partial X_k} dV \qquad \text{[B-5]}$$

Giving:

$$= -\frac{1}{4A_e}\left[\left(Y_I^{m+1} - Y_I^{m+2}\right)\left(Y_J^{n+1} - Y_J^{n+2}\right)\tilde{k}_x + \left(X_I^{m+2} - X_I^{m+1}\right)\left(X_J^{n+2} - X_J^{n+1}\right)\tilde{k}_y\right] \qquad \text{[B-6]}$$

The node number of the element at the local-scale (*n*) applies to node *j* of the *ij* pair, and are numbered similarly to *m*. The non-advective flux term influence coefficient is found through a similar method, with the exception that the harmonic mean permeability is replaced with the dispersion tensor:

$$\gamma'_{IJ} = -(S_w)_{IJ+1/2}^{N+1} \int \frac{\partial N_I}{\partial X_j}\left(\frac{\phi S_w D_{iw_k}}{S_w}\right)^N \frac{\partial N_J}{\partial X_k} dV \qquad \text{[B-7]}$$

where:

$$\phi S_w D_{iw} = (\alpha_l - \alpha_t)\frac{v_i v_j}{|v_i|} + \alpha_t |v_i| \delta_{ij} + \phi S_w \tau D_w^* \delta_{ij} \qquad \text{[B-8]}$$

The division of the dispersion tensor within the integral by an explicit representation of the saturation and the subsequent multiplication by a weighted implicit form allows for partial implicit evaluation of the dispersion dependence upon saturation. The advantage of this form is that the integral in (B7) has only to be evaluated at the start of a Newton iteration.

B.3 Other Modifications

B.3.1 Mass Transfer

During the development of the two-dimensional model the mass transfer relationship was finalized, the form taken from the work of Mason and Kueper (1996) which effectively handles the dependence of mass transfer on both velocity and saturation:

$$K = \left(aq^b + k\right)\left(S_w^3 - S_w^5\right) \qquad \text{[B-9]}$$

The evaluation of the mass transfer term is entirely explicit, to prevent possible perturbations in the Newton procedure. The coefficients a and b are taken from the published literature, or can be calibrated from laboratory experiments. The intrinsic mass transfer coefficient (k) is a function of the medium and the particular chemical being used in the simulation.

B.3.2 Flux Limitation

Recently work has been performed to investigate variations to the standard methods of spatial and temporal weighting used in the solution of compositional models (Unger et al., 1995, Liu et al., 1994, and Blunt and Rubin, 1992). Unger et al. (1995) compared the solutions to a set of sample problems achieved by varying the spatial weighting techniques between upstream, central, and flux-limited, and the temporal weighting techniques between fully implicit and Crank-Nicholson. They found that even though Crank-Nicholson is second order correct, no advantage was gained over the first order correct fully implicit weighting method.

In terms of spatial weighting of the advective mole fraction of contaminant in the aqueous phase, however, noticeable improvement was found with the use of a non-linear Van Leer (Van Leer, 1974) type flux limitation scheme. This weighting factor is defined as:

$$(X_{iw})_{FL(i,j)} = (X_{iw})_{ups(i,j)} + \sigma(r_{ij})\left[\frac{(X_{iw})_{dwn(i,j)} - (X_{iw})_{ups(i,j)}}{2}\right] \qquad \text{[B-10]}$$

where $Xiw_{dwn(i,j)}$ is the downstream point between nodes i and j. The smoothness sensor for the mole fraction front, r_{ij}, is defined by:

$$r_{ij} = \begin{cases} \dfrac{(X_{iw})_i - (X_{iw})_{i2up(i,j)}}{(X_{iw})_j - (X_{iw})_i} & \text{if} \quad i = ups(i,j) \\ \dfrac{(X_{iw})_j - (X_{iw})_{j2up(i,j)}}{(X_{iw})_i - (X_{iw})_j} & \text{if} \quad j = ups(i,j) \end{cases} \qquad \text{[B-11]}$$

where *i2up(i,j)* is a second upstream point. The flux limiter is therefore formulated as:

$$\sigma(r_{ij}) = \begin{cases} 0 & \text{if} \quad r_{ij} \le 0 \\ \dfrac{2r_{ij}}{1+r_{ij}} & \text{if} \quad r_{ij} > 0 \end{cases} \qquad \text{[B-12]}$$

The flux limiting scheme for the advective mole fraction is employed to minimize numerical dispersion while maintaining monotonicity of the solution. The choice of the second upstream point in the flux limiter is based upon the node which has the greatest fluid potential of all nodes connected to the first upstream point. The use of a flux limiter requires the modification of the off-diagonal terms in the development of the Jacobian. For simplicity, these were dropped in the assembly routine.

The application of non-linear flux limiters cannot be performed indiscriminately across an entire domain. In portions of the domain where aqueous phase mole fractions are near or at the solubility limit, the application of flux limiters can cause oscillations in the Newton iterations which cannot be resolved (Unger et al., 1995). To avoid this, the limiter was only applied in regions where no non-aqueous phase was present, no sink or source term (other than dissolution) was present, and the aqueous phase mole fraction was less than 95% of saturation.

B.3.3 Equilibrium Sorption

The expansion of the model to two-dimensions presented the opportunity to incorporate another physical phenomenon important in subsurface contamination simulation. The sorption of the dissolved non-aqueous phase to the aquifer material can, depending on the material, be of great importance in the assessment of contamination scenarios. The governing equations for the system described to this point are slightly modified to include the effects of sorption:

$$\frac{\partial}{\partial t}\left(c_{i\beta}\phi\ \ S_\beta x_{i\beta} + \rho_b K_d c_{i\beta} x_{i\beta}\right) + \nabla\cdot\left(c_{i\beta} x_{i\beta} v_\beta\right) - \nabla\cdot\left[\phi\ \ S_\beta D_{i\beta}\nabla\left(c_{i\beta} x_{i\beta}\right)\right] - q_{i\beta} - I_{i\beta} = 0 \qquad \text{[B-13]}$$

$$\beta = 1..n_p, i = 1..n_c$$

where ρ_b is the bulk density of the aquifer material, and K_d is the distribution coefficient for the contaminant.

B.3.4 Storage

The final physical phenomenon included in the model during the expansion to a two-dimensional format was the incorporation of the transient behaviour of flow due to the effects of storage in

$$\frac{\partial}{\partial t}\left(c_{i\beta}\phi\ \ S_\beta x_{i\beta} + \rho_b K_d c_{i\beta} x_{i\beta} + c_{i\beta} x_{i\beta}(\alpha + \beta_w\phi)P_\beta\right) + \nabla\cdot\left(c_{i\beta} x_{i\beta} v_\beta\right) - \nabla\cdot\left[\phi\ \ S_\beta D_{i\beta}\nabla\left(c_{i\beta} x_{i\beta}\right)\right]$$

$$- q_{i\beta} - I_{i\beta} = 0 \qquad \text{[B-14]}$$

$$\beta = 1..n_p, i = 1..n_c$$

the porous medium and the fluids. The inclusion of storage adds another temporal derivative to the governing partial differential equation:

where α is the porous medium compressibility, and β_w is the compressibility of water. The final form of the discretized equation used in the two-dimensional model is:

$$R_{i,I}^{\beta} \equiv \left\{\left[S_\beta c_{i\beta} x_{i\beta}\phi + \rho_b K_d c_{i\beta} x_{i\beta} + c_{i\beta} x_{i\beta}(\alpha + \beta_w\phi)P_w\right]_I^{N+1} - \left[S_\beta c_{i\beta} x_{i\beta}\phi + \rho_b K_d c_{i\beta} x_{i\beta} + c_{i\beta} x_{i\beta}(\alpha + \beta_w\phi)P_w\right]_I^{N}\right\}\frac{V_I}{\Delta t}$$

$$- \left[\sum_{J\in n_c}\left(\psi_{\beta J}^{N+1} - \psi_{\beta I}^{N+1}\right)\left(c_{i\beta} x_{i\beta}\frac{k_{r\beta}}{\mu_\beta}\right)_{upst(I,J)}^{N+1}\gamma_{IJ}\right]$$

$$- \left[\sum_{J\in n_c}\left(c_{i\beta}\right)_{IJ+1/2}^{N+1}\left(\gamma'_{IJ}\right)_\beta\left(x_{i\beta_J} - x_{i\beta_I}\right)^{N+1}\right]$$

$$- \left\{q_{i\beta} - I_{i\beta}\right\}^{N+1} V_I = 0$$

B.4 Model Verification – Two Phase Flow

The two-dimensional model was also verified against the analytical solution of Mcwhorter and Sunada (1990). [B-15] A different physical scenario was used this time, but the boundary conditions and model limitations remained essential the same. The particular values used in this verification are summarized in Table B-1.

Table B-1. Fluid and media properties in the two-phase flow verification

Porosity	0.35
Permeability	5.0×10^{-11} m^2
Brooks-Corey Pore Size Distribution Index	2.0
Displacement Pressure	2000.0 Pa
Residual Wetting Saturation	0.05
Wetting Phase viscosity	0.001 Pa s
Nonwetting Phase Viscosity	0.0005 Pa s
Length	10 m
Inflow Boundary Saturation	0.525
Outflow Boundary Pressure	0.0 Pa

Figure B-1 presents the comparison of the two-dimensional numerical model to the analytical solution, and shows that the results agree within the accuracy of the discretization. The small amount of smearing at the leading edge of the invading NAPL front is due to the use of upstream weighting in the model, but it should be pointed out that this error does not increase with time, as is the case with parabolic equations.

The domain used in this verification consisted of 101 nodes in the longitudinal direction, and 11 in the transverse direction. The value of gravity for the simulation was set to zero, as the analytical solution does not include the effects of gravity. The numerical model's results consisted of 11 identical "flow-tubes" each in turn identical to a one-dimensional representation of the domain.

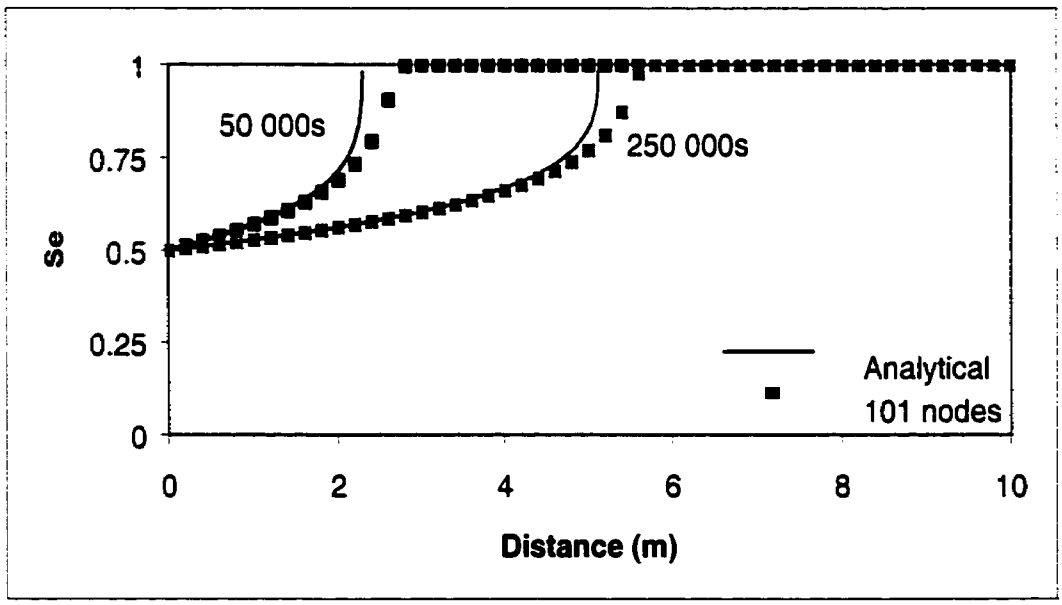

Figure B-1. Model Comparison to Analytical Solution for Two-Phase Flow

The Mcwhorter-Sunada analytical solution represents the limit to which the multi-phase flow behaviour of the numerical model can be verified. Further validation was performed, however, by comparing results of the model to published results of another two-dimensional model that has been verified and validated against a laboratory experiment.

The model of Kueper and Frind (1991) was validated against a parallel plate experiment consisting of infiltrating PCE into a two-dimensional cell packed with lenses of four types of sand. The model of Kueper and Frind (1991) accurately reproduced the laboratory experiment, showing that the governing equations of the model properly represented the mechanics of two-phase flow. The model was then used to predict flow behaviour above a single lens (Kueper and Frind, 1991b). The two-dimensional model developed here was used to re-create one of the simulations which consisted of continuous infiltration of a nonwetting fluid into a two-dimensional domain with a centrally located low permeability lens. Figure B-2 depicts the modelled domain, with the grey area representing the low permeability lens. The entire domain is initially saturated with water, under hydrostatic conditions. The domain is discretized with a uniform 0.02m horizontal node spacing, and a uniform 0.01 m vertical node spacing. The source area is assigned a constant wetting phase saturation of 0.5.

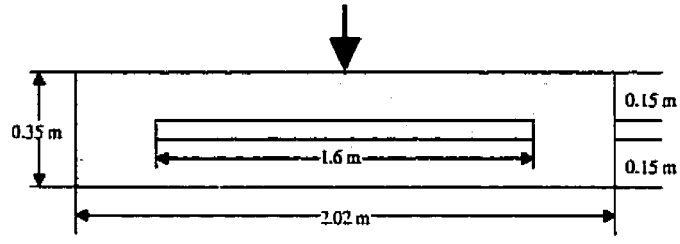

Figure B-2. Two-dimensional Lens Validation Model Domain

The porous media properties for the simulation are provided in Table B-2, and the comparison of results is presented in Figure B-3. Figure B-3 is a snap-shot of the wetting phase saturations of both models after 16550 seconds of infiltration resulting in 0.0177 m^3 of TCE entering the domain. The models are in excellent agreement, with slight lateral spreading along the low permeability lens and higher wetting phase saturations beneath the lens.

Table B-2. Fluid and Media Properties in the 2-D Lens Flow Validation

Host Permeability	7.0×10^{-12} m^2
Lens Permeability	5.0×10^{-12} m^2
Host Displacement Pressure	2218.2 Pa
Lens Displacement Pressure	2760.4 Pa
Porosity	0.34
Brooks-Corey Pore Size Distribution Index	2.48
Residual Wetting Phase Saturation	0.078
Wetting Phase Density	1000 kg/m^3
Nonwetting Phase Density	1460 kg/m^3
Wetting Phase Viscosity	1.0×10^{-3} Pa s
Nonwetting Phase Viscosity	0.57×10^{-3} Pa s

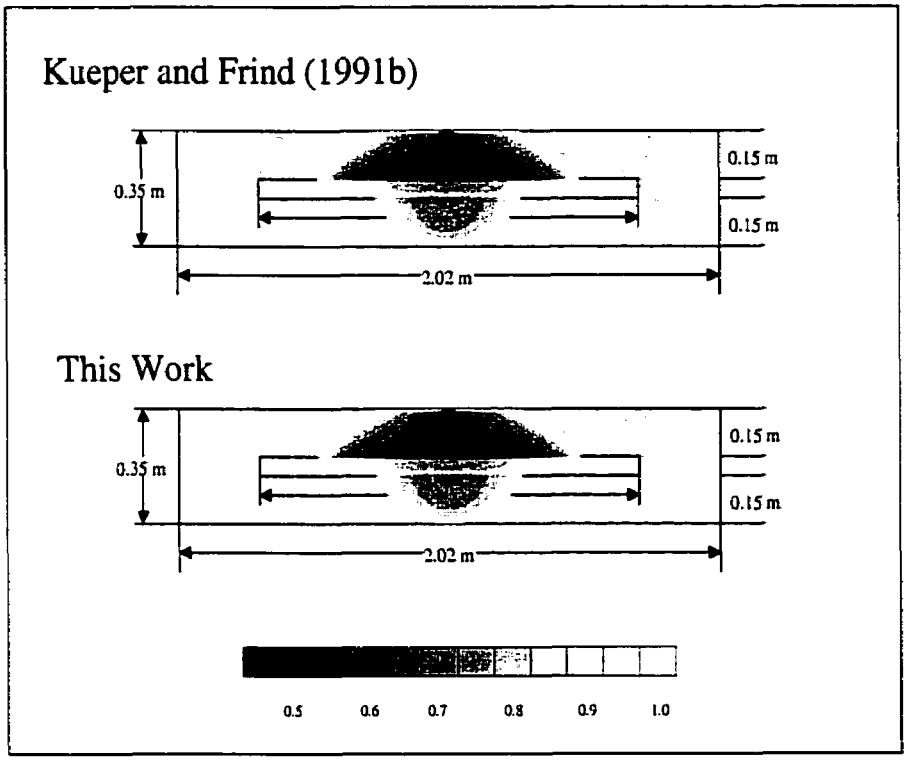

Figure B-3. Comparison of Two-dimensional Model Results to Results of Kueper and Frind (1991b)

B.5 Model Validation – Capillary Hysteresis and Residual Formation

Capillary pressure-saturation relationships have been well documented in the literature for two-phase flow in porous media (Aziz and Settari, 1979). Experimental results have shown that the behaviour of the system changes drastically, depending on whether the saturations are increasing for the first time (main drainage), decreasing or increasing after a previous decrease (wetting), or not changing due to "trapping" of the nonwetting phase. Figure B-4 presents a standard capillary pressure-saturation relationship for a porous system. The capillary pressure-saturation relationship incorporated into the model to this point has simulated the main drainage curve only.

This introduces error into the simulations when nonwetting saturations decrease along an imbibition curve. To overcome this, the ability to recognize the current "state" of each node in the system was added to the model.

An exact representation of the hysteretic behaviour portrayed in Figure B-4 requires large and complex codes that are extremely inefficient from a computational standpoint. To overcome this, but to allow for hysteretic behaviour, the approach of Gerhard et al. (1998) is adopted. The main component of this method involves the linear approximation of the wetting curves from Figure B-4. The line representations are based on the highest saturation achieved along main drainage, and the incorporation of an initial-residual relationship that sets the saturation of the system at a capillary pressure of zero.

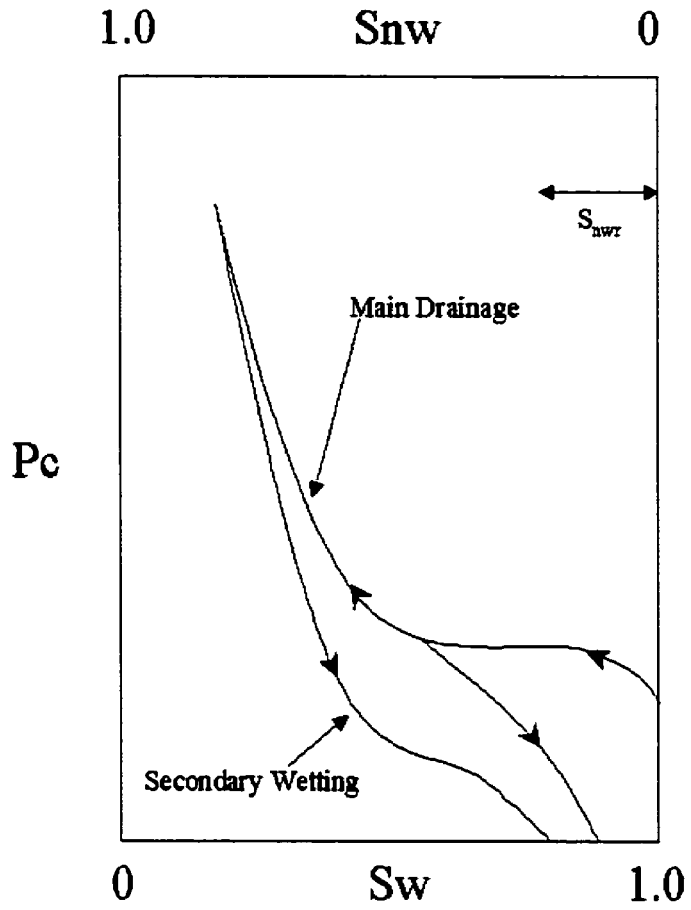

Figure B-4. Typical Capillary Pressure – Saturation Curve

The initial-residual relationship used in this work was developed from the experimental data of Mah (1992). The general form for a straight-line relationship is:

$$S_{wr}^{\cdot} = m * S_{w}^{\cdot} + b \qquad \text{[B-16]}$$

where S_{wr} is the wetting phase residual saturation, $S_w^{\cdot}$ is the minimum wetting phase saturation achieved along main drainage, m is the slope, and b is the intercept. Gerhard (1995) formulated

the equation in terms of the theoretical maximum nonwetting phase residual value (S_{nr}^{max}) which should be determined experimentally:

$$S_{wr}^{'} = S_{nr}^{\max}(S_{w}^{'} - 1) + 1 \qquad \text{[B-17]}$$

The work of Mah (1992) showed that the initial-residual relationship was relatively insensitive to fluid properties, and was primarily a function of medium properties. Gerhard (1995) felt this assumption fair and reasonable, given that a common pore size distribution parameter is used on all drainage curves independent of permeability.

Incorporation of the effects of hysteresis into the model required the identification of the "state" of each node in the model. That is, whether the node was on primary drainage, wetting, or at residual saturation. The functional relationship for capillary pressure would then depend on the state of the node, and would be unchanged for a node on drainage, equal to zero for a node at residual and, for a node on an imbibition curve equal to:

$$P_c = \frac{P_D S_e^{\left[\frac{-1}{\lambda}\right]}\left[S_{nr}^{\max}\left(S_e^{'} - 1\right) - S_e + 1\right]}{\left[S_{nr}^{\max}\left(S_e^{'} - 1\right) - S_e^{'} + 1\right]} \qquad \text{[B-18]}$$

The second functional relationship that will be affected by the incorporation of hysteresis is that of relative permeability. Recall that the relative permeability function for the nonwetting phase used in this work is the Brooks and Corey (1964) relationship:

$$k_{rn} = (1 - S_e)^2\left(1 - S_e^{\left(\frac{2+\lambda}{\lambda}\right)}\right) \qquad \text{[B-19]}$$

which is based upon the relative permeability being equal to zero at a wetting phase saturation of 1.0. Given that the model now allows for the trapping of nonwetting phase, the relative permeability will become zero at the nonwetting phase residual saturation (S_{nr}^{max}):

$$k_{rn} = \left(S_{nr}^{\max} - S_e\right)^2 \left(S_{nr}^{\max} - S_e^{\left(\frac{2+\lambda}{\lambda}\right)} \right) \qquad \text{[B-20]}$$

Testing of the hysteresis relationships incorporated into the code could not be compared to analytical solutions, as such solutions do not exist. In addition, comparison to other codes with non-linear hysteresis would not have been an adequate comparison, given the differences between the two methods.

The model was compared to Gerhard (1995), which used the identical hysteretic approach. The simulations consisted of a 1.0 m vertical column with the same porous media properties as described in Table B-1, discretized into 100 0.01 m elements and a constant hydrostatic wetting phase pressure distribution. Nonwetting phase was allowed to freely infiltrate the column from the top through a constant saturation boundary condition of S_w=0.5, but was prevented from exiting the bottom of the column. After 100s the boundary condition on the top was switched to free-exit and the NAPL was allowed to redistribute for 1×10^9 s. Figure B-5 shows the close agreement between the two models. The bottom 12 elements are still on the drainage curve, the elements up to approximately 0.3 m are on primary or secondary wetting, and the elements above the noticeable inflection point around 0.3 m are at residual.

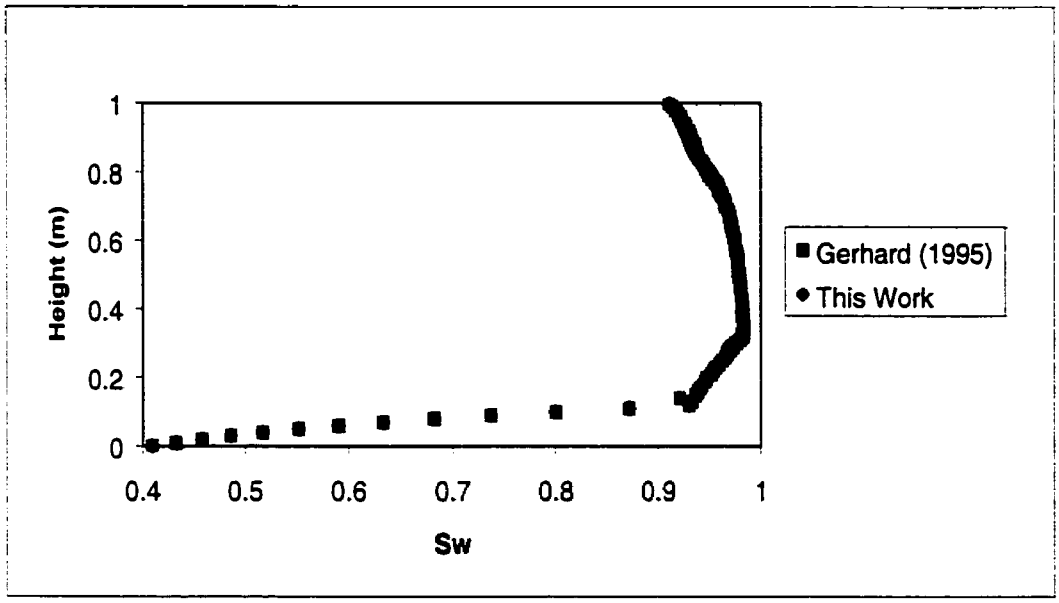

Figure B-5. Comparison of Hysteresis Behaviour to Gerhard et al. (1998)

B.6 Model Verification - Storage

Given the difficulties in matching conditions between available analytical models and the numerical model, it was felt that comparing the developed model to the USGS finite difference groundwater flow model MODFLOW would be sufficient to demonstrate the numerical model's abilities to accurately represent the effects of storage. The simulation domain consisted of a 10m by 10m horizontal aquifer of unit thickness with constant unit head boundary conditions on all exterior edges. A drainage well was simulated in the middle of the domain by assigning a constant head of 0m to the central node. The porous medium was a fine sand with a porosity of 0.35, a hydraulic conductivity of 1.0×10^{-6} m/s, and a compressibility of 1.0×10^{-8} m^2/N. Figure B-6 is a comparison of the two model's results along a line from the drainage well to the boundary, taken perpendicular to the boundary. Excellent agreement is evidenced in this figure.

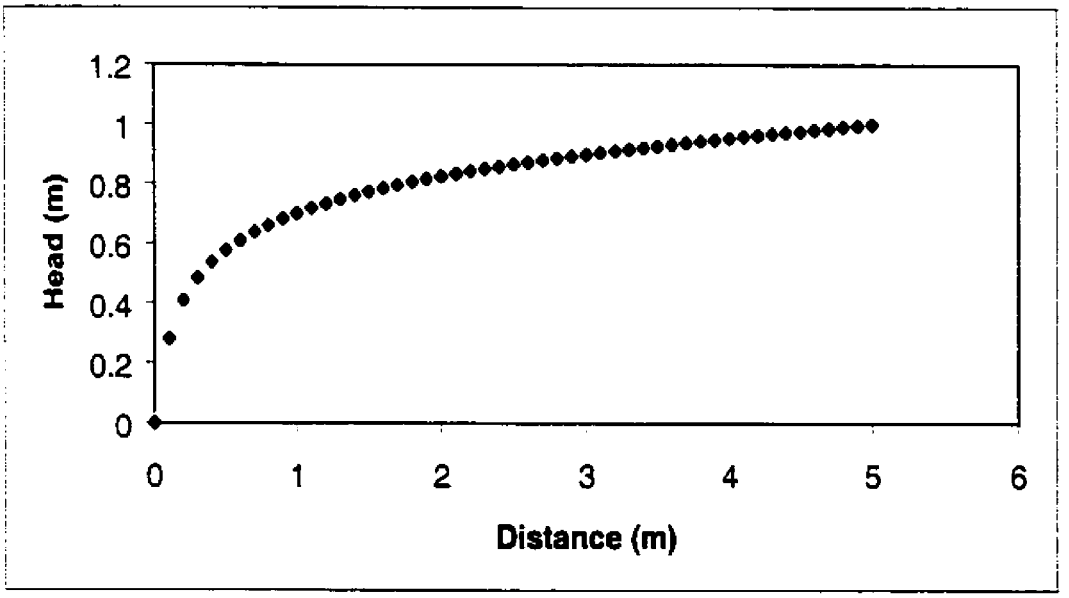

Figure B-6. Comparison of 2D Model to MODFLOW to Verify Storage Routine

B.7 Model Verification – Mass Transport

The previous sections have covered the verification and validation of the model with respect to single and two-phase flow phenomena. As was performed for the one-dimensional verification, it remains to demonstrate the model's ability to correctly simulate advection and dispersion. The problem considered in this section concerns the two-dimensional transport of solute from a fully penetrating injection well. Several assumptions are inherent in the analytical solution presented by Moench and Ogata (1981):

1) The injection rate of the well is constant
2) Groundwater velocity is entirely due to the injection well
3) A homogeneous, isotopic and infinite aquifer, and
4) Steady-state flow.

These assumptions are easily incorporated into the numerical simulation by ensuring the simulation is terminated before the contaminant front reaches the boundaries. The initial and boundary conditions are:

$$C(r,0)=0$$
$$C(r_w,t)=C_o \quad t>0 \qquad \text{[B-21]}$$
$$\left.\frac{\partial C}{\partial r}\right|_{r\to\infty}=0 \quad t>0$$

Where r_w is the radius of the injection well.

The numerical solution domain was discretized into 5202 triangular elements, each 0.06 m per side in the x and y directions. The injection rate used was 0.01 m^3/s, the permeability $1.02x10^{-12}$ m^2, the porosity was 0.3, D^* was set to 0, and the longitudinal and transverse dispersivities were identical and equal to 0.1 m.

The distribution of the simulated concentrations along the x-axis from the point source to the edge of the domain is plotted in Figure B-7 and is in good agreement with the analytical solution.

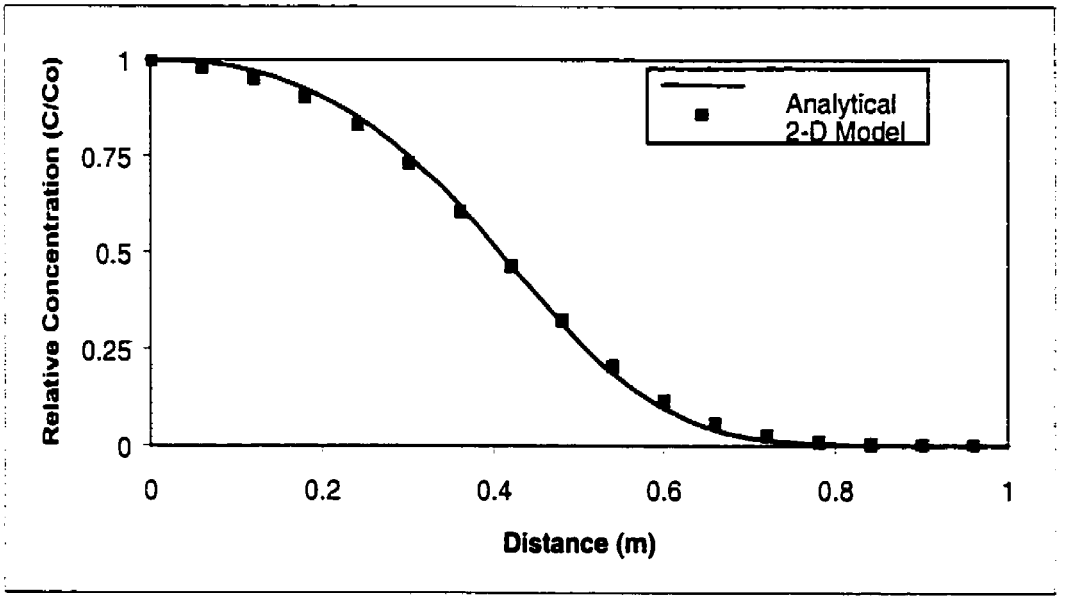

Figure B-7. Model Comparison to Analytical Solution for Mass Transport

B.8 Continuum Concept Modification

The modifications described to this point have involved transforming the model from a one-dimensional line element formulation into a more powerful two-dimensional form. The testing and verification that has been performed to this point has been exclusively performed on physical scenarios mimicking porous media applications. The two-dimensional model developed to this point could, however, be used to simulate two-phase flow and transport in a single fracture in the plane of the fracture. This, however, was not the overall goal of this research, and some method was required to allow for the simulation of flow and transport in fractures as well as in the intervening matrix.

The continuum concept of modelling was applied to the formulation to allow for the representation of flow and transport in both the fractures and the matrix. The matrix blocks of

the domain are discretized using triangular elements, similar to the methods used for porous media representation. The discretization is performed such that any rock fractures lie along edges of adjacent elements. The fractures are then discretized as one-dimensional line elements, and since they correspond to the sides of the triangular elements, the nodes comprising the fracture elements are coincident to those comprising the matrix elements. The use of the continuum concept allows for continuity of both wetting phase pressures and mole fractions at the fracture-matrix intersection. In addition it circumvents the need to explicitly calculate the fluid leakage and dispersion terms between the fracture and the matrix. The final system of discretized equations representing the superimposed fracture-matrix system is:

$$
\begin{aligned}
R^{\beta}_{i,I} \equiv & \left\{ \left[\phi c_{i\beta} x_{i\beta} + \rho_b K_d c_{i\beta} x_{i\beta} \right]_I^{N+1} \left[\phi c_{i\beta} x_{i\beta} + \rho_b K_d c_{i\beta} x_{i\beta} \right]_I^{N} \right\}_m \frac{V_{I_m}}{\Delta t} \\
& + \left\{ \left[\phi S_\beta c_{i\beta} x_{i\beta} + \rho_b K_d c_{i\beta} x_{i\beta} \right]_I^{N+1} - \left[\phi S_\beta c_{i\beta} x_{i\beta} + \rho_b K_d c_{i\beta} x_{i\beta} \right]_I^{N} \right\}_f \frac{V_{I_f}}{\Delta t} \\
& - \left[\sum_{J \in n_{c_m}} \left(\psi_{\beta J}^{N+1} - \psi_{\beta I}^{N+1} \right) \left(\frac{c_{i\beta} x_{i\beta}}{\mu_\beta} \right)_{ups(I,J)}^{N+1} \gamma_{IJ_m} \right] \\
& - \left[\sum_{J \in n_{c_f}} \left(\psi_{\beta J}^{N+1} - \psi_{\beta I}^{N+1} \right) \left(c_{i\beta} x_{i\beta} \frac{k_{r\beta}}{\mu_\beta} \right)_{ups(I,J)}^{N+1} \gamma_{IJ_f} \right] \\
& - \left[\sum_{J \in n_{c_m}} \left(c_{i\beta} \right)_{IJ+\frac{1}{2}}^{N+1} \left(\gamma'_{IJ_m} \right)_\beta \left(x_{i\beta_J} - x_{i\beta_I} \right)^{N+1} \right] \\
& - \left[\sum_{J \in n_{c_f}} \left(c_{i\beta} \right)_{IJ+\frac{1}{2}}^{N+1} \left(\gamma'_{IJ_f} \right)_\beta \left(x_{i\beta_J} - x_{i\beta_I} \right)^{N+1} \right] \\
& - \left\{ q_{i\beta} - I_{i\beta} \right\}^{N+1} V_I = 0
\end{aligned}
$$

[B-22]

where the added subscripts refer to contributions from the matrix connections (m) and the fracture connections (f). It should also be pointed out that in this formulation the nonwetting phase is prevented from entering the matrix under any circumstances. This property allows for the exclusion of the saturation and relative permeability terms from equation (B22) for the matrix connections. It is felt that this simplification is valid given the extreme physical scenario that would be required to cause entry into a rock matrix in a three-dimensional application.

B.9 Verification of the Continuum Model

A close analysis of the continuum modification shows that no alterations were made to the governing differential equations or to the discretized solution equations. This means that no changes were made to the basis functions or the influence coefficients. To ensure this, the two-phase flow scenario that was used in section B.4 was solved with the continuum model subject to the same parameters and boundary conditions. The difference now being that the flow is through a fracture rather than through porous media, and that the flow path is surrounded by permeable matrix. By setting the permeability of the matrix to an extremely small value ($\sim 10^{-25}$ m^2) the results predicted by the continuum model were identical to those of the non-continuum model.

The final verification exercise undertaken with the continuum model involved a combined steady-state flow and transient transport in a single fracture surrounded by a relatively impermeable but porous matrix. An analytical solution (CRAFLUSH, Sudicky and Frind, 1982) describing the transport of a solute in a system of parallel fractures is used for comparison.

The simulated domain is shown in Figure B-8, and consisted of a single vertical 30 um fracture surrounded by porous matrix rock. A fine discretization was required adjacent to the fracture to correctly catch the steep initial mole fraction gradients. The discretization is 0.005 m immediately adjacent to the fracture, grading to 0.25 m at the outer edge of the domain. A similar discretization is used in the vertical direction.

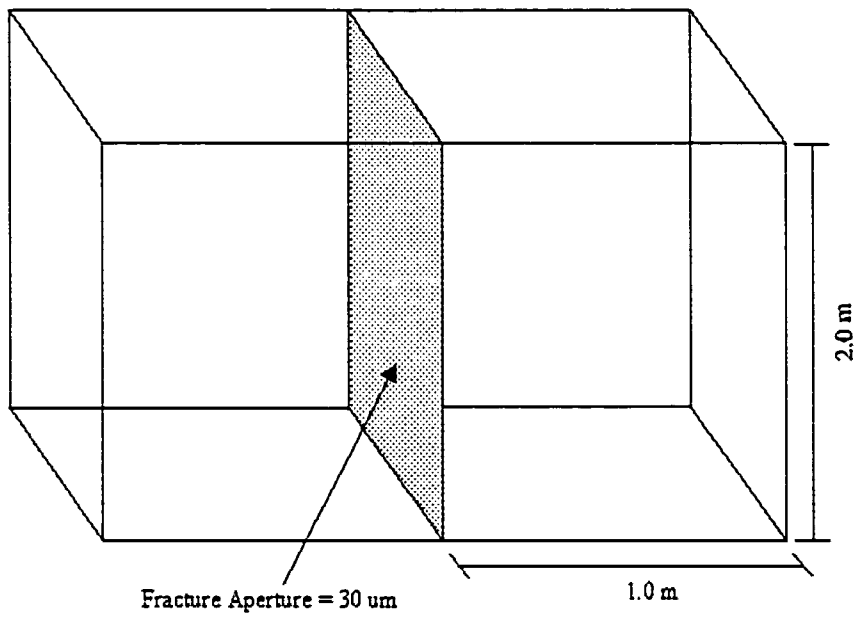

Figure B-8. Model Domain for Verification of Continuum Model

The parameters used in the verification are shown in Table B-3. Due to symmetry, only one side of the domain was modelled. The steady-state groundwater velocity within the fracture was 8.1717×10^{-5} m/s and contained a mole fraction of 9.2×10^{-4} at the upper inlet boundary of the fracture. Advective transport within the matrix was less than 10^{-10} m/s.

Figure B-9 shows the numerical solution of the concentration profiles along the fracture at times equal to 10 000s and 50 000s, and compares them to the analytical solution. The agreement between the two is excellent, with some numerical dispersion evident along the leading edge of the profiles.

Table B-3. Media Properties for Continuum Model Verification

Fracture Aperture	30 um
Fracture Longitudinal Dispersivity	0.01 m
Fracture Horizontal Dispersivity	0.001 m
Ground water Velocity in Fracture	8.1717×10^{-5} m/s
Fracture Porosity	1.0
Matrix Permeability	1.0×10^{-17} m/s
Matrix Longitudinal Dispersivity	0.1 m
Matrix Horizontal Transverse Dispersivity	0.03 m
Matrix Vertical Transverse Dispersivity	0.001 m
Matrix Porosity	0.3
Diffusion Coefficient	1.0×10^{-11}

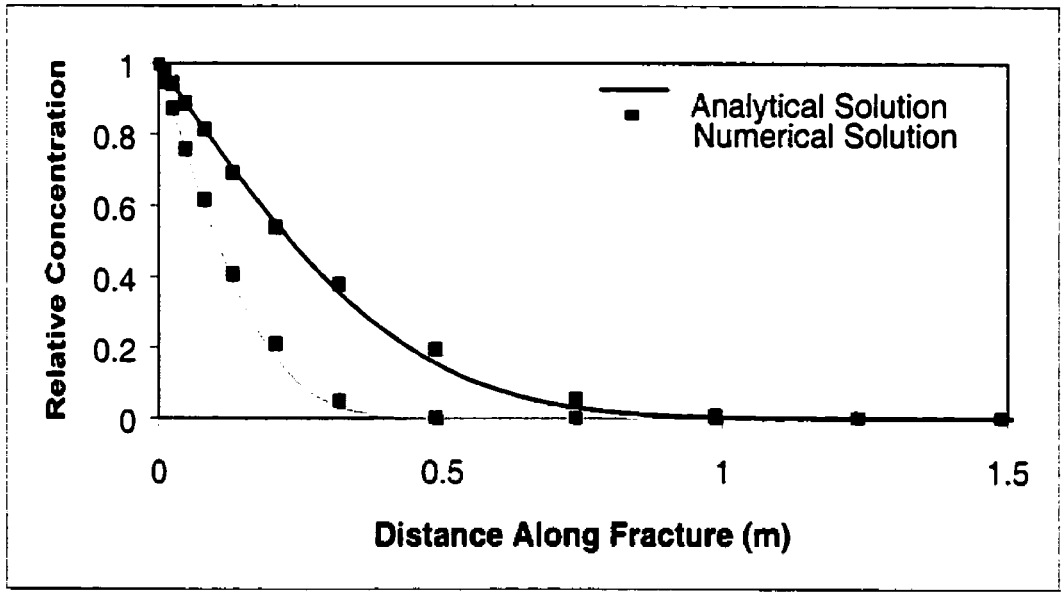

Figure B-9. Comparison of Model to CRAFLUSH

B.10 Sensitivity of the Continuum Model to Node Spacing

Recent work has found that the discretization of the model domain can have a significant influence on the predicted behaviour of DNAPL in a fractured environment (Slough et al., 1999). To investigate the sensitivity of the continuum model to this parameter, two tests were performed.

The first test consisted of simulating the intersection of a pair of identical 5m long fractures, one oriented vertically and the other oriented horizontally. DNAPL was introduced to the system through a constant capillary pressure boundary condition at the top end of the vertical fracture, and was allowed to exit freely out of the other ends of the fractures. Two sets of simulations were performed, with 100 μm fractures and 10 μm fractures. Three discretizations were used each time, ranging from 12.5 cm to 50 cm. The results of these tests are presented in Figure B-10 and B-11, and show that the DNAPL penetrated into the horizontal fracture in all cases. The

graph also shows the expected behaviour with respect to accuracy, that decreasing the node spacing decreases the depth of penetration into the horizontal fracture by reducing the smearing of the nonwetting front.

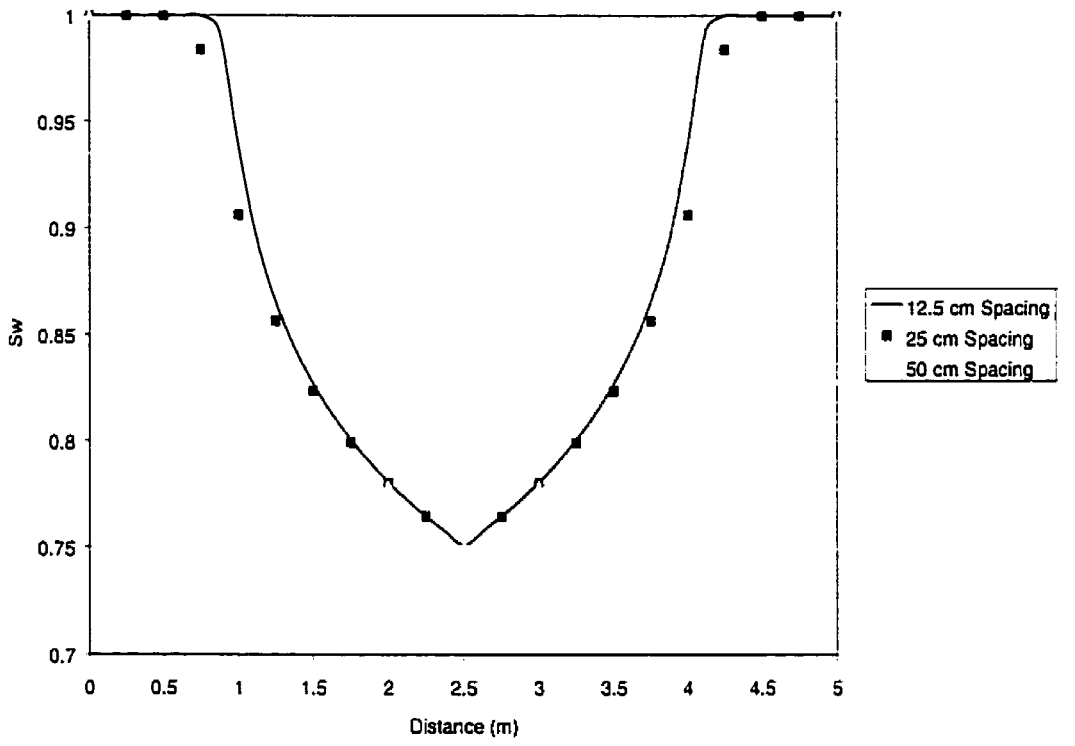

Figure B-10. Wetting Phase Saturations in Horizontal Fracture Showing Sensitivity to Nodal Discretization in 100 μm Fracture

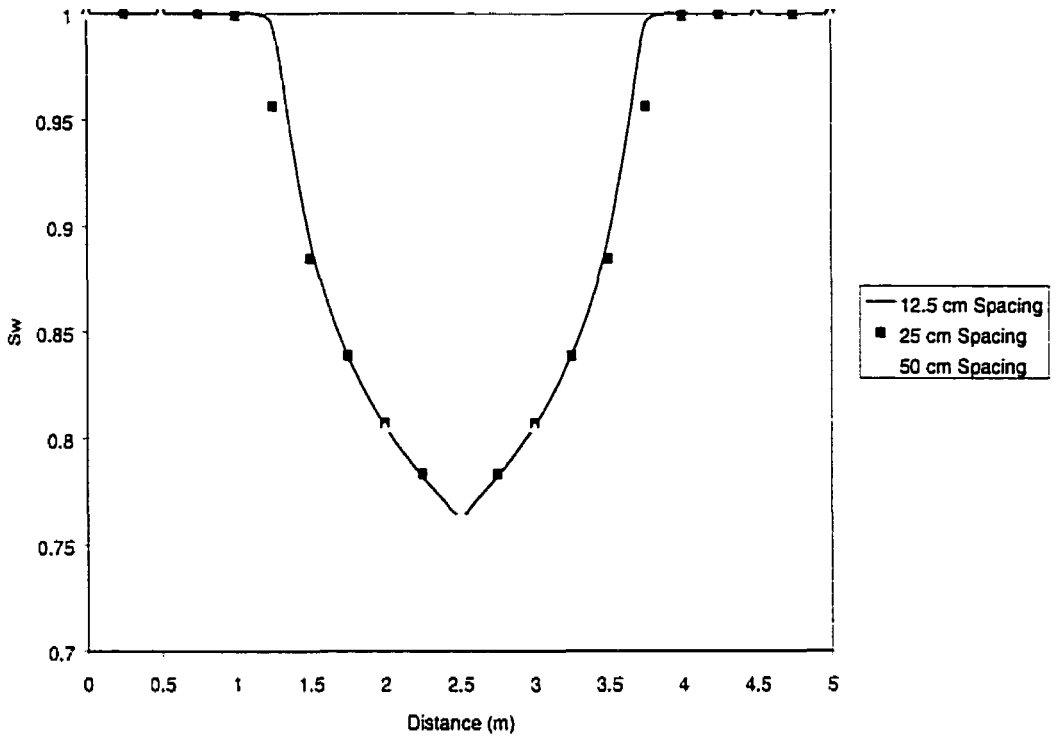

Figure B-11. Wetting Phase Saturations in Horizontal Fracture Showing Sensitivity to Nodal Discretization in 10 μm Fracture

The second test performed to investigate the sensitivity of the CVFE model to discretization was at a larger scale, and involved the simulation of DNAPL flow through a network of intersecting fractures of different apertures. The domain simulated is pictured in Figure B-12, and consisted of a 50m by 50 m granite block containing 144 fractures oriented horizontally and vertically. The upper boundary was again fixed at a constant capillary pressure, and the DNAPL was allowed to freely exit from the other three boundaries. The domain was discretized at three levels; coarse, fine, and extra fine, representing average element sizes of 0.514m, 0.331m, and 0.085m respectively. The simulation was allowed to run until the nonwetting phase flux out of the domain was equal to 99% of the nonwetting phase flux into the domain.

Figure B-13 displays the average nonwetting phase saturations in the domain in terms of invaded nodes (along fractures with entry pressures low enough to allow DNAPL entry) and in terms of all fracture nodes. The results are quite encouraging, showing that overall gross behaviour is the same in the system regardless of discretization, and that as the discretization gets finer the differences in the predicted values gets smaller. It is also to be noted that in the invaded nodes only case, the three discretizations are converging to the same solution at steady-state.

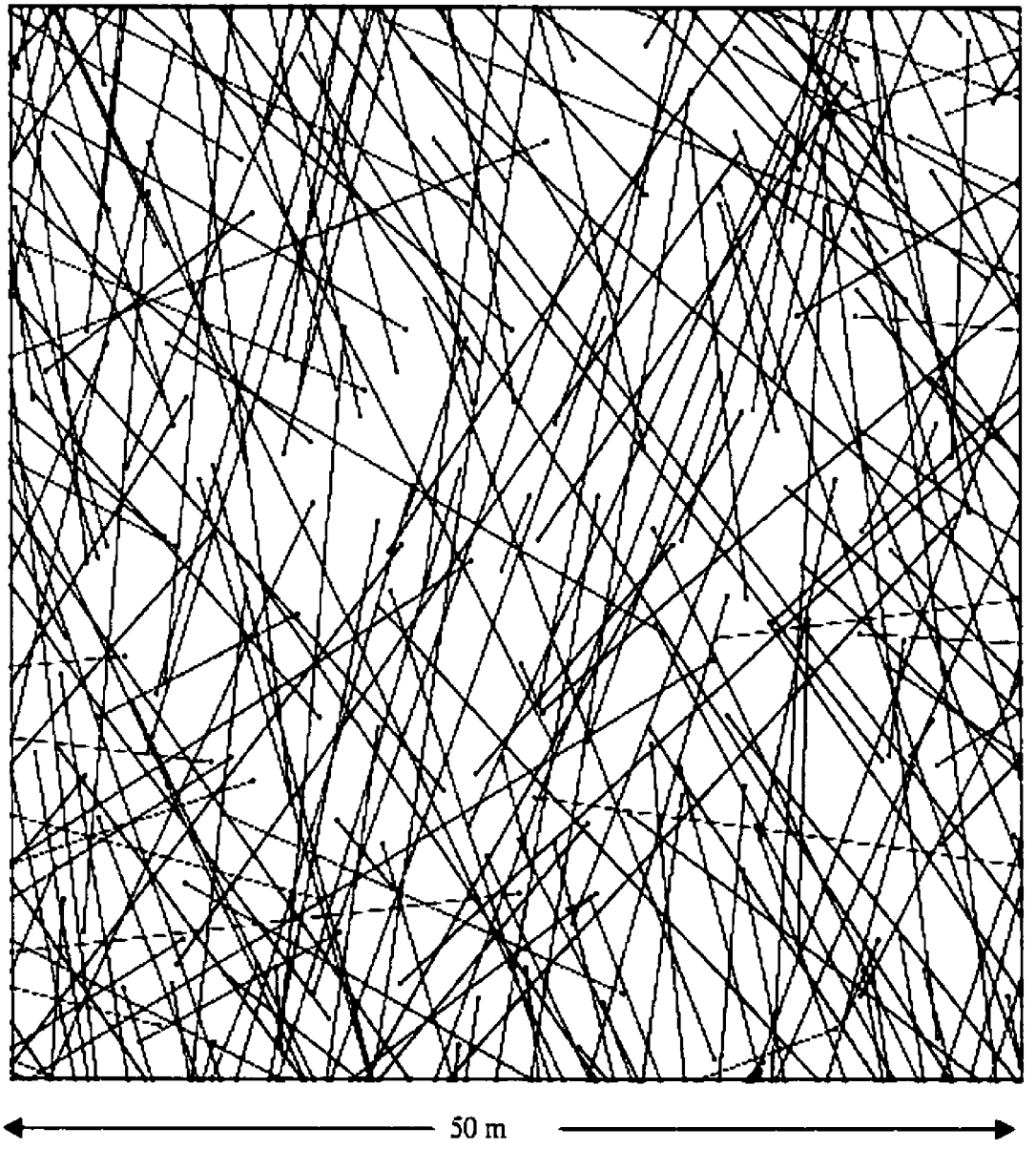

Figure B-12. Domain for Large-scale Discretization Sensitivity Check

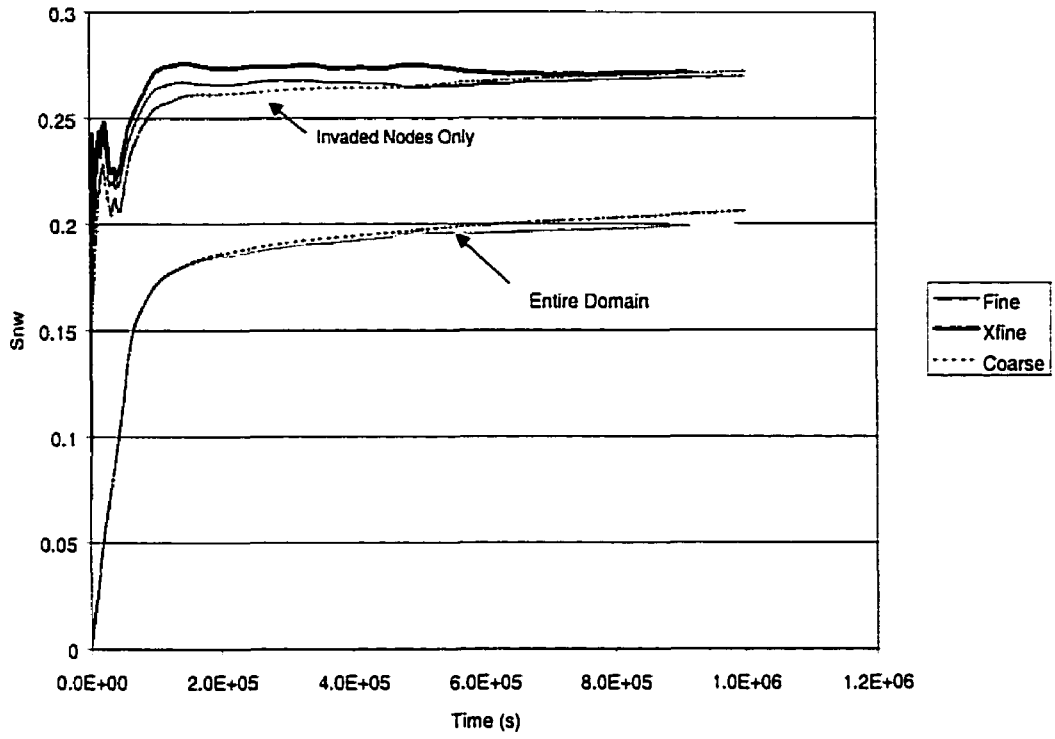

Figure B-13. Nonwetting Phase Saturations Averaged Over Entire Domain Showing Sensitivity to Nodal Discretization in Large-Scale Simulation

B.11 References

Aziz, K., and A. Settari. 1979. Petroleum Reservoir Simulation, Applied Science, London

Brooks, R.H., and A.T. Corey. 1964. Hydraulic Properties of Porous Media, Hydrol. Pap. 3, Colorado State University, Fort Collins, Co.

Blunt, M. and B. Rubin. 1992. Implicit Flux Limiting Schemes for Petroleum Reservoir Simulation, *J. Comp. Phys.*, 102, p 194-210

Liu, J., Delshad, M., Pope, G.A., and K. Sepehrnoori. 1994. Application of Higher-order Flux-limited Methods in Compositional Simulation, *Tran. Por. Media*, 16, p 1-29.

Moench, A.F., and A. Ogata. 1981. A Numerical Inversion of the Laplace Transform Solution to Radial Dispersion in a Porous Medium, *Water Res. Res.*, 17(1), p 250-253.

Saad, Y., and M. Schultz. 1988. GMRES: A Generalized Minimal Residual Algorithm for Solving Non-symmetric Linear Systems, *SIAM J. Sci. Stat. Comp.*, 7, p 856-869.

Slough, K.J., E.A. Sudicky, and P.A. Forsyth. 1999. Importance of Rock Matrix Entry Pressure on DNAPL Migration in Fractured Geologic Materials, *Ground Water*, 37(2), p 237–244.

Sudicky, E.A. and E.O. Frind. 1982. Contaminant Transport in Fractured Porous Media: Analytical Solution for a System of Parallel Fractures, *Water Res. Res.*, 18, p 1634–1642.

Unger, A.J.A., Forsyth, P.A., and E.A. Sudicky. 1995. Variable Spatial and Temporal Weighting Schemes for use in Multi-Phase Compositional Problems, *Adv. Water Res.*, 19, p 1-27.

van der Vorst, H.A. 1992. Bi-CGSTAB: A Fast and Smoothly Convergent Variant of BiCG for the Solution of Nonsymmetric Linear Systems, *SIAM J. Sci. Stat. Comp.*, 13, p 631-645.

van Leer, B. 1974. Toward the Ultimate Conservative Scheme. II. Monotonicity and Conservation Combined in a Second Order Scheme, *J. Comp. Phys.*, 14, p 361-370.

VanderKwaak, J.E. and E.A. Sudicky. 1996. Dissolution of Non-aqueous-phase Liquids and Aqueous-phase Contaminant Transport in Discretely-fractured Porous Media, *J. Cont. Hyd.*, 23, p 45-68

APPENDIX C - THREE-DIMENSIONAL MODEL DEVELOPMENT AND VERIFICATION

Model Description

The three-dimensional model developed in this appendix is solved through the use of a finite volume approach, and can handle the advection of the wetting and nonwetting phases, as well as the dispersion, diffusion, and sorption of the aqueous phase. The fractures are represented by two-dimensional planar elements, and must be aligned parallel to the Cartesian axes. The planar and polyhedral elements are fully linked, allowing for full transfer of the wetting and nonwetting phases.

C.1 Solution of the Governing Equations

The governing partial differential equation for the three dimensional model was identical to that of the two-dimensional model presented in appendix B. The model therefore has the ability to simulate the multiphase advective, dispersive, and diffusive flux of NAPL contaminants in a discrete fracture network, and allows for the equilibrium and non-equilibrium partitioning of NAPL between phases.

The most significant difference between the two- and three-dimensional formulations is that in the three-dimensional version the governing equations are discretized using the finite volume method, with three-dimensional block cells being used to represent the matrix of the system, and

two-dimensional rectangular planar cells used to represent the discrete fracture volumes. This separates the nodes representing the fractures from those representing the matrix unlike the continuum representation of the CVFE approach. The final form of the discretized equations is similar to that used for the finite element models previously discussed:

$$
\begin{aligned}
R^{\beta}_{i,I} \equiv & \left\{ \begin{array}{l} \left[S_\beta c_{t\beta} x_{i\beta} \phi + \rho_b K_d c_{t\beta} x_{i\beta} + c_{t\beta} x_{i\beta} (\alpha + \beta_w \phi) P_w \right]_I^{N+1} - \\ \left[S_\beta c_{t\beta} x_{i\beta} \phi + \rho_b K_d c_{t\beta} x_{i\beta} + c_{t\beta} x_{i\beta} (\alpha + \beta_w \phi) P_w \right]_I^{N} \end{array} \right\} \frac{V_I}{\Delta t} \\
& - \left[\sum_{J \in n_c} \left(\psi_{\beta J}^{N+1} - \psi_{\beta I}^{N+1} \right) \left(c_{t\beta} x_{i\beta} \frac{k_{r\beta}}{\mu_\beta} \right)_{ups(I,J)}^{N+1} \gamma_{IJ} \right] \\
& - \left[\sum_{J \in n_c} \left(c_{t\beta} \right)_{IJ+1/2}^{N+1} \left(\gamma'_{IJ} \right)_\beta \left(x_{i\beta_J} - x_{i\beta_I} \right)^{N+1} \right] \\
& - \left\{ q_{i\beta} - I_{i\beta} \right\}^{N+1} V_I = 0
\end{aligned}
\qquad \text{[C-1]}
$$

the difference between the two formulations being the form of the influence coefficients:

$$V_I = \Delta x \Delta y \Delta z \qquad \text{[C-2]}$$

$$\gamma_{IJ} = -k_{IJ+1/2} \frac{A_{IJ}}{\Delta x_{IJ}} \qquad \text{[C-3]}$$

$$\left(\gamma_{ij}^{\cdot} \right)_\beta = -(S_w)_{IJ+1/2}^{N+1} \left(\frac{\phi \, D_{iw\beta}}{S_w} \right)^N \frac{A_{IJ}}{\Delta x_{IJ}} \qquad \text{[C-4]}$$

where:

$$k_{IJ+1/2} = \frac{2 k_I k_J}{k_I + k_J} \quad \textit{(if I and J are both nodes of the same cell type)} \qquad \text{[C-5]}$$

$k_{IJ+\frac{1}{2}} = k_f$ *(if I is a matrix node and J is a fracture node)*

[C-6]

$A_{IJ} = Cross-sectional\ area\ between\ nodes\ I\ and\ J$

[C-7]

$\Delta X_{IJ} = Distance\ between\ nodes\ I\ and\ J$

[C-8]

And all other terms have been previously defined in Appendices A and B.

A limitation of the three-dimensional model is that all fracture plans must be in mutually perpendicular orientations. This would not be a limitation in a three-dimensional version of the CVFE formulation, but such a model would require that the 3-D discretization have the Delaunay property. Unfortunately it remains to be proven that a Delaunay discretization exists for any general three-dimensional volume (Shewchuk, 1986).

C.2 Model Verification

The identical two physical components of the three-dimensional model are verified against analytical solutions in this appendix. Simulations representing one-dimensional two-phase flow, and two-dimensional mass transport are presented. The use of identical governing equations for the three-dimensional model and the two-dimensional model means that any discrepancies between the two must lie in the accuracy of their respective discretization methods. Results for both models will be presented for two of the presented verification examples. Comparison of the two models is straight forward, but requires some precision given the tendency of nodes in identical dicretizations of finite element and finite volume (FV) domains to not be co-incident

(nodes in the CVFE formulation lie on the edges of volumes, nodes in the FV formulation lie in the middle of volumes).

C.2.1 Two-Phase Flow

The three-dimensional model was used to simulate the identical physical scenario as presented in Appendix B, section 4. Figure C-1 demonstrates that the results of the three-dimensional numerical model agree very well with the analytical solution of McWhorter and Sunada (1989). As was found with the one- and two-dimensional models there is a slight smearing of the advancing front due to the use of upstream weighting of the relative permeabilities. The predicted saturations of both the two- and three-dimensional models are essentially identical, as would be expected given their identical spatial discretizations and governing equations.

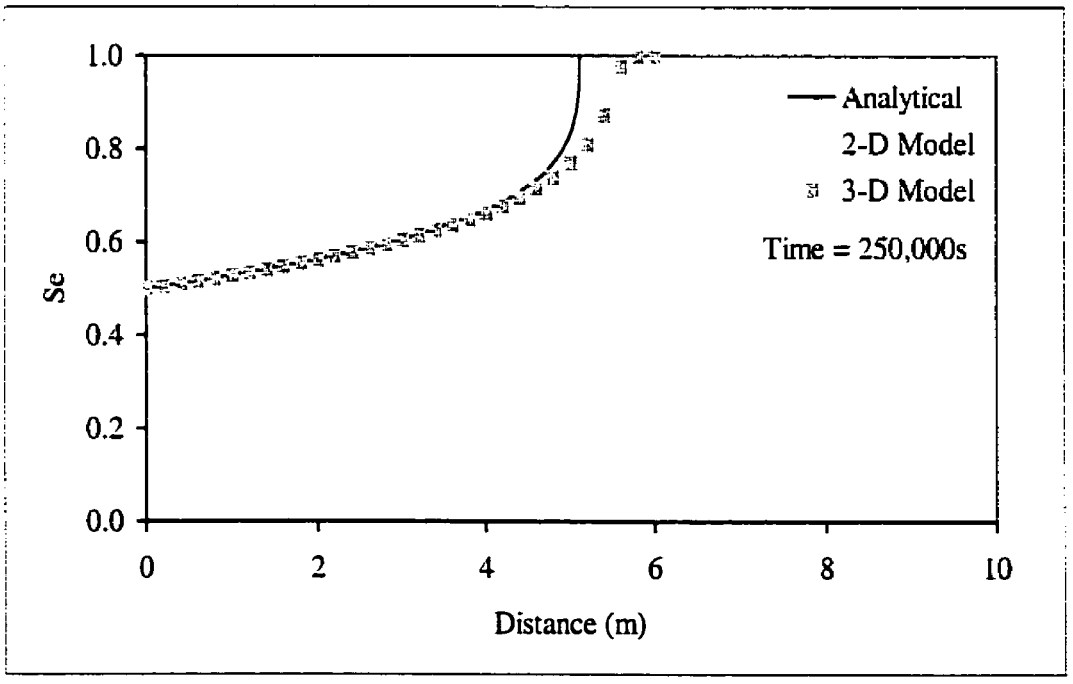

Figure C-1. Comparison of Numerical Simulation and Analytical Solution for Two-Phase Flow in Porous Media

C.2.2 Mass Transport in Porous Media

The ability of QUMPFS (Queen's University Multi-Phase Flow Simulator) to accurately simulate advection and dispersion in three-dimensions was verified through the use of AT123D (Yeh, 1993) a semi-analytical code for simulating mass transport in 1, 2, or 3 dimensions. The domain for the simulation is presented in Figure C-2 and consists of a source zone located within the middle of an aquifer 200 m in length, 50 m in width, and 20m in depth. The source function is a mass loading of contaminant to the aquifer without any wetting phase injection. Groundwater flow within the system is uni-directional along the x-axis. The hydrogeochemical properties of the simulation are presented in Table C-1.

The centre of the source zone for the simulations is located at $x=11m$, $y=25m$, and $z=10m$ and is 2m by 2m by 1m in size in the x, y, and z directions respectively. Given the discretization in QUMPFS into hexahedral elements, and the requirement of mass addition only at nodes, the actual source zone volume is somewhat larger at 3m by 3m by 1m. This was mimicked in AT123D to ensure compatibility between the models.

The results of the verification are presented in figures C-3 to C-5, which consist of comparisons of predicted concentrations along the three primary axes passing through the point (13.0, 25.0, 10.0). Due to numerical limitations AT123D is unable to render a stable solution for nodes within the source zone, thus the lack of data presented for AT123D in Figure C-3. These three figures show excellent agreement between QUMPFS and the analytical solution.

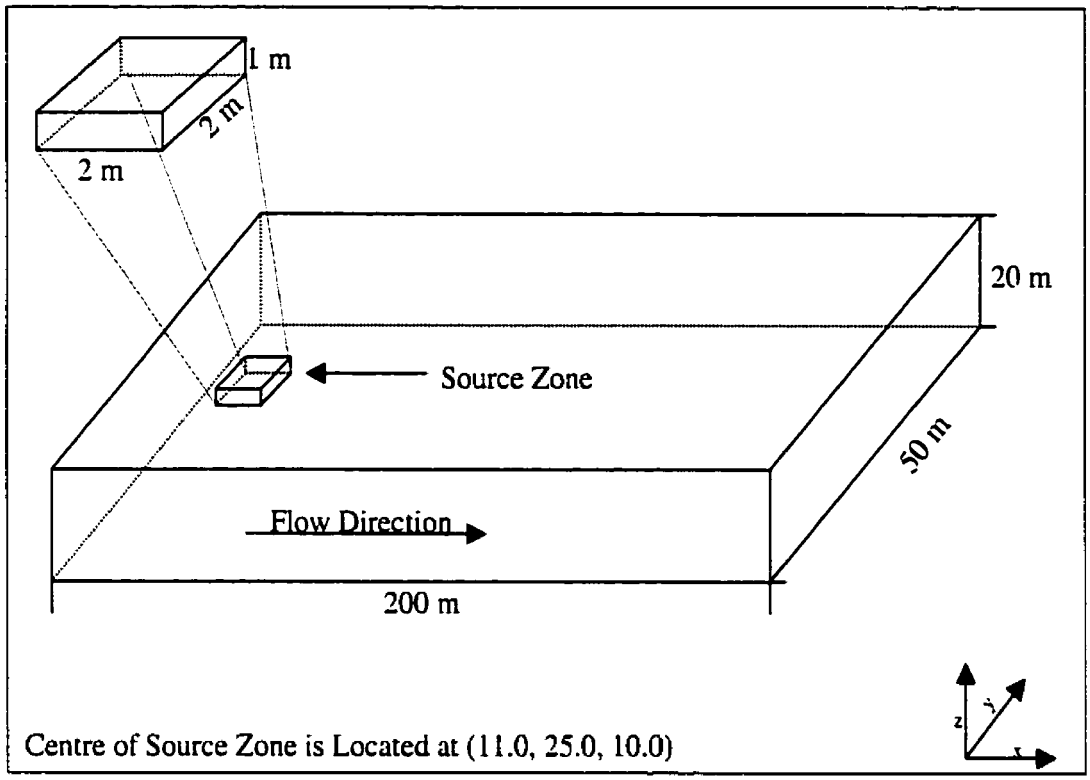

Figure C-2. Simulation Domain for Porous Media Mass Transport Verification

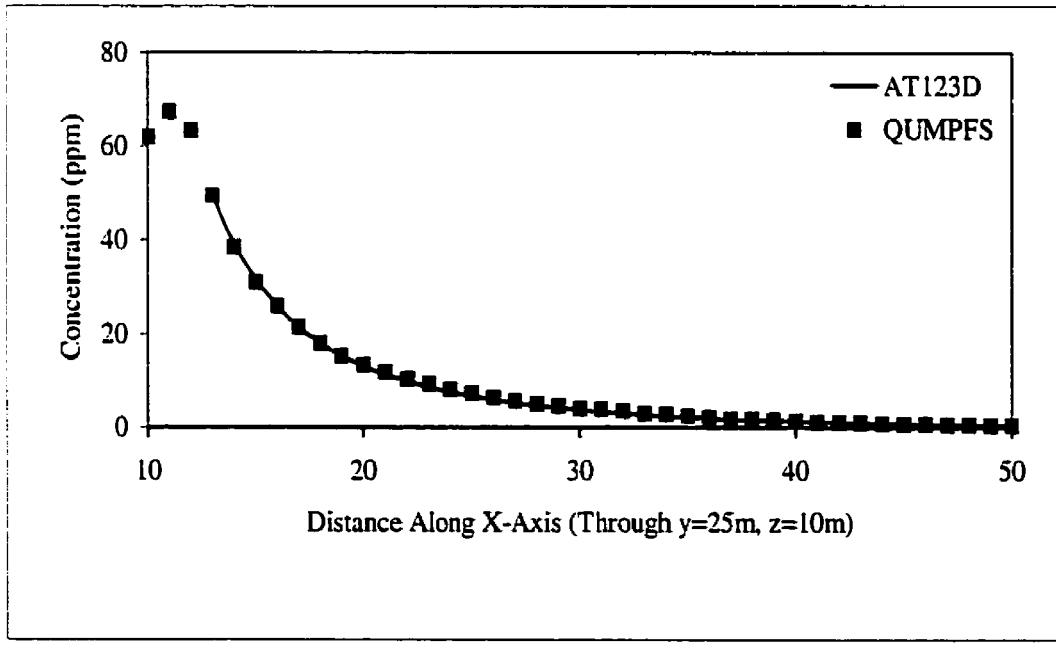

Figure C-3. Comparison of Numerical Simulation and Analytical Solution for Mass Transport in a Three-dimensional Aquifer (Comparison Along X-axis)

Table C-1. Media Properties for the Porous Media Mass Transport Verification

Porosity	0.2
Longitudinal Dispersivity	30.0 m
Transverse Dispersivity	5.0 m
Transverse Vertical Dispersivity	1.0 m
Ground water Velocity	1.25 m/d
Gradient (Along x-axis)	0.05
Aquifer Hydraulic Conductivity	5.787×10^{-5} m/s
Bulk Density	1400 kg/m^3
Distribution Coefficient	0.005 m^3/kg
Retardation Factor	8
Mass Loading Rate	1.0 kg/d
Time of Release	196 d

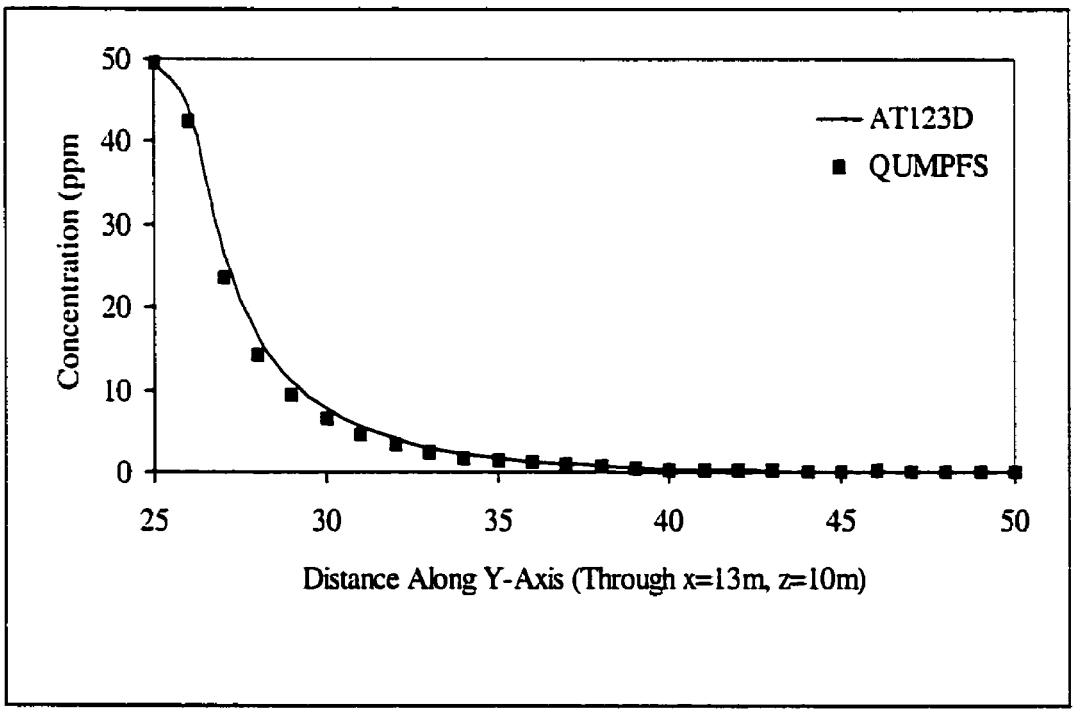

Figure C-4. Comparison of Numerical Simulation and Analytical Solution for Mass Transport in a Three-dimensional Aquifer (Comparison Along Y-axis)

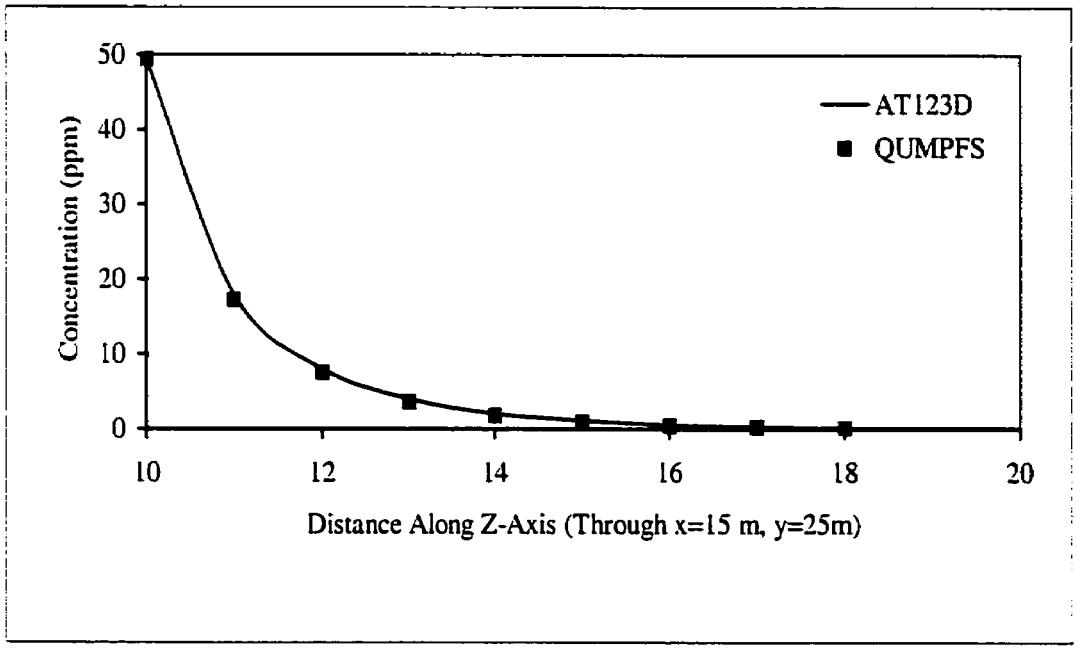

Figure C-5. Comparison of Numerical Simulation and Analytical Solution for Mass Transport in a Three-dimensional Aquifer (Comparison Along Z-Axis)

C.2.3 Mass Transport in Fractured Media

The results of section C.2.2 showed that the three-dimensional model was accurate in its simulation of advection and diffusion in a porous medium. The explicit representation of fractures through the use of two-dimensional planar elements, as employed in the three-dimensional model, discretizes the domain exactly without the need to employ the continuum assumptions of the two-dimensional model. This means that the treatment of advection-diffusion in a fractured medium is identical to the treatment of advection-diffusion in a porous medium.

The three-dimensional model's numerical simulation of advection-diffusion in a fractured medium was also tested against the analytical solution of Sudicky and Frind (1982) in a domain similar to that presented in Appendix B, section 9. The parameters used in the verification are shown in Table C-2. Due to symmetry, only one side of the domain was modelled. The steady-

state groundwater velocity within the fracture was 8.1717×10^{-6} m/s (an order of magnitude less than in Appendix B) and contained a mole fraction of 9.2×10^{-4} at the upper inlet boundary of the fracture. Advective transport within the matrix was less than 10^{-10} m/s.

Figure C-6 shows the numerical solution of the concentration profiles along the fracture after 115 days for both the two- and three-dimensional models, and compares them to the analytical solution. The agreement between the two is satisfactory, with some numerical dispersion evident along the leading edge of the profiles. As was found in the two-phase flow verification, the results of the two numerical simulations were virtually identical.

Table C-2. Media Properties for Fracture Mass Transport Verification

Fracture Aperture	10 um
Fracture Longitudinal Dispersivity	0.01 m
Fracture Horizontal Dispersivity	0.001 m
Ground water Velocity in Fracture	8.1717×10^{-6} m/s
Fracture Porosity	1.0
Matrix Permeability	1.0×10^{-17} m/s
Matrix Longitudinal Dispersivity	0.1 m
Matrix Horizontal Transverse Dispersivity	0.03 m
Matrix Vertical Transverse Dispersivity	0.001 m
Matrix Porosity	0.8
Diffusion Coefficient	2.0×10^{-10}

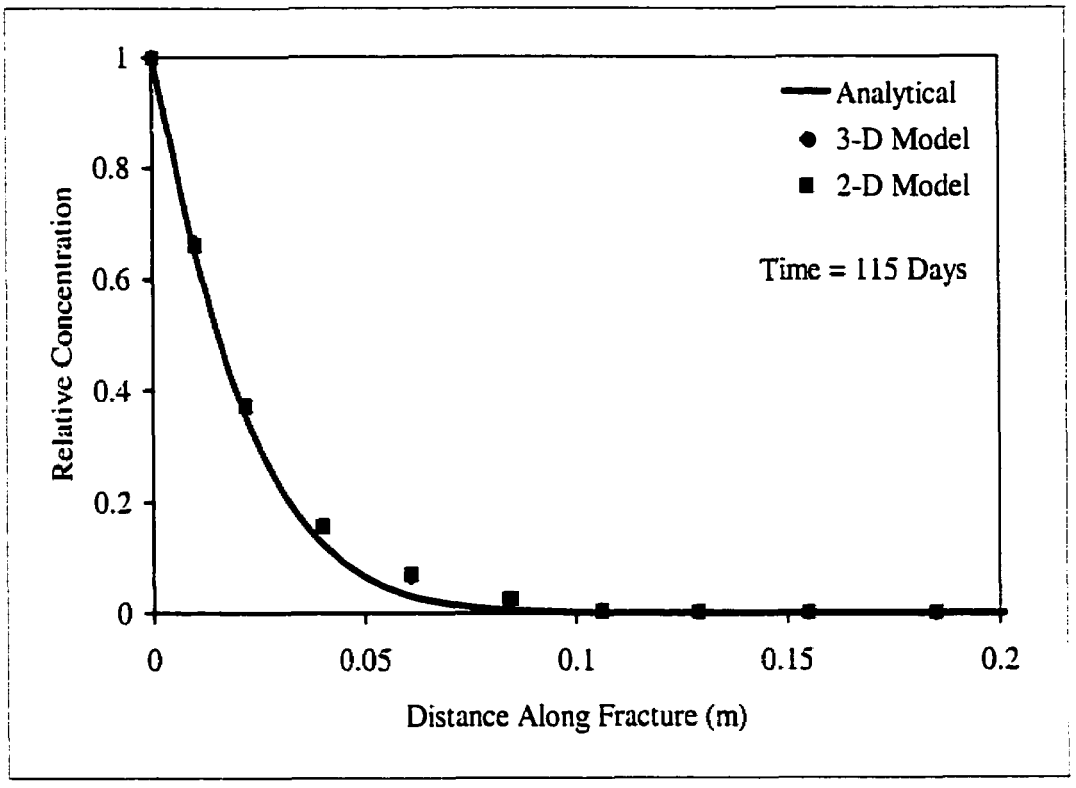

Figure C-6. Comparison of Numerical Simulation and Analytical Solution for Mass Transport in a Single Fracture System.

C.3 References

McWhorter, D.B., and D.K. Sunada. 1990. Exact Integral Solutions for Two-phase Flow, *Water Res. Res.*, 26(3), p 399-413.

Shewchuk, J.R. 1986. Triangle – A Two-dimensional Delaunay Triangulator, Carnegie Melon University, Pitt. PA.

Sudicky, E.A. and E.O. Frind. 1982. Contaminant Transport in Fractured Porous Media: Analytical Solution for a System of Parallel Fractures, *Water Res. Res.*, 18, p 1634–1642.

Yeh, G.T. 1993. Analytical Trnasient One-, Two- and Three-Dimensional Simulation of Waste Transport in the Aquifer System, International Ground water Modeling Centre, Colorado School of Mines, Golden, CO, 79 pgs.